Guidelines for Structural Control

by

Felix Weber, Glauco Feltrin, and Olaf Huth

Structural Engineering Research Laboratory,
Swiss Federal Laboratories for Materials Testing and Research
Dübendorf, Switzerland

Dübendorf, March 2006

CONTENTS

LIST OF FIGURES **4**

LIST OF TABLES **9**

1 INTRODUCTION **10**

1.1 GOAL 10
1.2 DEFINITION OF THE TERM "STRUCTURAL CONTROL" 10
1.3 STRUCTURE OF GUIDELINES 10

2 INCREASING DAMPING **11**

2.1 DAMPING DEVICES 11
2.1.1 Passive dampers *11*
2.1.1.1 Linear viscous damper 11
2.1.1.2 Nonlinear viscous damper 17
2.1.1.3 Viscoelastic damper 20
2.1.1.4 Coulomb friction damper 26
2.1.1.5 Structural friction damper 31
2.1.1.6 Hysteretic damper 33
2.1.1.7 Shape memory alloy damper 39
2.1.1.8 Passive tuned mass damper 47
2.1.1.9 Tuned liquid damper 67
2.1.2 Semi-active devices *71*
2.1.2.1 Defintion of term "semi-active" 71
2.1.2.2 Magnetorheological/electrorheological fluid damper 73
2.1.2.3 Controlled shape memory alloy 97
2.1.3 Actuators *100*
2.1.3.1 Actuators for increase of damping 100
2.1.3.2 Hydraulic aggregate 102
2.1.3.3 Piezo actuator 105
2.2 CONTROL ALGORITHMS 113
2.2.1 Control strategies *113*
2.2.1.1 Feedback control 113
2.2.1.2 Feed forward control 114
2.2.1.3 Passive control 114
2.2.1.4 References 114
2.2.1.5 Notations 115
2.2.2 Active damping with collocated pairs *117*
2.2.2.1 Linear compensators 117
2.2.2.2 Active damping with collocated actuator sensor pairs 120
2.2.2.3 References 126
2.2.2.4 Notations 126
2.2.3 Optimal control *128*
2.2.3.1 State space representation 128
2.2.3.2 Linear quadratic regulator 129
2.2.3.3 Linear Quadratic Gaussian noise control 131
2.2.3.4 References 136
2.2.3.5 Notations 137
2.2.4 Other control algorithms *140*

2.2.4.1 Fuzzy control 140
2.2.4.2 Neural network control 142
2.2.4.3 References 144
2.2.4.4 Notations 144

3 VIBRATION ISOLATION 146

3.1 PASSIVE VIBRATION ISOLATION 146
3.1.1 Theoretical background 146
3.1.2 Design issues 147
3.1.2.1 Low tuning 147
3.1.2.2 High tuning 148
3.1.2.3 Base isolation 148
3.1.3 Testing and validation 148
3.1.4 Implementation 149
3.1.5 References 149
3.1.6 Notations 150
3.2 ACTIVE VIBRATION ISOLATION 151
3.2.1 Scope 151
3.2.2 Passive isolator 151
3.2.3 Active isolator 153
3.2.3.1 Velocity feedback 153
3.2.3.2 Force feedback 154
3.2.3.3 Flexible clean body 154
3.2.4 References 155
3.2.5 Notations 155

LIST OF FIGURES

Figure 1: Linear viscous damping: a) force displacement and b) force velocity trajectories for periodic excitation. 12
Figure 2: Nonlinear viscous damping at small velocities due to seal friction. 12
Figure 3: Viscous damping device (Connor (2001)). 14
Figure 4: Viscous damper, 450 kN (http://www.taylordevices.com/3seismic.htm). 14
Figure 5: Schematic test set-up. 15
Figure 6: Measurement of damper behaviour at Empa. 15
Figure 7: Mean power equivalent nonlinear viscous damper. 18
Figure 8: Behaviour of: a) pure elastic materials, b) and c) of viscoelastic materials. 20
Figure 9: Example of a viscoelastic damping device according to Connor (2001). 22
Figure 10: Single bearing test machine (Aiken et al. (1989)). 23
Figure 11: Cyclic hysteresis loop of a bolted rubber bearing (Aiken et al. (1989)). 23
Figure 12: Bearing system design proposed by Aiken et al. (1989). 24
Figure 13: Coulomb friction: a) force displacement trajectory, b) force velocity trajectory; c) force velocity trajectory of real Coulomb friction dampers (e.g. MR dampers at constant current). 26
Figure 14: Limited Slip Bolted Joints (Pall et al. (1980)). 28
Figure 15: X-braced Friction Damper (Pall and Marsh (1982)). 28
Figure 16: Sumitomo Friction Damper (Aiken and Kelly (1990)). 29
Figure 17: Energy Dissipating Restraint (EDR) (Nims et al. (1993)). 29
Figure 18: Structural damping: a) force displacement trajectory and b) force velocity trajectory. 31
Figure 19: Hysteretic damping: a) stress strain relation, b) real hysteretic damper behaviour, c) idealized hysteretic damper behaviour. 33
Figure 20: Ideal elastic-plastic damping device according to Jones (2001). 34
Figure 21: X-shaped Plate Damper. 34
Figure 22: Stress strain curves and transformation temperature profiles for “actuator like” change of strain and stiffness at constant stress (Janke et al. (2005)). 39
Figure 23: Stress strain curves and transformation temperature profiles for shape memory effect in the case of free strain recovery and constraint strain recovery (Janke et al. (2005)). 40
Figure 24: Stress strain curves and transformation temperature profiles for the so-called superelastic behaviour (Janke et al. (2005)). 40
Figure 25: Stress strain curves and transformation temperature profiles for martensitic hysteretic damping (Janke et al. (2005)). 41
Figure 26: Hysteresis loops for: a) superelastic SMA behaviour and b) martensitic hysteretic damping (Janke et al. (2005)). 41
Figure 27: Torsion bar design (Witting and Cozzarelli (1992)). 41
Figure 28: Stress strain diagram used for bilinear damper model (Witting and Cozzarelli (1992)). 44
Figure 29: Force displacement loops (Witting and Cozzarelli (1992)). 44
Figure 30: Typical implementation of a TMD for vertical vibration mitigation of bridges. 48
Figure 31: Two degree of freedom model of a TMD attached to a primary structure. Left: Excitation force $f(t)$ acting on the primary mass. Right: Excitation through base acceleration $\ddot{u}_g(t)$ 49
Figure 32: Methods for H_∞ norm optimization of a TMD applying the fixed points method. 51
Figure 33: Methods for H_∞ norm optimization of a TMD applying the real roots method. 51
Figure 34: Effects of poor frequency tuning of a TMD on the dynamic magnification factor of the displacement of the primary system. 52

Figure 35: Effects of poor damping tuning of a TMD on the dynamic magnification factor of the displacement of the primary system. 52
Figure 36: Optimal TMD frequency for minimizing the displacement of the primary system with respect to the H_∞ norm. 53
Figure 37: Optimal TMD damping ratios for minimizing the displacement of the primary system with respect to the H_∞ norm. 53
Figure 38: Maximum of the non-dimensional transfer function of the displacement of the primary system for parameters minimizing the displacement of the primary system with respect to the H_∞ norm. 53
Figure 39: Maximum of the non-dimensional transfer function of the relative displacement for parameters minimizing the displacement of the primary system with respect to the H_∞ norm. 53
Figure 40: Mitigation factor of a TMD optimized for minimizing the displacement of the primary system with respect to the H_∞ norm. 53
Figure 41: Amplification due to a perturbation of frequency tuning of a TMD optimized for minimizing the displacement of the primary system with respect to the H_∞ norm ($\delta = \eta_t / \eta_{t,\infty} - 1,\ \mu = 0.02$). 53
Figure 42: Normalized variance of the displacement of the primary system. 55
Figure 43: Optimal TMD frequency for minimizing the variance of the displacement of the primary system with respect to the H_2 norm. 56
Figure 44: Optimal TMD damping ratios for minimizing the variance of the displacement of the primary system with respect to the H_2 norm. 56
Figure 45: Minimum of the non-dimensional variance of the displacement of the primary system for parameters minimizing the variance of the displacement of the primary system with respect to the H_2 norm. 56
Figure 46: Non-dimensional variance of the relative displacement of the mass of the TMD for parameters minimizing the variance of the displacement of the primary system with respect to the H_2 norm. 56
Figure 47: Mitigation factor of a TMD optimized for minimizing the displacement of the primary system with respect to the H_2 norm. 56
Figure 48: Amplification due to a perturbation of frequency tuning of a TMD optimized for minimizing the displacement of the primary system with respect to the H_2 norm ($\delta = \eta_t / \eta_{t,\infty} - 1,\ \mu = 0.02$). 56
Figure 49: Schematic illustration of a sloshing (a) and a column tuned liquid damper (b) coupled to a primary structure. 67
Figure 50: Principal parameters of sloshing and column TLD. 67
Figure 51: Definitions and characteristics of damping devices often used in structural control. 71
Figure 52: Rotational MR damper, force range approximately [10, 320] N. 73
Figure 53: Cylindrical MR damper with gas pocket (accumulator) for compensation of piston volume; force range approximately [70, 1800] N. 73
Figure 54: Schematic steady-state damper behaviour of MR dampers. 74
Figure 55: Measured MR damper behaviour in pre- and postyield regions (MR damper of Maurer Söhne). 74
Figure 56: Force displacement trajectories including transient measurement data from preyield to postyield regions (MR damper of Maurer Söhne). 74
Figure 57: Simple Bouc-Wen modelling approach for MR-dampers. 76
Figure 58: Fitted inverse MR damper function. 76
Figure 59: Testing damping devices. 77
Figure 60: Transient measurement data due to MR damper behaviour in preyield and postyield regions with force overshoot, fairly small MR fluid viscosity. 77
Figure 61: Transient measurement data due to MR damper behaviour in preyield and postyield regions, no force overshoot, fairly large MR fluid viscosity. 77

Figure 62: MR damper force response on approximate velocity step at 0 A. 78
Figure 63: MR damper force response on approximate velocity step at 4 A. 78
Figure 64: Cable-stayed “Dongting Lake Bridge” in China, equipped with MR dampers of LORD Corporation. 79
Figure 65: Cable-stayed ”Eiland Bridge“ nearby Kampen, The Netherlands, equipped with one MR damper of Maurer Söhne for long-term field tests and damping measurements. 79
Figure 66: Cable-stayed „Dubrovnik Bridge“ nearby Dubrovnik, Croatia. 80
Figure 67: Flow chart of damper design procedure. 82
Figure 68: Cable/damper system with distributed disturbance force according to the shape of the excited mode (here shown for the first vibration mode). 82
Figure 69: Characteristics of linear viscous and friction dampers. 83
Figure 70: Force displacement trajectories of MR damper of the “Eiland Bridge“. 84
Figure 71: Force current relation of MR damper of the “Eiland Bridge“. 84
Figure 72: Instrumentation of MR damper on the “Eiland Bridge” nearby Kampen, The Netherlands. 85
Figure 73: Taking decay measurements on the “Eiland Bridge” nearby Kampen, The Netherlands. 85
Figure 74: Sketch of decay measurements on the ”Eiland Bridge“ nearby Kampen, The Netherlands. 86
Figure 75: Clamping of cables. 86
Figure 76: Measured vibration decay at 12% cable length and damper position with MR damper at 0 A. 86
Figure 77: Measured vibration decay at 12% cable length and damper position with MR damper at 0.4 A. 86
Figure 78: Measured vibration decay at 12% cable length and damper position with MR damper at 2.0 A. 87
Figure 79: Measured vibration decay at 12% cable length and damper position of free cable. 87
Figure 80: Exponential approximation of linear decay within the amplitude range from 95% to 50%. 88
Figure 81: Evaluated mean logarithmic decrement. 89
Figure 82: Schematic controller structure. 89
Figure 83: Displacement sensor and MR damper on the “Eiland Bridge” nearby Kampen, The Netherlands. 90
Figure 84: Solar panel and controller box mounted on the lightning pylon on the “Eiland Bridge” nearby Kampen, The Netherlands. 90
Figure 85: Emulation of desired damping characteristics using feedback controlled actuators. 92
Figure 86: Characteristics of real “linear viscous dampers“. 92
Figure 87: Stress-strain curves for the superelastic behaviour of SMAs at different temperatures. 98
Figure 88: Different moduli of elasticity for martensite and austenite. 98
Figure 89: Hydraulic aggregate, mounted on a steel frame. 102
Figure 90: Schematic of a piezo-electric single layer element (http://www.piezomechanik.com/). 106
Figure 91: Schematic of an axially acting multilayer piezo stack (http://www.piezomechanik.com/). 106
Figure 92: Schematic of a stacked ring actuator (http://www.piezomechanik.com/). 107
Figure 93: Schematic of an actuator with prestress (http://www.piezomechanik.com/). 107
Figure 94: Schematic of a piezo actuated system (http://www.piezomechanik.com/). 108
Figure 95: Schematic voltage/stroke diagram of a stack actuator (http://www.piezomechanik.com/). 108
Figure 96: Schematic voltage force relation of a piezo stack (http://www.piezomechanik.com/). 109

Figure 97: Maximum piezo actuator stroke versus maximum (blocking) piezo actuator force (http://www.piezomechanik.com/). 109
Figure 98: Approximately linear relation between stroke and charge content of piezo actuators (http://www.piezomechanik.com/). 110
Figure 99: Creep of piezo actuators (http://www.piezomechanik.com/). 110
Figure 100: Closed-loop structure of feedback control. 113
Figure 101: Closed-loop structure of feedback control including actuator and sensor dynamics. 113
Figure 102: Structure of feed forward control. 114
Figure 103: Open-loop structure of passive control. 114
Figure 104: Structure of parallel PID controller with inverse plant model NL^{-1}. 117
Figure 105: Bode diagram of P, I, D elements, and of low pass filter of 2nd order. 117
Figure 106: Bode diagram of a parallel PID controller with low pass filter of 2nd order for a good “roll-off”. 118
Figure 107: Characteristics of Lead and Lag elements shown in the Bode Diagram. 118
Figure 108: Plant of 3rd order with proportional gain only. 120
Figure 109: Root Locus of 3rd order plant with feedback proportional gain K_P only. 120
Figure 110: Closed-loop structure of direct velocity feedback for collocated actuator sensor pairs. 121
Figure 111: Four mass system. 121
Figure 112: Transfer function of four mass system with force input and velocity output at mass no.1. 122
Figure 113: Placement of closed-loop pole for maximum additional damping of mode 1 (direct velocity feedback). 122
Figure 114: Comparison between very low damped plant and plant with optimally damped mode 1. 123
Figure 115: Location of closed-loop poles of all four modes for maximum damping of mode 1. 123
Figure 116: State space representation of the plant. 129
Figure 117: Plant in SSR, all state variables measured, full state feedback with stochastic LQ Regulator. 129
Figure 118: Real plant with full state observer and regulator. 135
Figure 119: Observer and regulator design. 135
Figure 120: Schematic operating range of magnetorheological fluid dampers. 136
Figure 121: Inverted pendulum on a cart. 141
Figure 122: Structure of a fuzzy controller. 141
Figure 123: The steps of fuzzification, inference, and defuzzification. 142
Figure 124: Black box identification by training of neural networks. 143
Figure 125: Neural network consisting of neurons (weights and transfer function) and layers. 144
Figure 126: Schematic representation of vibration isolation systems. Left: Isolation reducing the effects of the excitation force acting on the structure. Right: Isolation reducing the effects of a forced excitation of the support. 146
Figure 127: Force transmissibility for an isolator consisting of a linear spring and dashpot acting in parallel for different damping ratios. 147
Figure 128: Rubber bearing applied for base isolation. 149
Figure 129: Shear displacement test of a rubber bearing for base isolation. 149
Figure 130: i) Operating system (1) generating disturbance forces. ii) Sensitive device (1) excited by vibrating support structure (2). iii) Active vibration isolation with velocity feedback and force actuator (“skyhook damper”). 151
Figure 131: Magnitude of transmissibility for different damping ratios. 153

Figure 132: i) Velocity feedback for flexible clean body. ii) Force feedback for flexible clean body. 153

LIST OF TABLES

Table 1: Non-dimensional transfer functions for various excitations and response parameters. 62
Table 2: Approximate solutions of the H_∞ optimization problem for primary systems with vanishing structural damping ($\zeta_p = 0$). 63
Table 3: Closed form expressions of the non-dimensional H_2 norm for various excitations and response parameters. 64
Table 4: Exact solutions of the H_2 optimization problem for primary systems with vanishing structural damping ($\zeta_p = 0$). 65
Table 5: Approximate solutions of the H_2 optimization problem for primary systems with structural damping ($\zeta_p > 0$). 66
Table 6: Properties of longest stay cable of “Eiland Bridge”. 84
Table 7: Possible fuzzy rules for inverted pendulum. 141
Table 8: Fuzzy logic operations. 142
Table 9: Properties of critically damped active isolator. 154

1 INTRODUCTION

1.1 Goal

The goal of this guideline is to give an overview of damping devices and control algorithms that are often used in the field of structural control of civil structures. From this point of view, the guideline may represent a helpful document and a source of ideas and references for engineers and scientists working in this research area.

1.2 Definition of the term “Structural Control”

This guideline focuses on “Structural Control” of civil and large scale mechanical structures but not on macro or micro sized structures. Prestressing of structures using strain actuators in order to produce a desired shape or prestress of the structure will not be treated within this document although shape control belongs to the wide field of structural control. The presented guideline describes the common damping devices and control methods applied for suppression of undesired structural vibrations that occur after the erection of the structure. Hence, this guideline describes the tools for vibration mitigation of civil structures.

1.3 Structure of guidelines

In the second chapter, the guideline describes control devices and control methods that are implemented in order to increase the damping of structures. This is the case when additional dampers or actuators, respectively, are attached to vibrating structures and are controlled by a control law. The control algorithms may be part of an open loop system or may work in a closed loop, which allows for controlling the device force according to the actual vibration state.

In contrast to the second chapter, the third chapter gives an overview of vibration isolation systems. Here, the target is not to enhance the structural damping using external damping devices but to isolate sensitive structures from disturbances. This chapter is divided into two parts. First, passive isolators are described, then, active vibration isolation is presented.

2 INCREASING DAMPING

Within the first subchapter, an overview of existing damping devices is given. These damping devices include passive dampers, controllable dampers, and actuators. Passive dampers are characterized by constant damping properties given by their materials and construction. Controllable dampers are often called semi-active devices since their damping force may be adjusted or controlled, respectively. Actuators comprise such devices that are able not only to dissipate but also to generate energy. Thus, actuators are able to put energy into the vibrating structure.

The second subchapter describes the control algorithms that are usually applied when controllable dampers and actuators are used for vibration control. First, the main control strategies such as feedback, feed forward and passive control are shortly introduced. Then, active damping with collocated actuator sensor pairs is described, followed by the optimal control approach within the third subchapter. Finally, the most common, other linear control approaches used for structural control are presented.

2.1 Damping devices

In the following, the physics of the most common damping devices are described. The damping devices are split up in the sections passive damping devices, semi-active damping devices, and actuators.

2.1.1 Passive dampers

2.1.1.1 Linear viscous damper

Theoretical background

The equation of motion of a single degree of freedom system (SDOFS) with external damper force f_d and external disturbance force f_w is

$$m \cdot \ddot{x} + c \cdot \dot{x} + k \cdot x = f_d + f_w \tag{1}$$

where m denotes the SDOFS mass, c the SDOFS eigendamping and k the SDOFS stiffness. The viscous damper is a hypothetical device that creates a damping force which is directly proportional to the SDOFS velocity but with opposite sign (Fig. 1)

$$f_d = -c_d \cdot \dot{x} \tag{2}$$

The proportionality factor c_d is the damping coefficient of the external viscous damper. The reason why pure linear viscous dampers may be a preferable damping device demonstrates the following equation, which results from the substitution of Eq. (2) in Eq. (1)

$$m \cdot \ddot{x} + \underbrace{\left(c + c_d\right)}_{c_{tot}} \cdot \dot{x} + k \cdot x = f_w \tag{3}$$

This equation is again linear and therefore analytically solvable. Moreover, the main benefit of external viscous dampers is that they seem to enhance the material damping of the structure, in this case of the SDOFS, which is in good approximation pure viscous damping. The external viscous damper cannot compensate for the distur-

bance force f_w since the disturbance force f_w representing excitation forces caused by wind, earthquakes and other impacts is unknown.

Viscous damping devices are based on material damping which may be assumed to behave linear viscous. However, it must be mentioned that most dampers classified as “viscous dampers” do not behave completely linear over the entire velocity range due to sealing friction and nonlinear material behaviour which ends up in a nonlinear viscous behaviour at small velocities (Fig. 2).

The work W dissipated within the time interval $[t_1, t_2]$ can be formulated as

$$W_{1-2} = \int_{t_1}^{t_2} f_d \cdot \dot{x} \cdot dt \tag{4}$$

For periodic excitation, the energy dissipated per cycle becomes (Bachmann et al. (1995), Weber (2002))

$$W = \pi \cdot f_{\max} \cdot x_{\max} = \pi \cdot c_d \cdot x_{\max}^2 \tag{5}$$

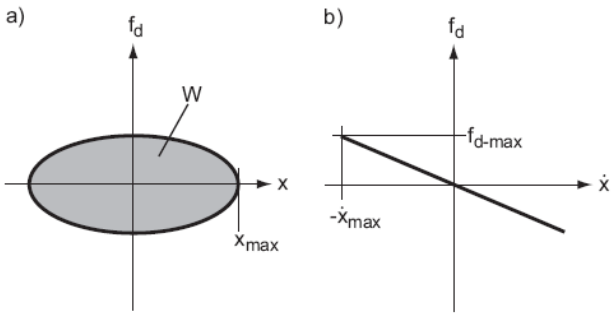

Fig. 1: Linear viscous damping: a) force displacement and b) force velocity trajectories for periodic excitation.

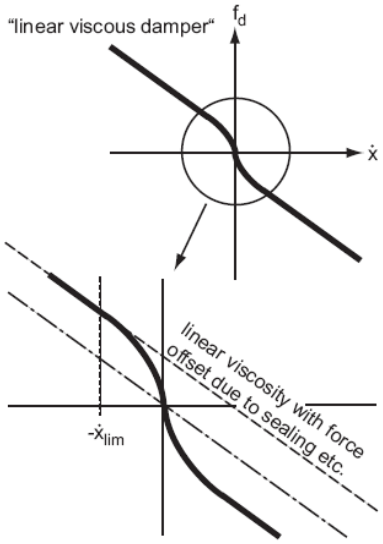

Fig. 2: Nonlinear viscous damping at small velocities due to seal friction.

Design issues

In practice, in order to produce damping devices with almost linear viscous characteristics, dampers on the base of fluids are produced. Basic principles of balance laws and explanations about inviscid fluids, Newtonian fluids, and temperature dependent Newtonian fluids are given in the books of Soong and Dargush (1997) and Constantinou et al. (1998).

A possible design for a viscous damping device is shown in Fig. 3 (Connor (2001)). The gap between plunger and external plates is filled with a linear viscous fluid which can be characterized by

$$\tau = -G_v \cdot \dot{\gamma} \tag{6}$$

The variables τ and $\dot{\gamma}$ are the shear stress and strain rate, respectively, and G_v is the viscosity coefficient. In case that slip does not exist between fluid and plunger, the shear strain is related to the plunger motion by

$$\gamma = \frac{x}{t_d} \tag{7}$$

where t_d represents the thickness of the viscous layer. With L as the wetted length and w as the width of the plunger, the damping force may be written as

$$f_d = 2wL\tau \tag{8}$$

Substituting τ by Eq. (6) and $\dot{\gamma}$ by Eq. (7) in Eq. (8) yields

$$f_d = -\left(\frac{2wLG_v}{t_d}\right)\dot{x} \tag{9}$$

According to Eq. (2), the viscous damping coefficient of the damping device becomes

$$c_d = \frac{2wLG_v}{t_d} \tag{10}$$

Hence, the design parameters of such linear viscous dampers based on fluids are:

- thickness t_d of the viscous layer,
- the wetted length L,
- the width w of the plunger, and
- the fluid viscosity coefficient G_v.

The design of viscous dampers (Fig. 3, Fig. 4) in order to enhance the overall viscous damping of, e.g., civil structures, comprises the following steps and may need iterations to meet the requirements:

1. Determination of structural properties of the civil structure and analysis of the structure.
2. Determination of the desired damping ratio.
3. Spatial placement of the damping devices.
4. Design of the viscous fluid damper.
5. Estimation of structural damping ratio.
6. Analysis of the overall structural behaviour with the enhanced damping ratio.

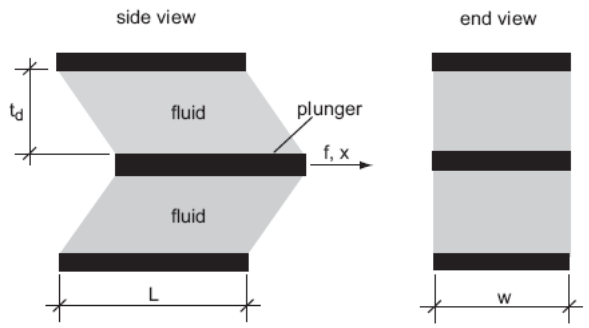

Fig. 3: Viscous damping device (Connor (2001)).

Fig. 4: Viscous damper, 450 kN (http://www.taylordevices.com/3seismic.htm).

If the dampers are well distributed over the structure, the design process can be reduced primarily to the selection of the desired damping ratio. The optimal locations are found if the results of structural analysis show that the targeted mode/modes are reduced maximally in amplitude. However, to find the optimal damper locations is a challenging and nontrivial issue. Since the implementation of dampers requires bracings, the structural stiffness and therefore its resonance frequencies are also affected. The design methodology has to be modified in presence of nonlinearities.

The physical properties of thick viscoelastic fluids are often quite sensitive to temperature changes. Therefore, temperature compensation is often included in the form of a bi-metallic orifice working similarly to a thermostat (Fig. 4). The thermal stability is combined with the steel construction that has internally threaded joints and no welded or bonded parts.

A critical issue in the design of orifice dampers concerns the durability of the high strength seals. Additionally, these of the high strength seals may be responsible for nonlinear viscous damping at small piston velocities since the sealing friction behaves like the force offset of friction dampers (Fig. 2).

Usually, typical buildings have internal critical structural damping of 1% to 3%. The critical damping of buildings should be increased by external viscous dampers to approximately 20% to 25% in order to guarantee that the building is not susceptible to vibrations of large amplitudes anymore. As a comparison, most conventional passenger cars use dampers with 20% to 30% percent of critical damping.

Testing and validation

The damper force characteristics are obtained with a simple testing procedure. The damping device is clamped between an actuator and a fixed panel, with a force transducer in series connected (Fig. 5, Fig. 6). Due to the sinusoidal displacement control of the actuator, the damping device is tested from zero velocity to maximum velocity. The first derivation of the measured displacement delivers the velocities. In conjunction with the measured force, the damping characteristics of the tested device are known. In case that the force transducer is moving together with the damping device, the measured force value has to be compensated for the inertia term due to the sensor's mass.

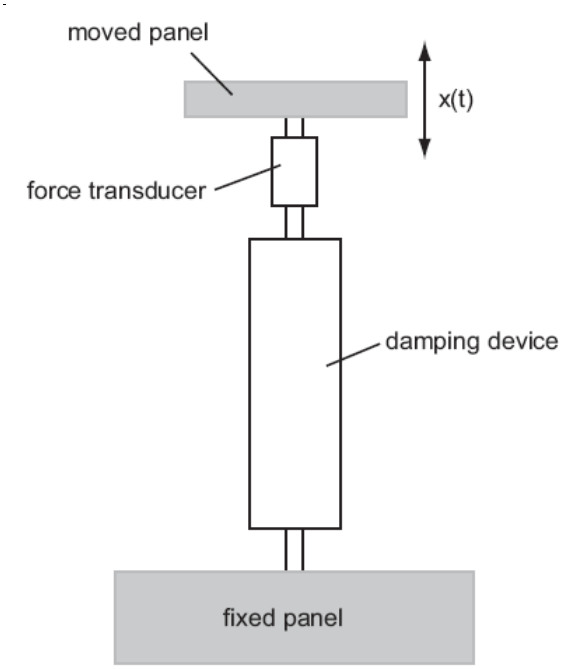

Fig. 5: Schematic test set-up.

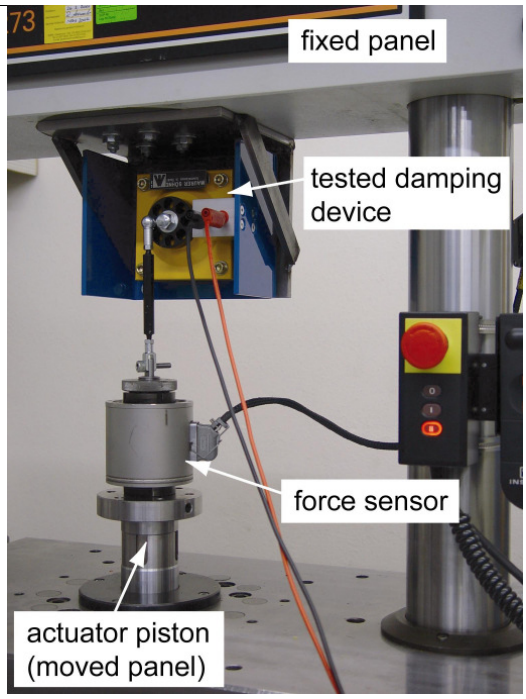

Fig. 6: Measurement of damper behaviour at Empa.

There exist dampers like, e.g., the orifice fluid damper (Constantinou and Symans (1993)), which behave as linear viscous dampers if operating at low frequencies. At high frequencies, many dampers based on fluids show also elastic force values caused by the fluid stiffness. These dampers are then called viscoelastic dampers (Jones (2001), see chapter 2.1.1.3).

Implementation

Viscous fluid dampers have been successfully used for structural control in the fields of:

- Automotive industries.
- Bridge design, foundation of superstructures.
- High buildings for the alleviation of wind and seismic vibrations (Martinez-Romero and Romero (2003)).

References

Bachmann, H., et al. (1995), *Vibration Problems in Structures: Practical Guidelines*, Birkhäuser Verlag Basel, ISBN 3-7643-5148-9.

Connor, J. J. (2001), *Introduction to Structural Motion Control*, http://www.mit.edu/afs/athena/course/1/1.561/Book/WebBook-July-2001.

Constantinou, M. C., and Symans, M. D. (1993), "Experimental Study of Seismic Response of Buildings with Supplemental Fluid Dampers", *Structural design Tall Buildings*, 2.

Constantinou, M. C., Soong, T. T., and Dargush, G. F. (1998), "Passive Energy Dissipation Systems for Structural Design and Retrofit", Multidisciplinary Center for Earthquake Engineering Research.

Jones, D. I. G. (2001), *Handbook of Viscoelastic Vibration Damping*, John Wiley & Sons LTD.

Martinez-Romero, M., and Romero, M. L. (2003), "An optimum retrofit strategy for moment resisting frames with nonlinear viscous dampers for seismic applications", *Engineering Structures*, 25, 913-925.

Soong, T. T., and Dargush, G. F. (1997), *Passive Energy Dissipation Systems in Structural Engineering*, John Wiley & Sons, New York.

Weber, B. (2002), "Damping of vibrating footbridges", *Proceedings of the International Conference on Footbridge*, Paris, France, 20-22 November 2002, on CD, AFGC – OTUA (eds.).

http://www.taylordevices.com/3seismic.htm

Notations

Symbol	*Description*	*Unit*
G_v	viscosity coefficient	Ns/m^2
L	length	m
W	work, energy	J
c	viscous damping coefficient	kg/s
f	force	N
k	stiffness	kg/s^2
m	mass	kg
t	thickness	m
w	width	m
x	displacement	m
γ	shear strain	-
τ	shear stress	N/m^2

Subscripts

d	damper
$\max$	maximum
tot	total
w	disturbance

2.1.1.2 Nonlinear viscous damper

Theoretical background

The force f_d of a damper with nonlinear viscous damping behaviour may be expressed as follows

$$f_d = -c_{d-nonlin} \cdot |\dot{u}|^{\eta} \cdot \mathrm{sgn}(\dot{x}) \quad (1)$$

where $\dot{x}$ is the relative velocity between the two damper ends, $c_{d-nonlin}$ is the viscosity of the nonlinear damper and η is a frictional power law exponent (**Fig. 7**, Tsai and Popov (1998), Weber (2002)). The case of $\eta = 1$ describes the linear viscous damper behaviour. Velocity exponents smaller than one are often chosen because of the fast increase of the damping force at low velocities (**Fig. 2**).

The main drawback of this kind of damper is that it may clamp the structure at small vibration velocities due to the relatively large damper force in the case of $\eta < 1$. If the structure is clamped at damper position, damper relative displacement and therefore energy dissipation become zero. Then, the structure is undamped and the structure at damper position becomes a nodal point. Consequently, the entire excitation energy excites the rest of the structure.

Design issues

In the case of linear viscous dampers, the optimum viscosity may be determined using the Matlab tool “root locus” (Preumont (2002)), which determines the optimum viscosity depending on:

- the structural properties,
- damper position, and
- the target mode that shall be damped maximally.

However, this tool fails for nonlinear viscous dampers. In this case, two possible design strategies are presented.

Martinez-Rodrigo and Romero (2003) proposed a trial and error method, where the maximum damper force of the nonlinear viscous damper is chosen to be smaller than its counterpart of the linear viscous damper. The relation is expressed by the so-called force index FI.

$$FI = \left[1 - \frac{f_{d-nonlin-\max}}{f_{d-lin-\max}}\right] * 100 \quad [\%] \quad (2)$$

In a first step, the maximum required damping force is estimated assuming linear viscous damping. Then, the maximum force of the nonlinear viscous damper is determined using Eq. (2). As a next step, the structure is damped with the nonlinear viscous damper with a chosen value of the nonlinear exponent η. Both damper parameters, FI and η (note: the parameter c_{lin} is already given by the optimum linear viscous damper, Krenk (2000)), are varied within an optimization procedure until the optimization criterion is fulfilled. Possible optimization criteria the may be:

- maximum damping of one target mode,
- maximum damping of several target modes, or
- minimum tip displacement of a high rise building for a given excitation time history (earthquake).

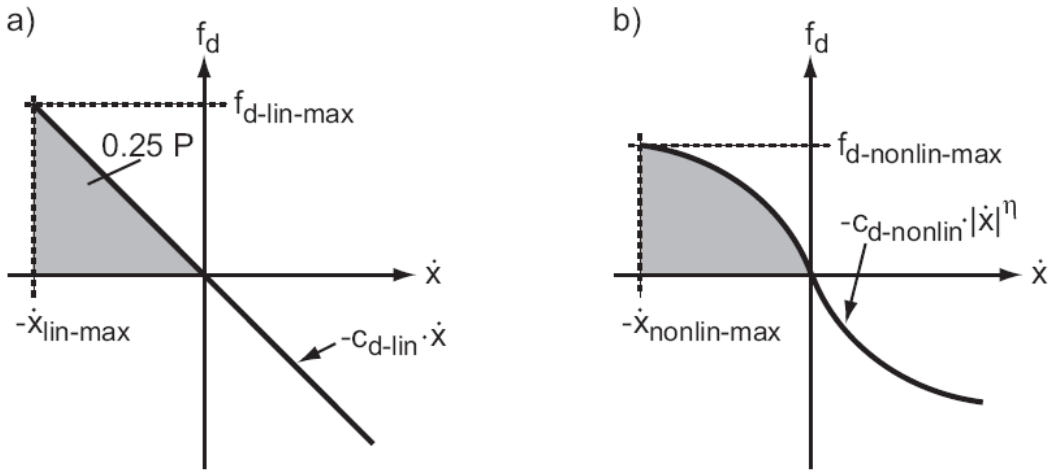

Fig. 7: Mean power equivalent nonlinear viscous damper.

Another design procedure is proposed by Pekcan et al. (1999). The idea is to determine a mean power equivalent nonlinear viscous damper based on the optimum linear viscous damper. The damper energy per cycle is

$$W = \int_0^{T_d} f_d \cdot \dot{x} \cdot dt \tag{3}$$

The mean power over one cycle is the first time derivative, hence

$$\overline{P} = \frac{dW}{dt} = \frac{d}{dt}\left\{\int_0^{T_d} f_d \cdot \dot{x} \cdot dt\right\} = \int_0^{T_d} f_d \cdot d\dot{x} = 4 \cdot \int_0^{T_d/4} f_d \cdot d\dot{x} = 4 \cdot (grey\ area) \tag{4}$$

The mean power over one cycle of the optimal linear viscous damper is

$$\overline{P}_{lin} = 4 \cdot \frac{c_{d-lin}^{opt} \cdot \dot{x}_{lin-\max}^2}{2} \tag{5}$$

The mean power over one cycle of the nonlinear viscous damper is

$$\overline{P}_{nonlin} = 4 \cdot \frac{c_{d-nonlin} \cdot \dot{x}_{nonlin-\max}^{\eta+1}}{\eta+1} \tag{6}$$

Equating both mean power values yields the tuning of mean power equivalent nonlinear viscous dampers

$$\frac{c_{d-nonlin} \cdot \dot{x}_{nonlin-\max}^{\eta+1}}{\eta+1} = \frac{c_{d-lin} \cdot \dot{x}_{lin-\max}^2}{2} \tag{7}$$

The formula shown in Eq. (7) indicates that the mean power equivalent nonlinear viscous damper still needs the choice of one of its design parameters and the assumption of equal maximum damper velocities.

References

Krenk, S. (2000), "Vibrations of a Taut Cable With an External Damper", *Journal of Applied Mechanics*, 67, 772-776.

Martinez-Romero, M., and Romero, M. L. (2003), "An optimum retrofit strategy for moment resisting frames with nonlinear viscous dampers for seismic applications", *Engineering Structures*, 25, 913-925.

Pekcan, G., Mander, J. B., and Chen, S. S. (1999), "Fundamental considerations for the design of nonlinear viscous dampers", *Earthquake Engineering and Structural Dynamics*, 28(11), 1405-1425.

Preumont, A. (2002), *Vibration Control of Active Structures*, Kluwer Academic Publishers, Dordrecht.

Tsai, K. C., and Popov, E. P. (1998), "Steel beam-column joints in seismic moment resisting frames", Berkeley, CA, Earthquake Engineering Research Center, University of California, 1998, report No. UCB/EERC-88/19.

Weber, B. (2002), "Damping of vibrating footbridges", *Proceedings of the International Conference on Footbridge*, Paris, France, 20-22 November 2002, on CD, AFGC – OTUA (eds.).

Notations

Symbol	*Description*	*Unit*
FI	force index	%
P	power	W
W	work, energy	J
c	viscous damping coefficient	kg/s
f	force	N
x	displacement	m
η	frictional power law exponent	-

Superscripts

opt	optimum
$\bar{a}$	mean value of a

Subscripts

d	damper
lin	linear
$nonlin$	nonlinear
$\max$	maximum

2.1.1.3 Viscoelastic damper

Theoretical background

The total force of a viscoelastic damper is the some of its viscous and stiffness parts (Jones (2001), Weber (2002))

$$f_d = k_d \cdot x - c_d \cdot \dot{x} \tag{1}$$

The stiffness part causes that the ellipse curve in the force displacement map has a mean slope of k_d (Fig. 8). The force velocity trajectory is also an ellipse curve. Its mean slope still indicates the damper viscosity c_d. The dissipated energy over one cycle is

$$E = \int_0^{T_d} f_d \cdot \dot{x} \cdot dt \tag{2}$$

In contrast to pure linear viscous dampers, the force velocity map does not only show dissipative but also active force values due to the damper's stiffness (within quadrants I and III in Fig. 8). Viscoelastic behaviour is typical for material dampers, not fluid dampers, since materials can withstand constant deformations.

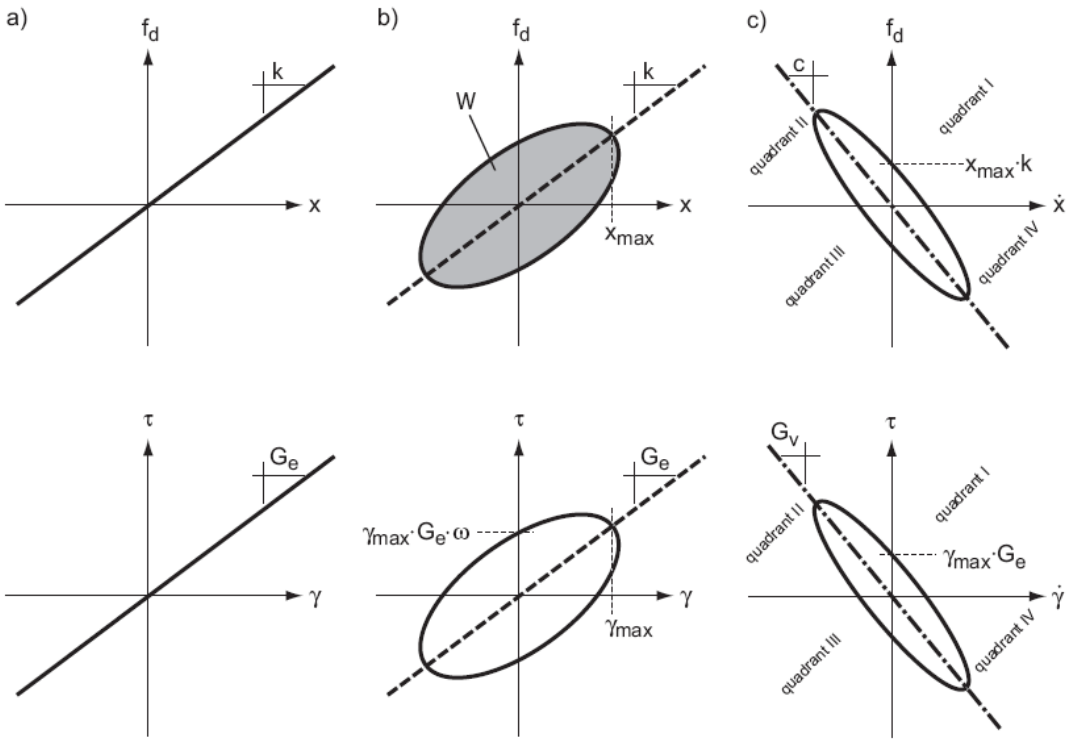

Fig. 8: Behaviour of: a) pure elastic materials, b) and c) of viscoelastic materials.

The stress strain relationship of a linear elastic material is

$$\tau = G_e \cdot \gamma \tag{3}$$

where τ and γ are the shear stress and strain, respectively, and G_e is the elastic shear modulus. The stress strain curve is depicted in Fig. 8. For the elastic behaviour, time lag between stress and strain and force and displacement, respectively, does not exist. The proportionality factor of course is G_e. In contrast, stress is $\pi/2$ radians out of phase with strain for linear viscous damping only. The linear combination of both produces the behaviour shown by the viscoelastic trajectories in Fig. 8 with a phase between stress and strain between 0 and $\pi/2$ according to the linear combination.

The hysteresis loops deliver an initial base for analytical modelling the viscoelastic material behaviour as a function of strain, frequency and temperature. For the periodic excitation, the basic strain stress relations may be written as follows

$$\gamma = \gamma_{\max} \cdot \sin(\omega \cdot t) \tag{4}$$

$$\tau = \gamma_{\max} \cdot \left[G_s \cdot \sin(\omega \cdot t) + G_l \cdot \cos(\omega \cdot t) \right] \tag{5}$$

where G_s is the storage modulus and G_l is the loss modulus. The ratio of loss modulus and storage modulus is called loss factor

$$\eta = \frac{G_l}{G_s} = \tan(\delta) \tag{6}$$

The angle δ signs the phase shift between stress and strain and ranges from 0 for elastic behaviour to $\pi/2$ for pure viscous behaviour. Equation Eq. (5) written in an alternative form yields

$$\tau = \gamma_{\max} \cdot G_{\max} \cdot \sin(\omega \cdot t + \delta) \tag{7}$$

$$G_{\max} = \sqrt{G_s^{\,2} + G_l^{\,2}} = \sqrt{1 + \eta^2} \tag{8}$$

Chang et al. (1993) performed several tests of three types of viscoelastic dampers. They concluded that the storage modulus and the loss modulus are functions of ambient temperature, material temperature, excitation frequency and shear strain. During damper operation, the energy is dissipated in form of heat producing temperature rise in the viscoelastic material. Therefore, the damper properties depend - up to a certain degree - on the number of loading cycles and the range of deformation, especially under large strain due to temperature increase of the damper material.

Bagley and Torvik (1983) characterized the frequency and temperature dependent shear storage modulus and shear loss modulus for most viscoelastic materials. Ferry (1980) proposed the method of reduced variables to determine the dependence of G_l and G_s on ambient temperature. This method is based on a simplification in separating the two variables, frequency and temperature, on which the viscoelastic properties depend. These properties are expressed in terms of a single function of each.

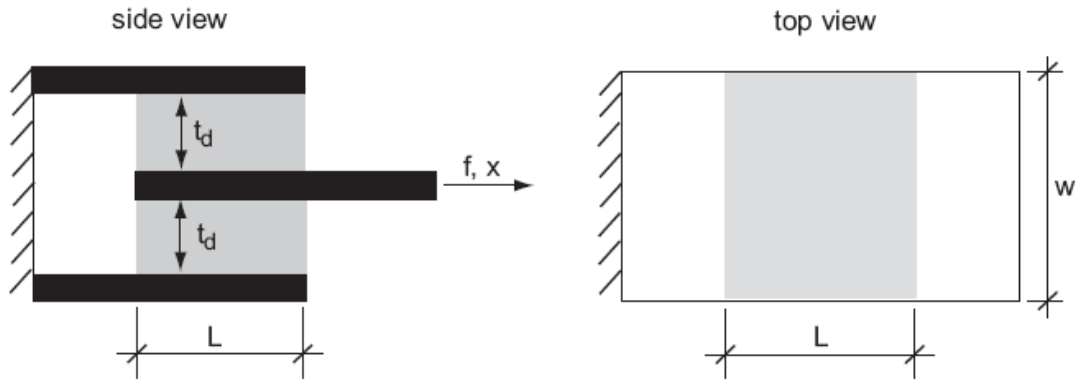

Fig. 9: Example of a viscoelastic damping device according to Connor (2001).

A serious problem with viscoelastic devices is an increase in force at low temperatures coupled with an accompanying overloading of the bonding agent used to glue the viscoelastic material to its steel attachments.

Design issues

There exists a large variety of different damper design procedures, which are collected in Soong and Dargush (1997).

The damper design procedure for application in structures follows approximately the steps described for pure viscous dampers. Aiken et al. (1989) reported that the general design methodology for elastomeric bearings for seismic isolation is substantial different from the currently used for bridge bearings, in particular in aspects of slenderness, rated loads and lateral displacements.

A possible viscoelastic damper design with bonding steel sheets of a viscoelastic material to steel plates is illustrated in Fig. 9 (Connor (2001)). The equation of shear strain rewritten becomes

$$\gamma = \frac{x}{t_d} \tag{9}$$

For a given shear strain γ, one determines τ with the stress strain relation. Then, the damping force may be estimated as

$$f_d = 2 \cdot w \cdot L \cdot \tau \tag{10}$$

For periodic excitation and substituting τ from Eq. (4), one obtains

$$f_d = \frac{2 \cdot w \cdot L}{t_d} \cdot G_s \cdot x_{\max} \cdot \left[\sin(\omega \cdot t) + \eta \cdot \cos(\omega \cdot t)\right] \tag{11}$$

Then, the dissipated energy per cycle becomes

$$W = \frac{2 \cdot w \cdot L}{t_d} \cdot \pi \cdot \eta \cdot G_s \cdot x_{\max}^2 \tag{12}$$

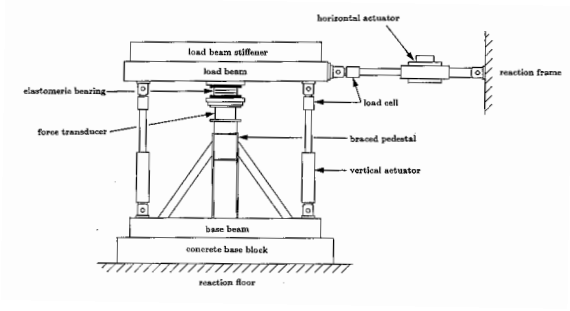

Fig. 10: Single bearing test machine (Aiken et al. (1989)).

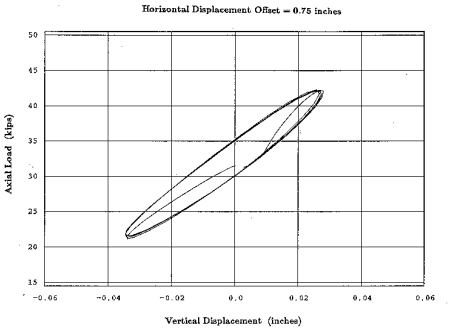

Fig. 11: Cyclic hysteresis loop of a bolted rubber bearing (Aiken et al. (1989)).

Testing and validation

The testing procedure of a viscoelastic damper needs one step more compared to the testing of pure viscous dampers because the elasticity has to be identified too. The damping device is clamped between actuator and fixed panel with a force transducer connected in series (Fig. 10). The spring constant k_d can be easily identified by applying a constant load and measuring the resulting displacement. With the known spring constant, the testing procedure follows the one of viscous dampers (Fig. 11).

If the actuator is displacement controlled, then the resulting force represents the measured system output. The first derivation of the displacement delivers the velocity. Together with the measured force, the damping coefficient c_d may be identified as the mean slope of the force velocity trajectory (Fig. 8). Please note that the measured total damper force has to be reduced by the inertia force of the sensor if the force transducer is moving together with the damping device.

Implementation

Basically, most material dampers behave viscoelastic. Even some fluid dampers show viscoelastic behaviour due to the fluid stiffness although the force due to their stiffness is small compared to the force resulting from their viscosity. Therefore, numbers of viscoelastic dampers have been implemented on real civil structures for structural control. They have been used in the fields of:

- vibration control and vibration mitigation of sensitive machines (e.g. nuclear industry and aerospace technology),
- base isolation systems, also foundation of superstructures (Huffmann (1985)),
- damping of vibrations of high rise buildings, and
- damping of bridge deck and cable vibrations (elastomeric bearings).

Elastomeric bearings

The bearing systems which have been implemented in buildings are either systems which include additional devices to enhance the overall damping of the isolation system or do not have extrinsic devices which increase the system damping. The latter type can be of the lead-rubber type, in which elastomeric bearings contain a lead-

plug insert to supplement damping. Another realization is the filled type, in which a filler material is added to the rubber to enhance the damping and stiffness properties of the compound. A bearing design, proposed by Aiken et al. (1989), is shown in Fig. 12. The bearing consists of three rubber layers separated by two steel shims and two end plates. An external rubber cover layer is used for protection. The material used for the bearings is a filled, natural rubber with high damping.

Kelly and Edgardo (1992) reported that if an isolation system uses high strength elastomers, such as polychloroprene rubber, connected with high quality bonding techniques, the ultimate capacity can be accurately predicted and very substantial safety margins can be established.

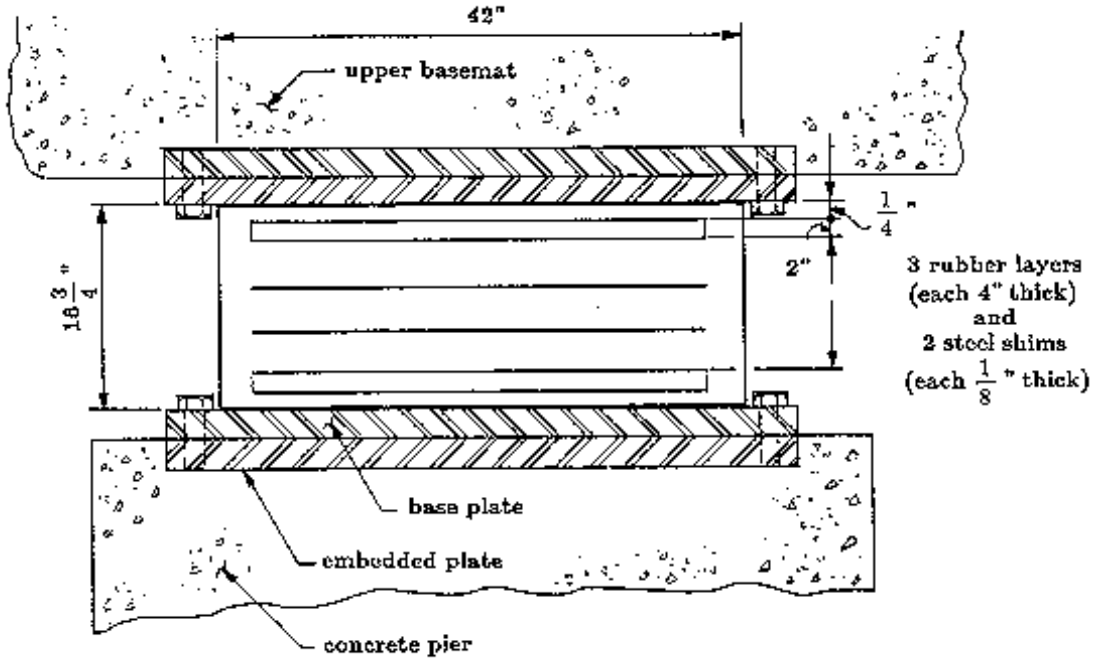

Fig. 12: Bearing system design proposed by Aiken et al. (1989).

References

Aiken, I. D., Kelly, J. M., and Tajirian, F. F. (1989), "Mechanics of Low Shape Factor Elastomeric Seismic Isolation Bearings," Report No. UCB/EERC-89/13, Earthquake Engineering Research Center, College of Engineering, University of California at Berkeley.

Bagley, R. L., and Torvik, P. J. (1983), "Fractional Calculus – A Different Approach of the Analysis of Viscoelastic Damped Structures", *AIAA Journal*, 1983.

Connor, J. J. (2001), *Introduction to Structural Motion Control*, http://www.mit.edu/afs/athena/course/1/1.561/Book/WebBook-July-2001.

Chang, K. C., Lai, M. L., Soong, T. T., Hao, D. S., and Yeh, Y. C. (1993), "Seismic Behaviour and Design Guidelines for Steel Frame Structures with Added Viscoelastic Dampers", NCEER 93-0009, National Center for Earthquake Engineering Research, Buffalo.

Ferry, J. D. (1980), *Viscoelastic Properties of Polymers*, John Wiley, New York.

Huffmann, G. K. (1985), "Full Base Isolation for Earthquake Protection by Helical Springs and Viscodampers", *Nuclear Engineering Design*, 84(2).

Jones, D. I. G. (2001), *Handbook of Viscoelastic Vibration Damping*, John Wiley & Sons LTD.

Kelly, J. M., and Edgardo, Q. (1992), "Mechanical Characteristics of Neoprene Isolation Bearings", Report No. UCB/EERC-92/11, Earthquake Engineering Research Center, College of Engineering, University of California at Berkeley.

Soong, T. T., and Dargush, G. F. (1997), *Passive Energy Dissipation Systems in Structural Engineering*, John Wiley & Sons, New York.

Weber, B. (2002), "Damping of vibrating footbridges", *Proceedings of the International Conference on Footbridge*, Paris, France, 20-22 November 2002, on CD, AFGC – OTUA (eds.).

Notations

Symbol	*Description*	*Unit*
G_e	elastic shear modulus	N/m^2
G_s	storage modulus	N/m^2
G_l	loss modulus	N/m^2
L	length	m
W	work, energy	J
c	viscous damping coefficient	kg/s
f	force	N
k	stiffness	kg/s^2
t	thickness	m
w	width	m
x	displacement	m
δ	phase angle	rad
γ	shear strain	-
η	loss factor	-
τ	shear stress	N/m^2
ω	radial frequency	rad/s

Subscripts

d	damper
max	maximum

2.1.1.4 Coulomb friction damper

Theoretical background

In friction dampers, irrecoverable work is done by tangential force required to slide one surface of solid body across to another. Contacting surfaces are intended to remain dry during operation. No additional hydrodynamic lubricating layer is needed. More detailed information in conjunction with numerous references can be found in Larssen-Basse (1992) and Taylor (1981).

Basic theory of solid friction is inferred from physical experiments involving planar sliding of rectangular blocks:

- The total frictional force is independent of the apparent surface area of contact
- The total frictional force is proportional to the total normal force acting across the interface.
- In case of sliding with low relative velocities, the total frictional force is independent of velocity.

Hence, the behaviour of a Coulomb friction damper may be described as

$$f_d = \mu \cdot N \cdot \left(-sign(\dot{x})\right) \tag{1}$$

where f_d represents the damper force, N the normal force and μ the friction coefficient for the two layers. In some cases, the friction coefficient is somewhat higher when slippage is imminent than during sliding. This is indicated by the two separate friction coefficients of static μ_{sta} and kinetic μ_{kin} friction coefficients.

The Coulomb friction force acts always against the direction of movement and therefore behaves dissipative like any pure damping force (Fig. 13). The Coulomb friction force is zero in the case of zero velocity since relative displacement between the two surfaces vanishes (Fig. 13). Therefore, the force of an ideal Coulomb friction damper "jumps" from its positive value to zero and then to its negative value when the velocity changes its sign. In contrast, real dampers that are seen as Coulomb friction dampers (e.g. MR dampers at constant current) show a force velocity trajectory as depicted in Fig. 13 c). Assuming periodic excitation, the work per one full cycle is represented by the rectangular area depicted in Fig. 13 (Weber (2002))

$$W = 4 \cdot f_{d-\max} \cdot x_{\max} \tag{2}$$

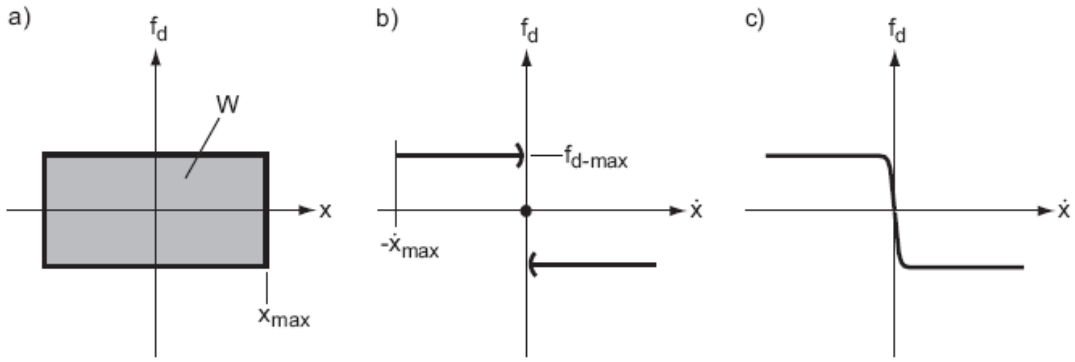

Fig. 13: Coulomb friction: a) force displacement trajectory, b) force velocity trajectory; c) force velocity trajectory of real Coulomb friction dampers (e.g. MR dampers at constant current).

In order to generalize and extend the theory, involving non-uniform distributions or non-planar surfaces, the basic assumptions mentioned above are often abstracted to the infinitesimal limit. The generalization of Eq. (1) becomes

$$\tau_t = \mu \cdot \tau_n \cdot \left(-sign(\dot{x})\right) \tag{3}$$

where τ_t represents the tangential traction and τ_n the normal traction. This equation can be also used for determining nominal contact stresses.

Design issues

In practice, the force trajectory of Coulomb friction dampers will follow qualitatively the trajectory depicted Fig. 13 c) due to sealing friction and viscous material behaviour. However, the main and only design variable of Coulomb friction dampers is their friction force level f_d. This force level has to be chosen the way that the damper does not clamp the main structure due to the constant damper force. However, the friction force level of the originally designed and manufactured Coulomb friction damper may change during lifetime for several reasons:

- The damper force level may change due to varying conditions of the sliding interfaces. Bimetal interfaces are susceptible to this behaviour because ongoing physical and chemical processes change the friction coefficient considerably. At microscopic level one finds that natural and engineered surfaces are not smooth. These irregularities are often categorized as waviness and roughness and they are typically present over a wide range of scales. It should be mentioned that true contact does occur directly between metals, adhesive bonds form across the interface often producing a friction coefficient larger than one ($\mu > 1$).
- Aging and corrosion of the surfaces may also affect the originally produced friction damper. The investigation of friction processes under such circumstances is a challenging issue since the mechanical characteristics of oxide films are not well understood.
- Finally, local deformational processes which occur in the vicinity of surfaces may change the friction force behaviour (Soong and Dargush (1997)). During the slippage, the dissipated energy will cause local heating along the interface of the constituent materials. The thermal effects can result in an aging process of surfaces caused by material softening or promoting oxidation. However, it may be assumed that the system response is not sensitive to relatively small variations of ambient temperature. The attention has to be more directed on physiochemical processes, often triggered by atmospheric moisture or containments. These processes may change the physical and chemical character of the surfaces, caused by formation of oxide layers. In more aggressive environments the interfaces tend to corrode. The formation of the geometry of the component is of prime importance to attenuate corrosion. For instance, exposed surfaces become a surplus of oxygen and other inaccessible regions have much less dissolved oxygen. Therefore, a mass transfer does occur between anode and cathode (Soong and Dargush (1997)).

Implementation

In the following, several types of friction damping devices are presented.

a) Limited Slip Bolted Joints

Pall et al. (1980) started with the realization of friction dampers as Limited Slip Bolted Joints varying simple sliding elements which have different surface treatments. Several surfaces like mill scale, sand blasted, inorganic metallic zinc-rich paint, brake lining pads and polyethylene coating were investigated by static and dynamic tests evaluating load displacement response under constant cyclic loading (Fig. 14). The maximum static slip is obtained for metallic surfaces. The cyclic response is quite erratic, with considerable stick-slip associated with the transition from static to kinetic frictional response.

Anagnostides and Hargreaves (1990) reported experimental results from a number of other frictional materials. Brake lining materials would perform well in dynamic tests. The characterization of their simple brake lining frictional system in terms of an elastic perfectly plastic model is quite appropriate. A mathematical model is given in Soong and Dargush (1997).

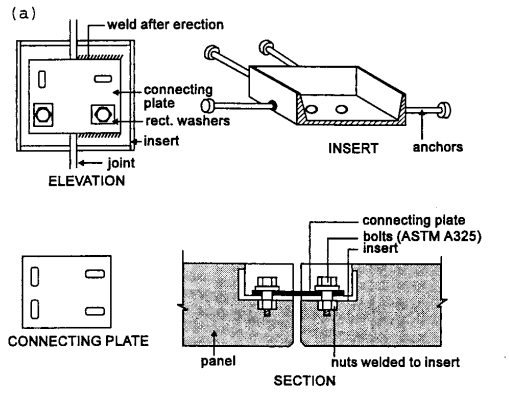

Fig. 14: Limited Slip Bolted Joints (Pall et al. (1980)).

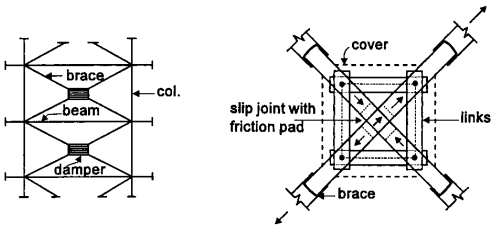

Fig. 15: X-braced Friction Damper (Pall and Marsh (1982)).

b) X-braced Friction Damper

A much more effective operation can be reached special damper mechanism, proposed by Pall and Marsh (1982) (Fig. 15). These devices utilize the brake lining pads. One principle of a typical X-braced system is based on braces that are designed to buckle at relatively low compressive loads, so the braces contribute only when subjected to tension. Installing uni-axial friction elements within each brace, slippage would only occur in the tensile direction and little energy dissipation would result during cyclic loading. The mechanism tends to straighten buckled braces and also enforces slippage in both tensile and compressive directions.

Pall and Marsh (1982) used a simple elastoplastic model to describe the behaviour of this X-braced friction damper. Filiatrault and Cherry (1988) proposed a more refined macroscopic model for this device, since the Pall-Marsh model overestimates the energy dissipation and the simple elastoplastic model is only valid if the device slips every cycle and if that the slippage is always sufficient to straighten completely the buckled braces. Wu et al. (2005) published an improved variant of the Pall-typed frictional dampers.

c) Sumitomo Friction Damper

The uni-axial friction damper made by Sumitomo Metal Industries Ltd. utilizes a more sophisticated design (Fig. 16). A precompressed internal spring exerts a force that is converted trough the action of inner and outer wedges into a normal force on the friction pads. The use of graphite plug inserts ensures dry lubrication in order to maintain a consistent friction coefficient between the pads and the inner surface of the steel casing. Aiken and Kelly (1990) reported that the response of this damper is extremely regular and repeatable with rectangular hysteresis loops. Effects of loading frequency, number of cycles, and ambient temperature are indicated as not sensitive.

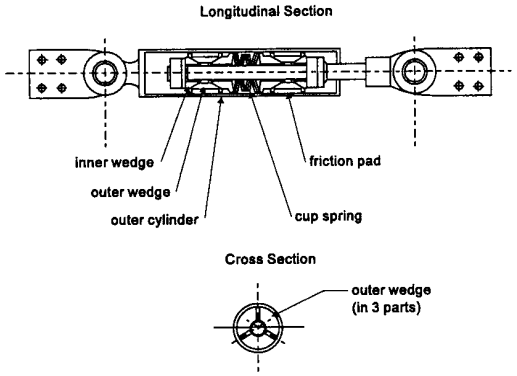

Fig. 16: Sumitomo Friction Damper (Aiken and Kelly (1990)).

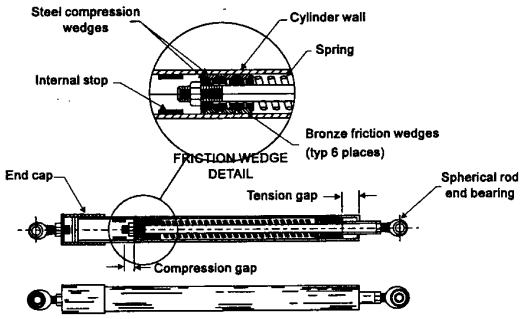

Fig. 17: Energy Dissipating Restraint (EDR) (Nims et al. (1993)).

d) Energy Dissipating Restraint

The Energy Dissipating Restraint (EDR), designed by Fluor Daniel, Inc., is similar to the Sumitomo concept, since this device also includes an internal spring and wedges encased in a steel cylinder (Fig. 17). A detailed description of the damper design is provided in Nims et al. (1993). The EDR uses steel compression wedges and bronze friction wedges in order to transform the axial spring force into normal pressure acting outward on the cylinder wall. The frictional surface is formed by the interface between the bronze edges and the steel cylinder. Internal stops are ensured within the cylinder in order to create the tension and compression gaps. It should be mentioned that the length of the internal spring can be altered during operation, providing a variable frictional slip force. Other realized friction dampers can be found in the book of Soong and Dargush (1997).

References

Aiken, I. D., and Kelly, J. M. (1990), “Earthquake Simulator Testing and Analytical Studies of Two Energy-Absorbing Systems for Multistory Structures”, Report No. UCB/EERC-90/03, University of California, Berkeley, CA.

Anagnostides, G., and Hargreaves, A. C. (1990), “Shake Table Testing On an Energy Absorption Device for Steel Braced Frames”, *Soil Dynamics Earthquake Engineering*, 9(3).

Filiatrault, A., and Cherry, S. (1988), “Comparative Performance and Friction Damped Systems and Base Isolation Systems for Earthquake Retrofit and Aseismic Design”, *Earthquake Engineering Structural Dynamics*, 16.

Larsen-Basse, J. (1992), *Basic Theory of Solid Friction, in Friction, Lubrication and Wear Technology*, ASM International Handbook Committee, American Society for Metals, Materials Park, Ohio.

Pall, A. S., Marsh, C., and Fazio, P. (1980), "Friction Joints for Seismic Control of Large Panel Structures", *Journal Prestressed Concrete Inst.*, 26(6).

Pall, A. S., and Marsh, C. (1982), "Response of Friction Damped Braced Frames", *Journal Structural Division*, ASCE, 108(ST6).

Nims, D. K., Richter, P. J., and Bachmann, R. E. (1993), "The Use of the Energy Dissipating Restraint for Seismic Hazard Mitigation", *Earthquake Spectra*, 9(3).

Soong, T. T., and Dargush, G. F. (1997), *Passive Energy Dissipation Systems in Structural Engineering*, John Wiley & Sons, New York.

Taylor, D. (1981), "Friction – The Present State of Our Understanding", *Journal Lubr. Technics*, ASME, 103.

Weber, B. (2002), "Damping of vibrating footbridges", *Proceedings of the International Conference on Footbridge*, Paris, France, 20-22 November 2002, on CD, AFGC – OTUA (eds.).

Wu, B, Zhang, J., Williams, M. S., and Ou, J. (2005), "Hysteretic behaviour of improved Pall-typed Frictional dampers", *Engineering Structures*, 27(3), 1258-1267.

Notations

Symbol	*Description*	*Unit*
W	work, energy	J
N	normal force	N
f	force	N
x	displacement	m
μ	friction coefficient	-
τ	traction	N/m^2

Subscripts

d	damper
kin	kinetic
$\max$	maximum
n	normal
sta	static
t	tangent

2.1.1.5 Structural friction damper

Theoretical background

Structural damping is the use of internal friction in a material to transform structural vibration energy into heat produced within the damper material. This reduces vibration amplitudes of the main structure. The definition equation of friction dampers is (Weber (2002))

$$f_d = k_d \cdot |x| \cdot (-\operatorname{sgn}(\dot{x})) \tag{1}$$

where k_s is called pseudo-stiffness factor. For periodic excitation, Fig. 18 shows the force displacement and force velocity trajectories of structural friction dampers. Please notice that the damper force "jumps" just before reaching its maximum value to zero (see the path direction in Fig. 18 indicated by arrows) because of the damper velocity that is zero at $t = \pi/(2 \cdot \omega)$ and at $t = 3 \cdot \pi/(2 \cdot \omega)$. The dissipated energy per full cycle is equal to

$$W = 4 \cdot \left(\frac{k_d \cdot x_{\max}^2}{2} \right) = 2 \cdot k_d \cdot x_{\max}^2 \tag{2}$$

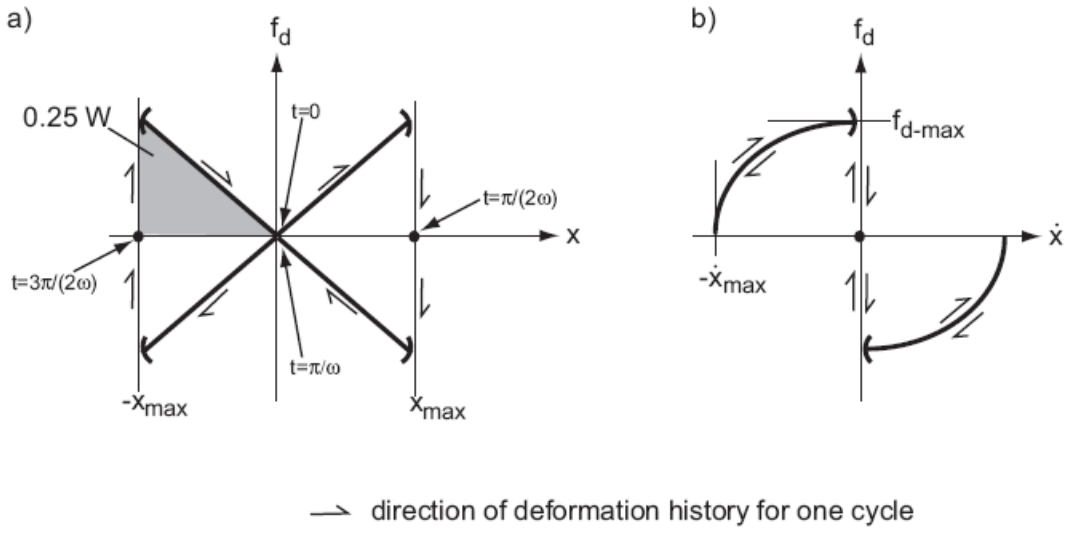

Fig. 18: Structural damping: a) force displacement trajectory and b) force velocity trajectory.

Testing and validation

The goal of testing structural friction dampers is to identify the single damper parameter k_d. Therefore, the testing procedure of structural friction dampers follows the one of linear viscous dampers except that not the damper's viscosity but the damper's stiffness is identified. The identification can be realized by simply measuring pairs of force deformation values. Several pairs have to be measured in order to be able to identify nonlinear stiffness behaviour.

Implementation

Structural friction dampers are often implemented as vibration mitigation devices directly within pylons and struts in order to dissipate vibration energy and therefore to mitigate the structure. Especially, they are used in:

- base isolation systems,
- damping of belfries,
- gear boxes as damping materials,
- hollow parts or profiles as damping material, and
- automotive applications.

References

Weber, B. (2002), "Damping of vibrating footbridges", *Proceedings of the International Conference on Footbridge*, Paris, France, 20-22 November 2002, on CD, AFGC – OTUA (eds.).

Notations

Symbol	*Description*	*Unit*
W	work, energy	J
f	force	N
k	stiffness	kg/s^2
x	displacement	m

Subscripts

d	damper
$\max$	maximum

2.1.1.6 Hysteretic damper

Theoretical background

The inelastic deformation capability of metallic substances represents an effective energy dissipation mechanism for damping of engineering structures. The stress strain curve depicted in Fig. 19 a) is typical for most metals. For strain values less or equal than ε_Y, the stress strain relation is linear and the initial state O is fully recoverable if the applied load is removed. For strain values larger than ε_Y, the metal yields and deforms irreversible. The plastic deformation occurs directly with energy dissipation. If the load in point B is removed, static deformation remains due to the inelastic deformation from Y to B, therefore denoted as ε_{ine}. Only the elastic part ε_{ela} is recovered. At point M, the maximum load is reached. The ultimate failure occurs at point Ω (Soong and Dargush (1997)).

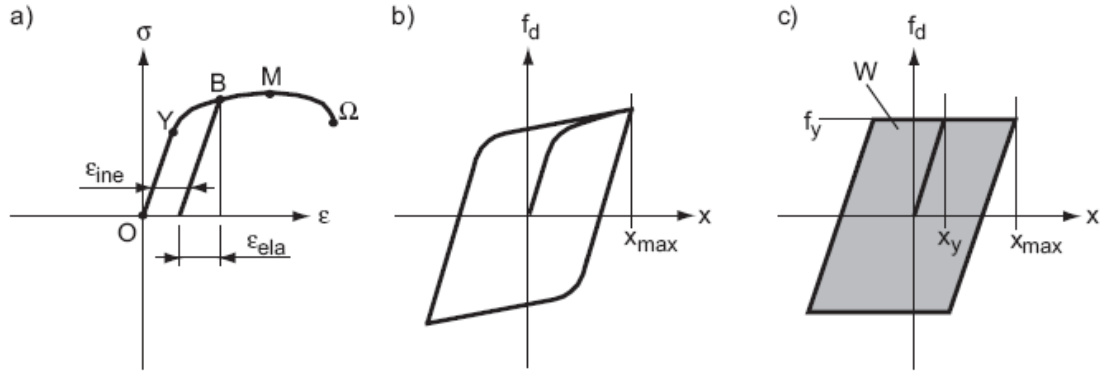

Fig. 19: Hysteretic damping: a) stress strain relation, b) real hysteretic damper behaviour, c) idealized hysteretic damper behaviour.

The shape of the force displacement trajectory depends on the stress strain relationship of the material and the device design (Fig. 19 b)). For the case of an ideal elastic-plastic material behaviour, the relation between damping force and displacement is as shown in Fig. 19 c). The dissipated energy per cycle of an ideal elastic-plastic material becomes

$$W = 4 \cdot f_y \cdot \left(x_{\max} - x_y\right) = 4 \cdot \left(k_y \cdot x_y\right) \cdot \left(x_{\max} - x_y\right) = 4 \cdot k_y \cdot x_y^2 \cdot \left(\mu - 1\right) \tag{1}$$

where f_y is the yield force, x_y the displacement at which the material starts to yield, $x_{\max}$ the maximum displacement, k_y the elastic damper stiffness and the ductility ratio μ denotes the ratio between maximum displacement and yield displacement (Jones (2001))

$$\mu = \frac{x_{\max}}{x_y} \tag{2}$$

Design issues

An example

Jones (2001) presents an example how to design a hysteretic damping device. The damping device consists of a cylindrical rod of length L and cross sectional area A (Fig. 20). Provided that the damper material behaves ideal elastic-plastic, the yield force may be expressed as follows

$$f_y = A \cdot \sigma_y = k_y \cdot x_y \tag{3}$$

Considering the relationship between strain and deformation

$$x_y = L \cdot \varepsilon_y \tag{4}$$

the linear stiffness describing the elastic behaviour becomes

$$k_y = \frac{A}{L} \cdot \frac{\sigma_y}{\varepsilon_y} = \frac{A}{L} \cdot E \tag{5}$$

Equation Eq. (5) describes the known relation between stiffness and elasticity modulus E. Hence, by appropriate choice of material (E) and geometry (A, L), the desired damper with maximum expected deformation and maximum tolerable damper force may be designed.

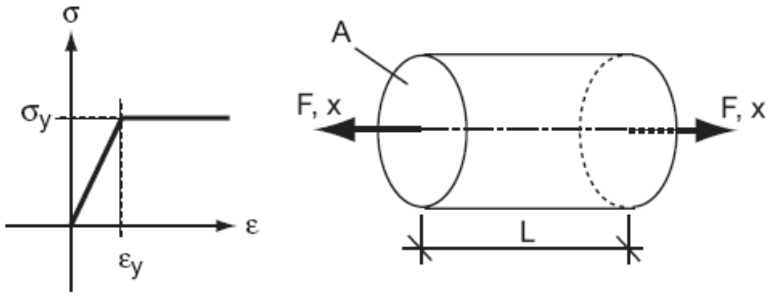

Fig. 20: Ideal elastic-plastic damping device according to Jones (2001).

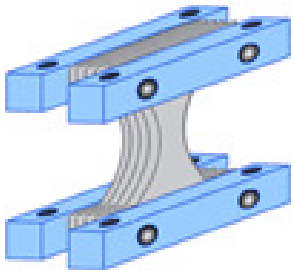

Fig. 21: X-shaped Plate Damper.

The idea of utilizing separate metallic hysteretic dampers in order to improve the resistance of structures in the case of earthquakes was formulated firstly by the conceptual work of Kelly et al. (1972) and Skinner et al. (1975). In recent years, many new designs of metallic dampers have been produced. Two examples are shown in Fig. 21. An X-shaped plate damper or ADAS (Added Damping And Stiffness) device has been studied via experiments by Bergman and Goel (1987), Whittaker et al. (1989), Whittaker et al. (1993), and subsequently employed in the seismic retrofit projects discussed by Martinez-Romero (1993) and Perry et al. (1993). The hourglass shape produces nearly uniform curvature throughout the plate during infinitesimal deformation. Similar reasoning has also led to the development of triangular plate systems by Tsai et al. (1993).

Modelling approaches

In order to characterize the metallic damper response, a couple of different suitable force displacement models can be taken. The first approach involves the direct

use of experimental data from damper tests. The whole damper behaviour is described by the static damper map, which consists of the fitted force displacement trajectories.

Another way of modelling is that the damper model is constructed from an appropriate constitutive relationship for metals by applying the principles of mechanics. From a constitutive model of a metal, the force displacement relationship can be developed introducing a geometric description of the device and employing principles of mechanics. The geometric description may require a finite element discretization or can be adequately modelled, for instances by simple strength of materials representation. For the example of a triangular plate damper, Tsai et al. (1993) introduced a set of equations to describe the following force displacement model

$$f_d = \left(\frac{N \cdot E \cdot w_0 \cdot h^3}{6 \cdot L^3} \right) \cdot x \qquad (6)$$

where f_d represents the damper force, N the number of identical triangular structural steel plates, which are positioned in parallel, x the damper displacement, h the thickness of the cantilevered plate, L the length and w_0 the base width. This model agrees reasonably well with performed experiments. However, the model is valid only for the elastic response of the damper. Thus, the dissipated energy of the device cannot be estimated using this model.

Soong and Dargush (1997) recommended a finite element analysis methodology. For the example of triangular plate damper model, development and subsequent calculations were described. Generally, in the same way, a wide range of metallic dampers, including the X-shaped plate dampers, can be developed. A more detailed description of a mechanic based modelling approach for triangular plate dampers is provided in Dargush and Soong (1990) and in Tsai and Tsai (1995).

In the analysis of single-degree-of-freedom systems (SDOFS), the addition of a pure viscous device increases the system damping independently of the excitation forces. Although the insertion of metallic dampers into SDOFS generally reduces the response by the portion of the dissipated energy, the SDOFS response may increase for some specific seismic inputs due to the added stiffness of the hysteretic damper. Soong and Dargush (1997) have illustrated a particular case in which an elastoplastic damper is either ineffective or even detrimental under special ground motion. This experience suggests that a detailed analysis of the nonlinear transient dynamics is required to evaluate the effectiveness of metallic dampers for seismic protection of civil structures.

On the basis of the finite element method, the Newton-Raphson time domain approach is directly applicable for structures that include metallic dampers. Applications of nonlinear structural analysis to building frames using X-shaped dampers are provided by Xia et al. (1990) and for the case of using triangular plate dampers by Tsai et al. (1993). Another approach is provided by Soong (1990), which allows for rewriting the governing equations in state space representation and solving in an efficient and accurate way by application of first order differential equation solvers.

Effect of viscoplasticity

For steel at approximately room temperature and in the case of moderate strain rates, it can be assumed that the plastic flow occurs instantaneously compared to the time variation of the applied load. In cases of lead dampers or steel at high tempera-

ture or under very high strain rates, the creep and relaxation phenomenon must be considered. Creep signifies increasing strain with time under constant stress. Relaxation is defined as continual reduction of stress with time for a material under constant strain. In order to model the motion of dislocations, it is necessary to incorporate the physics of time independent plastic strains and time dependent creep strains to a unified theory. Özdemir (1976) proposed the following uni-axial model

$$\dot{\varepsilon} = \frac{\sigma}{E} + \frac{1}{\tau} \cdot \left(\frac{\sigma_d}{E} \right) \cdot \left(\frac{\sigma - \sigma_b}{\sigma_d} \right)^n \tag{7}$$

where $\dot{\varepsilon}$ is the strain decrement, τ and σ_b represent the relaxation time and back stress, respectively. The drag stress σ_d is a material constant. The quantity $\sigma - \sigma_b$ is denoted as overstress. This allows the modelling of the kinematical hardening effect. A detailed discussion can be found in the book of Soong and Dargush (1997).

Effect of temperature

The mechanical properties of steel in structures at approximately room temperature are both consistent and stable. Therefore, steel is often used as a building material. In case of impacts by major earthquakes, the structural steel within metallic dampers will cycle into the inelastic range. A significant portion of dissipated energy will be converted into heat. The surrounding metal will be heated. The quantity of temperature increase can be estimated by considering the energy balance. The dissipated energy represents a heat source, while conduction and convection processes lead to a redistribution of energy. For reasonable large steel damper design, it may be assumed that temperature increase does not significantly alter the mechanical properties of the device.

The behaviour of lead dampers is much more sensitive to moderate increases beyond room temperatures. Thus, in this case, thermal effects must be considered.

Consideration of failure

The theories of plasticity and viscoplasticity describe the behaviour of metals in the inelastic range during cycling loading but not the fail due to fatigue. The phenomenon of the low-cycle fatigue is of main interest. Low cycle fatigue results from a limited number of excursions into the inelastic range. Growth and interconnection of micro sized cracks lead eventually to failure at macroscopic level. In practice, a more phenomenological approach is used based upon the concept of material damage. It should be recognized that these plate dampers represent critical elements in the overall seismic protective system and therefore must be engineered to a high level of reliability. Dargush and Soong (1995) used a simple modelling approach for the mechanics of materials in order to study the behaviour of triangular metallic plate dampers under cyclic load.

Testing and validation

Soong and Dargush (1995) reported that, from a review of literature, much effort has been expended on experimental testing of metallic dampers and test structures. For determination of the mechanical characteristics of the damping devices, an in-plane

testing frame is employed and the horizontal displacement and the vertical force as well are controlled. The investigations should include:

- the force response at several displacement levels,
- fatigue history, and
- temperature rise of the specimen during cycling loading.

Implementation

Hysteretic dampers have been successfully applied for structural control in the fields of:

- design of seismic passive energy dissipation systems (Constantinou et al. (1998), Paulay and Priesley (1992)), and
- base isolation systems and foundation of superstructures (Bhatti et al. (1978)).

References

Bergman, D. M., and Goel, S. C. (1987), "Evaluation of Cyclic Testing of Steel Plate Devices for Added Damping and Stiffness", Report No. UMCE 87-10, University of Michigan, Ann Arbor, MI.

Bhatti, M. A., Pister, K. S., and Polek, E. (1978), "Optimal design of an Earthquake Isolation System", Report No. UCB/EERC-78/22, University of California.

Constantinou, M. C., Soong, T. T., and Dargush, G. F. (1998), "Passive Energy Dissipation Systems for Structural Design and Retrofit", MCEER Monograph Series 1, Multidisciplinary Center for Earthquake Engineering Research, Buffalo, NY.

Dargush, G. F., and Soong, T. T. (1995), "Behaviour of Metallic Plate Dampers in Seismic Passive Energy Dissipation Systems", *Earthquake Spectra*, 9(3).

Jones, D. I. G. (2001), *Handbook of Viscoelastic Vibration Damping*, John Wiley & Sons LTD.

Kelly, J. M., Skinner, R. I., and Heine, A. J. (1972), "Mechanisms of Energy Absorption in Special devices for Use in Earthquake Resistant Structures", *Bull. N.Z. Society Earthquake Engineering*, 5(3), 63-88.

Martinez-Romero, E. (1993), "Experiences on the Use of Supplemental Energy Dissipators on Building Structures", *Earthquake Spectra*, 9(3).

Özdemir, H. (1976), *Nonlinear Transient Dynamic Analysis of Yielding Structures*, Ph.D. Dissertation, University of California, Berkeley, CA.

Paulay, T., and Priesley, M. J. N. (1992), *Seismic Design of Reinforced Concrete and Masonry Buildings*, John Wiley & Sons, New York.

Perry, C. L., Fierro, E. A., Sedarat, H., and Scholl, R. E. (1993), "Seismic Upgrade in San Francisco Using Energy Dissipation Devices", *Earthquake Spectra*, 9(3).

Skinner, R. I., Kelly, J. M., and Heine, A. J. (1975), "Hysteresis Dampers for Earthquake-Resistant Structures", *Earthquake Engineering and Structural Dynamics*, 3, 287-296.

Soong, T. T. (1990), *Active Structural Control: Theory and Practise*, Wiley, New York.

Soong, T. T., and Dargush, G. F. (1997), *Passive Energy Dissipation Systems in Structural Engineering*, John Wiley & Sons, New York.

Tsai, K. C., Chen, H. W., Hong, C. P., and Su, Y. F. (1993), "Design of Steel Triangular Plate Energy Absorbers for Seismic-Resistant Construction", *Earthquake Spectra*, 9(3).

Tsai, C. S., and Tsai, K. C. (1995), "TPEA Device as Seismic Damper for High-Rise Buildings", *Journal Engineering Mechanics*, ASCE, 121(10).

Whittaker, A., Bertero, V., Alonso, J., and Thompson, C. (1989), "Earthquake Simulator Testing of Steel Plate Added Damping and Stiffness Elements", Report No. UCB/EERC-89/02, College of Engineering, University of California at Berkeley.

Whittaker, A., Aiken, I., Bergman, D., Clark, P., Cohen, J., Kelly, J., and Scholl, R. (1993), "Code Requirements for the Design and Implementation of Passive Energy Dissipation Systems", *Proc. ATC 17-1 on Seismic Isolation, Energy Dissipation, and Active Control*, 2, 497-508.

Xia, C., Hanson, R. D., and Wight, J. K. (1990), "A Study of ADAS Element Parameters and Their Influence on Earthquake Response of Building Structures", Report No. UMCE 87-10, The University of Michigan, Ann Arbor, MI.

Notations

Symbol	*Description*	*Unit*
A	cross sectional area	m^2
E	elasticity modulus	N/m^2
L	length	m
W	work, energy	J
f	force	N
k	stiffness	kg/s^2
x	displacement	m
ε	strain	m
μ	ductility ratio	-
σ	stress	N/m^2
τ	relaxation time	s

Subscripts

d	damper
$\max$	maximum
y	yield

2.1.1.7 Shape memory alloy damper

Theoretical background

Shape memory alloys (SMAs) are metallic materials that mainly exist in two different crystal structure types, namely martensite and austenite or a combination of both. Martensite is characterized by a body centred tetragonal crystal structure and austenite by a body centred cubic crystal structure. Since the properties of SMAs change according to the two input variables temperature and strain, SMAs are often called “smart materials”. The phase transformation of SMAs is reversible. Profound information about material behaviour of SMAs and their applications may be found in Duerig (1990), Funakubo (1987), Humbeeck (2001), Janke et al. (2005), Otsuka and Wayman (1999), and in Otsuka and Kakeshita (2002).

Due to the fairly high damping characteristics of SMAs, these materials are also used as dampers. If the material properties are changed according to the actual material temperature and material strain, respectively, SMAs represent controllable dampers or semi-active damping devices, respectively. Within this chapter, SMAs used as passive dampers are introduced, whereas the use of controllable SMAs is described in chapter 2.1.2.2.

According to Janke et al. (2005), primarily, one may distinguish between four different behaviours of SMAs:

1. SMAs may behave “actuator like” (Fig. 22),
2. SMAs show the so-called “shape memory effect” (Fig. 23),
3. SMAs behave super elastically (Fig. 24), and
4. SMAs may act as hysteretic material dampers in pure martensitic state (Fig. 25).

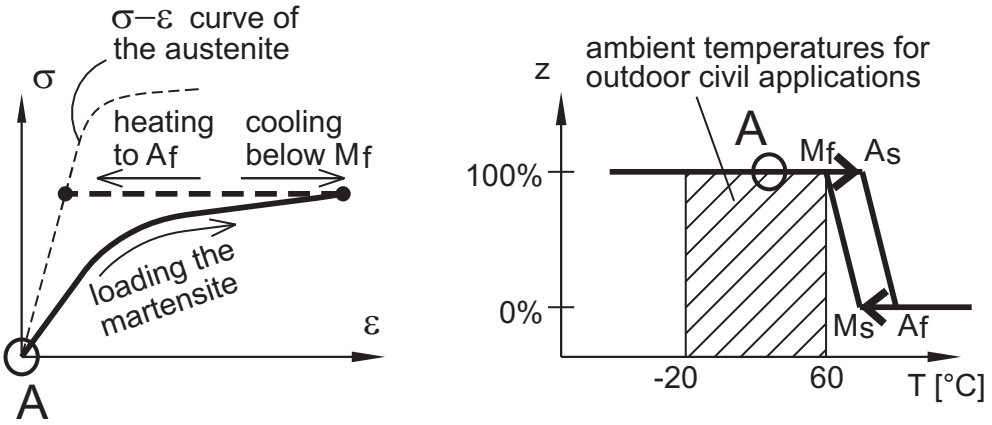

Fig. 22: Stress strain curves and transformation temperature profiles for “actuator like” change of strain and stiffness at constant stress (Janke et al. (2005)).

If SMAs behave “actuator like”, ambient temperature is below the temperature “martensite finish” (Mf). After pure martensite has been deformed, the crystal structure of the SMA may be changed from martensite to austenite and back by heating and cooling (horizontal dashed line in Fig. 22). Since austenite has a larger elasticity modulus than martensite, a device with two different elasticity moduli may be produced. If a spring is produced with such an SMA and connected with another steel

spring, the connecting point will move when heating and cooling. This is the reason why this SMA behaviour is called “actuator like”.

If ambient temperature lies between “martensite finish” and “austenite start” (As), the so-called “shape memory effect” of SMA occurs. First, pure martensite is deformed plastically. Then, the load is removed and plastic deformation results (Fig. 23). From this point, two scenarios are feasible. If the SMA is heated without geometrical constraints, martensite will change to austenite which ends up in a full shape recovery of the initial shape in point A. If the SMA is heated at constant strain, stress increase results due to the phase change to austenite, which has a larger elasticity modulus.

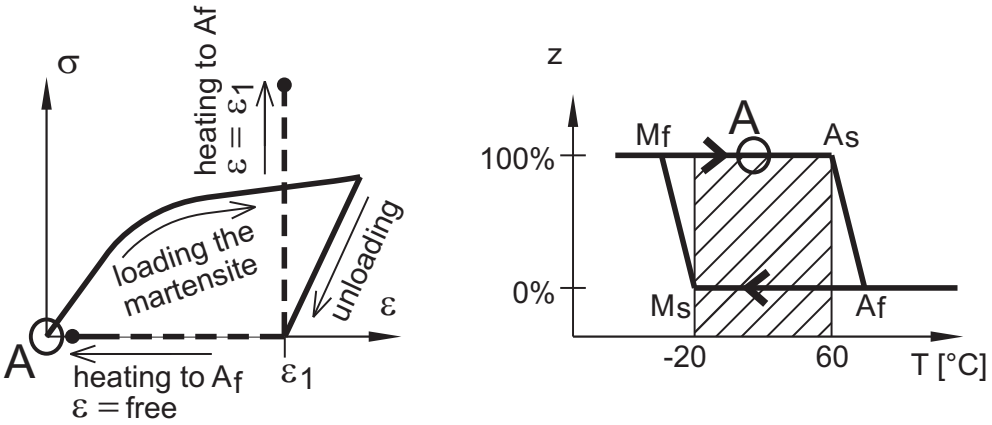

Fig. 23: Stress strain curves and transformation temperature profiles for shape memory effect in the case of free strain recovery and constraint strain recovery (Janke et al. (2005)).

If ambient temperature lies above “austenite finish” (Af), the SMA behaves “super elastically” (Fig. 24). Pure austenite is deformed until it reaches plastic state. Then, austenite will transform to martensite with increasing strain (see plateau in Fig. 24). When the state of pure martensite is reached, the plateau ends and the stress strain curve goes up with smaller slope due to smaller elasticity modulus of martensite relatively to austenite. During unloading, martensite will change to austenite on a lower stress plateau. Finally, the SMA consists again of pure austenite. The area enclosed by the stress strain trajectory is equivalent to the dissipated energy per cycle. Therefore, SMA working in superelastic mode may be used as dampers.

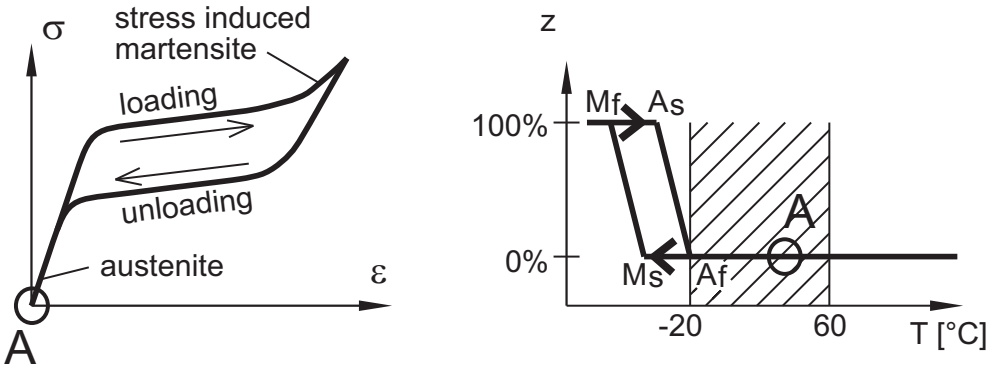

Fig. 24: Stress strain curves and transformation temperature profiles for the so-called superelastic behaviour (Janke et al. (2005)).

If ambient temperature lies between “martensite finish” and “austenite start”, SMAs may work as pure martensitic, hysteretic dampers if temperature is constant (Fig. 25). Basically, also pure austenitic SMAs may work as hysteretic dampers. However, the main advantages of martensitic hysteretic dampers are:

- The elasticity modulus of martensite is smaller than of austenite. Therefore, the stress strain trajectory encloses a larger area for the same stress which results in larger damping for the target structure.
- Due to the reorientation of martensite variants, martensite can withstand many more deformation cycles than austenite without failure for the same dissipated energy.

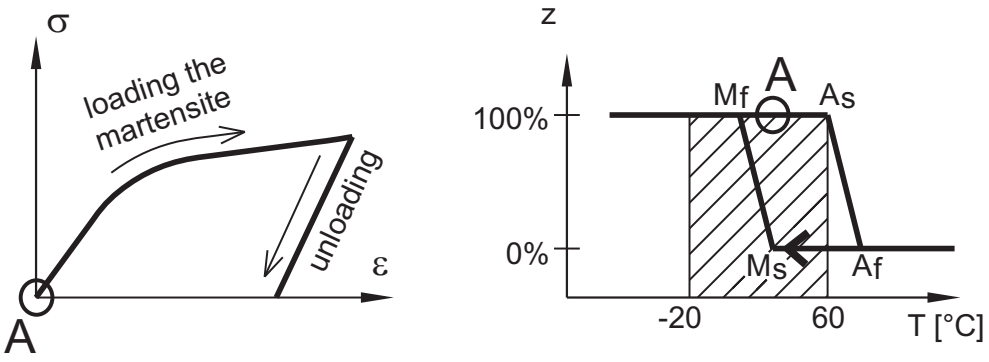

Fig. 25: Stress strain curves and transformation temperature profiles for martensitic hysteretic damping (Janke et al. (2005)).

Due to the larger hysteresis loop of SMAs working as pure martensitic hysteretic dampers compared to the hysteresis area of SMAs operating in superelastic mode (Fig. 26), SMA passive dampers are usually based on the former effect.

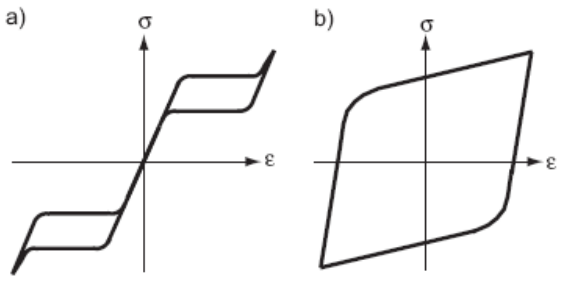

Fig. 26: Hysteresis loops for: a) superelastic SMA behaviour and b) martensitic hysteretic damping (Janke et al. (2005)).

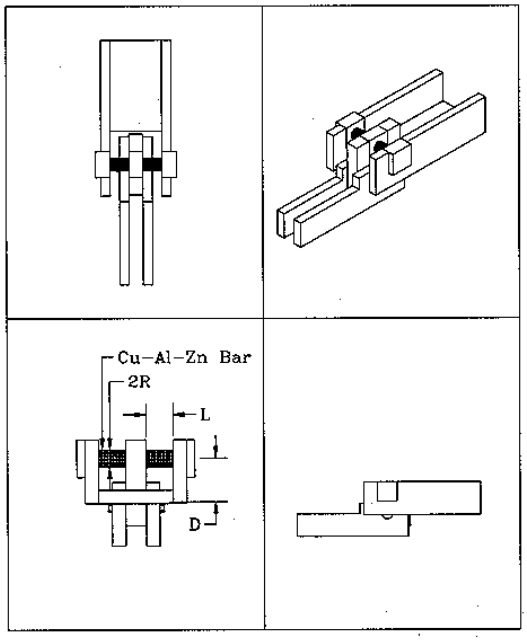

Fig. 27: Torsion bar design (Witting and Cozzarelli (1992)).

Design issues

Witting and Cozzarelli (1992) investigated four principal design mechanisms for producing an SMA based damping device. They used a Cu-Zn-Al alloy. It was a bar in torsion and beam in bending, which was axially loaded, and the clamped plate was loaded in the centre (Fig. 27). They found that the annular clamped plate was much too stiff and resulted in very small strains. The axially loaded beam was also found unsuitable because the constraints of stiffness and strain would cause the beam to buckle. A direct comparison between torsion and bending beam showed that more energy was put into higher strain regions in the torsion bar design than in the bending beam design. The larger strain resulted in a bigger amount of energy absorbed. Therefore, the torsion bar design apparently resulted in a more effective damper.

For the first assessment of the damper capabilities, a linear constitutive mode was used. The basic dimensions of the damper are torsion arm length D, radius of torsion bar R, and length of torsion bar L (Fig. 27). The angle of twist Θ of a solid round bar of radius R, length L, with torque T applied at the end of the bar and shear modulus G is

$$\Theta = \frac{2 \cdot T \cdot L}{G \cdot R^4} \tag{1}$$

The angle of twist Θ due to the displacement x is expected to be small, which allows the following simplification

$$\frac{x}{D} = \sin(\Theta) \approx \Theta \tag{2}$$

The shear strain ε_{xy} may be expressed in terms of L, D, x and the radial distance r from the centre of the bar as follows

$$\varepsilon_{xy} = \frac{\Theta \cdot r}{2 \cdot L} = \frac{x \cdot r}{2 \cdot L \cdot D} \tag{3}$$

The damper force is given by

$$f_d = \frac{\pi \cdot G \cdot R^4 \cdot x}{L \cdot D^2} \tag{4}$$

Considering that the damper force is the product of damper stiffness and damper displacement, the damper stiffness can be expressed as

$$k_d = \frac{\pi \cdot G \cdot R^4}{L \cdot D^2} \tag{5}$$

The maximum shear strain occurs at $r = R$ if the displacement x reaches its maximum $x_{\max}$. This yields for the maximum strain

$$\varepsilon_{\max} = \frac{x_{\max} \cdot R}{2 \cdot L \cdot D} \tag{6}$$

Solving Eqs. (5) and (6) for D yields

$$D = \frac{2 \cdot \pi \cdot G \cdot R^3 \cdot \varepsilon_{\max}}{x_{\max} \cdot k_d} \tag{7}$$

which leads to the length L as follows

$$L = \frac{k_d \cdot x_{\max}}{4 \cdot \pi \cdot G \cdot R^2 \cdot \varepsilon_{\max}^2} \tag{8}$$

Upon substitution of Eq. (7) into Eq. (3) leads to the shear strain as follows

$$\varepsilon_{xy} = \frac{\varepsilon_{\max} \cdot r}{R} \tag{9}$$

The equation of strain energy density is

$$U_0 = 2 \cdot G \cdot \varepsilon_{xy}^2 \tag{10}$$

This equation must be integrated over the high strain region. Since the strain is independent of y, the integration limits for Θ become 0 and 2π. The maximum of r is R. The minimum value of r can be calculated by substituting $\varepsilon_{\min}$ for ε_{xy} in Eq. (9) which leads to

$$r_{\min} = \frac{R \cdot \varepsilon_{\min}}{\varepsilon_{\max}} \tag{11}$$

Using Eq. (7) in order to eliminate L, the total strain energy may be estimated by

$$W = 2 \cdot \int_0^{2\pi} \int_0^a \int_b^R \frac{2 \cdot G \cdot \varepsilon_{\min}^2}{R^2} \cdot r^3 \cdot dr \cdot dy \cdot d\Theta \tag{12}$$

with:

$$a = \frac{x_{\max}^2 \cdot k_d}{4 \cdot \pi \cdot G \cdot R^2 \cdot \varepsilon_{\max}^2} \tag{13}$$

$$b = \frac{R \cdot \varepsilon_{\min}}{\varepsilon_{\max}} \tag{14}$$

For the final design, a more accurate nonlinear model is developed. The constitutive law used in the analysis is bilinear

$$\tau_{xy} = 2 \cdot G_1 \cdot \varepsilon_{xy} + \{2 \cdot (G_1 - G_2) \cdot (\varepsilon_t - \varepsilon_{xy})\} \cdot U(\varepsilon_{xy} - \varepsilon_t) \tag{15}$$

The two shear moduli G_1 and G_2 represent the elastic and inelastic shear modulus. The variable ε_t is the strain value at which the stress strain trajectory changes its slope. The term $U(\varepsilon_{xy} - \varepsilon_t)$ denotes the step function as follows

$$U(x) = \begin{cases} 0 : x \le 0 \\ 1 : x > 0 \end{cases} \tag{16}$$

The stress strain curve described by Eq. (15) is depicted in Fig. 28. The torque produced from the two torsion bars within the damper (Fig. 27) may be calculated as

$$T = f_d \cdot D = 2 \cdot \int_0^{2\pi R} \int_0 \left(\tau_{xy} \cdot r\right) \cdot r \cdot dr \cdot d\Theta \tag{17}$$

Substituting τ_{xy} from the constitutive law in Eq. (17) and using Eq. (3) for the shear strain, the damper force becomes

$$f_d = \frac{4}{D} \cdot \int_0^{2\pi R} \int_0 \left\{ \frac{G_2 x^2}{2 \cdot L \cdot D^2} + \left[\left(G_1 - G_2\right) \left(\varepsilon_t - \frac{x}{2 \cdot L \cdot D} r \right) \right] \cdot W\left(\varepsilon_{xy} - \varepsilon_t\right) \right\} \cdot r^2 \cdot dr \cdot d\Theta \tag{18}$$

Assuming $R > 2 \cdot L \cdot D \cdot \varepsilon_t / x$, integration of Eq. (18) simplifies to

$$f_d = \frac{\pi \cdot G_2 \cdot R^4}{L \cdot D^2} \cdot x + \frac{8 \cdot \pi \cdot \varepsilon_t}{3 \cdot D} \cdot \left(G_1 - G_2\right) \cdot \left[R^3 - \frac{2 \cdot \left(L \cdot D \cdot \varepsilon_t\right)^3}{x^3} \right] \tag{19}$$

The two presented design approaches delivered two estimates of the damper force. By choosing the geometrical design parameters L, D, and R and selecting the appropriate material, which defines G_1, G_2, and ε_t, the damper force may be estimated using the simplified approach of Eq. (4) or the more accurate approach given by Eq. (19).

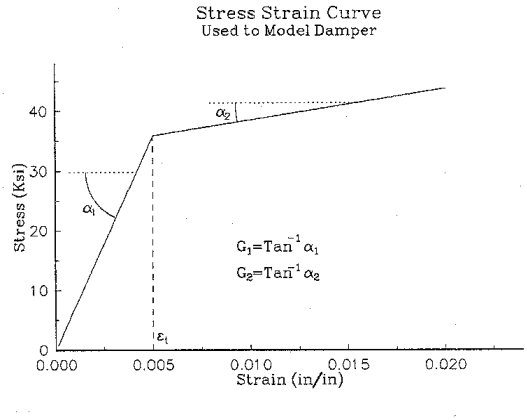

Fig. 28: Stress strain diagram used for bilinear damper model (Witting and Cozzarelli (1992)).

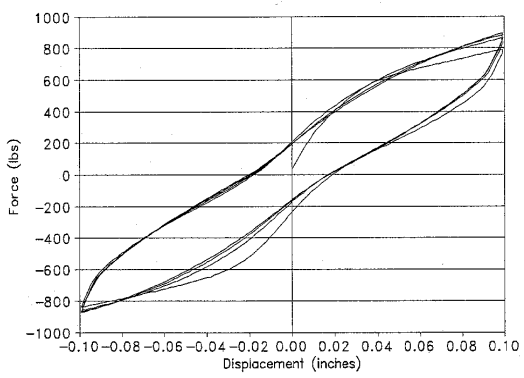

Fig. 29: Force displacement loops (Witting and Cozzarelli (1992)).

The application of the SMA dampers is limited due to dimensions of civil structures which makes relatively high damping forces necessary. Therefore, in case of damping civil structures using SMAs, large amount of material is needed compared to other applications as in the case of, e.g., automotive engineering or medical micro technologies. Probably one of the most important reasons why SMA dampers are not so often used in civil engineering for vibration mitigation is that the increase of damping is low compared to the financial investment. Another reason might be that a value

of 40% material damping is quite high but only a part of all mechanical energy can be transmitted to the damping part in devices (Humbeeck and Kustov (2005)).

Testing and validation

SMA dampers are tested similarly to other damper types; see the test set-up configuration depicted in Fig. 5 and Fig. 6. An example of measured force displacement trajectories of SMA dampers is depicted in Fig. 29 (Witting and Cozzarelli (1992)). The tested SMA is a CU-Zn-Al alloy.

Implementation

Due to the fairly large material costs of SMAs, such dampers are rarely implemented in civil structures in order to enhance structural damping. If SMA based passive dampers shall be used for vibration reduction, the SMA operating as a martensitic hysteretic damper should be used because this operating mode provides maximum additional damping to the structure.

Basically, the main motivation to use SMA as damping element is to have a semi-active damping device available, where, e.g., the force may be adapted to the structure by heating and cooling the SMA device (Li et al. (2004), Rustighi et al. (2005), Williams et al. (2002)). Such kind of applications is shortly described in chapter 2.1.2.3.

References

Duerig, T. W. (1990), *Engineering Aspects of Shape Memory Alloys*, Butterworth-Heinemann, London.

Funakubo, H. (1987), “Precision Machinery and Robotics, Vol. 1 – Shape Memory Alloys”, Gordon and Breach.

Humbeeck, J. V. (2001), “Shape memory alloys: A material and a technology”, Adv. Eng. Mater, 3(11), 837-850.

Humbeeck, J. V., and Kustov, S. (2005), “Active and passive damping of noise and vibrations through shape memory alloays: applications and mechanisms”, *Smart materials Structures,* 14, 171-815.

Janke, L., Czaderski, C., Motavalli, M., and Ruth, J. (2005), “Applications of shape memory alloys in civil engineering structures – Overview, limits and new ideas”, Journal of Materials and Structures, 38(279), 578-592.

Li, H., Liu, M., and Oh, J. (2004), “Vibration mitigation of a stay cable with one shape memory alloy damper“, Journal of Structural Control and Health Monitoring, 11(1), 21-36.

Otsuka, K., and Wayman, C. M. (1999), *Shape Memory Materials*, Cambridge University Press.

Otsuka, K., and Kakeshita, T. (2002), “Science and technology of shape-memory alloys. New developments", Mrs Bulletin 27(2), 91-100.

Rustighi, E., Brennan, M. J., and Mace, B. R. (2005), “A shape memory alloy adaptive tuned vibration absorber: design and implementation“, Journal of Smart Materials and Structures, 14, 19-28.

Williams, K., Chiu, G., and Berhard, R. (2002), “Adaptive-passive absorbers using shape-memory alloys“, Journal of Sound and Vibration, 249(5), 835-848.

Witting, P.R., and Cozzarelli, F.A. (1992), *Shape Memory Structural Dampers: Material Properties, Design and Seismic Testing,* Report No. NCEER-92-0013, State University of New York at Buffalo.

Notations

Symbol	*Description*	*Unit*
D	torsion arm length	m
G	shear modulus	N/m^2
L	length	m
R	radius	m
T	temperature; torque	K; Nm
W	work, energy	J
f	force	N
k	stiffness	kg/s^2
r	radial distance	m
x	displacement	m
Θ	angle of twist	rad
ε	shear strain	-
τ	shear stress	N/m^2

Subscripts

d	damper
$\max$	maximum

2.1.1.8 Passive tuned mass damper

Introduction

A passive tuned mass damper (TMD) or tuned vibration absorber is basically an energy dissipation device that in its simplest form consists of a mass that is attached to a structure (primary system) with spring and damper elements (Fig. 30). Due to the damper, energy dissipation occurs whenever the mass of the TMD oscillates with non-vanishing displacement or velocity relative to the primary system. This is achieved by transferring as much energy as possible from the primary system to the TMD by a careful tuning of the natural frequency and damping ratio of the TMD. Since the mass of the TMD is significantly smaller that that of the primary system, transferring energy from the primary system to the TMD generates a great relative oscillation of the mass of the TMD.

Contrary to a standard damper which generally provides additional energy dissipation in a wide frequency band, a TMD operates efficiently only in a narrow frequency band. This behaviour is closely related to the mechanism of energy transfer from the primary system to the TMD. High energy transfer arises whenever the natural frequency of the TMD is tuned to the natural frequency of the primary structure. Therefore, if attached to a continuous structure, the TMD mitigates only one specific vibration mode.

The concept of a TMD without integrated damping device was invented by Frahm in 1909 (Frahm (1909)) to reduce the rolling motion of ships. A first theory of the TMD with integrated damping device was presented years later by Ormondroyd and Den Hartog (Ormondroyd and Den Hartog (1928)). In Den Hartog's monograph (Den Hartog (1947)), a detailed analysis of optimal parameters of a TMD is presented. There, the model of a primary structure with an attached TMD is represented by the two degree of freedom system shown in Fig. 31. Den Hartog used the fixed-points method for obtaining an accurate approximate solution of the optimal parameters, natural frequency f_t and damping ratio ζ_t, of a TMD that minimizes the displacement of the primary structure where the latter has vanishing structural damping. A list of optimal parameters for different minimization objectives obtained by the fixed-points method is given in Warburton (1982) and in the textbook of Korenev and Reznikov (1993). Recently, a method for computing exact closed form solutions of optimal parameters that minimizes the maximum of transfer functions was presented by Nishihara and Asami (2002). For structures with vanishing structural damping, exact solutions with respect to different minimization objectives are given in Asami and Nishihara (2003).

If the primary system is subjected to random white noise excitation, that is, an excitation that contains any frequency with exactly the same amplitude, the design of a TMD is based on the minimization of the integral of the square of the absolute value of the transfer function (Crandall and Mark (1963)). Exact closed form solutions of the optimal parameters of a TMD for different minimization objectives and undamped primary system are given by Warburton (1982) and Korenev and Reznikov (1993).

In practical applications, the primary system has non-vanishing structural damping and therefore many attempts have been made to find exact, closed form solutions of the optimal parameters. Unfortunately, so far, no exact algebraic solutions to this problem are known. Empirical formulas for several minimization objectives, that are based on numerical optimization results, were given by Ioi and Ikeda (1978). Recently, analytical approximations obtained by perturbations techniques were constructed by Asami et al. (2002).

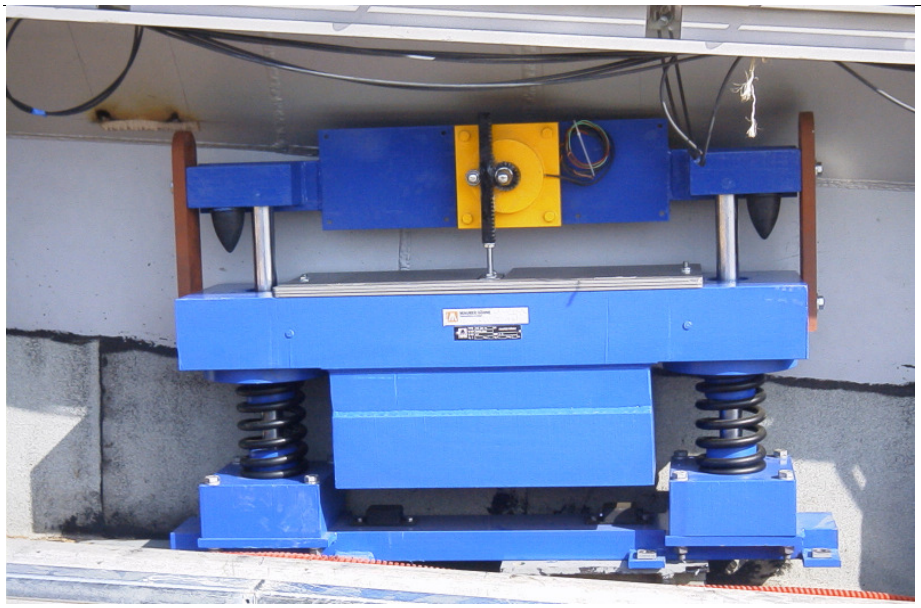

Fig. 30: Typical implementation of a TMD for vertical vibration mitigation of bridges.

Basic equations of the passive TMD

The standard model of a linear elastic structure with a linear TMD is the two degree of freedom model displayed in Fig. 31. The equations of motion of this model are given by

$$\begin{aligned} m_p\ddot{u}_p(t)+(c_p+c_t)\dot{u}_p(t)+(k_p+k_t)u_p(t)-c_t\dot{u}_t(t)-k_tu_t(t)&=f(t)-\tilde{m}_p\ddot{u}_g(t),\\ m_t\ddot{u}_t(t)+c_t\dot{u}_t(t)+k_tu_t(t)-c_t\dot{u}_p(t)-k_tu_p(t)&=-m_t\ddot{u}_g(t), \end{aligned} \quad (1)$$

where $u_p(t)$ is the displacement of the primary system $u_t(t)$ the displacement of the mass of the TMD (see Fig. 31). Both displacements are measured relative to the base. m_p, c_p, k_p are the modal mass, damping constant and stiffness of the primary system, and m_t, c_t, k_t are the mass, damping constant and stiffness of the TMD. $f(t)$ is the force acting the primary system, $\ddot{u}_g(t)$ is the base acceleration and $\tilde{m}_p$ is the participating mass of the primary system (see the end of this section for further details).

When formulated with respect to $u_p(t)$ and $u_r(t)=u_t(t)-u_p(t)$, the relative displacement of the TMD mass with respect to the displacement of the primary system, the equations of motion are

$$\begin{aligned} m_p\ddot{u}_p(t)+c_p\dot{u}_p(t)+k_pu_p(t)-c_t\dot{u}_r(t)-k_tu_r(t)&=f(t)-\tilde{m}_p\ddot{u}_g(t),\\ m_t\ddot{u}_p(t)+m_t\ddot{u}_r(t)+c_t\dot{u}_r(t)+k_tu_r(t)&=-m_t\ddot{u}_g(t), \end{aligned} \quad (2)$$

The standard model of a structure with a TMD is obtained by modelling the structure as a one-degree-of-freedom system using modal displacements. This dramatic simplification is justified by the particularity of properly tuned TMDs to operate effectively only in a narrow frequency band. TMDs are therefore designed to mitigate the oscillations of a specific vibration mode. A linear elastic structure with TMD can be mod-

elled by multi-degree-of-freedom system with N degree-of-freedoms where the TMD is connected with the k'th degree-of-freedom of the structure. The $N+1$ equations of motion are given by

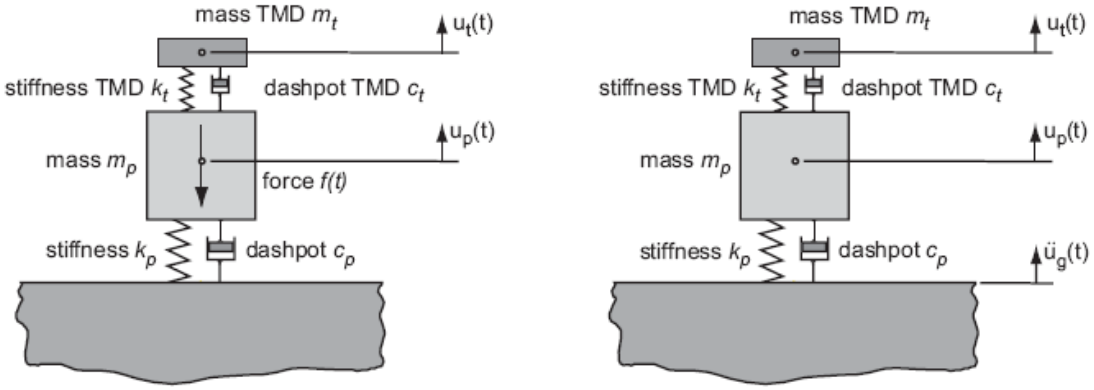

Fig. 31: Two degree of freedom model of a TMD attached to a primary structure. Left: Excitation force $f(t)$ acting on the primary mass. Right: Excitation through base acceleration $\ddot{u}_g(t)$.

$$M_p\ddot{U}_p(t)+C_p\dot{U}_p(t)+K_pU_p(t)-(c_t\dot{u}_t(t)+k_tu_t(t))E_k=F(t)-(M_pE)\ddot{u}_g(t),$$
$$m_t\ddot{u}_{p,k}(t)+m_t\ddot{u}_r(t)+c_t\dot{u}_r(t)+k_tu_r(t)=-m_t\ddot{u}_g(t),$$

(3)

where M_p, C_p and K_p are the mass, damping and stiffness matrices of the multi-degree-of-freedom model of the structure, E is the column vector with a one in each row, E_k is the column vector with a one in the k'th row and a zero in all other rows and $u_{p,k}$ is the displacement of the k'th degree-of-freedom of the structure. We assume that the TMD shall be designed to mitigate the vibrations associated to the mode shape ψ_k, where ψ_k is a solution of the eigenvalue problem $M_p\psi_k\omega_k^2-K_p\psi_k=0$ and is normalized in such a way to display a one in its k'th row. Using the mode shape ψ_k, the displacement of the primary structure associated to this mode shape can be described by $U_{p,k}=\psi_k u_{p,k}$. The two-degree-of-freedom model is obtained by multiplying the first equation in Eq. (3) from the left with the transpose of the mode shape ψ_k. By this operation, the relationship between the parameters describing the structure of the two-degree-of-freedom system and the N-degree-of-freedom system are given by

$$m_p=\psi_k^TM_p\psi_k,\ c_p=\psi_k^TC_p\psi_k, k_p=\psi_k^TK_p\psi_k, f(t)=\psi_k^TF(t), \tilde{m}_p=\psi_k^TM_pE.$$

(4)

Observe that $\psi_k^TE_k=1$ because of the specific normalization of the mode shape ψ_k. In general, the participating mass is not equal to the modal mass of the primary system: $\tilde{m}_p\neq m_p$. By introducing the participation factor

$$\Gamma_m = \frac{\psi_k^T M_p E}{\psi_k^T M_p \psi_k} = 1 + \frac{\psi_k^T M_p (E - \psi_k)}{\psi_k^T M_p \psi_k} \tag{5}$$

$\tilde{m}_p$ can be expressed as $\tilde{m}_p = \Gamma_m m_p$. In general, because TMDs are connected to the degree-of-freedom with maximum modal amplitude, the participation factor Γ_m is greater than unity. Γ_m has an effect on optimal tuning parameters of the TMD in the cases of base excited structures (e.g. earthquake loadings). Since the ratio of the mass of the TMD and the modal mass m_p is small, in general, this effect is also small.

H∞ optimization

Until now, many optimization criteria for the TMD have been proposed. The most common criteria are the H∞ and H_2 norm optimization criteria. The H∞ norm of a scalar transfer function $G(z)$ is defined by

$$\left\| G(z) \right\|_\infty = \max_z \left| G(z) \right|, \tag{6}$$

that is, the H∞ norm represents the maximum amplitude of the absolute value of the transfer function. The absolute value of the complex transfer function $|G(z)|$ is also known as the dynamic magnification factor. The H∞ norm provides a bound of the output gain, where the gain is defined in terms of the H_2 norm:

$$\left\| y(t) \right\|_2 \le \left\| G(z) \right\|_\infty \left\| f(t) \right\|_2. \tag{7}$$

That is, given a square integrable excitation $f(t)$, the H∞ norm provides a bound of the integral of the square response. Near equality is achieved for a harmonic excitation $f(t) = F \sin(\omega t)$ provided that the integral is taken over a finite time interval $0 \ldots t_{\max}$, since any harmonic function is not square integrable over an infinite time interval. Therefore, Eq. (7) provides a sharp bound for harmonic excitations acting over a long but finite period of time. It is important to note that Eq. (7) does not provide any information about the maximum amplitude of the output $y(t)$ within a time interval for an arbitrary excitation $f(t)$. Dimensionless complex transfer functions $G(z)$ of various response parameters of the primary system $u_p(t)$ and the relative displacement $u_r(t)$ of the TMD mass with respect to the primary system are given in Table 1.

The objective of the H∞ norm optimization is to find the frequency ratio η_t and damping ratio ζ_t of the TMD that minimize $\left\| G(z) \right\|_\infty$:

$$\min_{\eta_t, \zeta_t} \left\| G(z) \right\|_\infty = \min_{\eta_t, \zeta_t} \max_z \left| G(z) \right|. \tag{8}$$

With respect to the graph of the absolute value of the transfer function $G(z)$, the minimum of $\left\| G(z) \right\|_\infty$ is achieved if and only if there exist two local maxima and both have exactly the same amplitude (see Fig. 32 and Fig. 33).

Den Hartog's fixed-points method (Den Hartog (1947)) for computing approximations of the optimal parameters η_∞ and $\zeta_{t,\infty}$ is based on the observation that for primary

systems with vanishing damping ($\zeta_p \equiv 0$), there exist at least two frequencies z_1 and z_2 where $|G(z)|$ is invariant with respect to a variation of ζ_t (η_t is fixed), that is,

$$\frac{\partial |G(z_1)|}{\partial \zeta_t} = \frac{\partial |G(z_2)|}{\partial \zeta_t} = 0 . \tag{9}$$

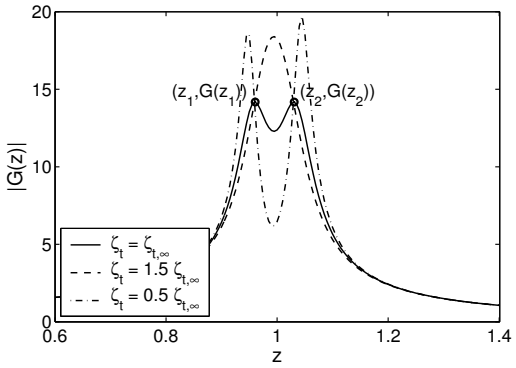

Fig. 32: Methods for H∞ norm optimization of a TMD applying the fixed points method.

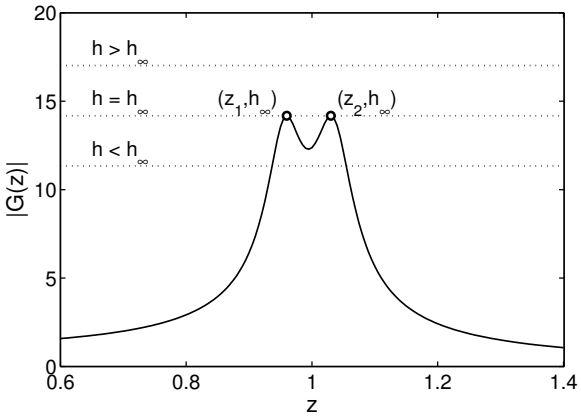

Fig. 33: Methods for H∞ norm optimization of a TMD applying the real roots method.

Hence, all graphs of $|G(z)|$ with fixed η_t and variable ζ_t cross the points $(z_1, |G(z_1)|)$ and $(z_2, |G(z_2)|)$. The approximations of the optimal parameters $\eta_{t,\infty}$ and $\zeta_{t,\infty}$ are obtained by maximizing $|G(z_1)|$ and $|G(z_2)|$ using the condition $|G(z_1)| = |G(z_2)|$. The fixed-points method provides simple closed form approximations of the optimal parameters $\eta_{t,\infty}$ and $\zeta_{t,\infty}$ that are accurate to a few percent within the range of mass ratios that are typical for civil engineering applications of a TMD ($0.01 \le \mu \le 0.1$) (Fig. 32). Unfortunately, the fixed-points method is limited to primary systems with vanishing damping since the presence of structural damping destroys the fixed points.

A method that provides exact closed form solutions of the H∞ norm optimization problem was recently proposed by Nishihara and Asami (2002). Their method is based on the observation that the function $H(z) = h - |G(z)|$, where h is an arbitrary real constant, has exactly two positive real roots z_1 and z_2 of multiplicity two if and only if $h = h_\infty = \min_{\eta,\zeta_t} \|G(z)\|_\infty$. This concept is sketched in Fig. 33. For $h = h_\infty$ and $\eta_{t,\infty}$ and $\zeta_{t,\infty}$ the graph of $|G(z)|$ touches the horizontal line h_∞ at the two points $(z_1, |G(z_1)|)$ and $(z_2, |G(z_2)|)$. The algebraic expressions of the exact closed form solutions are more complicated than those obtained by the fixed-points method.

Table 2 lists approximate solutions of the H∞ norm optimization problem for a primary structure with vanishing damping. The formulas are obtained by simplifying the exact solutions by using a rational functions approximation technique. The error of the formulas with respect to the exact solutions is smaller than 1% for $\mu \le 0.1$. The formulas regarding $h_\infty = \min_{\eta,\zeta_t} \|G(z)\|_\infty$ show that the effectiveness of the TMD increases with increasing mass ratio μ. The effectiveness is very sensitive to an inaccurate frequency tuning. A tuning error of ±5% with respect to the optimal frequency increases significantly the peak value of the transfer function of the primary structure (see Fig.

34). Much less critical is the correct tuning of the damping ratio of the TMD. A tuning error of ±5% has little influence on the peak value of the transfer function of the primary structure (see Fig. 35).

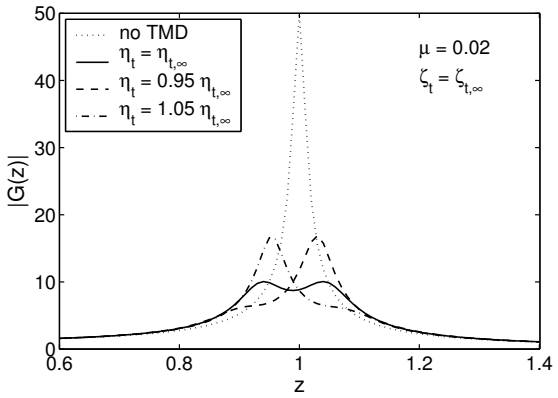

Fig. 34: Effects of poor frequency tuning of a TMD on the dynamic magnification factor of the displacement of the primary system.

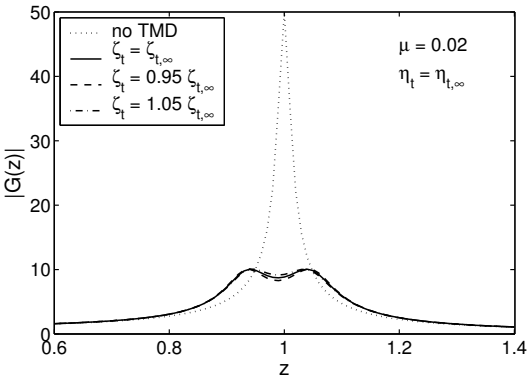

Fig. 35: Effects of poor damping tuning of a TMD on the dynamic magnification factor of the displacement of the primary system.

In most practical applications, the primary structure has non-vanishing damping so that the equations given in Table 2 represent an approximation of the optimal parameters. Unfortunately, no simple equations exist for non-vanishing damping. However, if the damping ratio of the primary system ζ_p is less than 1%, the optimal parameters given in Table 2 are still a reasonable good approximation for engineering applications. With increasing damping of the primary system, the equations of Table 2 become increasingly inaccurate. Fig. 36 and Fig. 37 display the optimal parameters $\eta_{t,\infty}$ and $\zeta_{t,\infty}$ that achieves the minimum of the displacement of the primary system $u_p(z)$ for several damping ratios ζ_p of the structure. The H∞ norm of the non-dimensional transfer function of the displacement of the primary system $u_p(z)$ and of the relative displacement of the TMD mass $u_r(z)$ is displayed in Fig. 38 and Fig. 39. The figures show that the maximum displacement of the primary system as well as the maximum relative displacement decreases with increasing mass ratio. It is important to note that the maximum amplitude of the relative displacement $u_r(z)$ is large for small mass ratios μ.

The effectiveness of a TMD can be described by using the mitigation factor that is defined as the ratio of the non-dimensional H∞ norm of the primary system without TMD $\|G_p(z)\|_\infty$, to the non-dimensional H∞ norm of the primary system with optimally tuned TMD $\|G(z)\|_\infty$:

$$\lambda_\infty = \frac{\|G_p(z)\|_\infty}{\|G(z)\|_\infty} \approx \frac{1}{2\zeta_p \|G(z)\|_\infty}. \qquad (10)$$

Fig. 40 shows that that the mitigation factor of an optimally tuned TMD increases with increasing mass ratio and decreases with increasing damping ratio of the structure. The increase with increasing mass ratio is particularly strong for small structural damping. In the range of practically realizable mass ratios, a TMD provides good performance only for lightly damped structures ($\zeta_p \le 0.01$). The smaller the damping

ratio the better is the performance of a TMD. In structures with a structural damping ratio of 5%, the dynamic response of the primary system can only be reduced by approximately a factor of two.

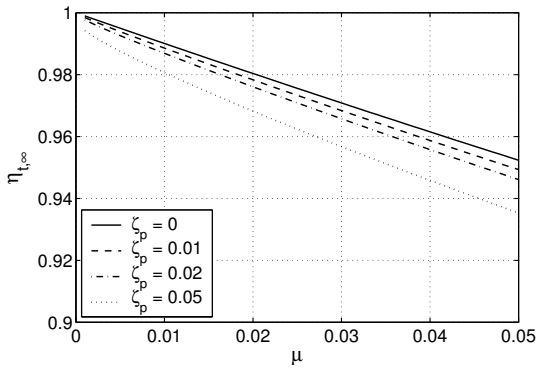

Fig. 36: Optimal TMD frequency for minimizing the displacement of the primary system with respect to the H∞ norm.

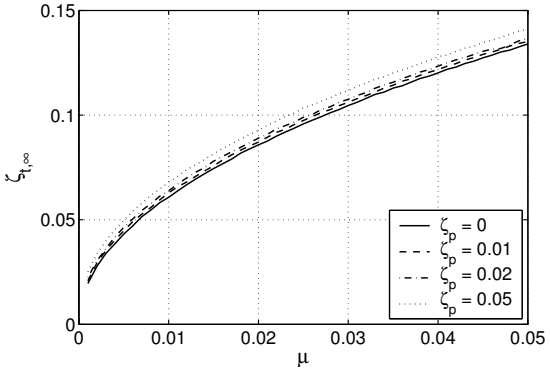

Fig. 37: Optimal TMD damping ratios for minimizing the displacement of the primary system with respect to the H∞ norm.

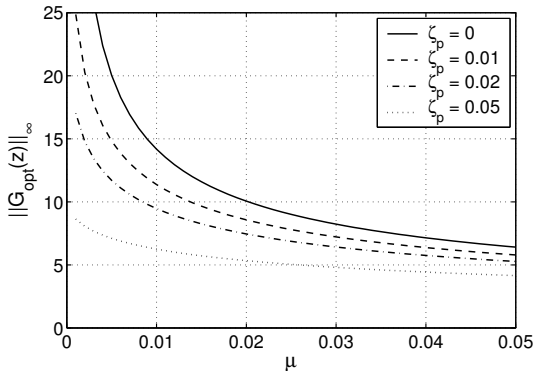

Fig. 38: Maximum of the non-dimensional transfer function of the displacement of the primary system for parameters minimizing the displacement of the primary system with respect to the H∞ norm.

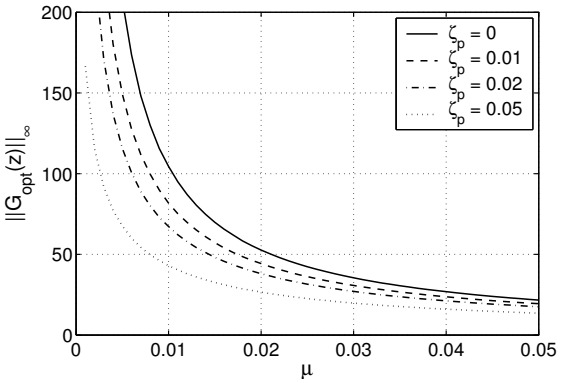

Fig. 39: Maximum of the non-dimensional transfer function of the relative displacement for parameters minimizing the displacement of the primary system with respect to the H∞ norm.

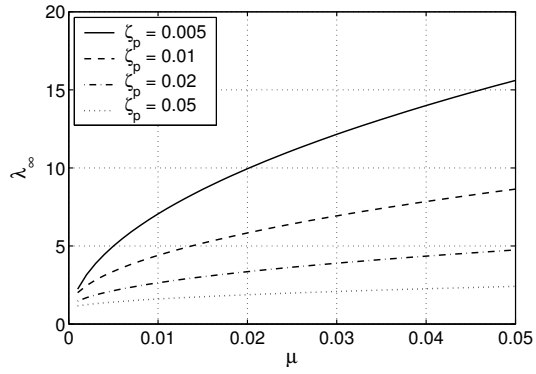

Fig. 40: Mitigation factor of a TMD optimized for minimizing the displacement of the primary system with respect to the H∞ norm.

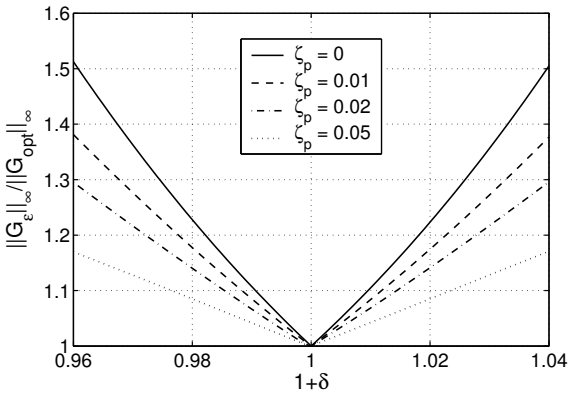

Fig. 41: Amplification due to a perturbation of frequency tuning of a TMD optimized for minimizing the displacement of the primary system with respect to the H∞ norm ($\delta = \eta_t / \eta_{t,\infty} - 1$, $\mu = 0.02$).

The performance of a TMD with respect to H_∞ norm is very sensitive to incorrect frequency tuning. The frequency detuning amplification with respect to an optimally tuned damper can be defined as the ratio of the non-dimensional H_∞ norm of the response of the detuned primary system $\|G_\varepsilon(z)\|_\infty$, to the non-dimensional H_∞ norm of the primary system with optimally tuned TMD $\|G_{opt}(z)\|_\infty$:

$$\lambda_{\varepsilon,\infty} = \frac{\|G_\varepsilon(z)\|_\infty}{\|G_{opt}(z)\|_\infty}. \tag{11}$$

$\lambda_{\varepsilon,\infty}$ increases with increasing frequency detuning and decreasing mass ratio, and decreases with increasing damping of the structure. Fig. 41 displays the frequency detuning amplification due to a perturbation of frequency tuning of a TMD optimized for minimizing the displacement of the primary system with respect to the H_∞ norm. The amplification is considerable and must be accounted for in the design since live loads or environmental effects induce changes of the natural frequencies of a structure. Frequency detuning increases also the H_∞ norm of the relative displacement. However, the detuning amplification is much smaller than that of the response of the primary system.

H_2 optimization

The H_2 norm of a transfer function $G(z)$ is defined by

$$\|G(z)\|_2 = \sqrt{\int_{t=-\infty}^{t=\infty} G(t)^2 dt} = \sqrt{\frac{1}{2\pi}}\sqrt{\int_{z=-\infty}^{z=\infty} |G(z)|^2 dz} \tag{12}$$

and is essentially a measure of the area between the square of the absolute value of the transfer function $|G(z)|^2$ and the z-axis. If the system is subjected to a random, white noise excitation, the H_2 norm of the transfer function $G(z)$ is directly related to the variance of the output associated to the transfer function. That is

$$\sigma_y = E[(y(t) - E[y(t)])^2] = \|G(z)\|_2^2 S_f, \tag{13}$$

where $y(t)$ is the response of the structure defined by $y(t) = G(t) \otimes f(t)$, $\otimes$ is symbolizing the convolution of the transfer function $G(t)$ with the excitation $f(t)$, $E[y(t)]$ is the average of the output that is usually zero, and S_f is the spectral density of the excitation $f(t)$. For ergodic processes, the variance can be estimated via temporal averages

$$\sigma_y = \lim_{T\to\infty} \frac{1}{2T} \int_{t=-T}^{t=T} (y(t) - E[y(t)])^2 dt = \|G(z)\|_2^2 S_f. \tag{14}$$

The objective of the H_2 norm optimization is to find parameters $\eta_{t,2}$ and $\zeta_{t,2}$ that minimize $\|G(z)\|_2$:

$$\min_{\eta_t,\zeta_t} \|G(z)\|_2 = \min_{\eta_t,\zeta_t} \sqrt{\frac{1}{2\pi}}\sqrt{\int_{z=-\infty}^{z=\infty} |G(z)|^2 dz}. \tag{15}$$

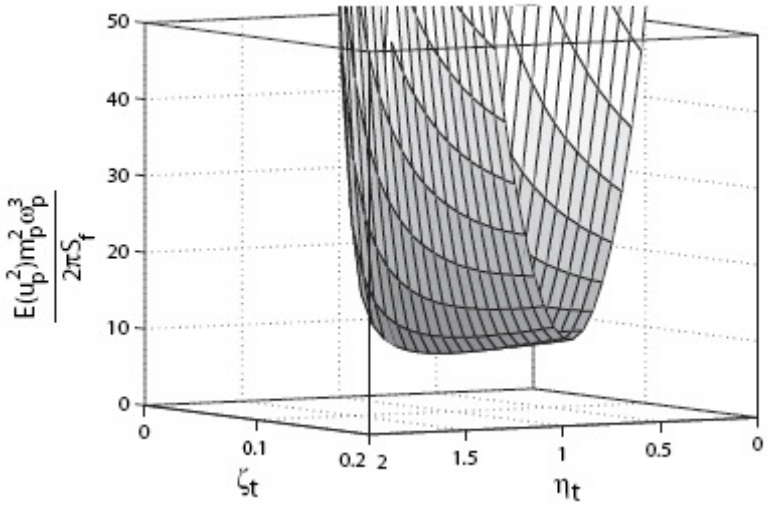

Fig. 42: Normalized variance of the displacement of the primary system.

$\|G(z)\|_2$ is a function of η_t, ζ_t, ζ_p and μ. Generally, closed form expressions of $\|G(z)\|_2$ can be obtained by evaluating the integral in Eq. (12) (Crandall and Mark (1963)) or by computing the observability grammian of the linear system described by the transfer function $G(z)$. Table 3 lists closed form expressions of $\|G(z)\|_2^2$ for the most common minimization objectives. Fig. 42 displays the normalized variance of the displacement of the primary system. Minimization of $\|G(z)\|_2$ is achieved if

$$\frac{\partial\|G(z)\|_2}{\partial\eta_t}=0 \text{ and } \frac{\partial\|G(z)\|_2}{\partial\zeta_t}=0 \tag{16}$$

hold. These conditions are usually sufficient and yields two nonlinear equations defining the optimal parameters $\eta_{t,2}$ and $\zeta_{t,2}$.

Exact closed form solutions have been obtained for systems with vanishing structural damping ($\zeta_p=0$). Table 4 lists exact solutions for various excitations and response parameters. For primary systems with structural damping, accurate closed form expressions can be obtained in form of a power series with respect to the damping ratio ζ_p. A list of first and second order terms for various excitations and response parameters can be found in Table 5. In general, the optimal parameters with respect to the H_2 norm are less sensitive to structural damping ζ_p than the optimal parameters with respect to the H_∞ norm (see Fig. 43 and Fig. 44). For small mass ratios, the optimal damping ratio $\zeta_{t,2}$ which minimizes the variance of the displacement of the primary system with respect to the H_2 norm is virtually independent of the structural damping ζ_p. Fig. 45 and Fig. 46 display the non-dimensional variance the displacement of the primary system $u_p(z)$ and of the relative displacement of the TMD mass $u_r(z)$ of a TMD optimally tuned with respect to minimization of displacement of the primary system.

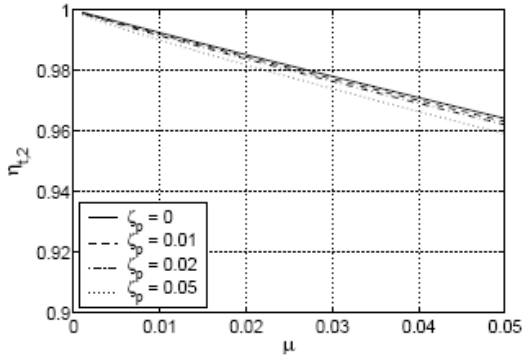

Fig. 43: Optimal TMD frequency for minimizing the variance of the displacement of the primary system with respect to the H_2 norm.

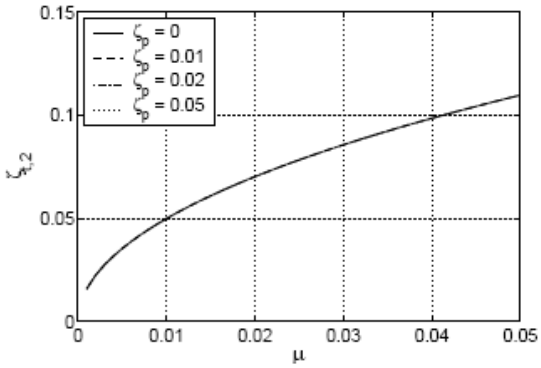

Fig. 44: Optimal TMD damping ratios for minimizing the variance of the displacement of the primary system with respect to the H_2 norm.

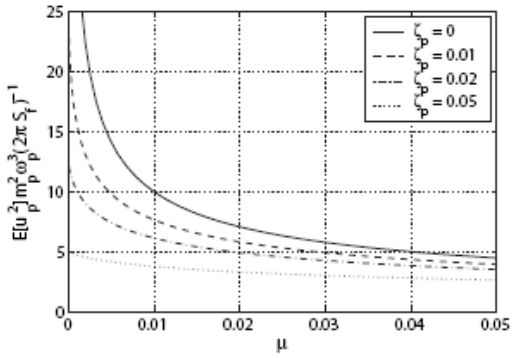

Fig. 45: Minimum of the non-dimensional variance of the displacement of the primary system for parameters minimizing the variance of the displacement of the primary system with respect to the H_2 norm.

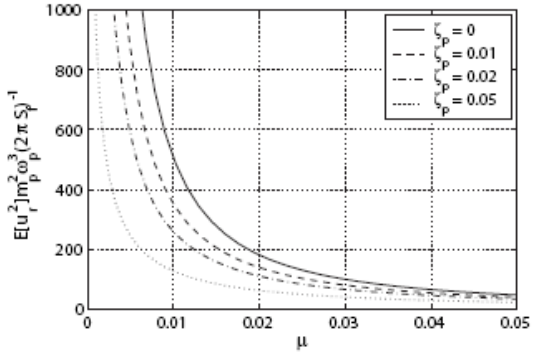

Fig. 46: Non-dimensional variance of the relative displacement of the mass of the TMD for parameters minimizing the variance of the displacement of the primary system with respect to the H_2 norm.

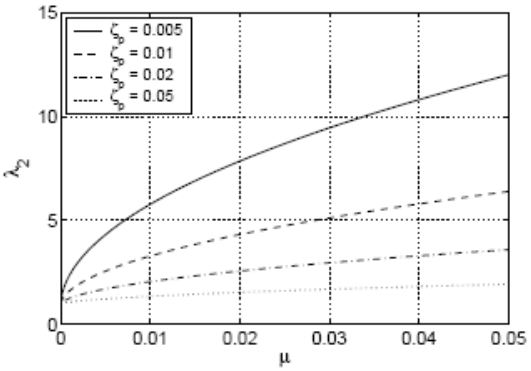

Fig. 47: Mitigation factor of a TMD optimized for minimizing the displacement of the primary system with respect to the H_2 norm.

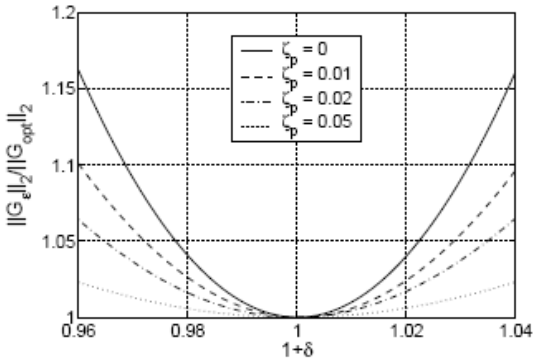

Fig. 48: Amplification due to a perturbation of frequency tuning of a TMD optimized for minimizing the displacement of the primary system with respect to the H_2 norm ($\delta = \eta_t / \eta_{t,\infty} - 1$, $\mu = 0.02$).

Similar to the case of H_∞ norm optimization, the mitigation factor is defined as the ratio of the non-dimensional H_2 norm of the primary system without TMD $\|G_p(z)\|_2$ to

the non-dimensional H_2 norm of the primary system with optimally tuned TMD $\|G(z)\|_2$:

$$\lambda_2 = \frac{\|G_p(z)\|_2}{\|G(z)\|_2} \approx \frac{1}{4\zeta_p \|G(z)\|_2}. \quad (17)$$

The effects of mass ratio and damping ratio of the structure on the mitigation factor λ_2 are equal to those observed for λ_∞ (see Fig. 47). For small structural damping, the overall performance is approximately 20% smaller than that of a TMD optimized with respect to H_∞ norm.

Similar to the H_∞ norm, the H_2 norm is sensitive to changes of the frequency ratio η_t and much less sensitive to changes of the damping ratio ζ_t. This is evident by observing the shape of the H_2 norm shown in Fig. 42. Defining the frequency detuning amplification factor with respect to an optimally tuned damper as

$$\lambda_{\varepsilon,2} = \frac{\|G_\varepsilon(z)\|_2}{\|G_{opt}(z)\|_2}, \quad (18)$$

where $\|G_\varepsilon(z)\|_2$ is the non-dimensional H_2 norm of the response of the detuned primary system and $\|G_{opt}(z)\|_2$ is the non-dimensional H_2 norm of the primary system with optimally tuned TMD. $\lambda_{\varepsilon,2}$ increases with increasing frequency detuning and decreasing mass ratio, and decreases with increasing damping of the structure. Fig. 48 displays the frequency detuning amplification factor due to a perturbation of frequency tuning of a TMD optimized for minimizing the displacement of the primary system with respect to the H_2 norm. Since the H_2 norm is defined via an integral, the amplification is significantly smaller than the amplification observed for TMDs optimized with respect to the H_∞ norm. Frequency detuning increases also the H_2 norm of the relative displacement. The amplification factor is of similar magnitude of the amplification of the response of the primary system.

Design consideration

Based on the theory developed in the last sections, a design procedure can be developed. The very first step in designing a TMD is to take a decision according to which norm the TMD should to be optimized. An optimization with respect to H_∞ norm is recommended for structures that are excited by loads exhibiting mainly periodical time components (e.g. loads generated by human activities like walking, running, jumping, dancing etc. or machines). For loads having mainly a wide band stochastic character (e.g. wind loads, earthquake loads), an optimization with respect to H_2 norm is more appropriate.

The second step is to identify the vibration mode of the structure that shall be damped. Using the shape of this mode, an equivalent single-degree-of-freedom model of the structure is generated by computing the associated modal mass and stiffness. For obtaining a scaling of the modal mass that is compatible with Eq. (1) or (2), the amplitude of the mode shape at the position where the TMD is attached to the primary structure has to be chosen equal to unity in the direction of action of the TMD. The modal stiffness is estimated using the modal mass and the natural frequency of the vibration mode. The natural frequency should be determined with field tests because the natural frequencies computed from analytical or numerical models

are too unreliable to be used for design purposes. As already pointed out, an inaccurate frequency tuning reduces significantly the effectiveness of a TMD. Although much less critical as the natural frequency, the structural modal damping should also be determined by field tests or estimated conservatively based on experience.

The third step regards the choice of the mass of the TMD. For a given damping ratio ζ_p of the structure, the mass ratio μ determines the optimal parameters $\eta_{t,opt}$ and $\zeta_{t,opt}$ as well as the response of the structure. The mass ratio is chosen to satisfy the maximum acceptable response level of the structure. In principle, the latter can always be achieved since the response of the primary structure decreases monotonically with increasing mass ratio. The maximum acceptable response level may be given by codes, guidelines, provisions or generally accepted rules.

In the design of a TMD, a number of issues have to be considered:

1. A TMD is effective if a sufficiently large TMD mass (mass ratio $\mu \geq 0.02$) can be accommodated and the vibration mode exhibit small structural damping $0.01 \leq \zeta_p$. Beyond a mass ratio of $\mu = 0.05$ a further increase of TMD mass results only in a modest further reduction of the response of the primary system.
2. A TMD is only effective when properly tuned to a specific natural frequency or, equivalently, to a specific vibration mode. Structures with several closely spaced natural frequencies which are all inside the frequency band of the excitation require a TMD for each natural frequency for achieving an effective vibration mitigation. Since each natural frequency is associated to a vibration mode and the coupling between the vibration modes is usually negligible, the design procedure for single modes can be applied.
3. The relative displacement, the displacement of the mass of the TMD with respect to the structure, can be considerable and requires space that must be accommodated within the structure. If the relative displacement of an optimally tuned TMD exceeds existing space constraints, the relative displacement can be reduced by increasing the mass of the TMD or, if the latter is not feasible, by increasing the damping ratio ζ_t of the TMD. For structures with structural damping $(\zeta_p > 0)$ a limitation of relative displacement can always be achieved. However, any restriction of the relative displacement that can not be accommodated by an increase of the mass of the TMD reduces the effectiveness of the TMD.
4. The mass of the TMD with respect to the modal mass of the structure determines the effectiveness of the TMD. In existing structures, the mass of the TMD may be restricted by the load bearing capacity of the structure and the installation of a single TMD may require a strengthening of the structure. A design with multiple TMDs having smaller masses may avoid a strengthening. However, the effectiveness decreases if not all TMDs can be installed at the locations with maximum amplitude of the mode shape. Furthermore, because of the smaller mass, the TMDs will exhibit a larger relative displacement and hence require more space than a single TMD and, finally, the costs of multiple TMDs is generally larger than the costs of a single TMD.
5. Natural frequency and damping ratio of structures may change because of the effect of live loads (e.g. pedestrians on footbridges) or environmental parameters (e.g. temperature). Since the effectiveness and response of

TMDs are very sensitive to an incorrect frequency tuning, changes of natural frequencies have to be considered in the design. Bad frequency tuning increases the response of the structure as well as the relative displacement of the TMD.

6. Since the relative displacement can be considerable, the fatigue behaviour of the TMD's springs has to be considered.

Testing and validation

For determining reliably the relevant absorber parameters, the natural frequencies and the damping ratios of the structure's relevant modes have to be established experimentally. This can be accomplished by ambient or forced vibration tests. A reliable estimation of the damping ratios can usually only be established by forced vibration tests. For lightweight structures, a simple and effective method is an impact test (e.g. by dropping a sandbag).

A TMD should be tuned in the laboratory before proceeding to it's installation on a structure. Natural frequency and damping ratio of a TMD are established by free vibration tests. Notice that the damping devices may contribute to the stiffness of the TMD and therefore affect its natural frequency. This has to be considered during the tuning of a TMD because of its high sensitivity with respect to frequency tuning.

The final tuning of the TMD's natural frequency is performed after installation. The easiest method for frequency tuning is to increase or reduce TMD's mass to fit the correct natural frequency. For lightweight structures, the validation can be performed by impact test (e.g. by dropping a sandbag). The impulsive force covers a wide frequency band so that the response of the structure is similar to the dynamic magnification curve shown in Fig. 34. Structures with an optimally tuned TMD show an amplification curve with two humps of equal height. Another useful test is to compare the response of the structure with locked and unlocked TMD. The effectiveness of the TMD can be obtained by computing the ratio of the maximum response with locked and unlocked TMD. Obviously, a reliable estimation requires a test with controllable excitation forces.

Implementation examples

The most common implementation of a TMD consists of a mass either hanging or being supported by several springs as shown in Fig. 30. This design is often used for controlling bridge and floor motions. However, there exist a large variety of different designs. Pendulum TMD are very often used for motion control of steel smoke stacks (Petersen (2001)). Solutions for space-limited applications include the tuned roller pendulum damper and the multi stage pendulum damper (Soong and Dargush (1997)). TMDs have been successfully installed for vibration response control of:

- Pedestrian bridges, stairs, spectator stands excited by walking or jumping people (Bachmann and Weber (1995)).
- Lightweight factory floors excited in one of their natural frequencies by machines.
- Tall free-standing structures (bridges, pylons of bridges, smoke stacks, towers) excited by wind-induced loads (Kwok (1984), Kwok and Samali (1995), Ohtake et al. (1992), Petersen (2001), Petersen (1980), Ueda et al. (1992)).

References

Asami, T., et al. (2002), "Analytical solutions to H-infinity and H-2 optimization of dynamic vibration absorbers attached to damped linear systems", *Journal of Vibration and Acoustics-Transactions of the Asme*, 124(2), 284-295.

Asami, T., and Nishihara, O. (2003), "Closed-form exact solution to H-infinity optimization of dynamic vibration absorbers (Application to different transfer functions and damping systems)", *Journal of Vibration and Acoustics-Transactions of the Asme*, 125(3), 398-405.

Bachmann, H., and Weber, B. (1995), "Tuned Vibration Absorbers for "Lively" Structures", *Structural Engineering International*, 5(1), 31-36.

Crandall, S. H., and Mark, W. D. (1963), Random vibration in mechanical systems, New York: Academic Press.

Den Hartog, J. P. (1947), *Mechanical Vibrations*, Third ed, New York and London: McGraw-Hill Book Company.

Frahm, H. (1909), Device for Damped Vibrations of Bodies. U. S. Patent No. 989958.

Ioi, T., and Ikeda, K. (1978), "On the Dynamic Vibration Damped Absorber of the Vibration System", Bulletin of the Japanese Society of Mechanical Engineering, 21, (151), 64-71.

Korenev, B., and Reznikov, L. M. (1993), Dynamic Vibration Absorbers: Theory and Technical Applications, Chichester, Eng-land: John Wiley & Sons Ltd..

Kwok, K. C. S. (1984), "Damping Increase in Building with Tuned Mass Damper", *Journal of Engineering Mechanics-Asce*, 110(11), 1645-1649.

Kwok, K. C. S., and Samali, B. (1995), "Performance of Tuned Mass Dampers under Wind Loads", *Engineering Structures*, 17(9), 655-667.

Nishihara, O., and Asami, T. (2002), "Closed-form solutions to the exact optimizations of dynamic vibration absorbers (mini-mizations of the maximum amplitude magnification factors)", *Journal of Vibration and Acoustics-Transactions of the Asme*, 124(4), 576-582.

Ohtake, K., et al. (1992), "Full-Scale Measurements of Wind Actions on Chiba Port Tower", *Journal of Wind Engineering and Industrial Aerodynamics*, 43(1-3), 2225-2236.

Ormondroyd, J., and Den Hartog, J. P. (1928), "The Theory of the Dynamic Vibration Absorber", *Transactions of the ASME*, APM-50-7, 9-22.

Petersen, C. (2001), *Schwingungsdämpfer im Ingenieurbau*, München: Fa. Maurer und Söhne, GmbH & Co. KG.

Petersen, N. R. (1980), "Design of Large Scale Tuned Mass Dampers", *Structural control*, June 4-7, 1979. Ontario, 581-596.

Soong, T. T., and Dargush, G. F. (1997), *Passive Energy Dissipation Systems in Structural Engineering*, Chichester: John Wiley & Sons.

Ueda, T., et al. (1992), "Suppression of Wind-Induced Vibration by Dynamic Dampers in Tower-Like Structures", *Journal of Wind Engineering and Industrial Aerodynamics*, 43(1-3), 1907-1918.

Warburton, G. B. (1982), "Optimum Absorber Parameters for Various Combinations of Response and Excitation Parameters", *Earthquake Engineering & Structural Dynamics*, 10(3), 381-401.

Often used notations

Symbol	*Description*	*Unit*
$G(z)$	non-dimensional complex transfer function	-
$\|G(z)\|_\infty$	H_∞ norm of non-dimensional complex transfer function	-
$\|G(z)\|_2$	H_2 norm of non-dimensional complex transfer function	-
c	dashpot constant	kg/s
f	frequency	Hz
k	stiffness constant	kg/s^2
m	mass	kg
η	frequency ratio	-
μ	mass ratio	-
ω	circular frequency	rad/s
ζ	damping ratio	-

Subscripts	*Description*
p	main structure
r	relative
t	tuned mass damper

Appendix

Table 1: Non-dimensional transfer functions for various excitations and response parameters.

Excitation	Output parameter	A(z)	B(z)
F	$\left\|\frac{u_p}{u_0}\right\|$	$\eta_t^2 - z^2$	$2\eta_t\zeta_t z$
F	$\left\|\frac{\dot{u}_p}{\omega_p u_0}\right\|$	$-2\eta_t\zeta_t z^2$	$z(\eta_t^2 - z^2)$
F	$\left\|\frac{\ddot{u}_p}{\omega_p^2 u_0}\right\|$	$-z^2(\eta_t^2 - z^2)$	$-2\eta_t\zeta_t z^3$
F	$\left\|\frac{u_r}{u_0}\right\|$	z	0
$\ddot{u}_g$	$\left\|\frac{\omega_p^2 u_p}{\ddot{u}_g}\right\|$	$(1+\mu)\eta_t^2 - z^2$	$2(1+\mu)\eta_t\zeta_t z$
$\ddot{u}_g$	$\left\|\frac{\omega_p \dot{u}_p}{\ddot{u}_g}\right\|$	$-2(1+\mu)\eta_t\zeta_t z^2$	$z((1+\mu)\eta_t^2 - z^2)$
$\ddot{u}_g$	$\left\|\frac{\ddot{u}_p + \ddot{u}_0}{\ddot{u}_g}\right\|$	$-z^2((1+\mu)\eta_t^2 - z^2)$	$-2(1+\mu)\eta_t\zeta_t z^3$
$\ddot{u}_g$	$\left\|\frac{\omega_p^2 u_r}{\ddot{u}_g}\right\|$	1	0

Legend

$G(z) = \frac{A(z) + iB(z)}{C(z) + iD(z)}$: non-dimensional transfer function with coefficients $A(z), B(z), C(z)$ and $D(z)$, where $C(z) = z^4 - ((1+\mu)\eta_t + 4\zeta_p\zeta_t)\eta_t + 1)z^2 + \eta_t^2$ and $D(z) = 2z(((1+\mu)\zeta_t\eta_t + \zeta_p)z^2 - (\zeta_t + \zeta_p\eta_t)\eta_t)$

F: excitation (force) applied to the primary system

$\ddot{u}_g$: excitation (acceleration) applied to the base

u_0: reference displacement ($u_0 = F_0 / k_p$ for harmonic excitation with $Fe^{i\omega t}$ and $u_0 = \sqrt{S_w} / k_p$ for white noise excitation $w(t)$ with autocorrelation $R_{ww}(t) = S_w\delta(t)$)

z: non-dimensional frequency $z = \omega / \omega_p$

Table 2: Approximate solutions of the H_∞ optimization problem for primary systems with vanishing structural damping ($\zeta_p = 0$).

Excitation	Minimized parameter	Transfer function	η_∞	$\zeta_{t,\infty}$	$\min \|G(z)\|_\infty$	$\frac{\|u_r(z)\|_\infty}{u_0}$
$Fe^{i\omega t}$	u_p	$\left\|\frac{u_p}{u_0}\right\|$	$\frac{1}{1+\mu}$	$\sqrt{\frac{3\mu}{8(1+\mu)}}\sqrt{1+\frac{3}{32}\mu}$	$\sqrt{\frac{2}{\mu}}\sqrt{1+\frac{17}{32}\mu}$	$\frac{4}{\sqrt{15}}\frac{1+\mu}{\mu}$
$Fe^{i\omega t}$	$\dot{u}_p$	$\left\|\frac{\dot{u}_p}{\omega_p u_0}\right\|$	$\frac{1}{1+\mu}\sqrt{1+\frac{\mu}{2}}$	$\sqrt{\frac{3\mu}{8(1+\mu)}}\sqrt{1+\frac{5}{24}\mu}$	$\sqrt{\frac{2}{\mu}}\sqrt{\frac{1+7\mu/12}{1+23\mu/24}}$	$\frac{4}{\sqrt{15}}\frac{1+\mu}{\mu}\sqrt{(1+\frac{\mu}{2})(1+\frac{2}{5}\sqrt{\mu}-\frac{49}{100}\mu)}$
$Fe^{i\omega t}$	$\ddot{u}_p$	$\left\|\frac{\ddot{u}_p}{\omega_p^2 u_0}\right\|$	$\sqrt{\frac{1}{1+\mu}}$	$\sqrt{\frac{3\mu}{8(1+\mu)}}\sqrt{1+\frac{27}{32}\mu}$	$\sqrt{\frac{2}{\mu}}\sqrt{\frac{1}{1+23\mu/32}}$	$\frac{4}{\sqrt{15}}\frac{1+\mu}{\mu}\sqrt{\frac{1+\mu/2}{1-4\sqrt{\mu}/5+11\mu/10}}$
$\ddot{u}_g e^{i\omega t}$	u_p	$\left\|\frac{\omega_p^2 u_p}{\ddot{u}_g}\right\|$	$\frac{\sqrt{1-\mu/2}}{1+\mu}$	$\sqrt{\frac{3\mu}{8(1+\mu)}}\sqrt{1+\frac{23}{48}\mu}$	$\sqrt{\frac{2}{\mu}}\sqrt{(1+\frac{65}{32}\mu+\frac{1085}{1024}\mu^2)}$	$\frac{4}{\sqrt{15}}\frac{(1+\mu)^2}{\mu}\sqrt{1+\frac{3}{5}\sqrt{\mu}+\frac{62}{75}\mu}$
$\ddot{u}_g e^{i\omega t}$	$\dot{u}_p$	$\left\|\frac{\omega_p \dot{u}_p}{\ddot{u}_g}\right\|$	$\frac{1}{1+\mu}$	$\sqrt{\frac{3\mu}{8(1+\mu)}}$	$\sqrt{\frac{2}{\mu}}\sqrt{1+\mu}$	$\frac{4}{\sqrt{15}}\frac{(1+\mu)^2}{\mu}\sqrt{1+\sqrt{\mu}+\frac{23}{16}\mu}$
$\ddot{u}_g e^{i\omega t}$	$\ddot{u}_p + \ddot{u}_g$	$\left\|\frac{\ddot{u}_p + \ddot{u}_0}{\ddot{u}_g}\right\|$	$\frac{1}{1+\mu}$	$\sqrt{\frac{3\mu}{8(1+\mu)}}\sqrt{1+\frac{3}{32}\mu}$	$\sqrt{\frac{2}{\mu}}\sqrt{1+\frac{17}{32}\mu}$	$\frac{4}{\sqrt{15}}\frac{(1+\mu)^2}{\mu}\sqrt{1+\sqrt{\mu}+\frac{7}{5}\mu}$

Legend

$Fe^{i\omega t}$: harmonic excitation applied to the primary system

$\ddot{u}_g e^{i\omega t}$: harmonic excitation applied at base

Table 3: Closed form expressions of the non-dimensional H_2 norm for various excitations and response parameters.

Excitation	Response parameter	$\|G(z)\|_2^2$
F	$\frac{E[u_p^2]\,m_p^2\omega_p^3}{2\pi S_f}$	$\frac{1}{4}\frac{(1+\mu)^2\zeta_t\eta_t^4+(\mu+4(1+\mu)\zeta_t^2)\zeta_p\eta_t^3-(2+\mu-4(1+\mu)\zeta_t^2-4\zeta_p^2)\eta_t^2+4\zeta_t^2\zeta_p\eta_t+\zeta_t}{(1+\mu)^2\zeta_t\zeta_p\eta_t^4+(\mu+4(1+\mu)\zeta_t^2)\zeta_p^2\eta_t^3-2(1-2(1+\mu)\zeta_t^2-2\zeta_p^2)\zeta_t\zeta_p\eta_t^2+(\mu+4\zeta_p^2)\zeta_t^2\eta_t+\zeta_t\zeta_p}$
F	$\frac{E[\dot{u}_p^2]\,m_p^2\omega_p}{2\pi S_f}$	$\frac{1}{4}\frac{(1+\mu)\zeta_t\eta_t^4+(\mu+4\zeta_t^2)\zeta_p\eta_t^3-2(1-2\zeta_t^2-2\zeta_p^2)\eta_t^2+4\zeta_t^2\zeta_p\eta_t+\zeta_t}{(1+\mu)^2\zeta_t\zeta_p\eta_t^4+(\mu+4(1+\mu)\zeta_t^2)\zeta_p^2\eta_t^3-2(1-2(1+\mu)\zeta_t^2-2\zeta_p^2)\zeta_t\zeta_p\eta_t^2+(\mu+4\zeta_p^2)\zeta_t^2\eta_t+\zeta_t\zeta_p}$
F	$\frac{E[\ddot{u}_p^2]\,m_p^2}{2\pi S_f\omega_p}$	$\frac{1}{4}\frac{N(\mu,\eta_t,\zeta_p,\zeta_t)}{(1+\mu)^2\zeta_t\zeta_p\eta_t^4+(\mu+4(1+\mu)\zeta_t^2)\zeta_p^2\eta_t^3-2(1-2(1+\mu)\zeta_t^2-2\zeta_p^2)\zeta_t\zeta_p\eta_t^2+(\mu+4\zeta_p^2)\zeta_t^2\eta_t+\zeta_t\zeta_p}-4(\mu\eta\zeta_t+\zeta_p)$ $N(\mu,\eta_t,\zeta_p,\zeta_t)=(1+4(1+\mu)\zeta_t)\mu^2\zeta_p^2\eta_t^5+(1+4(1+3\mu+2\mu^2(1+\zeta_t^2))\zeta_p^2)\zeta_t\eta_t^4+(\mu-4(1+\mu)\zeta_t^2+16\mu^2\zeta_t^4+4(\mu+4(1+2\mu)\zeta_t^2)\zeta_p^2)\zeta_p\eta_t^3$ $-(2-\mu-4(1+\mu-\mu^2)\zeta_t^2+4(1-4(1+\mu)\zeta_t^2)\zeta_p^2-16\zeta_p^4)\eta_t^2+4\zeta_p\zeta_t^2(1+2\mu+4\zeta_p^2)\eta_t+\zeta_t(1+4\zeta_p^2)$
F	$\frac{E[u_r^2]\,m_p^2\omega_p^3}{2\pi S_f}$	$\frac{1}{4}\frac{\zeta_p\eta_t+\zeta_t}{(1+\mu)^2\zeta_t\zeta_p\eta_t^4+(\mu+4(1+\mu)\zeta_t^2)\zeta_p^2\eta_t^3-2(1-2(1+\mu)\zeta_t^2-2\zeta_p^2)\zeta_t\zeta_p\eta_t^2+(\mu+4\zeta_p^2)\zeta_t^2\eta_t+\zeta_t\zeta_p}$
$\ddot{u}_g$	$\frac{E[u_p^2]\,\omega_p^3}{2\pi S_f}$	$\frac{1}{4}\frac{(1+\mu)^4\zeta_t\eta_t^4+(1+\mu)^2(\mu+4(1+\mu)\zeta_t^2)\zeta_p\eta_t^3-(1+\mu)^2(2+\mu-4(1+\mu)\zeta_t^2-4\zeta_p^2)\eta_t^2+(4(1+\mu)^2\zeta_t^2+\mu^2)\zeta_p\eta_t+\zeta_t}{(1+\mu)^2\zeta_t\zeta_p\eta_t^4+(\mu+4(1+\mu)\zeta_t^2)\zeta_p^2\eta_t^3-2(1-2(1+\mu)\zeta_t^2-2\zeta_p^2)\zeta_t\zeta_p\eta_t^2+(\mu+4\zeta_p^2)\zeta_t^2\eta_t+\zeta_t\zeta_p}$
$\ddot{u}_g$	$\frac{E[\dot{u}_p^2]\,\omega_p}{2\pi S_f}$	$\frac{1}{4}\frac{(1+\mu)^3\zeta_t\eta_t^4+(1+\mu)(\mu+4(1+\mu)\zeta_t^2)\zeta_p\eta_t^3-(1+\mu-2(1+\mu)^2\zeta_t^2-2\zeta_p^2)\eta_t^2+4\zeta_t^2\zeta_p\eta_t+\zeta_t}{(1+\mu)^2\zeta_t\zeta_p\eta_t^4+(\mu+4(1+\mu)\zeta_t^2)\zeta_p^2\eta_t^3-2(1-2(1+\mu)\zeta_t^2-2\zeta_p^2)\zeta_t\zeta_p\eta_t^2+(\mu+4\zeta_p^2)\zeta_t^2\eta_t+\zeta_t\zeta_p}$
$\ddot{u}_g$	$\frac{E[(\ddot{u}_p+\ddot{u}_g)^2]}{2\pi S_f\omega_p}$	$\frac{1}{4}\frac{(1+\mu)(1+\mu+4\zeta_p^2)\zeta_t\eta_t^4+(\mu+4(1+\mu+4\zeta_p^2)\zeta_t^2+4\mu\zeta_p^2)\zeta_p\eta_t^3-(2+\mu+4(1-4\zeta_p^2)\zeta_p^2-4(1+\mu+4\zeta_p^2)\zeta_t^2)\zeta_t\eta_t^2+4(1+4\zeta_p^2)\zeta_t^2\zeta_p\eta_t+(1+4\zeta_p^2)\zeta_t}{(1+\mu)^2\zeta_t\zeta_p\eta_t^4+(\mu+4(1+\mu)\zeta_t^2)\zeta_p^2\eta_t^3-2(1-2(1+\mu)\zeta_t^2-2\zeta_p^2)\zeta_t\zeta_p\eta_t^2+(\mu+4\zeta_p^2)\zeta_t^2\eta_t+\zeta_t\zeta_p}$
$\ddot{u}_g$	$\frac{E[u_r^2]\,m_p^2\omega_p^3}{2\pi S_f}$	$\frac{1}{4}\frac{(1+\mu)(1+\mu+4\zeta_p^2)\zeta_t\eta_t^3+(\mu+4(1+\mu)\zeta_t^2+4\zeta_p^2)\zeta_p\eta_t^2+(4\zeta_p^2+\mu)\zeta_t\eta_t+\zeta_p}{(1+\mu)^2\zeta_t\zeta_p\eta_t^4+(\mu+4(1+\mu)\zeta_t^2)\zeta_p^2\eta_t^3-2(1-2(1+\mu)\zeta_t^2-2\zeta_p^2)\zeta_t\zeta_p\eta_t^2+(\mu+4\zeta_p^2)\zeta_t^2\eta_t+\zeta_t\zeta_p}$

Legend

F:	random excitation applied to the primary system with spectral density S_f
$\ddot{u}_g$:	random excitation at base with spectral density S_f
$E[u_p^2]$, $E[\dot{u}_p^2]$, $E[\ddot{u}_p^2]$:	mean of the square of the displacement u_p, velocity $\dot{u}_p$ and acceleration $\ddot{u}_p$
$E[u_r^2]$:	mean of the square of the relative displacement u_r

Table 4: Exact solutions of the H_2 optimization problem for primary systems with vanishing structural damping ($\zeta_p = 0$).

Excitation	Minimized parameter	Parameter optimized	η_2	$\zeta_{t,2}$	$\min \|G(z)\|_2$	$\frac{E(u_r^2)\, m_p^2 \omega_p^3}{2\pi S_f}$
F	$\frac{E[u_p^2] m_p^2 \omega_p^3}{2\pi S_f}$	u_p	$\frac{\sqrt{1+\mu/2}}{1+\mu}$	$\sqrt{\frac{\mu}{4(1+\mu)}}\sqrt{\frac{1+3\mu/4}{1+\mu/2}}$	$\sqrt{\frac{1}{\mu}}\sqrt{\frac{1+3\mu/4}{1+\mu}}$	$\frac{1}{2}\left(\frac{1+\mu}{\mu}\right)^{3/2}\sqrt{\frac{1}{1+3\mu/4}}$
F	$\frac{E[\dot{u}_p^2] m_p^2 \omega_p}{2\pi S_f}$	$\dot{u}_p$	$\sqrt{\frac{1}{1+\mu}}$	$\sqrt{\frac{\mu}{4}}$	$\sqrt{\frac{1}{\mu}}\sqrt{\frac{1}{1+\mu}}$	$\frac{1}{2}\left(\frac{1+\mu}{\mu}\right)^{3/2}$
F	$\frac{E[\ddot{u}_p^2] m_p^2}{2\pi S_f \omega_p}$	$\ddot{u}_p$	$\sqrt{1-\mu/2}$	$\sqrt{\frac{\mu}{4(1+\mu)}}\sqrt{\frac{(1-\mu/4)(1+\mu)}{(1-\mu/2)(1-\mu+\mu^2)}}$	$\sqrt{\frac{1}{\mu}}\sqrt{(1-\mu+\mu^2)(1-\mu/4)}$	$\frac{1}{2}\left(\frac{1}{\mu}\right)^{3/2}\sqrt{\frac{(1-\mu+\mu^2)}{1-\mu/4}}$
$\ddot{u}_g$	$\frac{E[u_p^2] \omega_p^3}{2\pi S_f}$	u_{pr}	$\frac{\sqrt{1-\mu/2}}{1+\mu}$	$\sqrt{\frac{\mu}{4(1+\mu)}}\sqrt{\frac{1-\mu/4}{1-\mu/2}}$	$\sqrt{\frac{1}{\mu}}(1+\mu)^2\sqrt{\frac{1-\mu/4}{1+\mu}}$	$\frac{1}{2}\left(\frac{1+\mu}{\mu}\right)^{3/2}(1+\mu)^2\frac{1+\mu/2}{1-\mu/2}\sqrt{\frac{1}{1-\mu/4}}$
$\ddot{u}_g$	$\frac{E[\dot{u}_p^2] \omega_p}{2\pi S_f}$	$\dot{u}_{pr}$	$\frac{1}{1+\mu}$	$\sqrt{\frac{\mu}{4(1+\mu)}}$	$\sqrt{\frac{1}{\mu}}\sqrt{(1+\mu)}$	$\frac{1}{2}\left(\frac{1+\mu}{\mu}\right)^{3/2}(1+\mu)^3$
$\ddot{u}_g$	$\frac{E[(\ddot{u}_p+\ddot{u}_g)^2]}{2\pi S_f \omega_p}$	$\ddot{u}_{pr}+\ddot{u}_g$	$\frac{\sqrt{1+\mu/2}}{1+\mu}$	$\sqrt{\frac{\mu}{4(1+\mu)}}\sqrt{\frac{1+3\mu/4}{1+\mu/2}}$	$\sqrt{\frac{1}{\mu}}\sqrt{\frac{1+3\mu/4}{1+\mu}}$	$\frac{1}{2}\left(\frac{1+\mu}{\mu}\right)^{3/2}(1+\mu)^2\frac{1+3\mu/2}{1+\mu/2}\sqrt{\frac{1}{1+3\mu/4}}$

Legend

F: random excitation applied to the primary system with spectral density S_f

$\ddot{u}_g$: random excitation at base with spectral density S_f

$E[u_p^2]$, $E[\dot{u}_p^2]$, $E[\ddot{u}_p^2]$: mean of the square of the displacement u_p, velocity $\dot{u}_p$ and acceleration $\ddot{u}_p$

$E[u_r^2]$: mean of the square of the relative displacement u_r

Table 5: Approximate solutions of the H_2 optimization problem for primary systems with structural damping ($\zeta_p > 0$).

Excitation	Minimized parameter	η_2	$\zeta_{t,2}$
F	$\frac{E[u_p^2]m_p^2\omega_p^3}{2\pi S_f}$	$-\frac{(1+\mu/4)\mu^{1/2}}{(1+\mu)^{3/2}(1+\mu/2)^{1/2}(1+3\mu/4)^{1/2}}\zeta_p+\frac{\mu(3+19\mu/4+33\mu^2/16+13\mu^3/64)}{2(1+\mu)^3(1+\mu/2)^{3/2}(1+3\mu/4)}\zeta_p^2$	$-\frac{\mu^3}{32(1+\mu)(1+3\mu/4)(1+\mu/2)^{3/2}}\zeta_p-\frac{(1+5\mu/4-15\mu^2/64)\mu^{5/2}}{64(1+\mu)^{3/2}(1+\mu/2)^{5/2}(1+3\mu/4)^2}\zeta_p^2$
F	$\frac{E[\dot{u}_p^2]m_p^2\omega_p}{2\pi S_f}$	$\frac{\mu^{1/2}}{(1+\mu)}\zeta_p+\frac{\mu(1+7\mu/8)}{(1+\mu)^{3/2}}\zeta_p^2+\frac{7}{4}\frac{\mu^{1/2}(1+25\mu/28)}{(1+\mu)^2}\zeta_p^3$	$\frac{3}{4}\frac{\mu}{(1+\mu)^{1/2}}\zeta_p+\frac{3}{4}\frac{\mu^{1/2}(1+19\mu/12)}{(1+\mu)}\zeta_p^2+2\frac{\mu(1+63\mu/64)}{(1+\mu)^{3/2}}\zeta_p^3$
F	$\frac{E[\ddot{u}_p^2]m_p^2}{2\pi S_f\omega_p}$	$\frac{3}{2}\frac{\mu^{1/2}(1-25\mu/12+3\mu^2/4)}{(1-\mu/4)}\sqrt{\frac{(1-\mu/4)}{(1-\mu/2)(1-\mu-3\mu^2)}}\zeta_p+2\frac{(1-435\mu/112)}{(1-121\mu/28)}\sqrt{1-\mu/}$	$2\frac{(1-1279\mu/592)}{(1-1459\mu/592)}\mu\sqrt{1-\mu/2}\,\zeta_p+2(1+119\mu/4+1281\mu^2/4)\sqrt{\frac{\mu(1-\mu/4)}{(1-\mu/2)(1-\mu-3}$
$\ddot{u}_g$	$\frac{E[u_p^2]\omega_p^3}{2\pi S_f}$	$-\frac{(1+\mu/4)\mu^{1/2}}{(1+\mu)^{3/2}(1+\mu/2)^{1/2}(1+3\mu/4)^{1/2}}\zeta_p+\frac{\mu}{8}\frac{(11+83\mu/4+201\mu^2/16+157\mu^3/64)}{(1+\mu)^2(1+3\mu/4)^2(1+\mu/2)^{3/2}}$	$-\frac{\mu^3}{32(1+\mu)(1+3\mu/4)(1+\mu/2)^{3/2}}\zeta_p+\frac{\mu^{3/2}(1+215\mu/64+1163\mu^2/256+395\mu^3/128}{(1+\mu)^{3/2}(1+\mu/2)^{5/2}(1+3\mu/4)^2}$
$\ddot{u}_g$	$\frac{E[\dot{u}_p^2]\omega_p}{2\pi S_f}$	$-\frac{3}{2}\frac{\mu^{1/2}}{(1+\mu)^{3/2}}\zeta_p-\frac{\mu(1-7\mu/8)}{(1+\mu)^2}\zeta_p^2+\frac{5}{16}\frac{(12+\mu)}{(1+\mu)^{5/2}}\zeta_p^3$	$\frac{1}{4}\frac{\mu}{(1+\mu)}\zeta_p-\frac{1}{4}\frac{\mu^{1/2}(1-3\mu/4)}{(1+\mu)^{3/2}}\zeta_p^2+\frac{3}{2}\frac{\mu(1+11\mu/48)}{(1+\mu)^2}\zeta_p^3$
$\ddot{u}_g$	$\frac{E[(\ddot{u}_p+\ddot{u}_g)^2]}{2\pi S_f\omega_p}$	$-\frac{1}{2}\frac{\mu^{1/2}(1+\mu/4)}{(1+\mu)^{3/2}(1+\mu/2)^{1/2}(1+3\mu/4)^{1/2}}\zeta_p+\frac{1}{4}\frac{\mu(11+83\mu/4+201\mu^2/16+157\mu^3/6}{(1+\mu)^2(1+3\mu/4)^2(1+\mu/2)^{3/2}}$	$-\frac{\mu^3}{64(1+\mu)(1+3\mu/4)(1+\mu/2)^{3/2}}\zeta_p-\frac{(1+215\mu/64+1163\mu^2/256+395\mu^3/128)\mu^{3/}}{(1+\mu)^{3/2}(1+\mu/2)^{5/2}(1+3\mu/4)^{5/2}}$

Legend

F: random excitation applied to the primary system with spectral density S_f

$\ddot{u}_g$: random excitation at base with spectral density S_f

$E[u_p^2]$, $E[\dot{u}_p^2]$, $E[\ddot{u}_p^2]$: mean of the square of the displacement u_p, velocity $\dot{u}_p$ and acceleration $\ddot{u}_p$

$E[u_r^2]$: mean of the square of the relative displacement u_r

2.1.1.9 Tuned liquid damper

Theoretical background

The basic principle of a tuned liquid damper (TLD) is similar to that of a tuned mass damper (TMD). In particular, a moving secondary mass which is realized by the fluid mass is introduced into the primary structural system. The gravity acts as restoring force and energy dissipation is provided through viscous action mainly in the boundary layers of the fluid. A simple realization of TLD consists of rectangular or circular container with water inside (Fig. 49). A horizontal motion of the container produces a sloshing motion of the fluid. A variation of TLDs is the tuned liquid column damper (TLCD) which consists of a U-shaped container partially filled with fluid (Fig. 50). The fluid column starts oscillating as soon as the container is subjected to horizontal motion. The dynamic vibration absorber for ship applications proposed by Frahm was actually a forerunner of modern tuned liquid column damper (Den Hartog (1997), Frahm (1909)). For civil engineering applications, the first investigations started in the mid-1980s by the work of Bauer (1984).

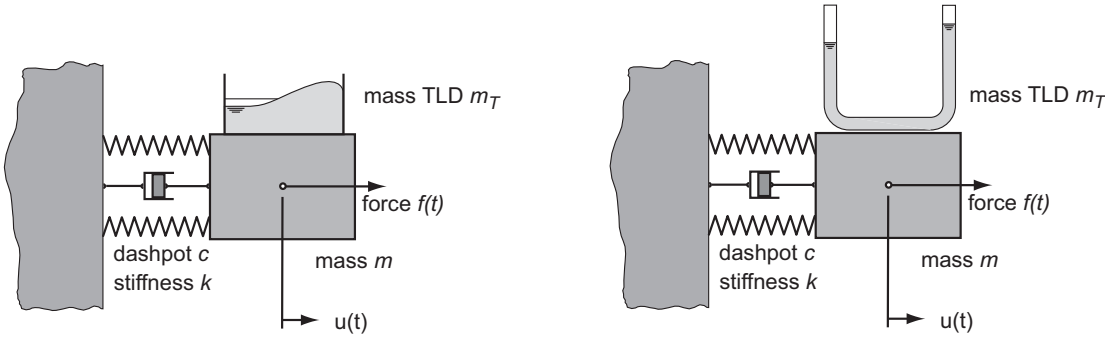

Fig. 49: Schematic illustration of a sloshing (a) and a column tuned liquid damper (b) coupled to a primary structure.

Unlike a TMD, generally the response of a TLD is highly nonlinear. Liquid sloshing or fluid flow through orifices is typically a highly nonlinear phenomenon. The response of the primary structure with a TLD is therefore amplitude dependent, even for primary structures operating within the linear elastic regime. Considerable research effort has been focused in understanding and quantifying the dynamic behaviour of nonlinear sloshing TLD. The most promising macroscopic models are based on extensions of classical theory of shallow water gravity waves with finite amplitude (Lepelletier and Raichlen (1988), Shimizu and Hayama (1987), Sun et al. (1992)). These models contain special terms to account for damping and fit reasonably well with test results. The steady state response curves of nonlinear sloshing TLD show some similarity with the steady state amplitude response curves of oscillating systems with nonlinear hardening properties (Fujino et al. (1992)). The fundamental frequency of sloshing TLD can be estimated from linearized small amplitude theory and is given by

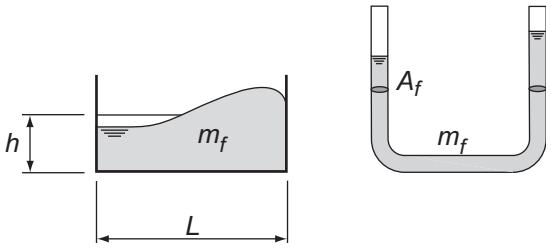

Fig. 50: Principal parameters of sloshing and column TLD.

$$f = \frac{1}{2\pi}\sqrt{\frac{\pi g}{L}\tanh\left(\frac{\pi h}{L}\right)} \quad (1)$$

The energy dissipation per cycle of a TLD depends strongly from the excitation frequency. For frequencies in the neighbourhood of the natural frequency the energy dissipation was found to be significantly higher than elsewhere.

The dynamic behaviour of tuned liquid column dampers (TLCD) is more suited for a description with simple one degree of freedom systems. Nevertheless, one degree of freedom systems are still nonlinear for significant vibration amplitudes of the fluid column (Hochrainer (2002), Saoka et al. (1988)). The nonlinearity mainly involves the damping term because of the energy dissipation due to turbulent flow. This term is usually modelled to be proportional to the square of the velocity of the oscillating fluid column. The natural frequency of a CTLD can be estimated using

$$f = \frac{1}{2\pi}\sqrt{\frac{2g}{L}} \quad (2)$$

Design issues

Because of the lack of reasonably simple models for describing the dynamic behaviour of a TLD, no generally accepted design procedure exists so far. In principle, because of the close similarity in the basic principle of operation between TMD and TLD, the same approach as described for TMDs can be applied for TLDs. In fact, a tuned mass damper analogy for the sloshing TLD was proposed for design issues with frequency dependent virtual mass and dashpot (Sun et al. (1995)). However, because the virtual mass and dashpot are amplitude-dependent, these had to be determined by experiments and may therefore change due to implementation details. Because of the much lower mass density of water with respect to steel, TLD needs much more space than TMD for installation. In addition, sloshing TLDs are usually implemented as a rack of tanks therefore requiring even more space. The fundamental frequency of sloshing TLDs can be estimated using the linearized theory of shallow water waves. Much more difficult is predicting the energy dissipation of a TLD. Therefore, laboratory tests are mandatory to optimize the dynamic behaviour of TLD with respect to the primary structure.

Because of the nonlinear hardening behaviour of sloshing TLD, its effectiveness is less sensitive to a correct frequency tuning of the damper. Rectangular tanks are applied for structures with different natural frequencies in the two principal directions. For a given water depth, the frequencies are tuned by an adequate selection of the plan dimensions of the tank. However, because the existing theories are only tested for unidirectional excitation, special care should be taken in designing sloshing TLD acting in two directions. For structures with nearly equal natural frequencies in the two principal directions, a circular tank may be used.

Testing and validation

The testing and validation of TLDs follows the same procedures as described for TMD.

Implementation

Tuned liquid dampers have been primarily used for mitigating wind-induced vibrations of tall structures with very small natural frequencies. The first applications of nonlinear sloshing TLD were implemented in Japan and include the Nagasaki Airport Tower, the Yokohama Marine Tower and the Shin-Yokohama Prince Hotel (Tamura et al. (1995), Tamura et al. (1996), Wakahara et al. (1992)). The hardware implementation of sloshing TLDs is much simpler as that for TMD. Each damper, generally, consists of a rack of fluid containers. The installation requirements are minimal. Sloshing TLD may be easily added in existing buildings and produce very little maintenance costs.

References

Bauer, H. F. (1984), "Oscillations of Immiscible Liquids in a Rectangular Container - a New Damper for Excited Structures", *Journal of Sound and Vibration*, 93(1), 117-133.

Den Hartog, J. P. (1947), *Mechanical Vibrations*. Third ed. 1947, New York and London: McGraw-Hill Book Company.

Frahm, H. (1909), *Device for Damped Vibrations of Bodies*. U. S. Patent No. 989958, 1909.

Fujino, Y., Sun, L., Pacheco, B. M., and Chaiseri, P. (1992), "Tuned Liquid Damper (Tld) for Suppressing Hori-zontal Motion of Structures", *Journal of Engineering Mechanics-Asce*, 118(10), 2017-2030.

Hochrainer, M. (2002), *Control of Vibrations of Civil Engineering Structures with Special Emphasis on Tall Building*, Institut für Allgemeine Mechanik, Vienna University of Technology, Wien.

Lepelletier, T. G., and Raichlen, F. (1988), "Nonlinear Oscillations in Rectangular Tanks", *Journal of Engineering Mechanics-Asce*, 114(1), 1-23.

Saoka, Y., Sakai, F., Takaeda, S., and Tamaki, T. (1988), "On the Suppression of Vibrations by Tuned Liquid Column Dampers", *in Annual Meeting of JSCE*, Tokyo: JSCE.

Shimizu, T., and Hayama, S. (1987), "Nonlinear Responses of Sloshing Based on the Shallow-Water Wave Theory", *Jsme International Journal*, 30(263), 806-813.

Sun, L. M., Fujino, Y., Pacheco, B. M., and Chaiseri, P. (1992), "Modelling of Tuned Liquid Damper (Tld)", *Journal of Wind Engineering and Industrial Aerodynamics*, 43(1-3), 1883-1894.

Sun, L. M., Fujino, Y., Chaiseri, P., and Pacheco, B. M. (1995), "The Properties of Tuned Liquid Dampers Using a Tmd Analogy", *Earthquake Engineering & Structural Dynamics*, 24(7), 967-976.

Tamura, Y., Fujii, K., Ohtsuki, T., Wakahara, T., and Kohsaka, R. (1995), "Effectiveness of Tuned Liquid Dampers under Wind Excitation", *Engineering Structures*, 17(9), 609-621.

Tamura, Y., Kohsaka, R., Nakamura, O., Miyashita, K., and Modi, V. J. (1996), "Wind-induced responses of an airport tower - efficiency of tuned liquid damper", *Journal of Wind Engineering and Industrial Aerodynamics*, 65(1-3), 121-131.

Wakahara, T., Ohyama, T., and Fujii, K. (1992), "Suppression of Wind-Induced Vibration of a Tall Building Using Tuned Liquid Damper", *Journal of Wind Engineering and Industrial Aerodynamics*, 43(1-3), 1895-1906.

Notations

Symbol	*Description*	*Unit*
A	cross sectional area	m^2
L	container length in the sloshing direction	m
g	gravity constant	m/s^2
h	depth	m
m	mass	kg
ρ	mass density	kg/m^3
μ	mass ratio	-

Subscripts	*Description*
f	fluid

2.1.2 Semi-active devices

2.1.2.1 Defintion of term “semi-active”

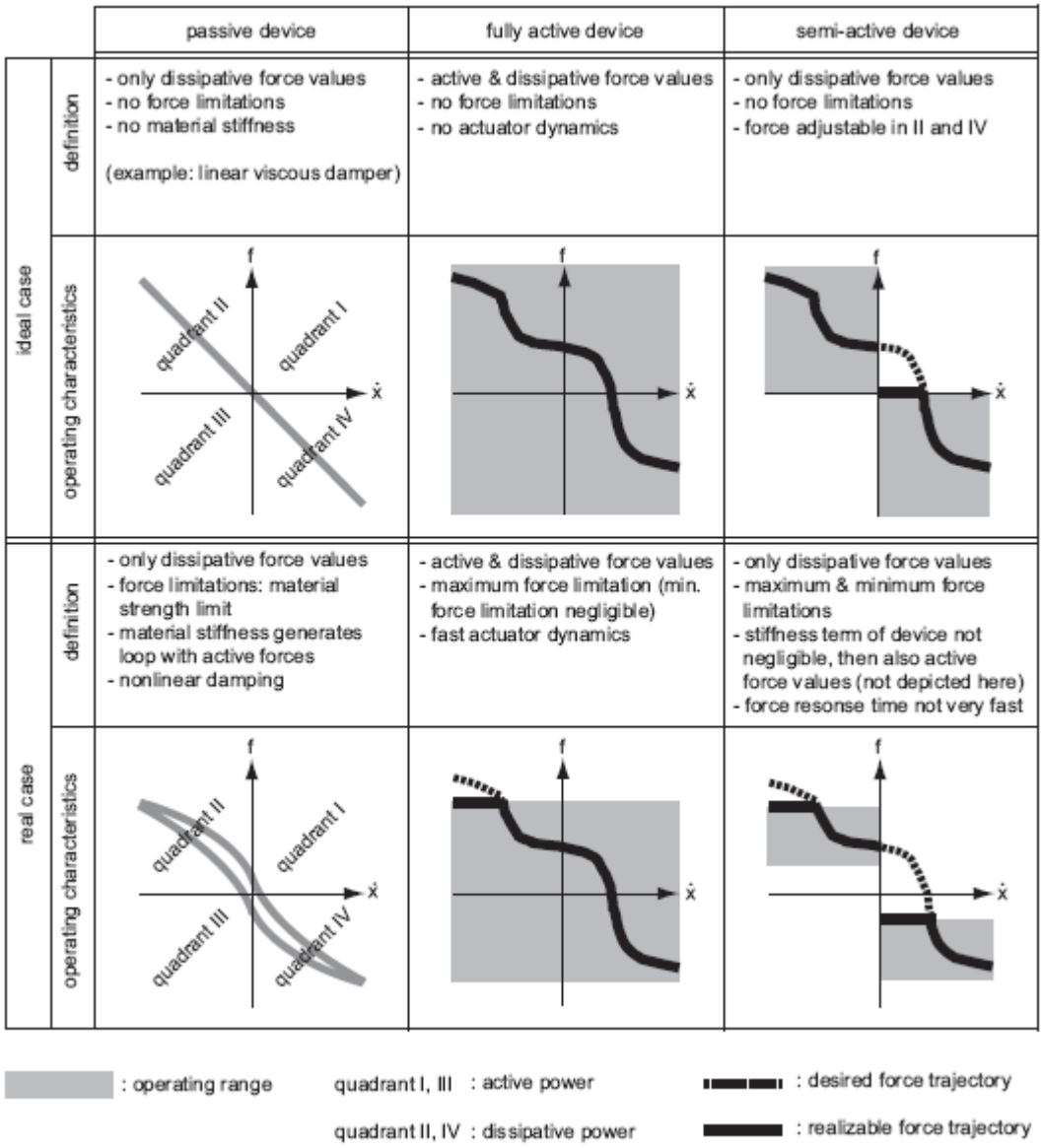

Fig. 51: Definitions and characteristics of damping devices often used in structural control.

Semi-active devices are “actuators” that cannot produce power and therefore, e.g., excite structures (Gavin and Alhan (2005), Spencer Jr. et al. (1997), Spencer Jr. and Nagarajaiah (2003), Xu et al. (2003)). However, they are able to dissipate structural vibration and - in contrast to passive dampers - the amount of energy dissipation within the semi-active device may adjusted by control of the device force. Thus, the operating range of semi-active devices may be defined by the force, which is desired by the controller, and the device velocity, which is the velocity of the piston, rod, shaft etc depending on the device design, as follows

$$P_{sa-device} = \begin{cases} 0 & : \left(f_{des} \cdot \dot{x}_{sa-device}\right) > 0 \\ P_{des} & : \left(f_{des} \cdot \dot{x}_{sa-device}\right) \leq 0 \end{cases} \quad (1)$$

The different operating ranges of passive dampers, semi-active devices such as controllable dampers and fully active devices, usually called actuators, are illustrated in Fig. 51. The operating range of many semi-active devices is not only constraint to quadrants II and IV, which include dissipative force values only (in view of the device), but further constraint by a maximum and minimum device force (Fig. 51, bottom right). The force limitation by a maximum value is nothing special since this property is common for any semi-active and fully active control device. However, the additional restriction by a minimum device force that is relatively large compared to the minimum force of actuators given by friction of seals, bearings, and gears, plays an important issue in control point of view. This fact implies that the desired force trajectory is not only bounded by the maximum device force but also constraint by a considerable minimum force value. Especially in the field of vibration mitigation, the minimum device force leads to clamping effects at position of the semi-active device if the desired damping force is far smaller than the minimum force of the semi-active device because then minimum force is applied to mitigate the structure. Clamping the structure at device position is equivalent with generating a nodal point of the structure at that position. Then, vibration velocity at device position is zero. As a result, structural vibration energy may not be dissipated anymore within the semi-active device. Hence, structural vibrations decay as without external semi-active damping device.

Consequently, not only the maximum force of semi-active devices but also the minimum device force must be taken into account for the design of semi-active devices.

In accordance with customers, engineers have to assume the maximum magnitude of expected structural vibrations (assumption of worst case scenario) in order to determine the maximum device force which is mandatory so that the desired maximum control force may be tracked. In order to determine the minimum force value of the semi-active device, engineers and customers together have to define this vibration magnitude threshold below which the semi-active device may clamp the structure and therefore cannot dampen vibrations.

According to the values of maximum and minimum damping forces, the semi-active device may be evaluated or designed and manufactured, respectively.

References

Gavin, H. P., and Alhan, C. (2005), “Guidelines for low-transmissibility semi-active vibration isolation“, *Journal of Smart Materials and Structures*, 14, 297-306.

Spencer Jr., B. F., Dyke, S. J., Sain, M. K., and Charlson, J. D. (1997), “Phenomenological Model of a Magnetorheological Damper”, *Journal of Engineering Mechanics, ASCE*, 123(3), 230-238.

Spencer Jr., B. F., and Nagarajaiah, S. (2003), “State of the Art of Structural Control”, *Journal of Structural Engineering*, 129(8), 845-856.

Xu, Z.-D., Shen, Y.-P., and Guo, Y.-Q. (2003), “Semi-active control of structures incorporated with magnetorheological dampers using neural networks”, *Journal of Smart Materials and Structures*, 12(1), 80-87.

2.1.2.2 Magnetorheological/electrorheological fluid damper

Main working principles

Magnetorheological and electrorheological fluid dampers (MR dampers, ER dampers) represent a class of controllable fluid dampers where the shear force of the fluid is controlled by an external magnetic and electric field, respectively (Chen and Yang (2003), Gordaninejad et al. (2002), Han et al. (2002), Kornbluh et al. (2004), Nakamura et al. (2002), Oh and Onoda (2002), Spencer Jr. and Nagarajaiah (2003)).

Basically, MR/ER dampers consist of a housing including the MR/ER fluid and the moving part of a disc or piston, depending if the dampers are built in rotational or cylindrical form (Fig. 52, Fig. 53, Liao and Lai (2002), Weber et al. (2002), Weber et al. (2005a), Weber et al. (2005c)). The MR/ER fluid is a suspension of oil, additives and particles whose polarisation may be influenced by an external magnetic/electric field. Hence, the control input variable of MR and ER dampers is current and voltage, respectively. The amount of polarised particles depends on the magnetic/electric field magnitude and influences the shear stress of the MR/ER fluid. Therefore, according to the applied current/voltage, the shear force of the MR/ER fluid and eventually the damper force acting on the piston may be controlled.

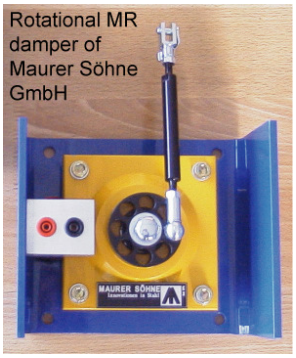

Fig. 52: Rotational MR damper, force range approximately [10, 320] N.

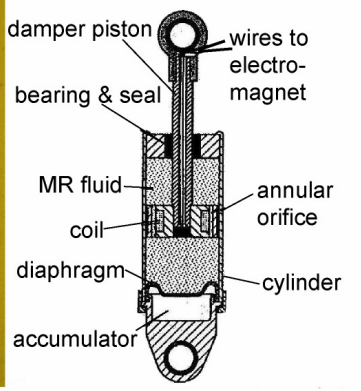

Fig. 53: Cylindrical MR damper with gas pocket (accumulator) for compensation of piston volume; force range approximately [70, 1800] N.

Besides the control input variable (current/voltage), the main difference between these two semi-active damping devices is that MR dampers produce far larger damping forces relatively to ER dampers for the same damper size. That is why MR dampers are often used for vibration mitigation in the field of large civil structures whereas ER dampers are used for vibration control of smaller structures. In the following, the working principles of these two damper types shall be explained on behalf of MR dampers.

Characteristics of MR dampers

The MR fluid consists of oil, magnetizable particles and additives. The viscosity of the oil defines the slope of the force-velocity trajectories at zero current (Fig. 54). The magnetizable particles may be polarized by the applied magnetic field which ends up in a controllable shear force depending on the amount of polarized particles. Since the shear force is controlled, the force trajectory in the force-velocity diagram approximately describes a Coulomb friction, superposed by oil viscosity (Guglielmino et

al. (2005), Zhou and Sun (2005)). Thus, MR dampers may be seen as controllable Coulomb dampers where the slope of the Coulomb force trajectories depends on the oil viscosity. Usually, the slope is of minor importance or even negligible compared to the force value at a certain velocity. At very small velocities, the force trajectories go into the zero-point tracking a very large viscosity. The reason for that phenomenon is that MR fluids behave more like rigid bodies (elastic) below yield stress and therefore at very small velocity values, whereas the fluid only starts to flow above yield stress, thus behaves plastic-viscous (Fig. 55, Fig. 56, Pignon et al. (1996), Powell (1995), Weiss et al. (1994)). This ends up in the fact that force-displacement trajectories or force-velocity trajectories of sinusoidal measurements include transient measurement data when the fluid changes between these two regions (Jung et al. (2003), Gordaninejad et al. (2002), Yang et al. (2000), Yang (2001)).

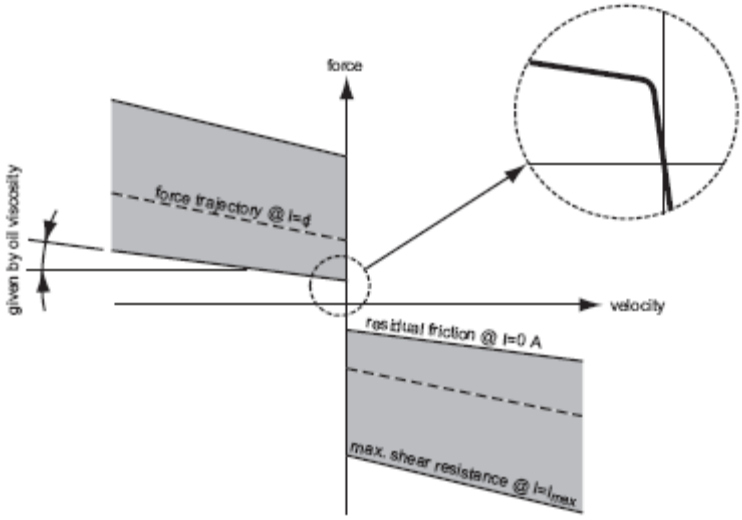

Fig. 54: Schematic steady-state damper behaviour of MR dampers.

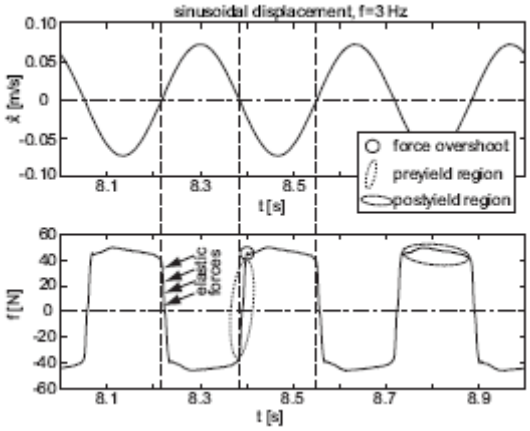

Fig. 55: Measured MR damper behaviour in pre- and postyield regions (MR damper of Maurer Söhne).

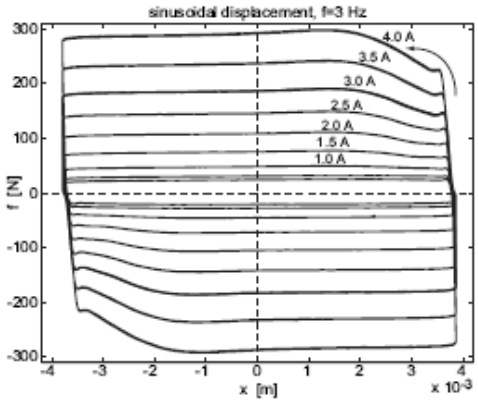

Fig. 56: Force displacement trajectories including transient measurement data from preyield to postyield regions (MR damper of Maurer Söhne).

Additives within the fluid should help to avoid agglomeration and sedimentation of the magnetizbale particles. Sedimentation effects are not of high priority if MR dampers are used to mitigate, e.g., cable vibrations due to wind loading because such vibrations exist for fairly long time compared to the time of one cycle. In this case, the MR fluid will be mixed up during the first couple of cycles. After that time, the particles are

distributed homogeneously again. Then, the MR damper works as expected. However, if dampers should optimally damp structural vibrations resulting from earthquakes, they have to react according to the programmed control strategy. Hence, dampers with sedimentation which changes the damper behaviour instantaneously are not appropriate.

Modelling

Numbers of phenomenological MR damper models have been presented by many researchers (Dominguez et al. (2004), Jiménez and Alvarez-Icaza (2005), Ramallo et al. (2004), Rosenfeld and Wereley (2004), Sahasrabudhe and Nagarajaiah (2005), Spencer Jr. et al. (1997), Wand and Liao (2005), Yang et al. (2004)). Most models are based the so-called Bouc-Wen model. This approach tries to model the MR damper behaviour by combining linear spring elements, linear dash-pot elements, nonlinear damping elements, friction elements with the Bouc-Wen element that describes the hysteresis phenomenon of MR dampers. Exemplarily, the simple Bouc-Wen model proposed by Spencer Jr. et al. (1997) is depicted in Fig. 57. The governing equation of the MR damper force including the force offset f_0 describing the friction due to seals or the so-called accumulator is

$$f - f_0 = m \cdot \ddot{x} + \underbrace{c(\dot{x})}_{\substack{nonlinear \\ damping \\ coefficient}} \cdot \dot{x} + k \cdot x + \alpha \cdot z \tag{1}$$

where z describes the evolutionary variable which is defined as follows

$$\dot{z} = -\gamma \cdot |\dot{x}| \cdot z \cdot |z|^{n-1} - \beta \cdot \dot{x} \cdot |z|^{n} + A \cdot \dot{x} \tag{2}$$

The nonlinear damping coefficient $c(\dot{x})$ describes the plastic, nonlinear damping characteristics within the post-yield region. According to Yang et al. (2004), this damping coefficient may be modelled as follows

$$c(\dot{x}) = a_1 \cdot e^{-(a_2 \cdot |\dot{x}|)^p} \tag{3}$$

A completely different modelling approach is the simple approach of fitting a two-dimensional function using measurement data (Song et al. (2005), Weber et al. (2002), Weber et al. (2005c)). The function is two-dimensional since the MR damper force depends on the actual damper piston velocity and actual damper current. The advantage of this “mapping” procedure is that the function may be simply inverted in order to have an inverse model of the steady-state MR damper behaviour available which compensates for the stationary main nonlinearities of MR dampers (Fig. 58).

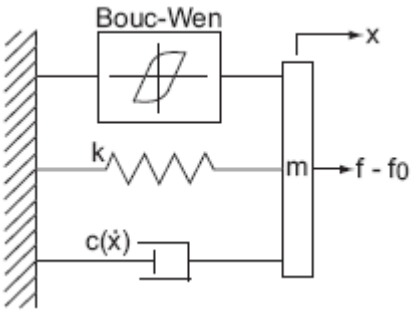

Fig. 57: Simple Bouc-Wen modelling approach for MR-dampers.

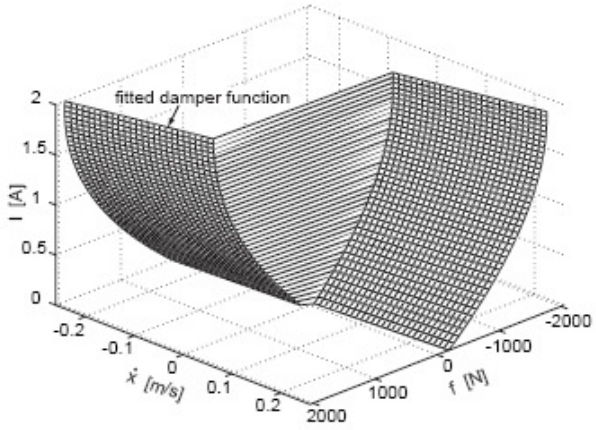

Fig. 58: Fitted inverse MR damper function.

Testing MR/ER dampers

The common way to determine the MR damper behaviour is to measure the MR damper characteristics at constant current level for sinusoidal controlled damper piston displacement (Oyadiji and Sarafianos (2000), Tse and Chang (2004), Zhang et al. (2004)). The reasons for sinusoidal controlled displacement are:

a) usually, hydraulic and pneumatic aggregates are displacement controlled (Fig. 59).

b) sinusoidal displacement with defined amplitude and frequency produces the velocity range of [0, $|\dot{x}_{\max}|$]. Hence, the dependency of the damper force on the velocity may be measured over the entire desired velocity range. However, it must be mentioned that this measurement data also includes transient data due to the change of MR damper behaviour between preyield and postyield regions (Fig. 56 and Fig. 60). That is the reason why force-velocity diagrams do not only show approximate Coulomb force trajectories at constant damper current but also trajectories including non-dissipative force values and transient force values, see Fig. 60. Depending on the viscosity of the MR fluid, the steady-state parts of the force trajectories describe a Coulomb friction behaviour superposed by a viscous part (Fig. 61).

The following points for damper measurements with high accuracy have to be respected:

- The joints must not have play. Therefore, fitting bolts have to be used (Fig. 59). Otherwise, knocking effects will falsify measurements.
- If the force sensor is mounted between aggregate and damping device, the sensor moves up and down according to the piston displacement. Due to the acceleration of the force sensor, the sensor signal has to be compensated by the acceleration term which results from the sensor's mass.
- It must be ensured that the aggregate piston at high frequencies of the desired displacement sinus really tracks the desired sinus signal. Depending on the aggregate properties, the actual piston displacement tends to triangular shape with increasing frequency of the desired displacement sinus.

- The force response of MR/ER dampers may be measured if the desired displacement is triangular. Then, the force response on velocity step may be measured (Fig. 62, Fig. 63).

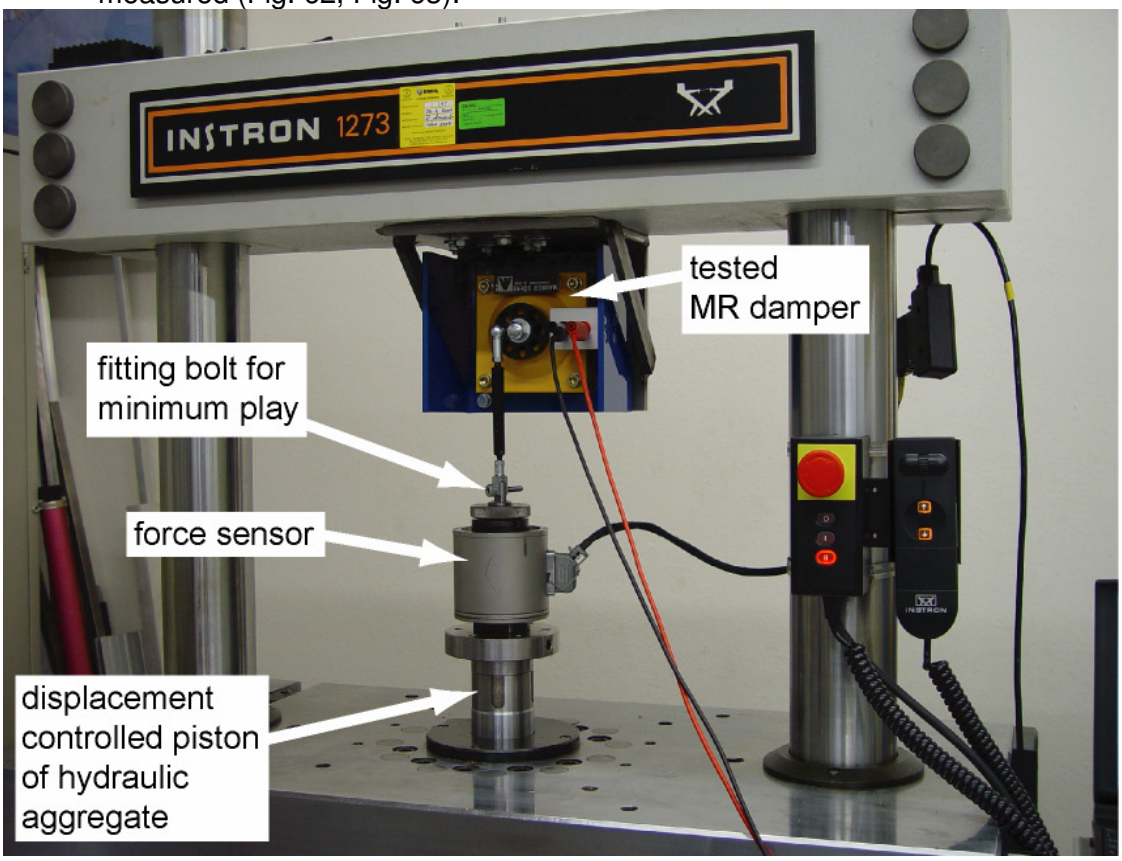

Fig. 59: Testing damping devices.

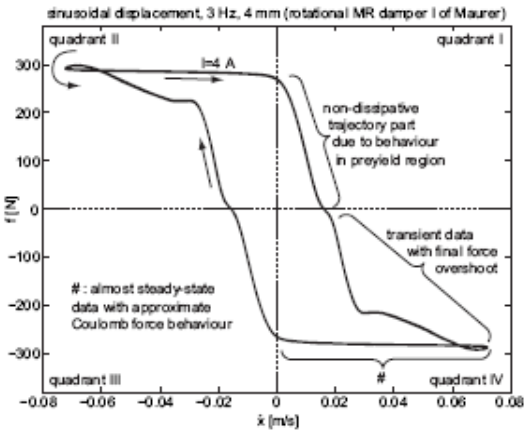

Fig. 60: Transient measurement data due to MR damper behaviour in preyield and postyield regions with force overshoot, fairly small MR fluid viscosity.

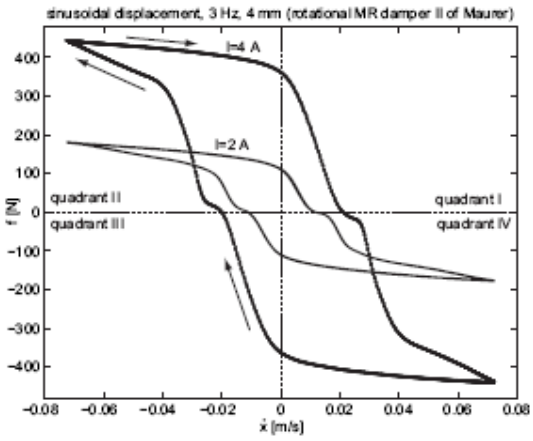

Fig. 61: Transient measurement data due to MR damper behaviour in preyield and postyield regions, no force overshoot, fairly large MR fluid viscosity.

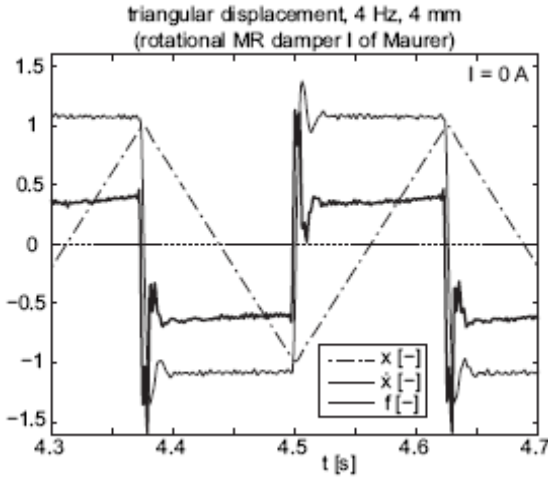

Fig. 62: MR damper force response on approximate velocity step at 0 A.

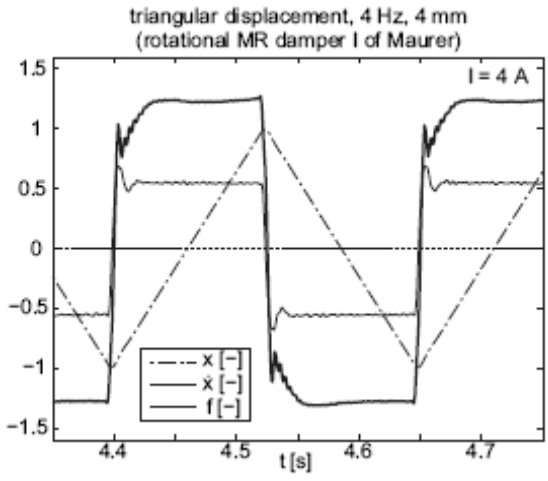

Fig. 63: MR damper force response on approximate velocity step at 4 A.

Implementation

Since forces of MR dampers are larger than those of ER dampers for the same housing dimensions, MR dampers have been installed on numbers of civil structures for mitigation of vibrations caused by wind, combined wind-rain, combined wind-snow, pedestrian, traffic, and earthquake loading. Wind and earthquake loading may evoke unacceptable large vibration amplitudes of tall buildings, especially skyscrapers. Large cable vibrations of stay cables of long span bridges are mainly due to wind loading or wind loading combined with rain or snow, which change the aerodynamic profile of cables. Pedestrian loading is mainly reported in the case of footbridges. In this case vibration amplitudes become too large if the first eigenfrequency of the footbridge is near the frequency of walking, namely around two Hertz (Bachmann et al. (1995)). Although e.g. bridge deck vibrations due to traffic loading exist, these vibrations are of minor importance due to the large deck mass and deck stiffness compared to the exciting forces caused by traffic.

MR dampers are primarily manufactured by LORD Corporation and Maurer Söhne, Munich, Germany. MR dampers of LORD have been installed on the “Dongting Lake Bridge” in China on all cables because vibrations due to combined rain-wind effects were unacceptable large (Fig. 64, Ko et al. (2002)). Each cable is equipped with two MR dampers in order to dampen in-plane and out-of-plane vibrations. In the case of cable amplitudes above a defined level, these MR dampers operate in the so-called “passive-on” mode which means that MR damper current is hold on a constant value different from zero (Lee and Jeon (2002), Wan and Gordaninejad (2002), Weber et al. (2005a)). If vibration amplitudes are below this defined threshold, MR damper current is zero. Then, MR dampers work in the so-called “passive-off” mode.

Maurer Söhne had the opportunity to install one MR damper on the longest stay cable of the “Eiland Bridge” nearby Kampen, The Netherlands, manly for long-term field tests (Fig. 65, please see the following case study, Weber et al. (2005b)). It must be mentioned that unacceptable large cable vibrations on this cable-stayed bridge have not been observed so far. In collaboration with Empa, the Swiss Federal Laboratories for Materials Testing and Research, this MR damper has been model-based designed using cable properties, damper position and assuming a worst-case scenario which has to be damped. When the MR damper was installed in October 2004 on the bridge, decay measurements of the cable without and with MR damper at different

current levels have been carried out. The target was to determine experimentally the optimal current level depending on vibration amplitude for maximum additional damping. Finally, an intelligent on/off control strategy was implemented and runs since late October 2004.

Fig. 64: Cable-stayed “Dongting Lake Bridge” in China, equipped with MR dampers of LORD Corporation.

Fig. 65: Cable-stayed ”Eiland Bridge“ nearby Kampen, The Netherlands, equipped with one MR damper of Maurer Söhne for long-term field tests and damping measurements.

The “Dubrovnik Bridge” nearby Dubrovnik, Croatia, is an example of a cable-stayed bridge, where cable vibration amplitudes during combined wind-snow events were that large that severe material damage resulted (Fig. 66). The damage was caused by contact friction between cables and bridge deck lightings. Again in collaboration with Empa, the Swiss Federal Laboratories for Materials Testing and Research, MR dampers were model-based designed and manufactured for cables no. 1-6, no. 11-

13 and for the backstays. These MR dampers were installed in March 2006. Maurer and Empa will perform field tests with forced cable vibrations in order to measure the additional damping provided by feedback controlled MR dampers. Each MR damper will be equipped with one displacement sensor between damper piston and damper cylinder. Based on the measured relative damper displacement at 100 Hz sampling frequency, two control concepts will be tested: velocity feedback and controlled friction force level. It is planned that all MR dampers will be real-time controlled by the friction force control.

Fig. 66: Cable-stayed „Dubrovnik Bridge“ nearby Dubrovnik, Croatia.

MR dampers have been also installed as tuneable damping element in tuned mass dampers in footbridges to mitigate vertical bridge deck vibrations due to pedestrian's impact from walking (Seiler et al. (2002)). In the field of earthquake engineering, MR dampers have been installed in skyscrapers using two different damping concepts. One idea is to increase the overall building damping by introducing damping forces that decrease the relative displacement between adjacent floors. Hence, MR dampers are installed on each floor and are connected with the adjacent floor. The other concept is base isolation. Here, dampers shall isolate the sensitive system - in this case the tall building – from the impact of the earthquake. Then, the MR damper pistons are, e.g., connected to the ceiling of the ground floor which is built as a soft story, whereas the MR damper cylinder must be fixed on the ground outside of the building. Hence, the whole soft story including the MR dampers represent the isolating system.

Case Studies

The case study described here is the implementation of one feedback controlled MR damper of Maurer Söhne on the “Eiland Bridge” nearby Kampen, The Netherlands (Weber et al. (2005b)). The entire procedure of implementation comprises the following steps:

1. MR damper design based on known cable properties, intended damper position on the cable and assumed worst case vibration scenario which still shall be possible to be damped.

2. MR damper fabrication and measurement of the force-displacement characteristics at constant damper current.
3. Measurements of the decay rate of the free cable and of the cable with connected MR damper operating at different settings.
4. Evaluation of measurement data in order to determine the optimum controller tuning that controls the MR damper force.
5. Controller design and implementation on the bridge.

1) Model-based MR damper design

The basic design variables of MR dampers are:

- Maximum damper force for given damper piston velocity: $f_{MR-\max}(\dot{x}_{MR}, I_{MR-\max})$
- Minimum damper force at zero current for given damper piston velocity: $f_{MR-\min}(\dot{x}_{MR}, I_{MR-\min} = 0)$
- Maximum damper piston displacement: $x_{MR-\max}$

According to these design variables, the MR fluid may be evaluated. Based on that evaluation, the MR damper geometry may be designed.

In order to be able to determine the above listed design variables, a worst-case stay cable amplitude of the expected predominant mode has to be assumed for the cable with connected MR damper, thus for the damped cable (Fig. 67).

Based on that assumption, the maximum damper force and maximum damper piston displacement may be model-based estimated. The basic idea is to simulate the vibrating cable with linear viscous damper that is optimally tuned for the target mode (Fig. 67). Although the linear viscous damper is characterized by a different force trajectory than the one of MR dampers operating at constant current, the simulated maximum damper force and damper displacement values may be transformed to their corresponding values of a Coulomb friction damper whose behaviour is close to the one of MR dampers operating at constant current. The reason to simulate a fairly simple linear cable model with a linear viscous damper is that the connected system is again linear. Thus, computing time is small and the correction of the disturbance force amplitude may be done also linearly (Fig. 67).

One run of the simulation is completed when steady-state conditions occur. Then, error ε and correction factor A may be determined using the steady-state results. The whole design procedure stops when the error of the actual amplitude is smaller than a defined maximum error. Then, the steady-state simulation results deliver the wanted values of maximum damper force and maximum damper displacement of the linear viscous damper that is optimally tuned for the vibrating mode according to (Fig. 68, Krenk (2000))

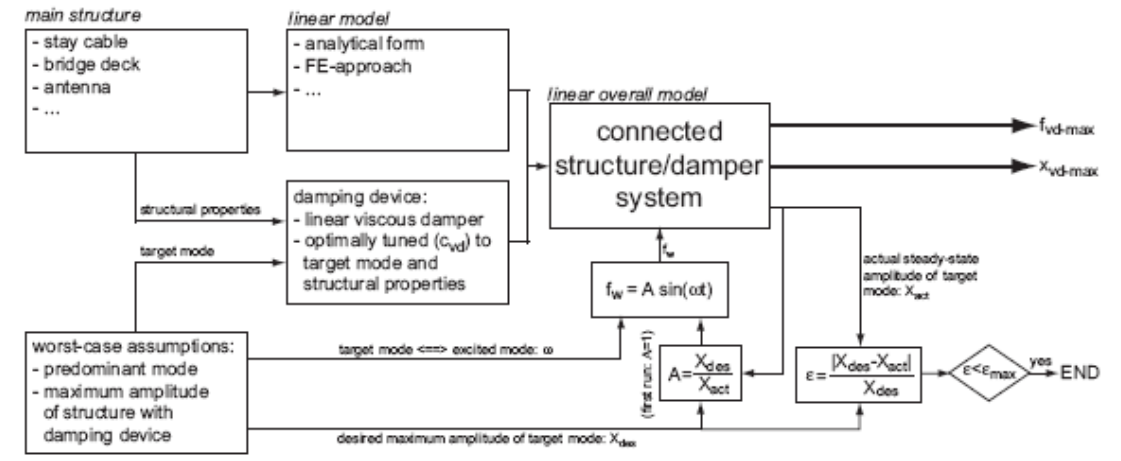

Fig. 67: Flow chart of damper design procedure.

$$c_n^{opt} = \frac{T}{x_d \cdot \omega_n} \tag{4}$$

The distribution of the disturbance force f_w accords to the shape of the mode to be excited (Fig. 68). This guarantees that other modes are not excited. The amplitude A of the external disturbance force is chosen the way that the steady-state amplitude of the cable with linear viscous damper accords to the worst-case amplitude (Fig. 67).

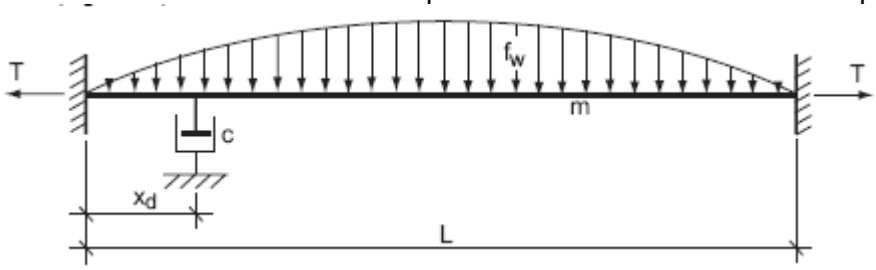

Fig. 68: Cable/damper system with distributed disturbance force according to the shape of the excited mode (here shown for the first vibration mode).

The maximum force of the linear viscous damper may be transformed to its counterpart of the energy equivalent Coulomb friction damper provided that the maximum displacements of both damper types are equal (Fig. 69)

$$f_{fri-\max} = \frac{\pi}{4} \cdot f_{vis-\max} \tag{5}$$

with:

$$x_{fri-\max} \approx x_{vis-\max} \tag{6}$$

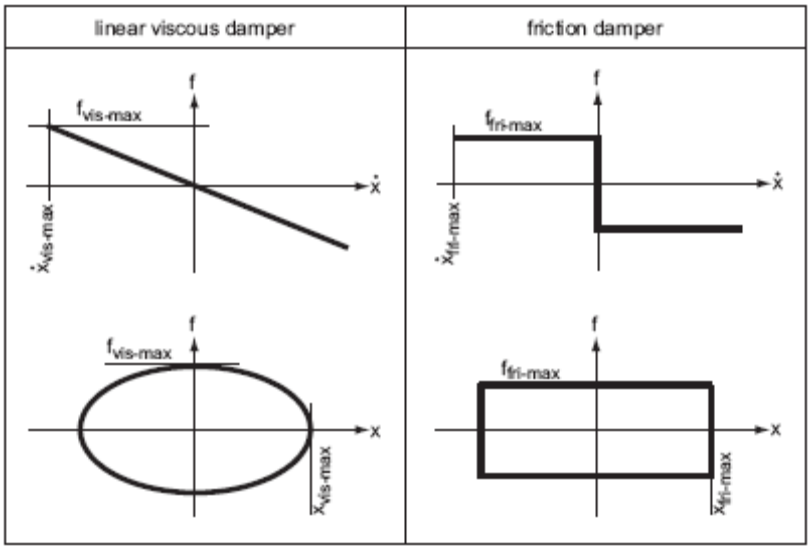

Fig. 69: Characteristics of linear viscous and friction dampers.

Since MR dampers working at constant current almost produce Coulomb force trajectories, the transformed values are the wanted values of maximum MR damper force and maximum MR damper displacement

$$f_{MR-\max} \approx f_{fri-\max} \tag{7}$$

$$x_{MR-\max} \approx x_{fri-\max} \tag{8}$$

The minimum friction force cannot be smaller than the sum of sealing friction and shear force of MR fluids at zero current. If the target is to produce MR dampers with maximum large operating range, then the friction force at zero current will be chosen to be equal to the minimum friction force mentioned above. If the target is to manufacture MR dampers that produce fairly large friction forces at zero current in order to enhance the fail safe behaviour against vibrations of large amplitudes (Weber and Feltrin (2003)), then the friction force at zero current may be increased by additional sealing and different type of MR fluids.

$$f_{MR-\min} = \begin{cases} f_{\min} = Min(seal\ friction + MR\ fluid\ friction @ 0\,A): & maximum\,operating\ range \\ > f_{\min} & :enhanced\ fail\ safe\,behaviour \end{cases} \tag{9}$$

Summarizing, the presented design procedure yields the maximum values of force and displacement of MR dampers operating at constant current for maximum damping of the target mode with defined, steady-state worst-case amplitude. The minimum MR damper force at zero current is bounded by MR fluid characteristics and damper construction. The minimum MR damper force may be chosen to be larger than that minimum value but not smaller.

The test MR damper had to be designed for the longest, 163 meter long stay cable of the “Eiland Bridge”. The worst-case assumptions for that cable with MR damper were:

- 0.40 meter amplitude at mid span, and
- only the first mode vibrates.

Using the known cable data listed in Table 6, the first eigenfrequency was estimated using the formula of a linear cable

$$f_{n=1} = \frac{1}{2} \cdot \sqrt{\frac{T}{m \cdot L^2}} \tag{10}$$

Table 6: Properties of longest stay cable of "Eiland Bridge".

L	m	T	x_d
[m]	[kg/m]	[kN]	[m]
163.7	66.55	5082	7.88

The estimated first eigenfrequency became 0.844 Hz. Applying Eq. (4), the optimum viscosity of a linear viscous damper located at 7.88 meter was determined as 121.6e3 kg/s. Using this optimum linear viscous damper, the results of the model-based damper design were the following required maximum MR damper values:

- $f_{MR-\max}$ = 40 kN, and
- $x_{MR-\max}$ = 0.035 m.

Further desired design properties were:

- The MR damper force at zero current shall be as small as possible in order to produce a maximum large operating range of the MR damper.
- The dependency of the MR damper force at constant current on the damper piston velocity shall be as small as possible. Then, the MR damper force is only a function of current. Hence, the inversion of the steady-state damper function for control purposes becomes simple and the actual velocity does not have to be measured.

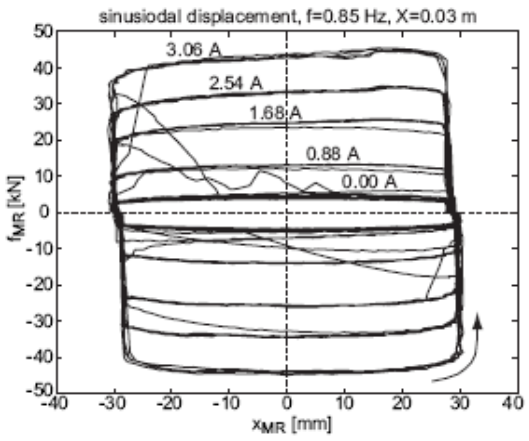

Fig. 70: Force displacement trajectories of MR damper of the "Eiland Bridge".

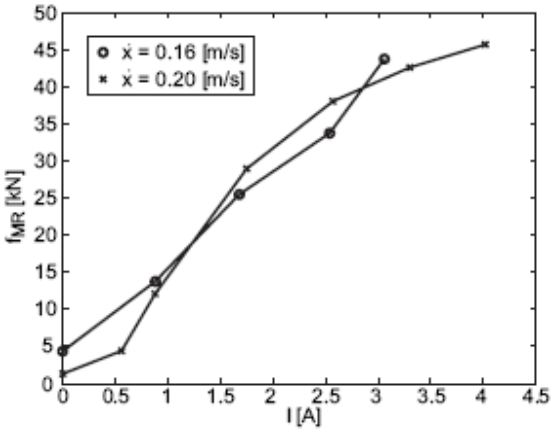

Fig. 71: Force current relation of MR damper of the "Eiland Bridge".

2) Measured MR damper characteristics

Based on the choice of MR fluid, the geometry of the MR damper was designed by Maurer Söhne GmbH & Co. KG, Munich, Germany, which also manufactured the MR damper. It was tested at the "Lehrstuhl für Konstruktiven Ingenieurbau der Universität der Bundeswehr" in Neubiberg, nearby Munich. As can be readily seen from **Fig. 70** and **Fig. 71**, the required MR damper characteristics could be fulfilled.

3) Damping measurements on the bridge

In order to know the amount of additional damping provided by the MR damper of Maurer Söhne on the "Eiland Bridge" (**Fig. 72**, **Fig. 73**), the decay rate of both the free cable and the cable with MR damper at different constant current levels were measured.

The stay cable was excited by man power with a perpendicularly connected rope at the frequency of the first vibration mode using a metronome (Fig. 74). The decay rate of the cable was evaluated at 12% relative cable length. The accelerometers on the top and bottom of the MR damper and the displacement sensor as well detected clamping of the cable due to the MR damper force which remained approximately constant during decay time as a result of constant current. The MR damper clamps the cable in its equilibrium position as soon as the cable force component in damper direction is smaller than the damper force (Fig. 75, Weber et al. (2005d))

$$\begin{aligned} &\left|f_{MR}(I)\right| < T\left(\sin(\alpha_2)-\sin(\alpha_1)\right) \Rightarrow \dot{x}_{MR} \neq 0 \Rightarrow P \neq 0 && : no\ clamping \\ &\sin(\alpha_1) \approx 0, \left|f_{MR}(I)\right| \geq T\left(\sin(\alpha_2)\right) \Rightarrow \dot{x}_{MR} = 0,\ x_{MR} = 0 \Rightarrow P = 0 && : clamping \end{aligned} \tag{11}$$

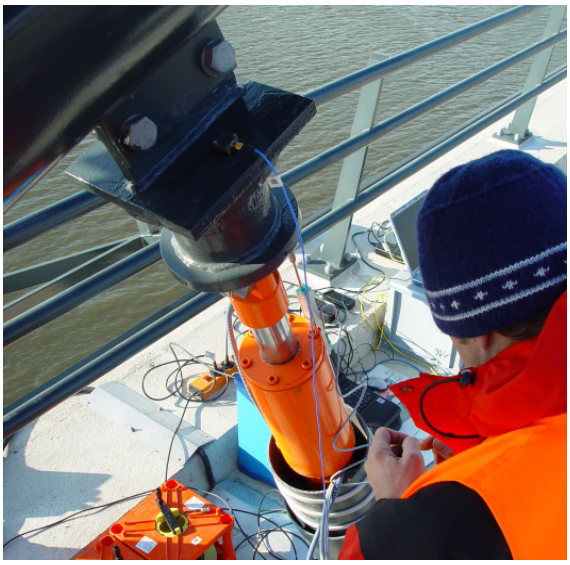

Fig. 72: Instrumentation of MR damper on the "Eiland Bridge" nearby Kampen, The Netherlands.

Fig. 73: Taking decay measurements on the "Eiland Bridge" nearby Kampen, The Netherlands.

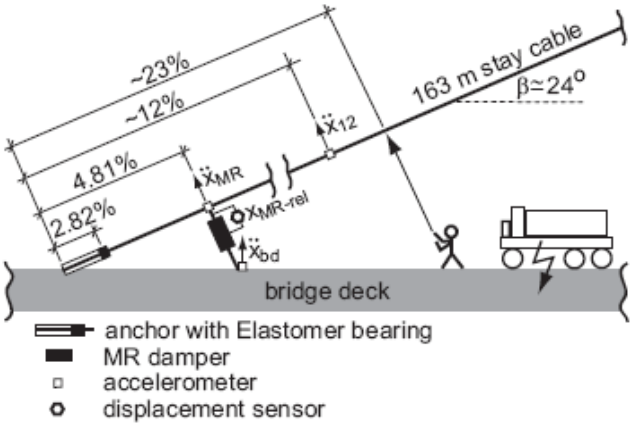

Fig. 74: Sketch of decay measurements on the ”Eiland Bridge“ nearby Kampen, The Netherlands.

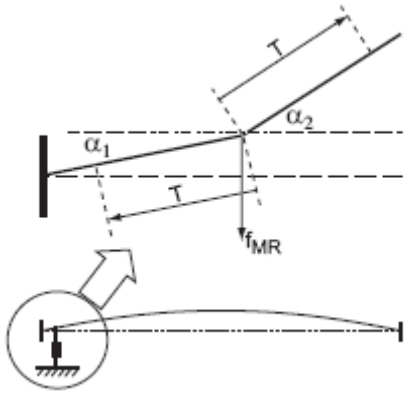

Fig. 75: Clamping of cables.

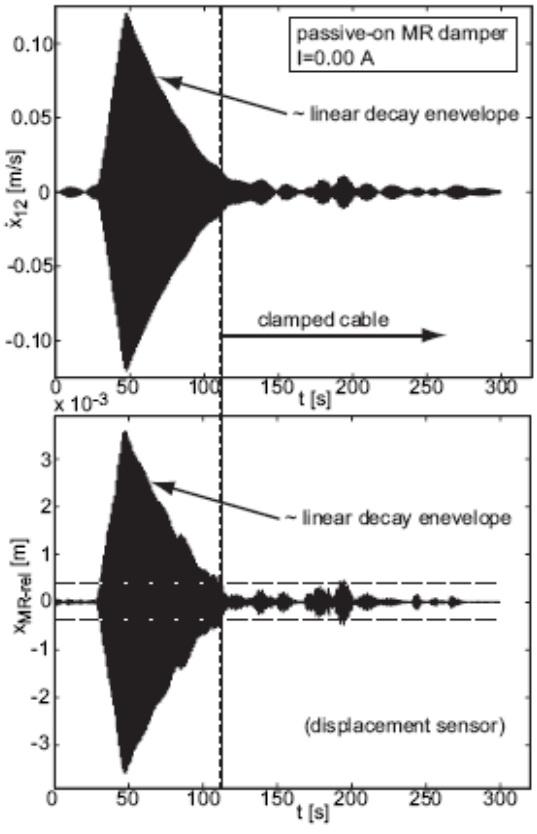

Fig. 76: Measured vibration decay at 12% cable length and damper position with MR damper at 0 A.

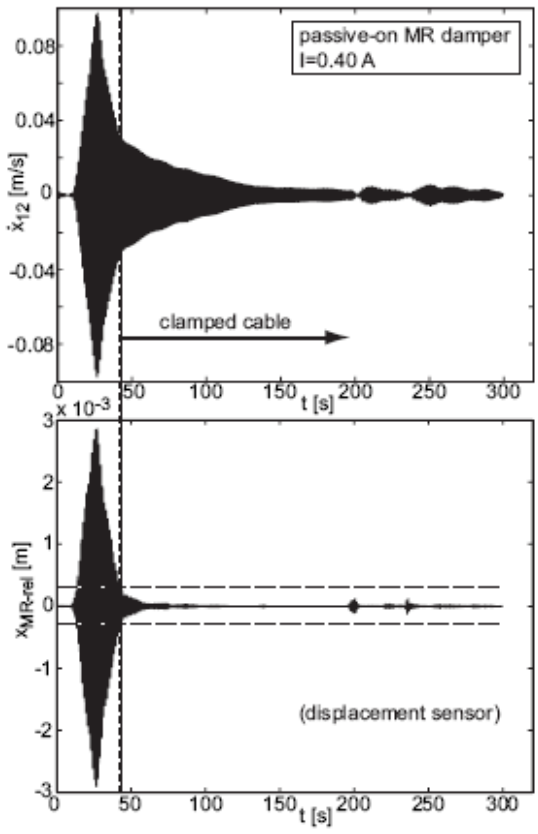

Fig. 77: Measured vibration decay at 12% cable length and damper position with MR damper at 0.4 A.

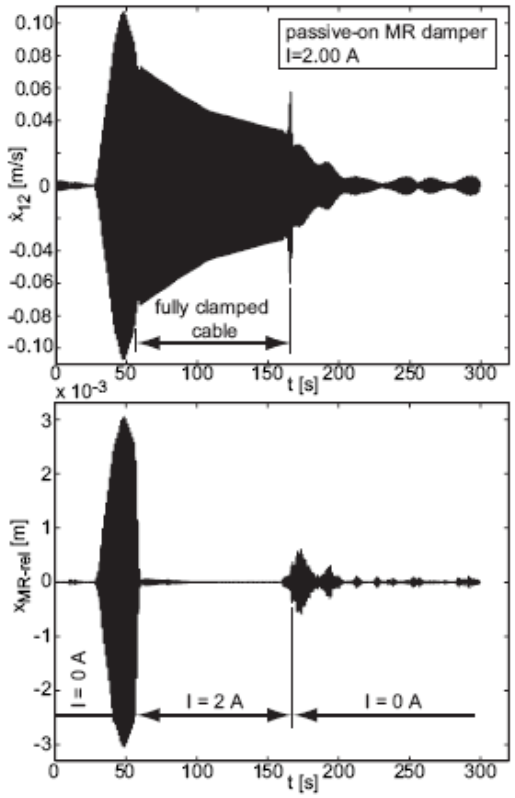

Fig. 78: Measured vibration decay at 12% cable length and damper position with MR damper at 2.0 A.

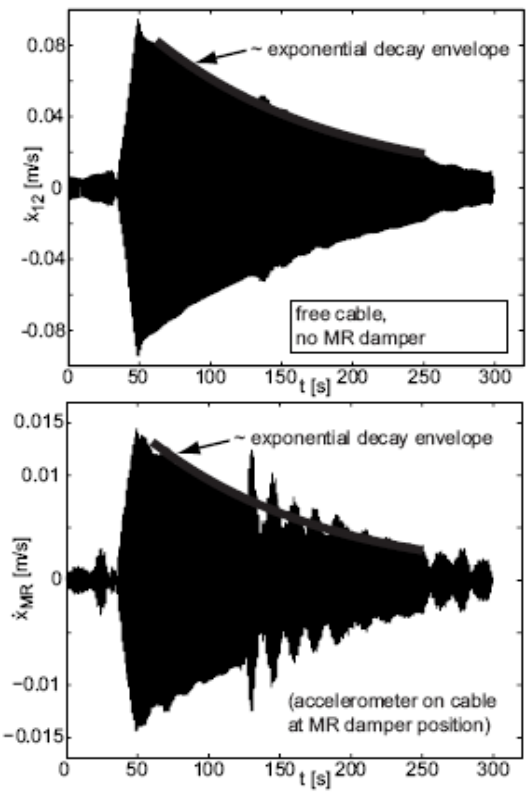

Fig. 79: Measured vibration decay at 12% cable length and damper position of free cable.

Due to the approximate Coulomb friction behaviour of the MR damper under consideration, vibrations at 12% relative cable length decay approximately linearly as long as the MR damper works. If the MR damper works, the MR damper relative displacement is larger than a certain band value which results from out-of-plane vibrations of the damper piston (Fig. 76, Fig. 77). If clamping occurs, the relative MR damper displacement becomes zero or is smaller than the band value, respectively. With the start of clamping, the decay envelope changes to an approximate exponential function. This indicates that the damping is dominated by the approximate viscous material damping of the cable only. If the damper current is set to 2 A, the MR damper fully clamps the cable at damper position. Hence, the decay envelope has an exponential shape and the decay rate is that of the free cable (Fig. 78, Fig. 79). At such high current level, the MR damper behaves like an almost completely stiff bearing.

4) Evaluation procedure of measurement data

Although the measured acceleration at 12% relative cable length decays almost with linear envelope during unclamped conditions (Fig. 76, Fig. 77), the damping was evaluated applying the approach of the logarithmic decrement that basically assumes linear viscous damping (Bachmann et al. (1995)). In that case, the ratio of two following maxima is constant

$$\frac{\dot{X}(t_i)}{\dot{X}(t_i + T_d)} = constant \tag{12}$$

where $2\pi/T_d$ denotes the radial eigenfrequency of the damped structure. The logarithmic decrement becomes

$$\delta = \frac{1}{n} \cdot \ln\left(\frac{\dot{X}(t_i)}{\dot{X}(t_i + nT_d)} \right) = \frac{1}{n} \cdot \ln\left(\dot{X}(t_i)\right) - \ln\left(\dot{X}(t_i + nT_d)\right) \tag{13}$$

which leads to the equivalent damping ratio as follows

$$\zeta = \frac{\delta}{\sqrt{4\pi^2 + \delta^2}} \approx \frac{\delta}{2\pi} \tag{14}$$

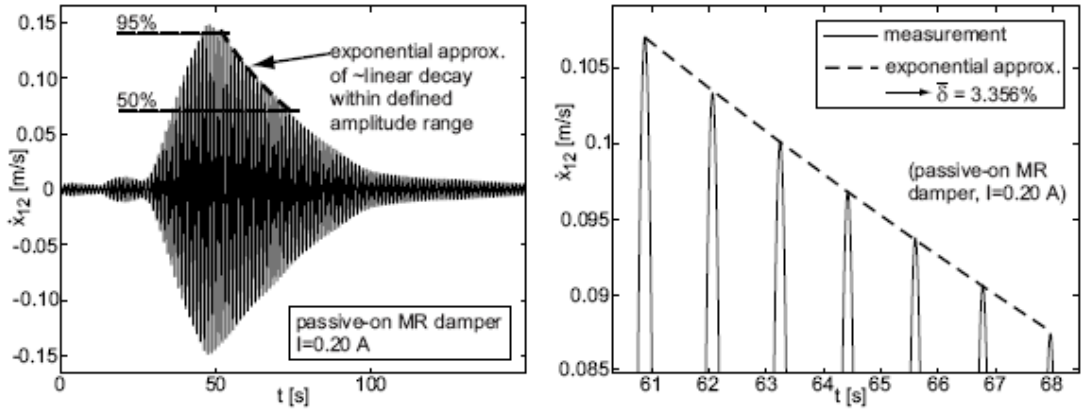

Fig. 80: Exponential approximation of linear decay within the amplitude range from 95% to 50%.

In order to keep the evaluation error due to the approximately linear decay envelope fairly small, the local maxima within the amplitude range of 95% to 50% of the maximum value were fitted by an exponential function in order to determine the logarithmic decrement and the equivalent damping ratio, respectively (Fig. 80). Moreover, this way, the decay rate is evaluated within the amplitude range of large values which could cause material damage. Hence, if the MR damper current is chosen for maximum logarithmic decrement for that amplitude range, the MR damper force is tuned in order to prevent from possible material damage.

Due to some small modulation of the decay measurements by higher modes, the evaluation procedure of the logarithmic decrement is modified as follows (Weber et al. (2005d)):

1. Band pass filtering of the measured signals for the excited mode, in that case mode number 1.
2. Determination of the local maxima within the amplitude range of 95% - 50%.
3. Linear fitting of the natural logarithm of the selected local maxima in order to derive an estimate of the logarithmic decrement with small error, Eqs.(16)-(18).

$$\ln\left\{\dot{X}(t_i)\right\},\ i=[1,k] \xrightarrow{\text{linear fitting}} fit = a + b\cdot t \rightarrow \bar{\delta} = \frac{b\cdot(t_k - t_1)}{k-1}$$

(15)-(17)

For the cable amplitudes within the range of 95% - 50% of the maximum mid span amplitude of approximately 0.075 m, 0.4 A turned out to be the optimum value of constant damper current for minimum decay time within the chosen amplitude (Fig. 81). The logarithmic decrement of the free stay cable was measured as 0.96% which is a typical value for lightly damped steel structures. By attaching the MR damper operating in the passive-off mode, thus 0 A, the overall damping could be increased by an approximate factor of four (Fig. 81). If the MR damper current is optimally tuned to the actual vibration amplitude, the overall damping was approximately eight times larger than the damping of the free cable. If the MR damper clamped the cable at damper position due to a far too large current, the overall damping was the same as for the free cable (see logarithmic decrement for 2 A in Fig. 81).

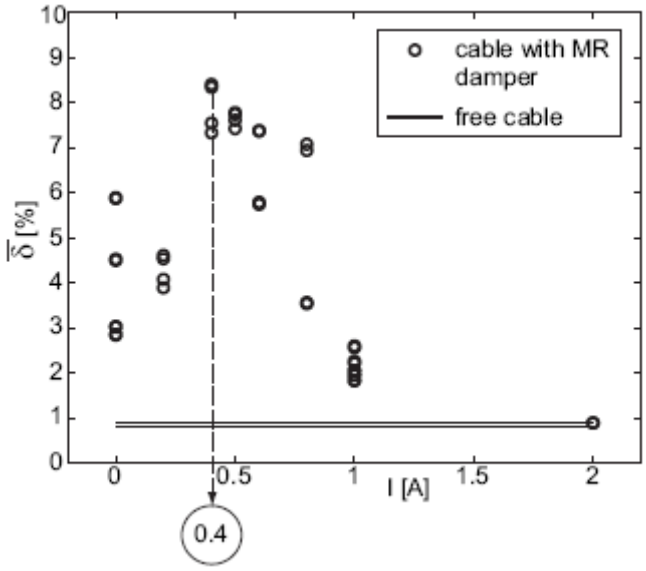

Fig. 81: Evaluated mean logarithmic decrement.

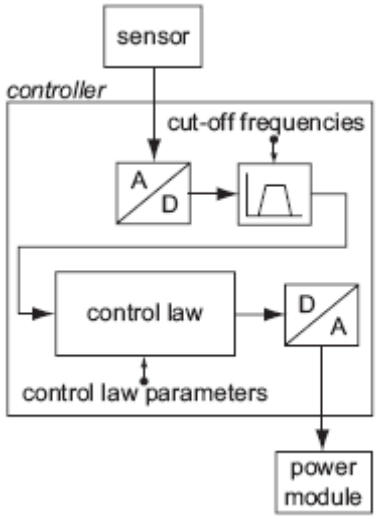

Fig. 82: Schematic controller structure.

5) Controller

The basic controller structure consists of analogue/digital converter, the band pass filter, the control law, and the digital/analogue converter (Fig. 82). The input is the measured relative damper displacement and the controller output is a voltage signal [-10, 10] V, which is the command signal of the power module that generates the desired MR damper current (Fig. 83). The controller parameters such as sample frequency, cut-off frequencies and control law parameters may be defined using a laptop computer connected to the controller by USB interface.

In the case of the “Eiland Bridge”, a fairly simple control approach has been implemented. Basically, it is an on/off strategy that applies 0.4 A to the MR damper if the actual relative damper displacement amplitude is above a defined threshold for a certain time and 0 A for relative damper displacement amplitude below the threshold for a certain time.

The memory function is taken into consideration in order to prevent from numerous on-off switching. The definition of a displacement amplitude threshold results in:

- Low coupling of cable to bridge deck in the case of relative displacement amplitude below the threshold. This guarantees that the MR damper does not operate in passive-on mode due to small, traffic induced bridge deck vibrations.
- MR damper energy consumption is small.

The required power in the passive-off mode counts for 0.25 W with a current of 21 mA and in the passive-on operating mode at 0.4 A is 2.6 W with a current of 220 mA. The required power is supplied by a solar panel und a battery 24Ah / 12V, made lead/gel technology, representing the necessary energy buffer (Fig. 84).

Fig. 83: Displacement sensor and MR damper on the “Eiland Bridge” nearby Kampen, The Netherlands.

Fig. 84: Solar panel and controller box mounted on the lightning pylon on the “Eiland Bridge” nearby Kampen, The Netherlands.

The control law may be extended to a gain scheduling approach where different current levels correspond to different relative damper displacement amplitude ranges. Due to the fairly small mid span amplitude that could have been excited by the presented man powered tests, only one optimum damper current value for one amplitude range could have been determined. Therefore, the control law consists of only one “gain”.

The physical reason for the gain scheduling approach depending on the actual relative damper displacement amplitude may be explained in the following. Depending on the MR fluid viscosity, the force trajectory of MR dampers describes more or less a Coulomb force trajectory (Fig. 54). Hence, the force of MR dampers operating at constant current is independent of the actual collocated cable velocity or displacement, respectively. As a result, during the decay of cable vibrations, the MR damper force remains constant and finally clamps the cable at damper position as soon as the MR damper force is larger than the cable force in damper direction (Fig. 75). In contrast, linear viscous dampers will not clamp the cable during a decay phase due

to the proportionality between force and velocity. Concluding, if MR dampers shall be used for cable vibration mitigation, control of their friction force is mandatory. The control law may be derived from the energy equivalent, optimum linear viscous damper as follows (Fig. 69)

$$W_{vis} = \pi \cdot f_{vis-\max} x_{vis-\max} = W_{fri} = 4 \cdot f_{fri-\max} x_{fri-\max} \tag{18}$$

Assuming sinusoidal displacement at damper position, the velocity amplitude may be expressed in terms of displacement amplitude and frequency

$$W_{vis} = W_{fri} = \pi c_n^{opt} \dot{x}_{vis-\max} x_{vis-\max} = \pi c_n^{opt} x_{vis-\max}^2 \omega_n \tag{19}$$

The optimum viscosity given by Eq. (4) may be substituted in Eq. (19). For the same maximum damper displacements, the force level of the energy equivalent friction damper becomes

$$f_{fri-\max}^{equiv} = x_{fri-\max} \cdot \frac{\pi}{4} \cdot \frac{T}{x_d} \tag{20}$$

Hence, if friction force dampers shall dissipate the same amount of vibration energy as an optimally tuned linear viscous damper, then the actual friction damper force has to be controlled proportionally to the actual damper displacement amplitude. The absolute force value of friction dampers remains constant during one cycle of steady state vibrations in contrast to the force of linear viscous dampers which changes sinusoidally during one cycle of steady state vibrations. For MR dampers with force trajectories at constant current with fairly small slope, the equations derived for the friction damper may be taken also for MR dampers working at constant current.

Provided that damper displacement amplitude may be measured directly, the feedback gain of energy equivalent friction dampers becomes

$$g_{fri}^{equiv} = \frac{\pi}{4} \cdot \frac{T}{x_d} \tag{21}$$

Linear viscous dampers represent the case of an ideal damping element where the damping coefficient is a constant independent variable. The force of an optimally tuned linear viscous damper is the product of viscosity and collocated velocity

$$f_{vis}^{opt} = c_n^{opt} \cdot \dot{x}_{vis} \tag{22}$$

If such an optimum linear viscous damper has to be realized using an ideal actuator (Fig. 51), then the optimum viscosity represents the optimum feedback gain if the collocated velocity is measured directly (Marathe et al. (2004), Preumont (2002))

$$g_{vis}^{opt} = c_n^{opt} \tag{23}$$

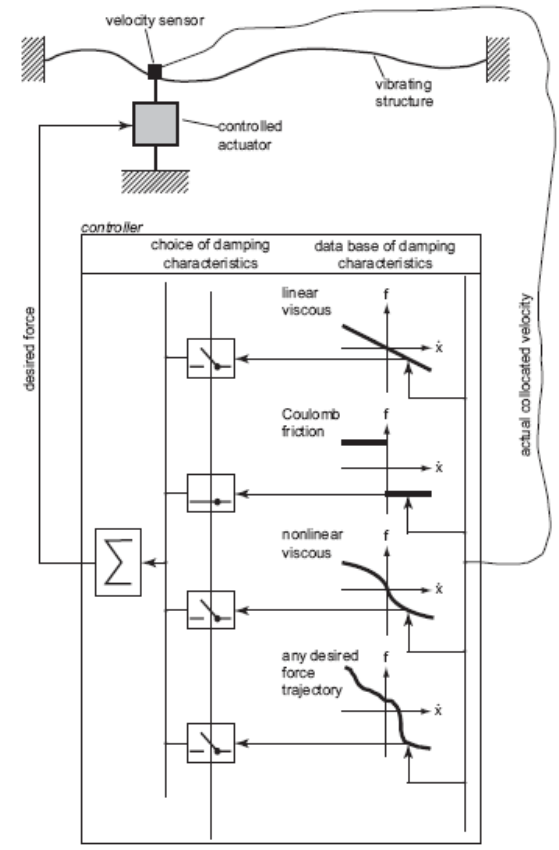

Fig. 85: Emulation of desired damping characteristics using feedback controlled actuators.

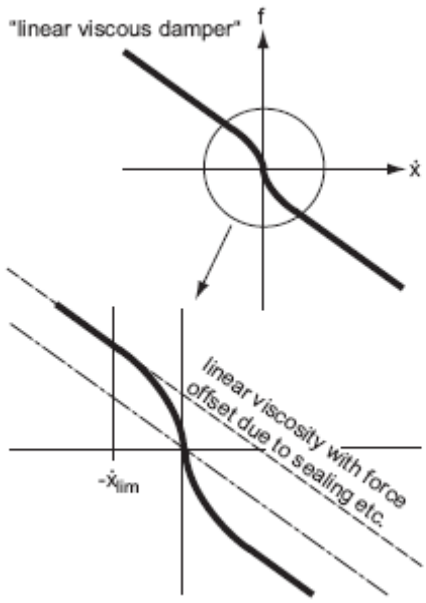

Fig. 86: Characteristics of real "linear viscous dampers".

Generating the force trajectory of a, e.g., linear viscous damper by feedback control of actuators is called "emulating" linear viscous dampers (Fig. 85, Nakamura and Nakazawa (2002), Marathe et al. (2004), Stelzer et al. (2003)). If a feedback controlled actuator emulates a linear viscous damper, the control strategy is called "velocity feedback". There are several reasons why emulation of, e.g., linear viscous dampers using feedback controlled actuators may be sensible:

1. the wanted linear viscous damper with the desired optimum viscosity is not available on the market,
2. the offered "linear viscous dampers" often do not have a pure linear force trajectory, especially below a certain velocity limit $\dot{x}_{\lim}$ due to the sealing friction which ends up in a highly nonlinear force trajectory below $\dot{x}_{\lim}$ (Fig. 86), and
3. the viscosity of a linear viscous damper cannot be tuned on site to the real structural properties in contrast to feedback controlled actuators, where the feedback gain allows for a fine tuning.

References

Bachmann, H., et al. (1995), *Vibration Problems in Structures: Practical Guidelines*, Birkhäuser Verlag Basel, ISBN 3-7643-5148-9.

Chen, S. H., and Yang, G. (2003), “A method for determining locations of electro-rheological dampers in structures”, *Journal of Smart Materials and Structures*, 12(2), 164-169.

Dominguez, A., Sedaghati, R., and Stiharu, I. (2004), “Modelling the hysteresis phenomenon of magnetorheological dampers “, *Journal of Smart Materials and Structures*, 13, 1351-1361.

Gordaninejad, F., Saiidi, M., Hansen, B. C., Ericksen, E. O., and Chang, F.-K. (2002), “Magneto-Rheological Fluid Dampers for Control of Bridges”, *Journal of Intelligent Material Systems and Structures*, 13(2/3), 167-180.

Guglielmino, E., Stammers, C. W., Edge, K. A., Sireteanu, T., and Stancioiu, D. (2005), “Damp-By-Wire: Magnetorheological Vs. Friction Dampers“, *Proceedings of the 16th IFAC World Congress*, Prague, Czech Republic, 4-8 July 2005.

Han, Y. M., Ham, M. H., Han, S. S., Lee, H. G., and Choi, S. B. (2002), “Vibration Control Evaluation of Commercial Vehicle Featuring MR Seat Damper”, *Journal of Intelligent Material Systems and Structures*, 13(9), 575-579.

Jiménez, R., and Alvarez-Icaza, L. (2005), “LuGre friction model for a magnetorheological damper“, *Journal of Structural Control and Health Monitoring*, 12, 91-116.

Jung, H.-J., Spencer Jr., B. F., M.ASCE; and Lee, I.-W., M.ASCE (2003), “Control of Seismically Excited Cable-Stayed Bridge Employing Magnetorheological Fluid Dampers”, *Journal of Structural Engineering*, 129(7), 873-883.

Ko, J. M., Zheng, G., Chen, Z. Q., and Ni, Y. Q. (2002), “Field vibration tests of bridge stay cables incorporated with magneto-rheological (MR) dampers”, *Proceedings of the International Conference on Smart Structures and Materials 2002: Smart Systems of Bridges, Structures, and Highways*, S.-C. Liu and Darryll J. Pines (eds.), Proceedings of SPIE (publ.), 4696, 30-40.

Kornbluh, R., Prahlad, H., Pelrine, R., Stanford, S., Rosenthal, M., and von Guggenberg, P. (2004), “Rubber to rigid, clamped to undamped: Toward composite materials with wide-range controllable stiffness and damping“, *Proceedings of the International Conference on Smart Structures and Materials 2004: Industrial and Commercial Applications of Structures and Technologies*, E. H. Anderson (ed.), Proceedings of SPIE (publ.), Vol. 5388, 372-386.

Krenk, S. (2000), “Vibrations of a Taut Cable With an External Damper”, *Journal of Applied Mechanics*, 67, 772-776.

Lee, Y., and Jeon, D. (2002), “A Study on The Vibration Attenuation of a Driver Seat Using an MR Damper”, *Journal of Intelligent Material Systems and Structures*, 13(7/8), 575-579.

Liao, W. H., and Lai, C. Y. (2002), “Harmonic Analysis of a Magnetorheological Damper for Vibration Control”, *Journal of Smart Materials and Structures*, 11(2), 288-296.

Marathe, S. S., Wang, K. W., and Gandhi, F. (2004), “Feedback linearization control of magnetorheological fluid damper based systems with model uncertainties“, *Journal of Smart Materials and Structures*, 13(5), 1006-1016.

Nakamura, T., Saga, N., and Nakazawa, M. (2002), “Impedance Control of a Single Shaft-type Clutch Using Homogeneous Electrorheological Fluid”, *Journal of Intelligent Material Systems and Structures*, 13(7/8), 465-469.

Oh, H.-U., and Onoda, J. (2002), "An Experimental Study of a Semiactive Magneto-Rheological Fluid Variable Damper for Vibration Suppression of Truss Structures", *Journal of Smart Materials and Structures*, 11(1), 156-162.

Oyadiji, S. O., and Sarafianos, P. (2000), "Comparing the Dynamic Properties Conventional and Electro-Rheological Fluid Shock Absorbers", *Proceedings of the 7th International Conference on Recent Advances in Structural Dynamics*, Southampton, England, July 2000, 579-590.

Pignon, F., Magnin, A., and Piau, J.-M. (1996), "Thixotropic colloidal suspensions and flow curves with minimum: Identification of flow regimes and rheometric consequences", *Journal of Rheology*, 40(4), 573-587.

Powell, J.A. (1995), "Application of a nonlinear phenomenological model to the oscillatory behavior of ER materials", *Journal of Rheology*, 39(5), 1075-1094.

Preumont, A. (2002), *Vibration Control of Active Structures*, Kluwer Academic Publishers, Dordrecht.

Ramallo, J. C., Yoshioka, H., and Spencer Jr, B. F. (2004), "A two-step identification technique for semi-active control systems", *Journal of Structural Control and Health Monitoring*, 11(4), 273-289.

Rosenfeld, N. C., and Wereley, M. (2004), "Volume-constrained optimization of magnetorheological and electrorheological valves and dampers *", Journal of Smart Materials and Structures*, 13, 1303-1313.

Sahasrabudhe, S., and Nagarajaiah, S. (2005), "Experimental Study of Sliding Base-Isolated Buildings with Magnetorheological Dampers in Near-Fault Earthquakes", *Journal of Structural Engineering*, 131(7), 1025-1034.

Seiler, C., Fischer, O., and Huber, P. (2002), "Semi-active MR dampers in TMD's for vibration control of footbridges, Part 2: Numerical analysis and practical realisation", *Proceedings of the International Conference on Footbridge*, Paris, France, 20-22 November 2002, AFGC – OTUA (eds.), on CD.

Song, X., Ahmadian, M., and Southward, S. C. (2005), "Modeling Magnetorheological Dampers with Application of Nonparametric Approach", *Journal of Intelligent Material Systems and Structures*, 16(5), 421-432.

Spencer Jr., B. F., Dyke, S. J., Sain, M. K., and Charlson, J. D. (1997), "Phenomenological Model of a Magnetorheological Damper", *Journal of Engineering Mechanics*, ASCE, 123(3), 230-238.

Spencer Jr., B. F., and Nagarajaiah, S. (2003), "State of the Art of Structural Control", *Journal of Structural Engineering*, 129(8), 845-856.

Stelzer, G., J., Schulz, M., J., Kim, J., and Allemang, R., J. (2003), "A Magnetorheological Semi-active Isolator to Reduce Noise and Vibration Transmissibility in Atomobiles", *Journal of Intelligent Materials Systems and Structures*, 14(12), 743-765.

Tse, T., and Chang, C. C. (2004), "Shear-Mode Rotary Magnetorheological Damper for Small-Scale Structural Control Experiments", *Journal of Structural Engineering*, 130(6), 904-911.

Wan, X., and Gordaninejad, F. (2002), "Lyapunov-Based Control of a Bridge Using Magneto-Rehological Fluid Dampers", *Journal of Intelligent Material Systems and Structures*, 13(7/8), 471-478.

Wand, D. H., and Liao, W. H. (2005), “Modeling and control of magnetorheological fluid dampers using neural networks“, *Journal of Smart Materials and Structures*, 14, 111-126.

Weber, F., Feltrin, G., Motavalli, M., and Aalderink, B. J. (2002), “Cable Vibration Mitigation Using Controlled Magnetorheological Fluid Dampers: A Theoretical and Experimental Investigation”, Proceedings of the International Conference on Foot-bridge, Paris, France, November 20-22 2002, AFGC – OTUA (eds.), on CD.

Weber, F., and Feltrin, G. (2003), “Influence of the offset friction of rheological fluid dampers on the vibration mitigation performance”, *Proceedings of Fifth International Symposium on Cable Dynamics*, Santa Margherita Ligure (Italy), September 15-18 2003, 427-435.

Weber, F., Feltrin G., and Motavalli, M. (2005a), “Passive damping of cables with MR dampers”, *Journal of Materials and Structures*, 38(279), 568-577.

Weber, F., Distl, H., and Nützel, O. (2005b), “Versuchsweiser Einbau eines adaptiven Seildämpfers in eine Schrägseilbrücke“, *Beton- und Stahlbetonbau 100(2005)*, Heft 7, 582-589.

Weber, F., Feltrin, G., and Motavalli, M. (2005c), “Measured LQG Controlled Damping“, *Journal of Smart Materials and Structures*, 14, 1172-1183.

Weber, F., Distl, H., Feltrin, F., and Motavalli, M. (2005d), “Evaluation Procedure of Decay Measurements of a Cable with passive-on operating MR Damper”, *Proceedings of Sixth International Symposium on Cable Dynamics*, Charleston, SC (USA), September 19-22 2005, 143-150.

Weiss, K. D., Carlson, J. D., and Nixon, D. A. (1994), “Viscoelastic properties of magneto- and electro-rheological fluids“, *Journal of Intelligent Material Systems and Structures*, 5(11), 772-775.

Williams, K., Chiu, G., and Berhard, R. (2002), “Adaptive-passive absorbers using shape-memory alloys“, *Journal of Sound and Vibration*, 249(5), 835-848.

Yang, G., Ramallo, J.C., Spencer, B.F., Jr., Carson, J.D., and Sain, M.K. (2000), “Large-scale MR fluid dampers: Dynamic performance considerations”, *Proceedings of the International Conference on Advances in Structure Dynamics*, Hong Kong, 341-348.

Yang, G. (2001), *Large-scale magnetorheological fluid damper for vibration mitigation: Modeling, testing and control*, PhD dissertation, University of Notre Dame, Notre Dame, Indiana.

Yang, G., Spencer Jr., B. F., Jung, H.-J., and Carlson, J. D. (2004), “Dynamic Modeling of Large-Scale Magnetorheological Damper Systems for Civil Engineering Applications“, *Journal of Engineering Mechanics*, 130(9), 1107-1114.

Zhang, T., Jiang, C., Zhang, H., and Xu, H. (2004), “Giant magnetostrictive actuators for active vibration control“, *Journal of Smart Materials and Structures*, 13(3), 473-477.

Zhou, H. and Sun, L. (2005), “A full-scale cable vibration mitigation experiment using MR damper“, *Proceedings of 6th International Conference on Cable Dynamics*, Charleston, SC (USA), September 19 – 22, 2005, 167-174.

Notations

Symbol	*Description*	*Unit*
I	current	A
L	cable length	m
P	power	W
T	cable force	N
W	energy, work	J
X	amplitude of x	m
c	viscosity	kg/s
f	force, frequency	N, Hz
g	gain	-
k	stiffness	kg/s^2
m	mass; cable mass per unit length	kg; kg/m
x	displacement	m
α	angle	rad
δ	logarithmic decrement	-
ε	error	-
ω	radial frequency	rad/s
ζ	damping ratio	-

Superscripts	*Description*
opt	optimal
$\bar{x}$	mean value of x
Subscripts	*Description*
MR	MR damper
act	actual
d	damper
des	desired
fri	friction damper
$\max$	maximum
$\min$	minimum
sa	semi-active
u	control input
vis	linear viscous damper
w	disturbance

2.1.2.3 Controlled shape memory alloy

Theoretical background

Shape memory alloys (SMAs) are mostly known for their so-called “shape memory effect”, where SMAs revert to their initial shape upon heating after having been deformed at low temperatures (Duerig (1990), Funakubo (1987), Humbeeck (2001), Janke et al. (2005), Otsuka and Wayman (1999), Otsuka and Kakeshita (2002)). This effect is also called pseudoplasticity. If the deformation recovery is restrained, mechanical stress results within the SMA. The stress may be used to introduce external forces into structures.

Another effect occurs when austenite phase transforms to martensite phase due to external mechanical load at constant temperature. This is called super- or pseudoelasticity, respectively. The alloy retransforms automatically to austenitic state if the SMA is unloaded. The stress-strain curve shows a hysteresis built by the two paths of transformation and retransformation.

The “two way SMA effect” describes the behaviour of some SMAs that may remember two different shapes depending on different temperatures.

Besides the transformation processes briefly described above, SMAs are characterized by high damping capacity due to internal friction which is based on mainly two different mechanisms. If martensite is the stable phase, martensite variants are reoriented within the SMA upon loading above yield stress. This effect produces large hysteresis areas if the loading is sinusoidal around zero. If the SMA is heated to a higher temperature, the hysteresis loop changes its form until it reaches the shape similar to the superelastic behaviour of SMAs. However, due to the complicated shape of the hysteresis trajectories between ambient temperature and high temperatures (Otsuka and Wayman (1999)), this “adaptive” material behaviour is not used to produce controllable damping devices.

The second mechanism is based on the superelasticity of SMAs (Fig. 87). The relative displacement between austenite and martensite interfaces and between martensite variants, respectively, produces friction and therefore damping. The hysteresis area during loading and unloading in the superelastic state is equivalent to the dissipated energy. Since the hysteresis curve appears within the stress-strain map, this kind of damping is structural damping. If the temperature of the SMA is increased, the hysteresis does change its area, form and location within the stress/strain map (Fig. 87). For small temperature variations, the hysteresis curve does hardly change its area and form, but moves slightly to higher stress/strain values (compare the thick solid line and thick dashed line in Fig. 87).

Adaptive shape memory alloy

In the field of structural control, the superelastic behaviour may be used to produce a damping device with variable damping characteristics. The crucial points of such a controllable damping device may be:

- Heating up the entire SMA is energy consuming and a constant, homogeneous temperature of the entire SMA is difficult to achieve and maintain.
- Fast cooling of SMAs is a challenging issue.
- Both, heating and cooling are rather slow processes due to the thermal capacity of the SMA material which results in a very small bandwidth of the semi-active damping device.

- The working area of the semi-actively working SMA is small compared to the entire area of the stress/strain area. Consequently, in many cases, the desired optimum control force cannot be tracked. The resulting suboptimal force leads to mediocre vibration mitigation performance.

Due to the difficulties listed above, the potential of SMAs working in the superelastic mode at different temperature is not a current issue. However, researchers have investigated numerically the damping potential of SMAs in superelastic mode at constant temperature (Li et al. (2004)).

A different way of using SMAs as an adaptive material is proposed by, e.g., Rustighi et al. (2005) and Williams et al. (2002). Here, the SMA is used as a spring element with two different stiffness values depending on the temperature. At ambient temperature, the SMA is completely in the martensite phase (Fig. 88). At temperature "austenite finish", the SMA is completely in the austenite phase. The two phases are characterized by two different moduli of elasticity within the elastic stress/strain region. By combining several SMA elements which are either in martensite or austenite state, a tuneable spring can be designed. Such an adaptive spring may be used in order to tune the frequency of a tuned mass damper to the actual structural target frequency (Rustighi et al. (2005), Williams et al. (2002)). It must be mentioned that the SMA stiffness does not change smoothly with increasing temperature. Therefore, each SMA element of the overall spring is either in full martensite or full austenite state (Williams et al. (2002)). That is the reason why the number of SMA elements has to be fairly high in order to be able to produce a spring element with almost continuously tuneable stiffness, bounded by the low stiffness of martensite and the high stiffness of austenite.

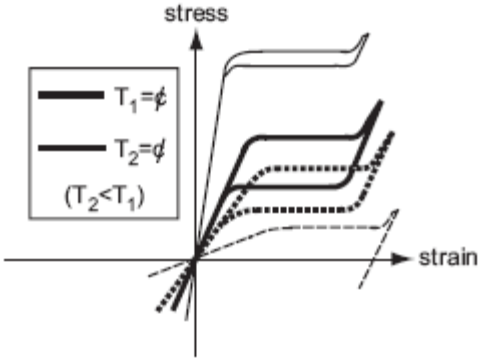

Fig. 87: Stress-strain curves for the superelastic behaviour of SMAs at different temperatures.

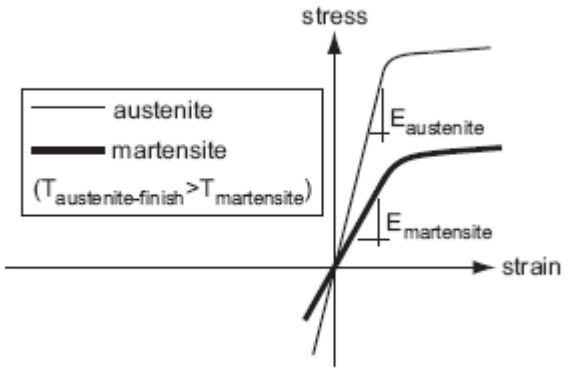

Fig. 88: Different moduli of elasticity for martensite and austenite.

References

Duerig, T. W. (1990), *Engineering Aspects of Shape Memory Alloys*, Butterworth-Heinemann, London.

Funakubo, H. (1987), "Precision Machinery and Robotics, Vol. 1 – Shape Memory Alloys", Gordon and Breach.

Humbeeck, J. V. (2001), "Shape memory alloys: A material and a technology", *Adv. Eng. Mater*, 3(11), 837-850.

Janke, L., Czaderski, C., Motavalli, M., and Ruth, J. (2005), “Applications of shape memory alloys in civil engineering structures – Overview, limits and new ideas”, *Journal of Materials and Structures*, 38(279), 578-592.

Li, H., Liu, M., and Oh, J. (2004), “Vibration mitigation of a stay cable with one shape memory alloy damper“, *Journal of Structural Control and Health Monitoring*, 11(1), 21-36.

Otsuka, K., and Wayman, C. M. (1999), *Shape Memory Materials*, Cambridge University Press.

Otsuka, K., and Kakeshita, T. (2002), “Science and technology of shape-memory alloys. New developments", Mrs Bulletin 27(2), 91-100.

Rustighi, E., Brennan, M. J., and Mace, B. R. (2005), “A shape memory alloy adaptive tuned vibration absorber: design and implementation“, *Journal of Smart Materials and Structures*, 14, 19-28.

Williams, K., Chiu, G., and Berhard, R. (2002), “Adaptive-passive absorbers using shape-memory alloys“, *Journal of Sound and Vibration*, 249(5), 835-848.

Notations

Symbol	*Description*	*Unit*
E	elasticity modulus	N/m^2
T	temperature	K

2.1.3 Actuators

2.1.3.1 Actuators for increase of damping

In the field of structural control, increasing structural damping is the main target because, in general, both frequency and spatial distribution of disturbance forces due to, e.g., wind loading, are unknown. If the structural damping c shall be augmented by the external control force f_u, the control force has to be controlled proportionally to the collocated structural velocity, which is shown for the simple case of a single degree of freedom system (SDOFS), see Eqs. (1) and (2).

$$m\ddot{x} + c\dot{x} + kx = f_u + f_w \rightarrow m\ddot{x} + \left(c - \frac{f_u}{\dot{x}} \right)\dot{x} + kx = f_w \tag{1}$$

$$f_u = -c_u \dot{x} \tag{2}$$

The overall damping of the SDOFS becomes

$$c_{tot} = \left(c + c_u\right) \tag{3}$$

The control concept described by Eq. (2) is called “velocity feedback” and will be discussed in detail in Chapter 2.2. According to Eq. (2), the control forces required are dissipative. Consequently, controllable dampers are sufficient to track the desired control force f_u. However, there are mainly three reasons, why actuators that can apply active forces to structures may be mandatory in the field of structural control:

- Besides increasing structural damping, structural control comprises also, e.g., displacement and shape control of structures.
- If the control force shall compensate for disturbance forces that influence the structure only at well known positions of the structure (Achkire et al. (1998), Caruso et al. (2003), Raja et al. (2002)).
- There exist many other control concepts used to mitigate structural vibrations which require dissipative and active force values (d’Azzo and Houpis (1995)).
- In the special case of “sky hook” damping requires dissipative and active force values (Lee and Jeon (2002), Preumont (2002), Preumont (2004), Stelzer et al. (2003)).

From the wide range of actuator types, two of them are described in the following which are fairly often used in the field of structural control, namely hydraulic aggregates and piezo actuators.

References

Achkire, Y., Bossens, F., and Preumont, A. (1998), “Active damping and flutter control of cable-stayed bridges”, *Journal of Wind Engineering and Industrial Aerodynamics*, 74-76, 913-921.

d’Azzo, J. J., and Houpis, C. H. (1995), *Linear Control System Analyzes and Design*, Conventional and Modern, Fourth Edition, McGraw-Hill (eds.), ISBN 0-07-016321-9.

Caruso, G., Galeani, S., and Menini, L. (2003), "Active Vibration Control of an Elastic Plate Using Piezoelectric Sensors and Actuators", *Journal of Simulation Modelling Practice and Theory*, 11(5-6), 403-419.

Lee, Y., and Jeon, D. (2002), "A Study on The Vibration Attenuation of a Driver Seat Using an MR Damper", *Journal of Intelligent Material Systems and Structures*, 13(7/8), 575-579.

Preumont, A. (2002), *Vibration Control of Active Structures*, Chapter 12, Kluwer Academic Publishers, Dordrecht.

Preumont, A. (2004), "Semi-active sky hook, does it work?", *EUROMECH Colloquium 455 on Semi-Active Vibration Suppression*, M. Valasek and A. Preumont (Eds.), CTU in Prague, Czech Republic, July 5-7 2004, on CD.

Raja, S., Prathap, G., and Sinha, P. K. (2002), "Active vibration control of composite sandwich beams with piezoelectric extension-bending and shear actuators", *Journal of Smart Materials and Structures*, 11(6), 63-71.

Stelzer, G., J., Schulz, M., J., Kim, J., and Allemang, R., J. (2003), "A Magnetorheological Semi-active Isolator to Reduce Noise and Vibration Transmissibility in Atomobiles", *Journal of Intelligent Materials Systems and Structures*, 14(12), 743-765.

Notations

Symbol	*Description*	*Unit*
c	viscous damping coefficient	kg/s
f	force	N
k	stiffness	kg/s^2
m	mass	kg
x	displacement	m

Subscripts

tot	total
u	control
w	disturbance

2.1.3.2 Hydraulic aggregate

Theoretical background

The force of hydraulic aggregates is produced by the oil pressure within the aggregate cylinder

$$f_{a-sta} = p \cdot A_p \tag{1}$$

where p is the oil pressure and A_p the cross sectional area of the piston.

The force level is controlled by servo valves (Fig. 89). Usually, hydraulic aggregates are equipped with both displacement and force sensor. This allows for controlling the hydraulic aggregate in displacement control mode or force control mode. The most often used control mode is displacement control and the reaction force between tested device and aggregate piston is measured by an additional force sensor or by the force sensor of the aggregate.

The maximum available displacement amplitude depends on the frequency assuming sinusoidal displacement because the dynamic force of the hydraulic aggregate is limited by a maximum tolerable value in order to avoid damage of the aggregate (Eq. (2)). The common way is that data sheets give information about the maximum values of frequency ω_p and amplitude X_p of a sinusoidal displacement.

$$f_{a-dyn-\max} \propto \ddot{x}_{p-\max} \propto \left(\omega_p^2 \cdot X_p\right) \tag{2}$$

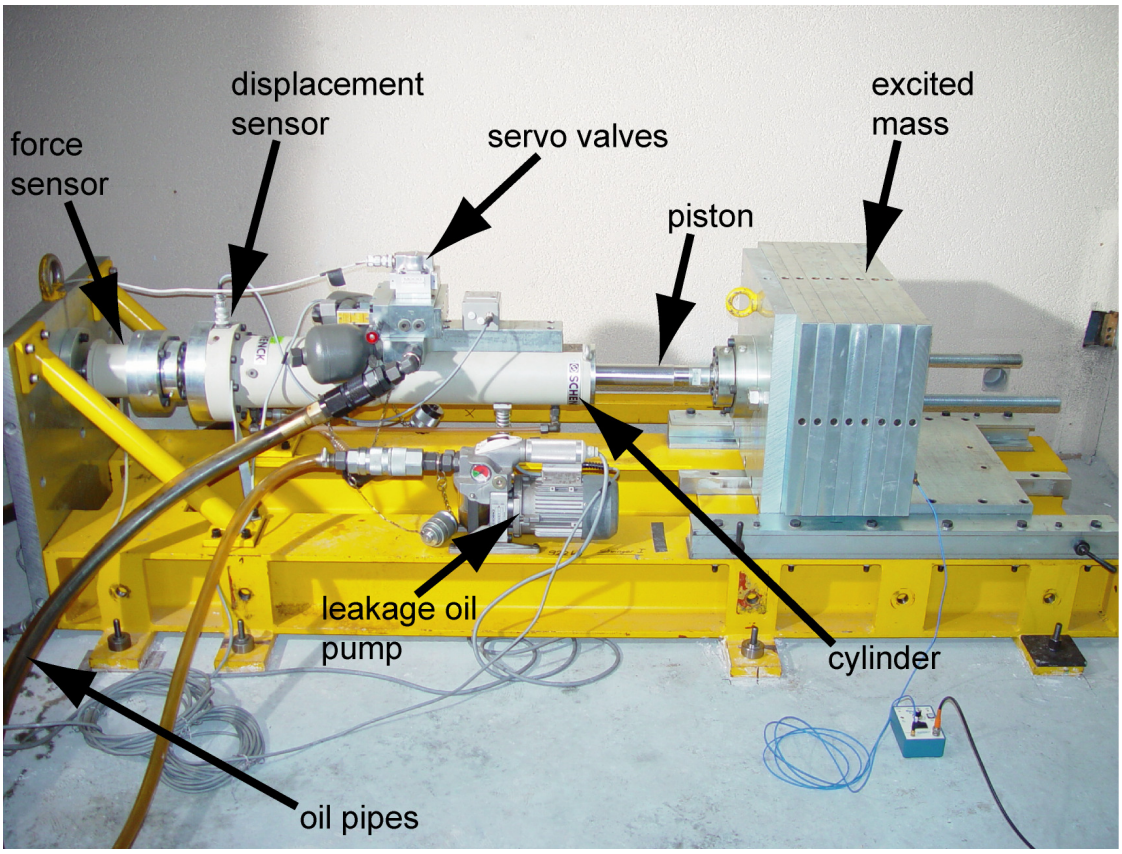

Fig. 89: Hydraulic aggregate, mounted on a steel frame.

The maximum value of the static aggregate force is usually approximately 20% higher than the maximum value of the dynamic aggregate force. However, since aggregates are used in dynamic testing of structures, the maximum dynamic force is relevant.

Implementation

Hydraulic aggregates are mainly used to test novel materials in the laboratory. Usually, the test material or test device is displacement controlled deformed and the reaction force as system output is measured (Krenk et al. (1996)). The results are the well known stress-strain or force-displacement curves, respectively. Another application of hydraulic aggregates is the forced excitation of structures such as buildings, bridges, and towers in order to identify structural parameters based on forced vibrations (Irwin and Stoyanoff (2005), Occhiuzzi et al. (2003), Stoyanoff et al. (2005), Weber and Huth (2005), Yang et al. (2004)). A third variant is simply to control the displacement or shape of large civil structures installing hydraulic aggregates between stories or between the first floor and ground.

As a result of the ability to produce active forces, the following points should be included in the displacement or force control loop of such actuators in order to avoid unintentional material or actuator damage:

- A maximum force value should be defined above which the controller shuts off.
- A maximum displacement value should be defined above which the controller shuts off.
- The first test should be run using a dummy.

Design and testing

Since hydraulic aggregates are commercially available, they are designed, manufactured and tested by the corresponding company. Operating maps of the aggregate are delivered together with the aggregate.

References

Irwin, P., and Stoyanoff, S. (2005), “Use of vibration testing as a diagnostic tool“, *Tutorial of 6th International Conference on Cable Dynamics*, Charleston, SC (USA), September 19 – 22, 2005.

Krenk, S., Jönsson, J., and Hansen, L. P. (1996), “Fatigue Analysis and Testing of Adhesive Joints“, *Journal of Engineering Fracture Mechanics*, 53(6), 859-872.

Occhiuzzi, A., Spizzuoco, M., and Serino, G. (2003), “Experimental analysis of magnetorheological dampers for structural control”, *Journal of Smart Materials and Structures*, 12(5), 703-711.

Stoyanoff, S., Theryo, T., and Garcia, P. (2005), “Full dynamic test of the stay cables of Sunshine Skyway Bridge“, *Proceedings of 6th International Conference on Cable Dynamics*, Charleston, SC (USA), September 19 – 22, 2005, 191-198.

Weber, F., and Huth, O. (2005), “Charakterisierung der dynamischen Eigenschaften eines Einfamilienhauses in Monthey / Wallis”, Empa Bericht Nr. 841173, Swiss Federal Laboratories for Materials Testing and Reserach, Dubendorf, Switzerland.

Yang, J., N., Lei, Y., Lin, S., and Huang, N. (2004), "Identification of Natural Frequencies and Dampings of In Situ Tall Buildings Using Ambient Wind Vibration Data", *Journal of Engineering Mechanics*, 130(5), 570-577.

Notations

Symbol	*Description*	*Unit*
A	cross sectional area	m^2
X	displacement amplitude	m
f	force	N
p	pressure	Pa
x	displacement	m
ω	radial frequency	rad/s

Subscripts

a	actuator
dyn	dynamic
$\max$	maximum
p	piston
sta	static

2.1.3.3 Piezo actuator

Besides books, information about piezo actuators may be found in the internet, e.g., on the following pages:

- http://de.wikipedia.org/wiki/Piezo
- http://www.efunda.com/Materials/piezo/general_info/gen_info_index.cfm
- http://www.marco.de/pb.html
- http://www.physikinstrumente.com/tutorial/index.html
- http://www.piezo.com/ (PIEZO SYSTEMS, INC., MA 02139 USA)
- http://www.piezo-kinetics.com/ (Piezo Kinetics, Inc. Bellefonte, PA 16823, USA)
- http://www.piezomechanik.com/ (Piezomechanik GmbH, D-81673 Munich, Germany)

Theoretical background

Piezo actuators like stacks, benders, tubes, and rings make use of the deformation of electroactive PZT-ceramics (PZT: lead (Pb), zirconia (Zr), Titanate (Ti)) when they are exposed to electrical fields. This deformation can be used to produce motions or forces if the deformation of the piezo element is constraint.

The above effect is the complementary effect to piezo electricity, where electrical charges are produced upon application of mechanical stress to the ceramics. As an analogy, the term “piezo mechanics” was introduced in the early 80’s of the past century by L. Pickelmann to describe the conversion of electricity into a mechanical action by piezo materials.

For piezo mechanical conversion in the simplest case a single PZT layer is used. Such a PZT monolayer structure as shown in Fig. 90 is a capacitive element. It consists of two thin conductive electrode coatings enclosing the piezo ceramic as dielectric. Applying a voltage to this “piezo capacitor”, the capacitor is charged and deformation results. Hence, PZT actuators may be seen as “actuating” capacitors.

If the maximum deformation of PZT actuators shall be increased, PZT actuators consist of several layers. These piezo stack actuators and stacked piezo rings make use of the increase of the ceramic thickness in direction of the applied electrical field (Fig. 91). This is called “d33 effect”. Stacking of several layers towards a multilayer structure increases equivalently the total stroke. In practice, axial strain rates up to 2‰ of stack’s length can be achieved under certain conditions.

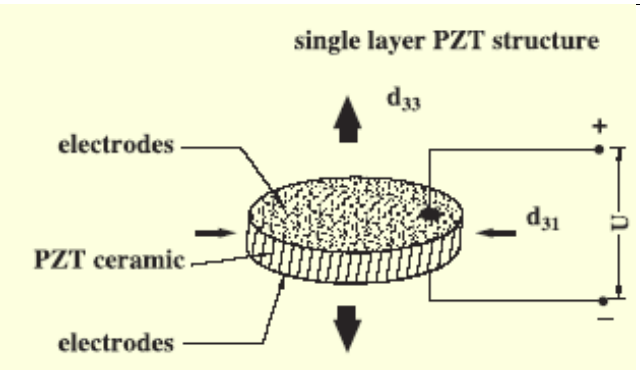

Fig. 90: Schematic of a piezo-electric single layer element (http://www.piezomechanik.com/).

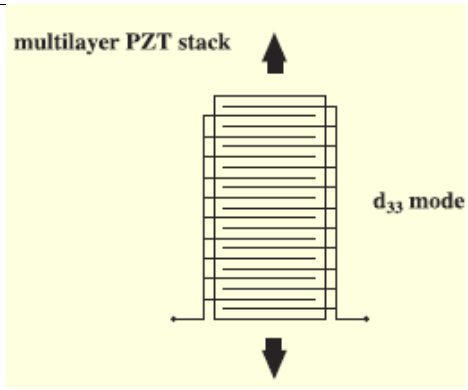

Fig. 91: Schematic of an axially acting multilayer piezo stack (http://www.piezomechanik.com/).

Similar to elastic deformation of solid bodies, the thickness expansion of a PZT layer is accompanied by an in-plane shrinking (Fig. 90). This is called the “d31 effect”, being complementary in motion and showing roughly half linear strain compared to the d33 effect. The d31 effect is mainly used for bending structures.

Design

Piezo actuators were used preferentially in the past for quasistatic precision positioning tasks, but find now increasing interest in completely new fields of application like dynamically actuated mechanics, e.g., valves, fuel injection devices, or adaptive smart structures such as shape tuning, vibration generation and cancellation, and mode tuning (Caruso et al. (2003), Herold et al. (2004), Ma (2002), Raja (2002), Sadri et al. (2002)). Of course, such a broad variety of applications cannot be covered by one general actuator type. The main parameters to adapt a piezo actuator to a distinct application are:

1. Selection of proper PZT material defining achievable strain, stroke, energy balance, temperature range etc.
2. Preparation of a highly reliable and efficient stack structure which is, e.g., shock and vibration resistant.
3. Sealing for corrosion resistance.
4. Packaging of the ceramic stack.
5. Actuator system design, e.g., systems able to push and pull.
6. Performance and reliability of actuator systems depend further on the electrical driving characteristics like voltage / charge / current control operating strategies and unipolar / semibipolar / bipolar operation.

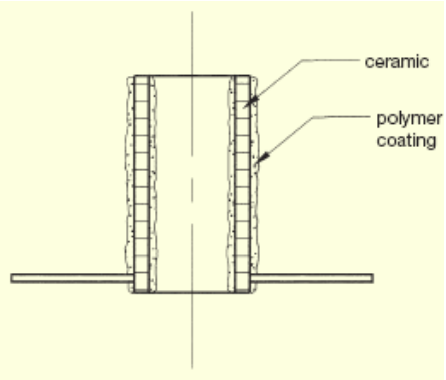

Fig. 92: Schematic of a stacked ring actuator (http://www.piezomechanik.com/).

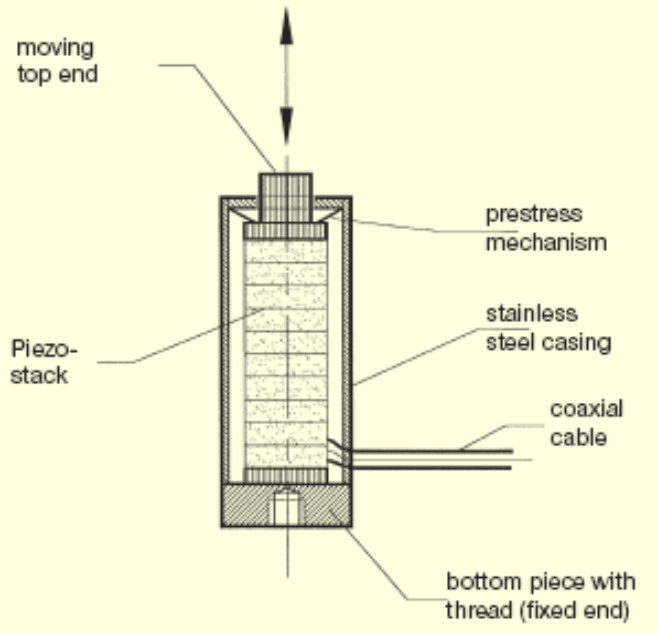

Fig. 93: Schematic of an actuator with prestress (http://www.piezomechanik.com/).

Some of the currently used basic stack designs are:

- Bare stacks: The mounting and motion transfer is always done via end faces. Bare stack must not be hold by sideway clamping.
- Ring stacks with centre hole (Fig. 92): Ring stacks are needed if an accessible system axis is needed for transmissive optical set-ups or the feed through of mechanical parts is required. Ring stacks may be also required in order to increase the bending stiffness by diameter enlargement of the stack without the need of increase of the operated ceramic volume (e.g. for long-stroke elements). Ring actuators provide further a fairly high cooling performance due to possible access of the inner and outer surface by cooling media.
- Cased stacks with internal preload mechanism (Fig. 93): The incorporation of piezo stacks into a metallic casing generally improves reliability and stability against mechanical impact and deteriorating environmental influences. The implementation of a preload mechanism compensates for tensile stress. In contrast, ceramics are extremely vulnerable to such impacts.

Actuator characterization

Like any other electrical actuator, piezo actuators convert electrical energy into motion and force, respectively, depending on the actuator stroke constraints. The generated motion or force is coupled to an external device (Fig. 94). In the simplest case, this device shall be shifted from the actual position to the desired one. More complex applications may be, e.g., position control of valves or controlled piezo mechanical elements incorporated in smart structures. In all these cases the interaction between the actuator and the driven mechanism must be analyzed. The mechanical interaction is defined by the stiffness values of both systems, namely of the piezo actuator and of the actuated mechanical system.

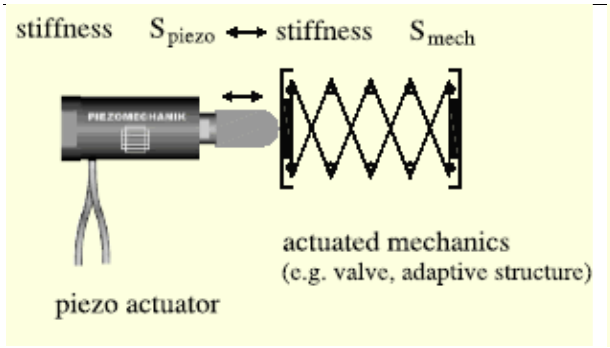

Fig. 94: Schematic of a piezo actuated system (http://www.piezomechanik.com/).

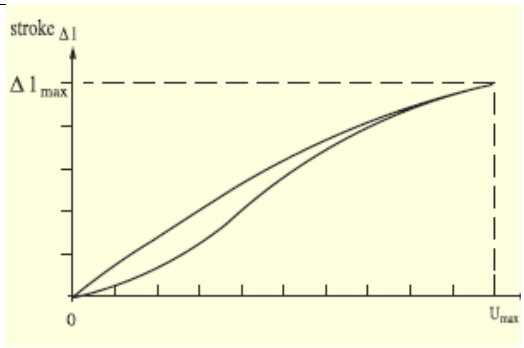

Fig. 95: Schematic voltage/stroke diagram of a stack actuator (http://www.piezomechanik.com/).

Two basic experiments are carried out in order to determine the actuator characteristics:

- actuator stroke generation as a function of the applied voltage (Fig. 95), and
- actuator force generation as a function of the applied voltage (Fig. 96).

The condition for determination of the stroke voltage relation is that the stiffness of the actuated mechanical system is zero or in other words that the piezo actuator displacement is not constraint. Then, the piezo actuator generates maximum stroke and minimum force.

The necessary condition for determination of the maximum actuator force, also called “blocking” force, is infinite large stiffness of the actuated mechanical system or zero piezo actuator displacement, respectively. The force response shows remarkably lower hysteresis than the stroke response. It must be noted that the hysteresis depends on preload conditions.

In practice, piezo actuators interact always with mechanical systems showing an intermediate stiffness value between the two theoretical limits 0 and ∞. Then, the piezo actuator distributes the electrical energy partially into generation of stroke and partially into generation of force (Fig. 97). The ratio between stroke and force generation depends on the quantitative relation of piezo actuator stiffness and mechanical system stiffness. The achievable force-stroke relations of a real system can be derived in the following way:

1. Draw a line from maximum stroke to maximum blocking force.
2. Draw a line from origin with a slope according the stiffness of the coupled mechanical system.
3. The intersection point A of these two lines describes the achievable stroke and force at maximum voltage of the piezo actuator. Notice that the schematic depicted in Fig. 97 represents a linearized actuator response. It does not take into account stroke enhancement effects.

If the stiffness values of the piezo actuator and of the coupled mechanical system are equal, the achievable displacement is 50% of its maximum value and the achievable force variation is 50% of the blocking force. Under this condition, the mechanical energy transfer efficiency from the piezo actuator to the mechanical system is maximized.

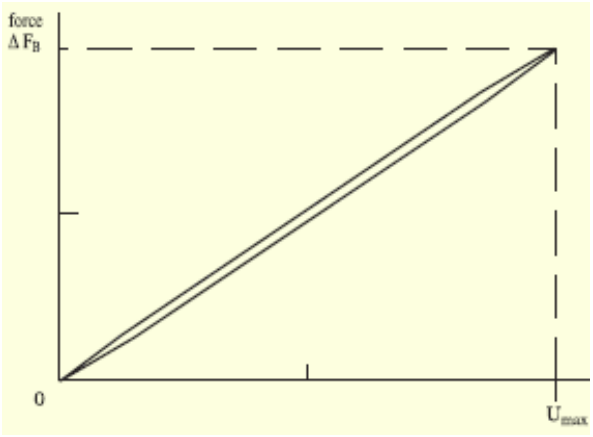

Fig. 96: Schematic voltage force relation of a piezo stack (http://www.piezomechanik.com/).

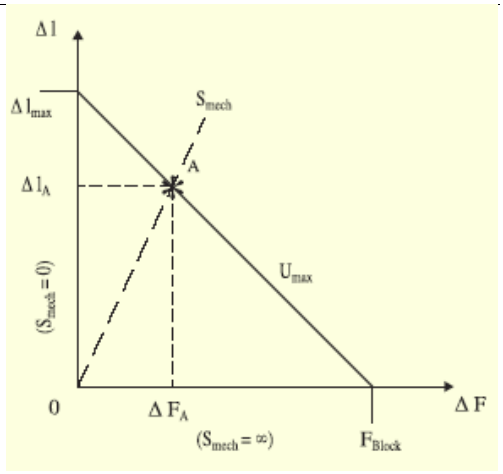

Fig. 97: Maximum piezo actuator stroke versus maximum (blocking) piezo actuator force (http://www.piezomechanik.com/).

Piezo actuators convert electrical energy into a mechanical energy, often called piezo mechanical response. The electrical energy content W of an electrically charged piezo actuator is

$$W = \frac{C \cdot U^2}{2} \tag{1}$$

where C is the actuator capacitance and U the applied voltage. The piezo mechanical response parameters are:

- stroke generation Δl,
- force generation ΔF, and
- mechanical energy $W = \Delta l \cdot \Delta F$.

Control of piezo actuators

The user of an actuator is mainly interested in the displacement of the actuator and, perhaps, in the ultra fine positioning capability down to the sub nano meter range. A variation of force or generation of mechanical energy during the action of the piezo actuator is not of high priority. However, piezo actuators then do not operate energy efficient because only a small part of the actuator energy content is needed to be transferred to the coupled mechanics.

Optimizing piezo actuators for dynamic positioning purposes means minimizing the electrical energy input for given desired displacement. This is equivalent with minimum actuator capacitance in relation to the driving voltage. Then, the electrical power requirements for a distinct dynamic response, e.g., oscillating arrangements, are minimal. Consequently, a PZT material with low dielectric constant ε together with a high piezoelectric constant d33 is required.

Position control of piezo actuators is the classical control target. However, in the case of smart structures of high stiffness, which shall be highly deformed by integrated piezo actuators, large displacements together with high force generation to achieve high mechanical energy transfer are required. Examples are adaptive frame struc-

tures of machines, car bodies, wings of air planes for active vibration excitation and cancellation or shape optimization (Caruso et al. (2003), Herold et al. (2004), Ma (2002), Raja (2002), Sadri et al. (2002)). To provide this large mechanical energy output, an increased electrical energy input is required via a reasonable large electrical capacitance of the actuator to get a high mechanical energy density within the ceramics. Therefore, PZT materials are requested showing an elevated dielectric constant ε combined with a very high strain and force generation rate. Notice that materials with large dielectric constant ε are widely offered but often do not show the wanted large piezo mechanical response.

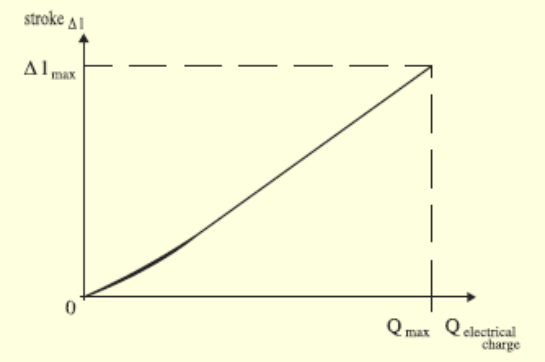

Fig. 98: Approximately linear relation between stroke and charge content of piezo actuators (http://www.piezomechanik.com/).

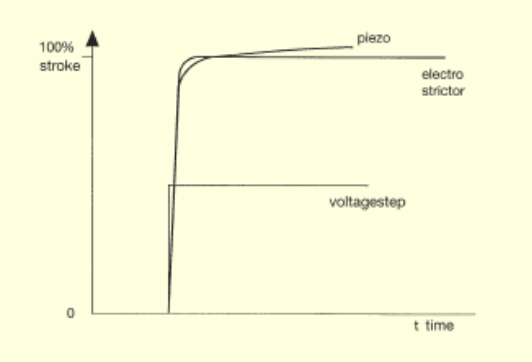

Fig. 99: Creep of piezo actuators (http://www.piezomechanik.com/).

According the simple capacitance equation

$$Q = U \cdot C \tag{2}$$

the voltage U at capacitor's contacts is proportional to the stored electrical charge content Q. For commercially available capacitors, the capacitance C is constant. Piezo actuators represent also electrical capacitors. In contrast to normal capacitors, the capacitance of piezo actuators is not constant but depends to some extent on driving conditions like voltage, load, temperature etc. Therefore, the position, velocity, and acceleration of piezo actuator do not depend linearly on the applied voltage U (Fig. 95). However, position, velocity, and acceleration are proportional to the charge content Q (Fig. 98). Consequently, if the nonlinear relation between voltage and displacement shall not be compensated, piezo actuators should be "charge"-controlled (Preumont (2002)). Summarizing, the controlled variables of the piezo actuator are:

- position, which is proportional to the electrical charge content

$$x \propto Q \tag{3}$$

- velocity, which is proportional to time derivative of the electrical charge content

$$dQ / dt = I \tag{4}$$

thus the velocity is proportional to current:

$$\dot{x} \propto I \tag{5}$$

- acceleration, which is proportional to the second time derivative of the electrical charge content ($d^2Q/dt^2 = dI/dt$), thus the acceleration is proportional to the change of current ($\ddot{x} \propto \dot{I}$).

As explained above, "charge"-control of piezo actuators within an open loop system since sensors are not needed results in linear position control. Besides this very important issue, charge control leads also to the following benefits:

- increase of actuator stiffness, and
- increasing actuator's reliability under very high dynamic operating conditions.

The slight nonlinear relation between stroke and charge shown in Fig. 98 may be compensated by the inverse function of that relation. The most important point is that hysteresis does almost not exist (approximately 1%) as in the case of voltage control (Fig. 95). The main advantage of linearization via the charge philosophy is the pure mode excitation. A sinusoidal electrical current will be converted into a sinusoidal oscillation of the piezo actuator velocity without any modulations due as it is the case for voltage controlled stroke due to nonlinearities and hysteresis.

Piezo actuators show small positive drift in expansion over a distinct time when a voltage step is applied (Fig. 99). This is called creep of piezo actuators. It is based on a "ferroelectric" effect, where the polarization state of the ceramic alters as long as an electrical charge flows that is delivered by the voltage supply. Hence, creep may be immediately stopped, when the charge content of piezo actuators is kept constant.

Sensing using piezo actuators is also possible (Law et al. (2003)). Then, the displacement of the connected mechanical system produces a charge and therefore a voltage within the piezo actuator.

References

Caruso, G., Galeani, S., and Menini, L. (2003), "Active Vibration Control of an Elastic Plate Using Piezoelectric Sensors and Actuators", *Journal of Simulation Modelling Practice and Theory*, 11(5-6), 403-419.

Herold, S., Mayer, D., and Hanselka, H. (2004), "Transient Simulation of Adaptive Structures", *Journal of Intelligent Material Systems and Structures*, 15(3), 215-224.

Law, W. W., Liao, W.-H., and Huang, J. (2003), "Vibration control of structures with self-sensing piezoelectric actuators incorporating adaptive mechanisms", *Journal of Smart Materials and Structures*, 12(5), 720-730.

Ma, K. (2002), "Vibration control of smart structures with bonded PZT patches: novel adaptive filtering algorithm and hybrid control scheme", *Journal of Smart Materials and Structures*, 12(3), 473-482.

Preumont, A. (2002), *Vibration Control of Active Structures*, Chapter 3, Kluwer Academic Publishers, Dordrecht.

Raja, S., Prathap, G., and Sinha, P. K. (2002), "Active vibration control of composite sandwich beams with piezoelectric extension-bending and shear actuators", *Journal of Smart Materials and Structures*, 11(6), 63-71.

Sadri, A. M., Wright, J. R., and Wynne, R. J. (2002), "LQG control design for panel flutter suppression using piezoelectric actuators", *Journal of Smart Materials and Structures*, 11(6), 834-839.

http://de.wikipedia.org/wiki/Piezo

http://www.efunda.com/Materials/piezo/general_info/gen_info_index.cfm

http://www.marco.de/pb.html

http://www.physikinstrumente.com/tutorial/index.html

http://www.piezo.com/ (PIEZO SYSTEMS, INC., MA 02139 USA)

http://www.piezo-kinetics.com/ (Piezo Kinetics, Inc. Bellefonte, PA 16823, USA)

http://www.piezomechanik.com/ (Piezomechanik GmbH, D-81673 Munich, Germany)

Notations

Symbol	*Description*	*Unit*
C	capacitance	F
F	force	N
I	electrical current	A
Q	charge	C
U	voltage	V
W	work, energy	J
l	stroke, displacement	m
t	time	s
x	displacement	m
Δ	difference	-
ε	dielectric constant	-

2.2 Control algorithms

The three basic control strategies, such as feedback, feed forward, and passive control are described in the first subchapter. The following subchapters present different control approaches often used in the field of structural control. Active damping using the Root Locus method is documented in the second subchapter. It is extended with a short introduction into PID control. The third subchapter describes the approach of optimal control. This chapter also introduces the state space representation. The fourth subchapter summarizes other linear control approaches often used in the field of structural control.

2.2.1 Control strategies

Basically, there exist three ways how to control actuators connected to dynamic systems:

- feedback control,
- feed forward control, and
- passive control.

Within the following subchapters, these three control strategies are explained. In the case of structural control, controlled actuators may also be controllable damping devices since the main target of structural control in the field of civil engineering is damping increase. Actuators and dampers will be called “control device”, the controlled dynamic systems such as tall buildings, slender bridges, long cables, and other civil structures will be called “plant”.

2.2.1.1 Feedback control

When the main disturbance w of the plant $G_P(s)$ is unknown or not measurable (Fig. 100), feedback control may be applied. The basic idea is to measure the system response y, which includes measurement noise v, then to compare the variable y to the desired value of y, the so-called reference signal r, and feed back the resulting error *e* through the controller $G_C(s)$ to the plant $G_P(s)$ (d’Azzo and Houpis (1995), Geering (1990), Preumont (2002), Soong (1990)). The controller is designed in order to minimize the error signal *e* with the constraint that the closed-loop system must not become unstable.

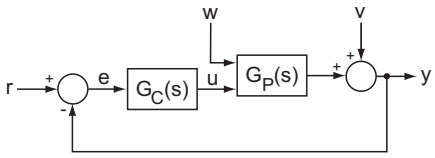

Fig. 100: Closed-loop structure of feedback control.

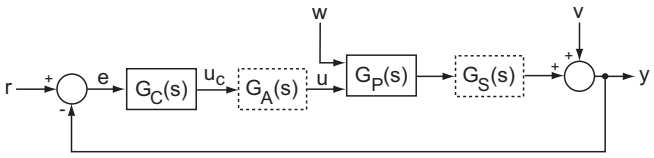

Fig. 101: Closed-loop structure of feedback control including actuator and sensor dynamics.

In reality, the closed-loop structure additionally consists of the control device dynamics and of the sensor dynamics, represented by the corresponding transfer functions $G_A(s)$ and $G_S(s)$ in Fig. 101 (Dyke and Spencer Jr. (1997), Yeo et al. (2002)). The

controller output u_C, e.g., a voltage signal, is the input signal of the actuator which eventually produces the desired control signal u, e.g., the desired force. Usually, it is assumed that both the dynamics of the control device and the dynamics of the sensor as well are much faster than the dynamics of the plant and therefore negligible for model-based controller design. However, the dynamics of the control device may limit the controller band width, especially in the case of vibration control of high frequencies. The sensors have to be chosen the way that the plant state variables of interest may be measured without any aliasing.

2.2.1.2 Feed forward control

Feed forward control can be applied when a reference signal is available, which is correlated to the disturbance acting on the plant (Fig. 102). The measured reference signal is passed to an adaptive filter $G_F(s)$ whose output signal influences the structure as a second disturbance. The criterion for the adaptation of the filter coefficients is the minimization of the measured error e, e.g., minimizing the displacement at a certain location of the structure (Ma (2002)). Thus, the basic idea of adaptive filtering is producing such an additional disturbance that the effect of the primary disturbance on the plant is compensated. However, the full compensation is only possible at sensor location.

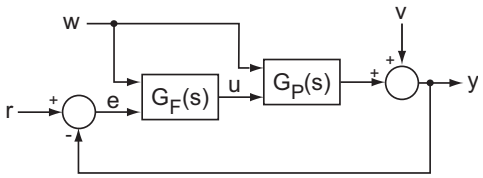

Fig. 102: Structure of feed forward control.

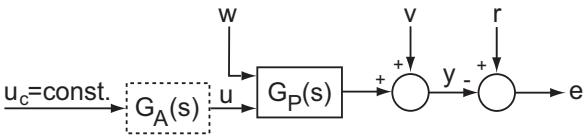

Fig. 103: Open-loop structure of passive control.

2.2.1.3 Passive control

In the field of structural control, passive control (Fig. 103) has been implemented in many cases thanks to its simplicity and robustness (Gordaninejad et al. (2002), Ko et al. (2002), Xu and Yu (1998a/b):

- Passive control does not require any PC including control soft- and hardware.
- Stability is not an issue because the loop is not closed.

Usually, the optimal value of the constant input signal u_C of the control device is determined experimentally. The criterion for the optimal value u_C is minimum error e, e.g., the minimum of the measured velocities at certain positions of the plant.

2.2.1.4 References

d'Azzo, J. J., and Houpis, C. H. (1995), *Linear Control System Analyzes and Design, Conventional and Modern*, Fouth Edition, McGraw-Hill (eds.), ISBN 0-07-016321-9.

Dyke, S. J., and Spencer Jr., B. F. (1997), "A Comparison of Semi-Active Control Strategies for the MR Damper", *Proceedings of the IASTED International Conference, Intelligent Information Systems*, The Bahamas, 8-10 December 1997, 580-584.

Geering, H. P. (1990), *Mess- und Regelungstechnik*, 2. Auflage, Springer-Verlag Berlin Heidelberg.

Gordaninejad, F., Saiidi, M., Hansen, B. C., Ericksen, E. O., and Chang, F.-K. (2002), "Magneto-Rheological Fluid Dampers for Control of Bridges", *Journal of Intelligent Material Systems and Structures*, 13(2/3), 167-180.

Ko, J. M., Zheng, G., Chen, Z. Q., and Ni, Y. Q. (2002), "Field vibration tests of bridge stay cables incorporated with magneto-rheological (MR) dampers", *Proceedings of the International Conference on Smart Structures and Materials 2002: Smart Systems of Bridges, Structures, and Highways*, S.-C. Liu and Darryll J. Pines (eds.), Proceedings of SPIE (publ.), 4696, 30-40.

Ma, K. (2002), "Vibration control of smart structures with bonded PZT patches: novel adaptive filtering algorithm and hybrid control scheme", *Journal of Smart Materials and Structures*, 12(3), 473-482.

Preumont, A. (2002), *Vibration Control of Active Structures*, Kluwer Academic Publishers, Dordrecht.

Soong, T. T. (1990), *Active structural control: theory and practice*, Cheng, W.F. (advisory editor), Longman Scientific & Technical, ISBN 0-582-01782-3.

Xu, Y. L., and Yu, Z. (1998a), "Mitigation of three dimensional vibrations of inclined sag cable using discrete oil dampers – I. formulation", *Journal of Sound and Vibration*, 214(4), 659-673.

Xu, Y. L., and Yu, Z. (1998b), "Mitigation of three dimensional vibrations of inclined sag cable using discrete oil dampers – II. application", *Journal of Sound and Vibration*, 214(4), 675-693.

Yeo, M. S., Lee, H. G., and Kim, M. C. (2002), "A Study on the Performance Estimation of Semi-active Suspension System Considering the Response Time of Electro-rheological Fluid", *Journal of Intelligent Material Systems and Structures*, 13(7/8), 485-489.

2.2.1.5 Notations

Symbol	*Description*	*Unit*
$G(s)$	transfer function	-
e	error	-
r	desired value / desired trajectory	-
s	complex frequency variable	-
u	controlled input variable of the plant	-
v	measurement noise	-
w	system noise / disturbance input variable of the plant	-
y	plant output variable	-

Subscripts	*Description*
A	actuator
C	controller

F	filter
P	plant
S	sensor

2.2.2 Active damping with collocated pairs

The following chapter describes active vibration suppression using collocated pairs of actuators and sensors (Achkire et al. (1998), d'Azzo and Houpis (1995), Preumont (2002), Soong (1990)). Actuator and sensor pairs are denoted as collocated if they are physically located at the same place and energetically conjugated, e.g., force and velocity or torque and angle. One main property of such collocated pairs is that the closed-loop structure of each pair is independent from the others. This leads to as many independent single input single output (SISO) loops as collocated pairs.

In order to explain the different control schemes of active damping, first, linear compensators will be introduced. Within this subchapter, the terms of "loop shaping", "Nyquist Diagram", "Bode Diagram", and "Root Locus" will be described (d'Azzo and Houpis (1995), Geering (1990), Preumont (2002)). Then, the different closed-loop structures using different combinations of collocated actuator sensor pairs will be presented.

2.2.2.1 Linear compensators

PID control elements

The transfer function of a parallel PID controller (Fig. 104, Fig. 105) consists of the proportional gain K_P, integral gain K_I, and derivative gain K_D (d'Azzo and Houpis (1995), Geering (1990), Preumont (2002), Soong (1990))

$$G_{PID}(s) = K_p + \frac{K_I}{s} + K_D \cdot s = K_P \cdot \left(1 + \frac{1}{T_N \cdot s} + T_V \cdot s\right) \qquad (1)$$

The proportional gain is responsible for the "basic work" of the controller. The proportional gain K_P amplifies the error e. This forces the measured plant output y to follow the desired variable r (y tracks r). The integral gain makes it possible to reach a tracking error equal to zero during steady-state conditions. The derivative gain adds damping to the closed-loop structure which makes controlled plant response fast to changes of r.

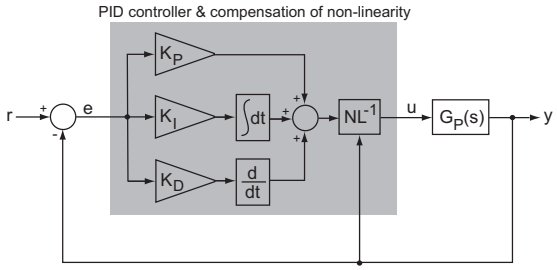

Fig. 104: Structure of parallel PID controller with inverse plant model NL^{-1}.

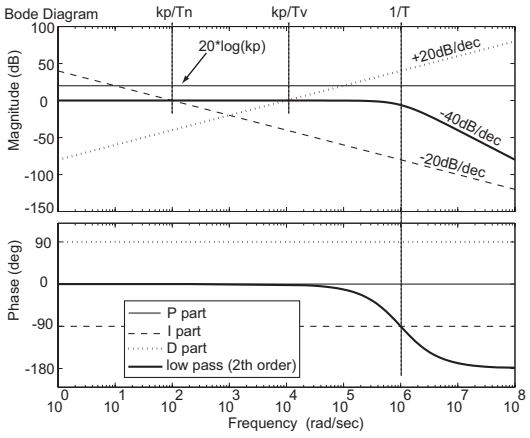

Fig. 105: Bode diagram of P, I, D elements, and of low pass filter of 2nd order.

However, large values of K_D may lead to unstable closed-loop behaviour.

Since PID control assumes a linear behaviour of the plant, the main non-linearity (NL) between u and y must be compensated within the control algorithm by an inverse model of the nonlinearity (NL^{-1}). Besides non-linearities of the plant itself, the nonlinear relation between actuator input (voltage, current) and actuator output (force, strain, displacement,…) has to be considered as well. In order to suppress measurement noise, a low pass filter of order n is added in series to the PID controller. The low pass filter is responsible for the so called "roll-off" behaviour of the controller, which suppresses measurement and system noise (Fig. 106). A first order filter produces -10 dB/dec "roll-off", which is not seen as sufficient for measurement and system noise suppression. Usually, filters of 2nd order (-20 dB/dec) or higher are applied.

$$G_{PID-rf}(s) = \left\{ K_P \cdot \left(1 + \frac{1}{T_N \cdot s} + T_V \cdot s \right) \right\} \cdot \frac{1}{(T \cdot s + 1)^n} \qquad (n \geq 1) \tag{2}$$

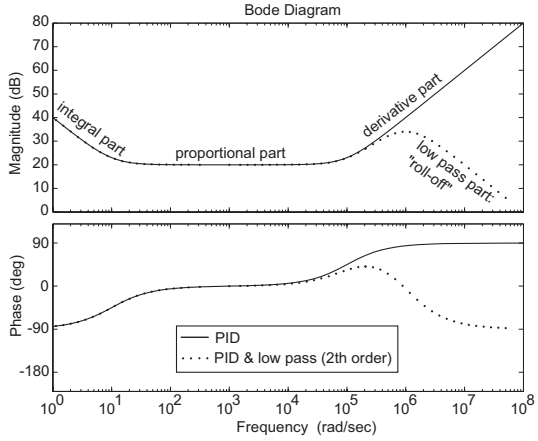

Fig. 106: Bode diagram of a parallel PID controller with low pass filter of 2nd order for a good "roll-off".

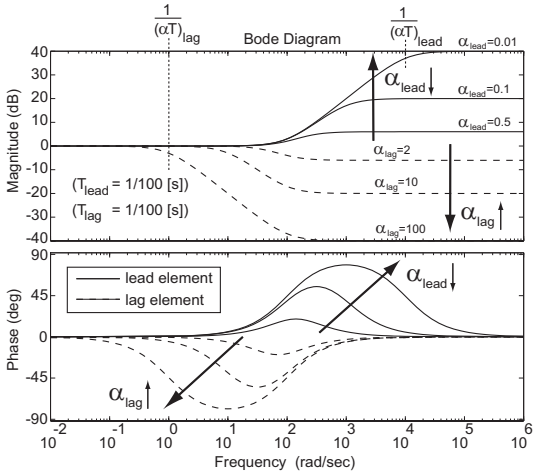

Fig. 107: Characteristics of Lead and Lag elements shown in the Bode Diagram.

Lead / Lag element

The Lead and Lag elements allow for adjusting the transfer function of the controller in the frequency domain (d'Azzo and Houpis (1995), Preumont (2002)). Since these elements change the shape of the transfer function in the "Nyquist Diagram", where the transfer function is a trajectory in the real-imaginary-plane and therefore appears as a line or "loop", this procedure is called "loop shaping". The Lead element may increase the phase margin, whereas the Lag element may increase the gain margin (Fig. 107).

$$G_{Lead}(s) = \frac{T \cdot s + 1}{\alpha \cdot T \cdot s + 1} \qquad : \alpha < 1 \tag{3}$$

$$G_{Lag}(s) = \frac{T \cdot s + 1}{\alpha \cdot T \cdot s + 1} \qquad : \alpha > 1 \tag{4}$$

Controller tuning

Besides the trial and error method for tuning the parameters of PID controllers, the most common way of model-based controller parameter design is presented here (Geering (1990)):

1. Given the transfer function of the plant together with a single P controller, the value of K_P may be determined where the closed-loop structure just becomes unstable. This value of K_P is called K_{P-crit} Then, the real parts of the closed-loop poles are zero. The imaginary parts of the closed-loop poles are identical to the critical frequency in radiant per second ($\rightarrow T_{crit}$). For higher values of K_P, the real parts of the closed-loop poles get positive and the closed-loop structure becomes unstable.

$$K_{P-crit}\,,\; T_{crit} = 2\pi/\omega_{crit} \qquad (5),\ (6)$$

2. Based on the values of K_{P-crit} and T_{crit}, the PID controller parameters may be tuned according to *Ziegler/Nichols*:

P controller: $$K_p = 0.5 \cdot K_{P-crit} \qquad (7)$$

PI controller: $$K_p = 0.45 \cdot K_{P-crit}\,, T_N = 0.85 \cdot T_{crit} \qquad (8),\ (9)$$

PID controller: $$K_p = 0.6 \cdot K_{P-criti}\,, T_N = 0.5 \cdot T_{criti}\,, T_V = 0.12 \cdot T_{crit}$$

(10)-(12)

Please notice that the determination of K_{P-crit} requires a model of the plant. For this reason, the controller design may be called model-based.

Root Locus method

In the following, the determination of the values of K_{P-crit} and T_{crit} shall be demonstrated. It is assumed that the plant has the only real poles -1, -2, and -3 (Fig. 108, Geering (1990)). The transfer function of the closed-loop system with the P controller only and negative unity feedback becomes

$$G_{cl}(s) = \frac{Y(s)}{U(s)} = \frac{G_C(s) \cdot G_P(s)}{1 + G_C(s) \cdot G_P(s)} = \frac{K_P}{s^3 + 6s^2 + 11s + (6 + K_P)}$$

(13)

The poles of G_C are the zeros of the denominator of G_{cl}. The poles of the closed-loop system are plotted in the real-imaginary-plane (Nyquist Diagram) with parameter K_P (Fig. 109). The resulting line or trajectory is called “Root Locus” of the closed-loop. For increasing values of K_P, the closed-loop inclines more and more to vibrate. For real parts of the closed-loop poles equal to zero, the closed-loop system does not have any damping. Then, the closed-loop system is on the border of instability. For the example presented, the critical values are:

$$K_{P-crit} = 60\,[-]\ ,\ \ T_{crit} = 2\pi/\sqrt{11}\,[s] \qquad (14), (15)$$

If K_P is further increased, the closed-loop system gets unstable or the damping of the closed-loop system becomes “negative”, respectively.

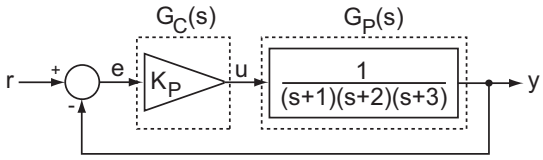

Fig. 108: Plant of 3rd order with proportional gain only.

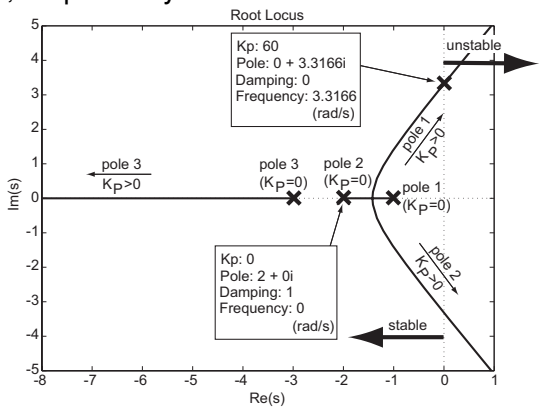

Fig. 109: Root Locus of 3rd order plant with feedback proportional gain K_P only.

2.2.2.2 Active damping with collocated actuator sensor pairs

Main idea

The equation of motion of a system excited by the disturbance force w and controlled by the force f is

$$\mathbf{M}\ddot{\mathbf{z}} + \mathbf{C}\dot{\mathbf{z}} + \mathbf{K}\,\mathbf{z} = \mathbf{w} + \mathbf{f} \qquad (16)$$

When the control target is increasing the damping of the plant, then the control force f must be proportional to the structural velocity at actuator location in order to increase apparently the plants damping

$$\mathbf{M}\ddot{\mathbf{z}} + \left(\mathbf{C}\dot{\mathbf{z}} - \mathbf{f}\right) + \mathbf{K}\,\mathbf{z} = \mathbf{w} \quad \Rightarrow \quad \mathbf{f} \sim -\dot{\mathbf{z}} \qquad (17), (18)$$

This leads to a control force, which acts like an external viscous damper. The collocated sensor may be, e.g., a velocity sensor. The matrix notation of the equations above points out that the damping of the closed-loop structure may be increased using numbers of collocated actuator sensor pairs (Fig. 110). Then, a decentralized controller may be realized by a proportional negative feedback

$$\mathbf{f} = -1 \cdot [g_1 \quad g_2 \quad \ldots \quad g_n]^T \cdot [\dot{z}_1 \quad \dot{z}_2 \quad \ldots \quad \dot{z}_n]^T \qquad (19)$$

The controller is called decentralized because every sensor builds a closed-loop only with its collocated actuator. Due to the positive definite values of g_i (similar to P element), this control law (negative feedback) guarantees power dissipation.

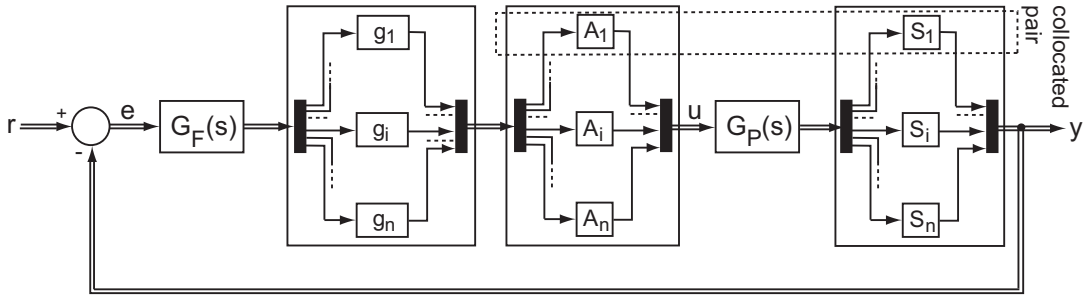

Fig. 110: Closed-loop structure of direct velocity feedback for collocated actuator sensor pairs.

The locations of the velocity sensors must be chosen the way that the vibration velocity of the mode of interest is not zero. If this is the case, the collocated actuator sensor pair is located at the structure where the mode of interest has a nodal point. In order to guarantee a proper working behaviour of the proportional controller, a low pass filter should be added, which attenuates the measurement noise. The resulting closed-loop structure is called direct velocity feedback (DVF, Nakamura et al. (2002), Preumont (2002), Subramanian (2002)).

Tuning the feedback gain for maximum additional damping

Given the four mass system depicted in Fig. 111 with identical values for mass, stiffness, and damping elements, the equation of motion with the external control forces f_i becomes

$$\begin{bmatrix} m & 0 & 0 & 0 \\ 0 & m & 0 & 0 \\ 0 & 0 & m & 0 \\ 0 & 0 & 0 & m \end{bmatrix} \cdot \begin{bmatrix} \ddot{z}_1 \\ \ddot{z}_2 \\ \ddot{z}_3 \\ \ddot{z}_4 \end{bmatrix} + \begin{bmatrix} 2c & -c & 0 & 0 \\ -c & 2c & -c & 0 \\ 0 & -c & 2c & -c \\ 0 & 0 & -c & 2c \end{bmatrix} \cdot \begin{bmatrix} \dot{z}_1 \\ \dot{z}_2 \\ \dot{z}_3 \\ \dot{z}_4 \end{bmatrix} + \begin{bmatrix} 2k & -k & 0 & 0 \\ -k & 2k & -k & 0 \\ 0 & -k & 2k & -k \\ 0 & 0 & -k & 2k \end{bmatrix} \cdot \begin{bmatrix} z_1 \\ z_2 \\ z_3 \\ z_4 \end{bmatrix} = \begin{bmatrix} f_1 \\ f_2 \\ f_3 \\ f_4 \end{bmatrix} \tag{20}$$

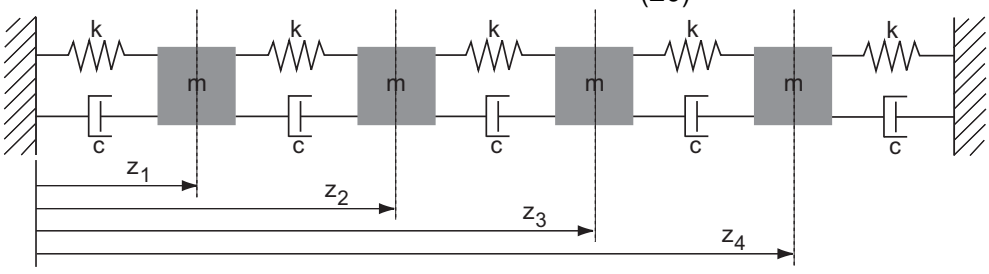

Fig. 111: Four mass system.

For the following investigation, one force actuator and one velocity sensor at the first mass are assumed. Then, as seen in the previous chapter, negative feedback with proportional gain K_P is able to damp structural vibrations. The measurement equation becomes

$$y = [0 \quad 0 \quad 0 \quad 0 \quad 1 \quad 0 \quad 0 \quad 0] \cdot [z_1 \quad z_2 \quad z_3 \quad z_4 \quad \dot{z}_1 \quad \dot{z}_2 \quad \dot{z}_3 \quad \dot{z}_4]^T \tag{21}$$

Due to the low structural damping and the collocation, the transfer function shows the alternating resonance/anti-resonance pattern (Fig. 112, Preumont (2002)). The resonances are the poles of the plant, where the velocity $\dot{z}_1$ (output) is infinite large for the external force f_1 (input) near to zero. The anti-resonances are the plant's zeros, where the velocity $\dot{z}_1$ becomes zero for any external force. The alternating pole/zero pattern is also visible in the real-imaginary plane (Fig. 113 and Fig. 115).

The control target shall be maximum damping of the structural mode with the lowest frequency, because this mode usually produces the largest displacement (the modes in Fig. 113 are numbered with increasing frequency). The goal is to find the optimum feedback gain g for maximum additional damping. Obviously, there exist two cases for g that cannot be optimal:

- $g = 0$: The feedback gain is zero. Hence, the closed-loop system behaves like the open-loop system. Then, the pole of the open-loop system is identical with the pole of the closed-loop system (Fig. 113).
- $g = \infty$: The feedback gain is infinite large. Then, the control force is also infinite large, which results in a nodal point of the structure at actuator position. The actuator force behaves like a completely stiff bearing. The closed-loop pole is identical with the open-loop zero due to vanishing velocity and displacement, respectively, at actuator position (Fig. 113).

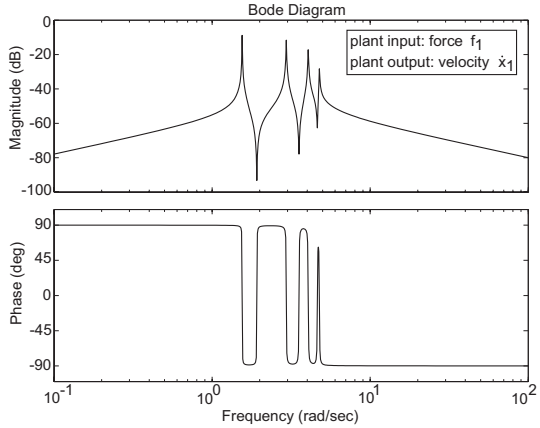

Fig. 112: Transfer function of four mass system with force input and velocity output at mass no.1.

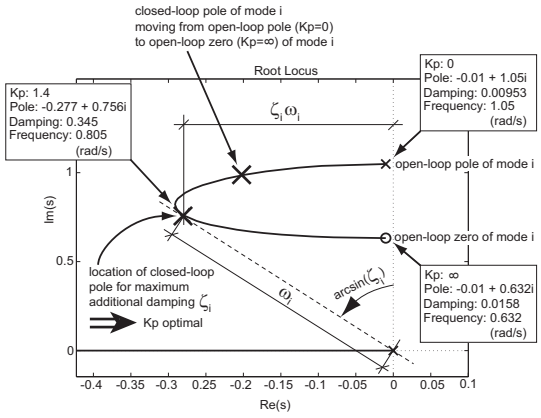

Fig. 113: Placement of closed-loop pole for maximum additional damping of mode 1 (direct velocity feedback).

As explained in the preceding chapter, the root locus is the trajectory of all closed-loop poles for g increasing from zero to infinity. Considering the following characteristics of the closed-loop pole

$$-real(pole_{cl-i}) = \zeta_i \omega_i \quad , \qquad |pole_{cl-i}| = \omega_i \tag{22), (23}$$

the closed-loop structure with maximum additional damping shows its pole on the root locus where the angle between real and imaginary parts reaches its maximum (Preumont (2002))

$$maximum\ damping\ of\ mode\ i:\ \zeta_{i-max} \Leftrightarrow \max\left\{\frac{-real\left(pole_{cl-i}\right)}{\omega_i}\right\} \tag{24}$$

This fact also points out that large damping may only be achieved for trajectories going far into the left half plane in the Nyquist Diagram. This is only possible for poles and zeros being well separated. The transfer function of the plant with optimally damped mode 1 is shown in the Bode Diagram depicted in Fig. 114. The resulting pole locations of all four structural modes are depicted in Fig. 115. This figure clearly demonstrates that single actuator sensor pairs may only damp one mode optimally.

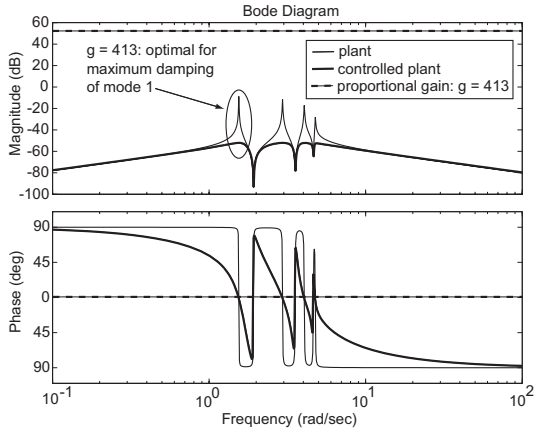

Fig. 114: Comparison between very low damped plant and plant with optimally damped mode 1.

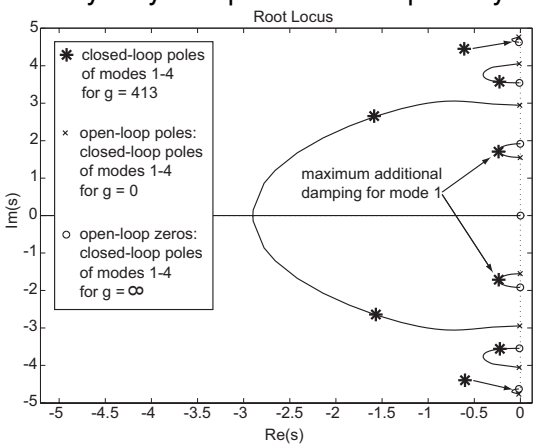

Fig. 115: Location of closed-loop poles of all four modes for maximum damping of mode 1.

Active damping with force actuators

As seen in the example of direct velocity feedback, the idea is to feed the force actuator with a signal being proportional to the actual vibration velocity at actuator position. Negative feedback guarantees energy dissipation and thus stability of the control loop. Basically, there are three ways how to measure the actual vibration velocity. These three possibilities are described in the following.

a) Displacement measurement

Notice that measuring displacements requires the differentiation of these signals in real time in order to get the actual velocities (Gandhi and Munsky (2002)). Due to the transfer function of derivative elements, measurement noise will be amplified. Therefore, when displacement sensors are used for active damping, the derivative element must be extended by a low pass filter of nth order (G_F) for a sufficient good “roll-off” behaviour of the closed loop system

$$G_C(s) = \underbrace{g \cdot s}_{\substack{\text{active damping} \\ \text{with displacement} \\ \text{sensor}}} \cdot \underbrace{\frac{\omega_{rf}^n}{\left(s+\omega_{rf}\right)^n}}_{G_F} \tag{25}$$

The filter order should be at least three ($n = 3$) in order to produce at least a "roll-off" of -40 dB/dec (d'Azzo and Houpis (1995), Preumont (2002)). The filter corner frequency is the frequency above which the signal parts are cut off. The filter is designed the way that the steady-state amplification is one ($G_F(s=0)=1$).

b) Velocity measurement

Although the signal does not have to be differentiated, again, it is recommended to add a low pass filter to the proportional gain for measurement noise suppression. The filter should be of 2nd order or higher in order to produce -40dB/dec or more.

$$G_C(s) = \underbrace{g}_{\substack{\text{active damping} \\ \text{with velocity} \\ \text{sensor}}} \cdot \underbrace{\frac{\omega_{rf}^n}{\left(s+\omega_{rf}\right)^n}}_{G_F} \tag{26}$$

c) Acceleration measurement

Measuring the acceleration requires the integration of the signal in real time. The integration helps already to suppress measurement noise, but only with a "roll-off" of -20 dB/dec

$$G_C(s) = \underbrace{g \cdot \frac{1}{s}}_{\substack{\text{active damping} \\ \text{with accelerometer}}} \tag{27}$$

In order to reach a "roll-off" behaviour of -40 dB/dec, a low pass filter of first order may be added. It may help not destabilizing modes of high frequencies. The first order low pass filter together with the integration of the acceleration signal gives the form of a 2nd order filter

$$G_C(s) = g \cdot \underbrace{\frac{1}{s^2 + 2\zeta_F \omega_F s + \omega_F^2}}_{\frac{1}{s} \cdot G_F} \tag{28}$$

The tuning parameters of the second order filter, the filter frequency and the filter damping ratio, allow for tuning the filter precisely to the mode of the plant to be damped. According to Preumont (2002), the rule of thumb for the filter tuning becomes (index F for filter, index P for plant, index i for mode number):

$$\omega_{F-i} \text{ close to } \omega_{P-i} \quad \left(\omega_{F-i} > \omega_{F-i}\right) \tag{29}$$

$$\zeta_F = 0.5 \ldots 0.7 \quad \left(\zeta_F \uparrow \Rightarrow \text{increase of damping ratio}\right) \tag{30}$$

By designing several second order filters, several structural modes may be damped. Here, the usual procedure is to determine the gains g_i by experiment, starting with the filter design for the mode with highest frequency. These n filters targeted to damp n structural modes do not necessarily need n actuator sensor pairs. The number of actuator sensor pairs may be smaller than n.

Active damping with strain actuators

Strain actuators may work in two principle ways:

i) If piezo elements deform freely, they produce a voltage signal (output) that is proportional to the deformation of the piezo element.

ii) If piezo elements are, e.g., glued to the structure surface, their deformation is not free. Then, they apply a strain to the structure which is proportional to the input voltage signal.

As a consequence of these two different working principles, either the displacement of the structure or the force generated by the piezo element is measured.

a) Displacement measurement

The output signal of the piezo element which acts as a strain sensor is proportional to displacements. Then, active vibration mitigation is feasible by producing a stress being proportional to the displacement if the entire feedback loop is positive (Preumont (2002))

$$G_C(s) = \underbrace{-g}_{\substack{\text{active damping} \\ \text{with strain sensor}}} \cdot \underbrace{\frac{1}{s^2 + 2\zeta_F \omega_F s + \omega_F^n}}_{G_F} \tag{31}$$

That is why this active control scheme is called Positive Position Feedback (PPF). For a sufficient “roll-off”, a second order filter should be designed similarly to the filter design for DVF using accelerometers.

b) Force measurement

In the case of force measurements, piezo elements are collocated with force transducers. If the force applied to the structure is measured, the measurement signal must be integrated and fed back in a positive feedback loop in order to produce a root locus being stable for all proportional gains. This active control scheme is called Positive Force Feedback (PFF). In order to avoid the problem of saturation for integral gains, the forgetting factor ε should be introduced, which moves the controller pole from the origin slightly to the negative real axis

$$G_C(s) = \underbrace{-g \cdot \frac{1}{s+\varepsilon}}_{\substack{\text{active damping} \\ \text{with force sensor} \\ (\text{including forgetting factor})}} \cdot G_F \tag{32}$$

2.2.2.3 References

Achkire, Y., Bossens, F., and Preumont, A. (1998), “Active damping and flutter control of cable-stayed bridges”, *Journal of Wind Engineering and Industrial Aerodynamics*, 74-76, 913-921.

d’Azzo, J. J., and Houpis, C. H. (1995), *Linear Control System Analyzes and Design, Conventional and Modern*, Fouth Edition, McGraw-Hill (eds.), ISBN 0-07-016321-9.

Gandhi, F., and Munsky, B. (2002), “Comparison of Damping Augmentation Mechanisms with Position and Velocity Feedback in Active Constrained Layer Treatments”, *Journal of Intelligent Material Systems and Structures*, 13(5), 317-326.

Geering, H. P. (1990), *Mess- und Regelungstechnik*, 2. Auflage, Springer-Verlag Berlin Heidelberg.

Nakamura, T., Saga, N., and Nakazawa, M. (2002), “Impedance Control of a Single Shaft-type Clutch Using Homogeneous Electrorheological Fluid”, *Journal of Intelligent Material Systems and Structures*, 13(7/8), 465-469.

Preumont, A. (2002), *Vibration Control of Active Structures*, Kluwer Academic Publishers, Dordrecht.

Soong, T. T. (1990), *Active structural control: theory and practice*, Cheng, W.F. (advisory editor), Longman Scientific & Technical, ISBN 0-582-01782-3.

Subramanian, P. (2002), “Vibration suppression of symmetric laminated composite beams”, *Journal of Smart Materials and Structures*, 11(6), 880-885.

2.2.2.4 Notations

Symbol	*Description*	*Unit*
$G(s)$	transfer function	-
K	feedback gain	-
$\mathbf{M, C, K}$	mass, damping, stiffness matrices	-
T	time constant	s
e	error	-
f	force	N
g	feedback gain	-
m, c, k	mass, viscosity, stiffness	kg, kg/s, kg/s^2
n	order	-
s	complex frequency variable	-
t	time	s
u	controlled input variable of the plant	-
v, w	measurement noise, disturbance	-
y	plant output variable	-
$z, \dot{z}, \ddot{z}$	displacement, velocity, acceleration	m, m/s, m/s^2

α	tuning factors for Lead / Lag elements	-
ε	forgetting factor	-
ω	circular frequency	rad/s
ζ	damping ratio	-

Superscripts	*Description*
T	transposed

Subscripts	*Description*
C	controller
D	derivative
F	filter
I	integral
P	plant, proportional
cl	closed-loop
$crit$	critical
f	filter
i	mode number
n	number of collocated actuator sensor pairs
rf	roll-off

2.2.3 Optimal control

Optimal controllers are state-feedback controllers which try to equalize the states to zero. The states are the state variables of the plant model that is represented in the so-called state space form. Hence, first, the state space representation of linear dynamic systems will be introduced. Then, the optimal control approaches such as Linear Quadratic Regulator (LQR) and Linear Quadratic Gaussian noise control algorithm (LQG) will be described.

2.2.3.1 State space representation

The representation of any dynamic system in state space representation shall be explained on behalf of a single degree of freedom system (SDFS) subjected to the external control force f and the external disturbance force w (d'Azzo and Houpis (1995), Geering (1990)). The differential equation of the SDFS becomes

$$m\ddot{z} + c\dot{z} + kz = f + w \tag{1}$$

The following substitutions

$$\omega_0 = \sqrt{\frac{k}{m}}\,,\ \zeta = \frac{c}{2\sqrt{mk}}\,,\ u = f \tag{2)-(4}$$

yield to the differential equation of a SDFS with resonance circular frequency ω_0 of the undamped SDFS and damping ratio ζ

$$\ddot{z} + 2\zeta\omega_0\dot{z} + \omega_0^2 z = \frac{u}{m} \tag{5}$$

By introducing the state variables

$$\begin{bmatrix} x_1 \\ x_2 \end{bmatrix} = \begin{bmatrix} z \\ \dot{z} \end{bmatrix} \tag{6}$$

the second order differential equation may be rewritten in state space representation (SSR) including only first order differential equations

$$\begin{bmatrix} \dot{x}_1 \\ \dot{x}_2 \end{bmatrix} = \begin{bmatrix} 0 & 1 \\ -\omega_0^2 & -2\zeta\omega_0 \end{bmatrix} \cdot \begin{bmatrix} x_1 \\ x_2 \end{bmatrix} + \begin{bmatrix} 0 \\ 1/m \end{bmatrix} \cdot u + \begin{bmatrix} 0 \\ 1/m \end{bmatrix} \cdot w \tag{7}$$

In order to measure the vibration state of this SDFS, the following possibilities exist:

- Measuring the displacement (x_1).
- Measuring the velocity (x_2).
- Measuring the acceleration ($\dot{x}_2$).

According to the sensor type, the measurement equation including measurement noise v looks as follows

$$y = x_1 = [1 \quad 0] \cdot \mathbf{x} + [0] \cdot u + [0] \cdot w + v \tag{8}$$

$$y = x_2 = [0 \quad 1] \cdot \mathbf{x} + [0] \cdot u + [0] \cdot w + v \tag{9}$$

$$y = \dot{x}_2 = [-\omega_0^2 \quad -2\zeta\omega_0] \cdot \mathbf{x} + [1/m] \cdot u + [1/m] \cdot w + v \tag{10}$$

The SSR of a any dynamic, linear, time-invariant system with several measured output variables (MO: mixed output), one input variable (SI: single input), the unknown process/system w, and the measurement noise v becomes in matrix notation (Fig. 116)

$$\dot{\mathbf{x}} = \mathbf{A} \cdot \mathbf{x} + \mathbf{B} \cdot u + \mathbf{G} \cdot \mathbf{w} \tag{11}$$

$$\mathbf{y} = \mathbf{C} \cdot \mathbf{x} + \mathbf{D} \cdot u + \mathbf{H} \cdot \mathbf{w} + \mathbf{v} \tag{12}$$

The SSR is called time-invariant if the system matrices $\mathbf{A}$, $\mathbf{B}$, $\mathbf{C}$, $\mathbf{D}$, $\mathbf{G}$, and $\mathbf{H}$ do not vary in time. Usually, the measurement noise is assumed to be a zero mean white noise signal. A white noise process is a mathematical idealization of a stationary random process, whose elements are completely uncorrelated in time. The matrix $\mathbf{G}$ describes the local distribution of the process/system noise w. Besides modelling errors, it may include unknown, external forces and noise in the vector of the input variable. Modelling errors may result from:

- neglected nonlinearities of the plant,
- neglected very fast dynamics of the plant,
- neglected very slow dynamics of the plant, and
- neglected nonlinearities and dynamics of actuators and sensors.

2.2.3.2 Linear quadratic regulator

A full state feedback may be designed with an Optimal Linear Quadratic Regulator (LQR, d'Azzo and Houpis (1995), Geering (1990), Preumont (2002), Ribakov et al. (2003)). This feedback approach requires that all (k) state variables are known and therefore measurable. The goal in structural control often is to place the poles of the closed-loop system with LQ Regulator the way that the damping of the closed-loop structure is increased compared to the damping of the uncontrolled plant.

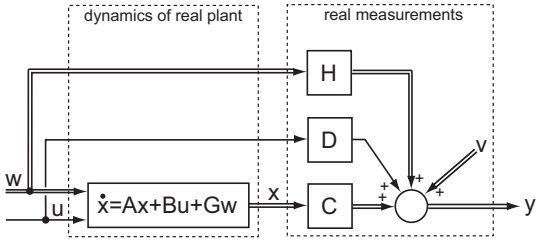

Fig. 116: State space representation of the plant.

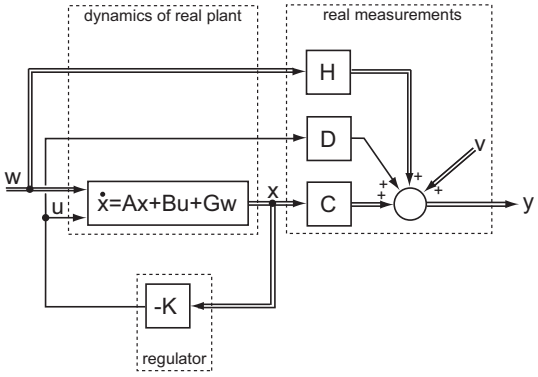

Fig. 117: Plant in SSR, all state variables measured, full state feedback with stochastic LQ Regulator.

One distinguishes between stochastic and deterministic LQ Regulators, according to the fact if an unknown disturbance w (assumed as white noise) is present or not. The stochastic LQ Regulator has to be designed for the following plant subjected to the white noise excitation w with intensity $\mathbf{W}$

$$\dot{\mathbf{x}} = \mathbf{A} \cdot \mathbf{x} + \mathbf{B} \cdot u + \mathbf{G} \cdot \mathbf{w} \quad \text{with} \quad E[\mathbf{w} \cdot \mathbf{w}^{\mathbf{T}}] = \mathbf{W}$$

(13), (14)

Then, the full state feedback

$$u = -\mathbf{K} \cdot \mathbf{x} \tag{15}$$

minimizes the performance index (cost functional in the case of deterministic LQR)

$$J = E[\mathbf{x}^{\mathbf{T}} \cdot \mathbf{Q} \cdot \mathbf{x} + u^{T} \cdot R \cdot u] \tag{16}$$

$$\mathbf{Q} = \begin{bmatrix} q_{11} & 0 & \cdots & 0 \\ 0 & q_{22} & & \vdots \\ \vdots & & \ddots & 0 \\ 0 & \cdots & 0 & q_{2j2j} \end{bmatrix}, \qquad R = 1 \tag{17), (18}$$

This example assumes one actuator, so u and R are scalar. The input weight factor R and the factors q_{ii} are design parameters of the LQ Regulator. For large values of (q_{ii}/R), the control output u will be large and consequently force the plant rapidly into its equilibrium position. Thus, the tracking error will be small for large values of (q_{ii}/R), but at the expense of large control effort. The state feedback, which is based on measurements, is not optimal due to the measurement noise v

$$\mathbf{y} = \mathbf{I} \cdot \mathbf{x} + \mathbf{v} \quad \Rightarrow \quad u = -\mathbf{K} \cdot \mathbf{x} \cong -\mathbf{K} \cdot \mathbf{y} \tag{19), (20}$$

Besides the regulator tuning parameters $\mathbf{Q}$ and R, the design of the regulator matrix $\mathbf{K}$ requires the knowledge of the system matrices $\mathbf{A}$ and $\mathbf{B}$. These matrices are based on the physical model of the real plant. Hence, they include modelling errors. In order to distinguish between the real plant behaviour and the model behaviour, the model matrices used for model-based controller design are indicated in the following with the index c

$$\mathbf{K} = f(\mathbf{A}_c, \mathbf{B}_c, \mathbf{Q}, R) \tag{21}$$

The resulting control system is a Single-Input-Mixed-Output System (SIMO, Fig. 117), however, also MIMO (mixed input, mixed output), SISO (single input, single output), and MISO (mixed input, single output) are conceivable. As mentioned above, LQR design makes it absolutely necessary knowing all state variables, but almost in all practical cases, the state variable vector is not completely known. In this case, the state variables must be reconstructed using a model of the plant (Zhang and Roschke (1999)). The procedure of full state reconstruction will be explained in the next subchapter.

2.2.3.3 Linear Quadratic Gaussian noise control

Modelling the plant

The procedure how to design a Linear Quadratic Gaussian noise control algorithm (LQG, d'Azzo and Houpis (1995), Christenson et al. (2001), Kim et al. (2003), Preumont (2002)) will be explained on behalf of a beam model. It is subjected to a white noise process w and the measured state variables include the measurement noise v. The one-dimensional finite element model (FE model) of a beam with displacement z perpendicular to the beam length and control force f becomes

$$\mathbf{M}_{fe}\ddot{\mathbf{z}} + \mathbf{C}_{fe}\dot{\mathbf{z}} + \mathbf{K}_{fe}\mathbf{z} = \mathbf{\Theta}_{fe}\mathbf{w} + \mathbf{\Lambda}_{fe} f \tag{22}$$

The SSR of this differential equation may be written with the following state variable

$$\mathbf{x} = [z_{n-1} \quad z_{n-2} \quad .... \quad z_{n-nn} \quad \dot{z}_{n-1} \quad \dot{z}_{n-2} \quad .... \quad \dot{z}_{n-nn}]^T \tag{23}$$

This state vector $\mathbf{x}$ has twice as many elements as nodal points (nn) of the FE model. For high spatial resolution, the order of the proposed SSR is fairly large (dimensions of SSR matrices large). Thus, the simulation of such an SSR would need large computing time. Moreover, vibrating modes with only a couple of nodal points per wave length may lead to "noisy" or scattering simulation results. In order to reduce simulation time and to avoid scattering effects, the original FE model may be:

a) simulated with the Newmark integration method, which adds fictitious damping to higher modes and this way helps to dampen "vibrations" or "scattering" produced by higher modes with insufficient spatial resolution, or

b) transformed from Cartesian coordinates into modal coordinates in order to truncate higher modes with insufficient spatial resolution.

Since the Newmark integration algorithm is commercially available, the second method of coordinate transformation shall be described hereafter.

The SSR in modal coordinates includes the displacements and velocities of the first mm modes of the plant and not of all nn nodal points of the original FE model. One method of transforming the FE model from Cartesian coordinates into modal coordinates is the Galerkin method (Ni et al. (2000), Raja et al. (2002))

$$z_i(r_i, t) \cong \sum_{j=1}^{mm} q_j(t) \cdot \varphi_j(r_i) \qquad (mm < nn) \tag{24}$$

The shape functions may be approximated by sinusoidal functions

$$\varphi_j(r_i) = \sin\{j \cdot \pi \cdot (r_i / L_{beam})\} \tag{25}$$

The resulting beam model in modal coordinates becomes

$$\mathbf{M}_m\ddot{\mathbf{q}} + \mathbf{C}_m\dot{\mathbf{q}} + \mathbf{K}_m\mathbf{q} = \mathbf{\Theta}_m\mathbf{w} + \mathbf{\Lambda}_m f \tag{26}$$

with the plant's matrices in modal coordinates

$$\mathbf{M}_m = \mathbf{\Phi}^T\mathbf{M}_{fe}\mathbf{\Phi}, \quad \mathbf{C}_m = \mathbf{\Phi}^T\mathbf{C}_{fe}\mathbf{\Phi}, \quad \mathbf{D}_m = \mathbf{\Phi}^T\mathbf{D}_{fe}\mathbf{\Phi}, \quad \mathbf{\Theta}_m = \mathbf{\Phi}^T\mathbf{\Theta}_{fe}, \quad \mathbf{\Lambda}_m = \mathbf{\Phi}^T\mathbf{\Lambda}_{fe} \tag{27)-(31}$$

and the transformation matrix

$$\mathbf{\Phi} = \begin{bmatrix} \varphi_1(r_1) & \cdots & \varphi_{mm}(r_1) \\ \vdots & \ddots & \vdots \\ \varphi_1(r_{nn}) & \cdots & \varphi_{mm}(r_{nn}) \end{bmatrix} \tag{32}$$

The beam model may take the first m modes into account. The according state variable vector becomes

$$\mathbf{x} = [q_{m-1} \quad q_{m-2} \quad .... \quad q_{m-mm} \quad \dot{q}_{m-1} \quad \dot{q}_{m-2} \quad .... \quad \dot{q}_{m-mm}]^T \tag{33}$$

Assuming that process noise w and measurement noise v are white noise processes with intensity matrices $\mathbf{W} \geq 0$ and $\mathbf{V} > 0$, and for the case that all nodal accelerations are measured, then the state and measurement equations for one actuator (u is scalar) become

$$\dot{\mathbf{x}} = \mathbf{A} \cdot \mathbf{x} + \mathbf{B} \cdot u + \mathbf{G} \cdot \mathbf{w} \tag{34}$$

$$\mathbf{y} = \mathbf{C} \cdot \mathbf{x} + \mathbf{D} \cdot u + \mathbf{H} \cdot \mathbf{w} + \mathbf{v} \tag{35}$$

with

$$\mathbf{A} = \begin{bmatrix} \mathbf{0} & \mathbf{I} \\ -\mathbf{M}_m^{-1}\mathbf{K}_m & -\mathbf{M}_m^{-1}\mathbf{C}_m \end{bmatrix}, \ \mathbf{B} = \begin{bmatrix} \mathbf{0} \\ \mathbf{M}_m^{-1}\mathbf{\Lambda}_m \end{bmatrix}, \ \mathbf{G} = \begin{bmatrix} \mathbf{0} \\ \mathbf{M}_m^{-1}\mathbf{\Theta}_m \end{bmatrix} \tag{36)-(38}$$

$$\mathbf{C} = [-\mathbf{\Phi}^T\mathbf{M}_m^{-1}\mathbf{C}_m \quad -\mathbf{\Phi}^T\mathbf{M}_m^{-1}\mathbf{K}_m], \qquad \mathbf{D} = [-\mathbf{\Phi}^T\mathbf{M}_m^{-1}\mathbf{\Lambda}_m], \qquad \mathbf{H} = [\mathbf{\Phi}^T\mathbf{M}_m^{-1}\mathbf{\Theta}_m] \tag{39)-(41}$$

Full state reconstruction

Since it would be too expensive or simply not feasible to measure all state variables because they are not available, the idea is to reconstruct the full state vector by a model of the plant (model matrices indicated by index c). The state reconstruction of the plant with the process and measurement noise described above is realized by the observer of the form

$$\dot{\hat{\mathbf{x}}} = \mathbf{A}_c \cdot \hat{\mathbf{x}} + \mathbf{B}_c \cdot u + \mathbf{L} \cdot \left(\mathbf{y} - \mathbf{C}_{c-red} \cdot \hat{\mathbf{x}} - \mathbf{D}_{c-red} \cdot u\right) \tag{42}$$

Here, $\mathbf{L}$ is the observer gain matrix, which is chosen the way that the difference between true state $\mathbf{x}$ and estimated state $\hat{\mathbf{x}}$ converges to zero

$$\mathbf{e} = \mathbf{x} - \hat{\mathbf{x}} \quad \rightarrow \quad 0 \tag{43}$$

If $\mathbf{L}$ is chosen the way that the error covariance matrix is minimized, the designed observer is called minimum variance observer or steady-state Kalman-Bucy Filter (KBF, Geering (1990)).

In order to design the observer gain matrix $\mathbf{L}$, model matrices must be available and the intensities of process and measurement noise must be assumed. The observer gain matrix is defined by the following input data

$$\mathbf{L} = f\left(\mathbf{A}_c, \mathbf{G}_c, \mathbf{C}_{c-red}, \mathbf{H}_{c-red}, E[\mathbf{w}\cdot\mathbf{w}^{\mathbf{T}}], E[\mathbf{v}\cdot\mathbf{v}^{\mathbf{T}}], E[\mathbf{w}\cdot\mathbf{v}^{\mathbf{T}}]\right) \tag{44}$$

Since only some of the nn nodal accelerations are measured, the system matrices $\mathbf{C}$, $\mathbf{D}$, and $\mathbf{H}$ must be reduced to those columns where the sensors are located

$$dimension(\mathbf{C}_c) = (number\ of\ nodes)\times(2\cdot number\ of\ modes) \tag{45}$$

$$\Rightarrow\ dimension(\mathbf{C}_{c-red}) = (number\ of\ sensors)\times(2\cdot number\ of\ modes) \tag{46}$$

$$dimension(\mathbf{D}_c) = (number\ of\ nodes)\times 1 \tag{47}$$

$$\Rightarrow\ dimension(\mathbf{D}_{c-red}) = (number\ of\ sensors)\times 1 \tag{48}$$

$$dimension(\mathbf{H}_c) = (number\ of\ nodes)\times 1 \tag{49}$$

$$\Rightarrow\ dimension(\mathbf{H}_{c-red}) = (number\ of\ sensors)\times 1 \tag{50}$$

Process and measurement noise must be assumed. Hence, they may be seen as observer design parameters (Kim et al. (2003), Sadri et al. (2002)). If measurements of, e.g., the disturbance forces and some nodal velocities are available, the intensities of process and measurement noise may be estimated from the alternating signal parts (AC) of these measurements. In this example, the measurement noise is assumed to count for 5% of the maximum value

$$E[w\cdot w^T] \approx \mathrm{var}(AC(w_{mea})) \tag{51}$$

$$E[v\cdot v^T] \approx \mathrm{var}(0.05\cdot AC(\dot{z}_{mea})) \tag{52}$$

Regulator design

The full state feedback (single actuator)

$$u = -\mathbf{K}\cdot\hat{\mathbf{x}} \tag{53}$$

minimizes the performance index

$$J = E[\mathbf{x}^{\mathbf{T}}\cdot\mathbf{Q}\cdot\mathbf{x} + u^T\cdot R\cdot u] \tag{54}$$

Besides the system matrices $\mathbf{A}_c$ and $\mathbf{B}_c$, the regulator gain matrix requires the state weight factor $\mathbf{Q}$ and the input weight factor R (single actuator) as regulator design parameters

$$\mathbf{K} = f(\mathbf{A}_c, \mathbf{B}_c, \mathbf{Q}, R) \tag{55}$$

$$\mathbf{Q} = \begin{bmatrix} q_{11} & 0 & \cdots & 0 \\ 0 & q_{22} & & \vdots \\ \vdots & & \ddots & 0 \\ 0 & \cdots & 0 & q_{2mm2mm} \end{bmatrix} \quad , \qquad R = 1$$

(56), (57)

The value of R may be set to 1 because the observer design only depends on the ratio of q_{ii} / R.

When designing the regulator, the following rule of thumb should be respected (Preumont (2002)): For every mode to be damped, the ratio of q_{ii} / R should be chosen the way that the negative real part of the observer pole is approximately 2-6 times larger than the negative real part of the corresponding regulator pole. The reason for this rule is that regulator poles are the poles of the closed-loop structure or, in other words, of the controlled plant (Fig. 118). Considering that large negative real parts of observer poles imply that estimation errors decay faster than the relevant dynamics of the plant, then, the reconstructed state variables follow closer the actual true state variables. Thus, small values of q_{ii} / R will produce a state estimate of high accuracy but with the drawback of increased tracking error. The ratio q_{ii} / R is the regulator tuning variable for the controller designer in order to find the desired compromise between tracking and estimation error. The example of pole placement depicted in Fig. 119 is the result of the following control requirements:

- The control target is to damp the first four structural modes.
- The observer poles should be at least 4 times “faster” than the regulator poles.
- If only the first four modes (control target) were observed, the estimated vibration state would be falsified due to the influence of the higher modes (5-…) of the real plant on the actual vibration state. However, a falsified state estimate leads to a non-optimal or even wrong state feedback and therefore to a deteriorated control performance. Hence, higher modes than only the controlled ones should be observed. The effect that unobserved modes falsify the state estimation and evoke a false state feedback is called spillover instability. The fact that the state estimation may only be based on a model of the plant is indicated again by the index c of the system matrices (Fig. 118). In the example shown here, the first eight modes are observed, although only the first four modes are to be controlled (damped).
- The matrix $\mathbf{Q}$ weights the modal state variables (Johnson et al. (1999)).

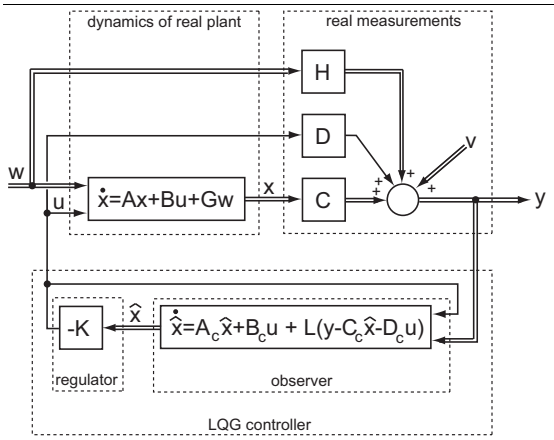

Fig. 118: Real plant with full state observer and regulator.

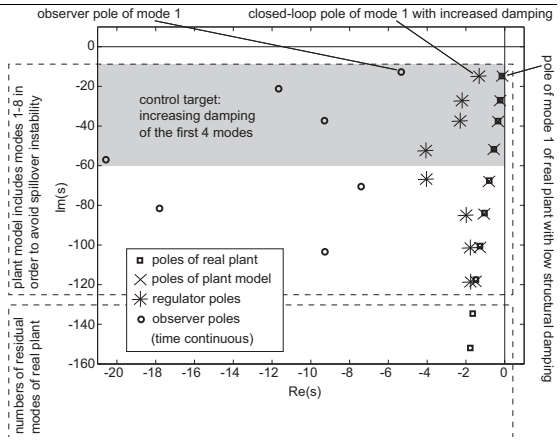

Fig. 119: Observer and regulator design.

Discrete-time control algorithm

For the implementation of control algorithms, nowadays, it is common to transform the algorithm into the discrete time domain. This enables to run the algorithm a defined clock rate (controller frequency). The algorithm is written in commercially available software which can be programmed on the host PC. The use of a PC makes it possible to adjust controller parameters on site. For real-time control, the software has to be downloaded on either a real-time controller box or on a PC real-time card. This is the normal procedure as long as the control algorithm is within the development process.

In the case of LQG control, the control algorithm consists of the following three steps: The measurement update at the time k, the extrapolation step from time k to $(k+1)$, and the step of state feedback (discrete-time system matrices indicated by index dt)

$$\hat{\mathbf{x}}[k \mid k] = \hat{\mathbf{x}}[k \mid k-1] + \mathbf{M}_{dt} \cdot \left(\mathbf{y}[k] - \mathbf{C}_{c-red-dt} \cdot \hat{\mathbf{x}}[k \mid k-1] - \mathbf{D}_{c-red-dt} \cdot u[k]\right) \tag{58}$$

$$\hat{\mathbf{x}}[k+1 \mid k] = \mathbf{A}_{c-dt} \cdot \hat{\mathbf{x}}[k \mid k] + \mathbf{B}_{c-dt} \cdot u[k] \tag{59}$$

$$u[k] = -\mathbf{K}_{dt} \cdot \hat{\mathbf{x}}[k \mid k] \tag{60}$$

The estimated measurements become as follows

$$\mathbf{y}_c[k] = \mathbf{C}_{c-red-dt} \cdot \hat{\mathbf{x}}[k \mid k] + \mathbf{D}_{c-red-dt} \cdot u[k] \tag{61}$$

The discretization may be realized using the Tustin approximation. Since the measurements $\mathbf{y}[k=0]$ at time $k=0$ already exist, the observation starts with a measurement update, followed alternating by an extrapolation step and measurement update (Geering (1990)).

Semi-active control

When controlling a structure using semi-active control devices such as, e.g., magnetorheological and electrorheological fluid dampers, the regulator should feed its output to the damping device only if structural energy shall be dissipated. Otherwise, if the state feedback desires active forces, the regulator output should be set to zero (Ying et al. (2002)), because semi-active devices cannot produce power (Fig. 120). This switching is called “clipping” of the control force which ends up in high frequency excitation and the fact that the clipped control force is not optimal anymore.

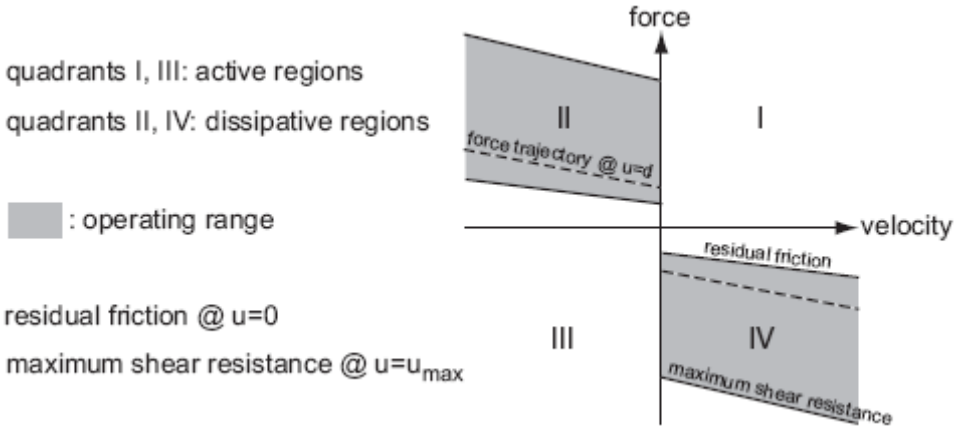

Fig. 120: Schematic operating range of magnetorheological fluid dampers.

The decision, if the regulator output is an active or passive force, may be based on the measured or estimated structural velocity at the position of the semi-active control device

$$u_{sa} = \begin{cases} -\mathbf{K}\cdot\hat{\mathbf{x}} & :\{(-\mathbf{K}\cdot\hat{\mathbf{x}}\cdot\dot{z}_{u-mea})<0\} \;\; or \;\; \{(-\mathbf{K}\cdot\hat{\mathbf{x}}\cdot\dot{z}_{u-est})<0\} \\ 0 & :\{(-\mathbf{K}\cdot\hat{\mathbf{x}}\cdot\dot{z}_{u-mea})\geq 0\} \;\; or \;\; \{(-\mathbf{K}\cdot\hat{\mathbf{x}}\cdot\dot{z}_{u-est})\geq 0\} \end{cases} \tag{62}$$

The force of magnetorheological and electrorheological fluid dampers, which represent often used semi-active control devices in the field of structural control, is not only limited by the maximum damper force but also by the residual friction at zero command input (Fig. 120). Hence, the optimum control force is not only constraint by the decision between active and dissipative forces but also by the limited operating range of magnetorheological and electrorheological fluid dampers. Not all desired forces, which are dissipative, may be tracked due to the limited damper’s operating range. This may be seen as a “secondary” clipping.

2.2.3.4 References

d’Azzo, J. J., and Houpis, C. H. (1995), *Linear Control System Analyzes and Design, Conventional and Modern*, Fouth Edition, McGraw-Hill (eds.), ISBN 0-07-016321-9.

Christenson, R. E., Spencer Jr., B. F., and Johnson, E. A. (2001), “Experimental Verification of Semiactive Damping of Stay Cables”, *Proceedings of the 2001 American Control Conference, IEEE*, Piscataway, NJ, USA, 6, 5058-5063.

Geering, H. P. (1990), *Mess- und Regelungstechnik*, 2. Auflage, Springer-Verlag Berlin Heidelberg.

Johnson, E. A., Spencer Jr., B. F., and Fujino, Y. (1999), "Semiactive Damping of Stay Cables: A Preliminary Study", *Proceedings of the 1999 17th International Modal Analysis Conference - IMAC*, 1, 417-423.

Kim, D.-H., Han, J.-H., Yang, S.-M., Kim, D.-H., Lee, I., Kim, C.-G., and Hong, C.-S. (2003), "Optimal Vibration Control of a Plate Using Optical Fiber Sensor and PZT Actuator", *Journal of Smart Materials and Structures*, 12(4), 507-513.

Ni, Y. Q., Cao, D. Q., Ko, J. M., and Chen, Y. (2000), "Neuro-Control of Inclined Sagged Cables Using Semi-Active MR Dampers", *Proceedings of International Conference on Advances in Structural Dynamics*, J. M. Ko and Y. L. Xu (eds.), Elsevier Science Ltd. (publ.), 2, 1373-1380.

Preumont, A. (2002), *Vibration Control of Active Structures*, Kluwer Academic Publishers, Dordrecht.

Raja, S., Prathap, G., and Sinha, P. K. (2002), "Active vibration control of composite sandwich beams with piezoelectric extension-bending and shear actuators", *Journal of Smart Materials and Structures*, 11(6), 63-71.

Ribakov, Y., and Reinhorn, A. M. (2003), "Design of Amplified Structural Damping Using Optimal Considerations", *Journal of Structural Engineering*, 129(10), 1422-1427.

Sadri, A. M., Wright, J. R., and Wynne, R. J. (2002), "LQG control design for panel flutter suppression using piezoelectric actuators", *Journal of Smart Materials and Structures*, 11(6), 834-839.

Ying, Z. G., Ni, Y. Q., and Ko, J. M. (2002), "Non-clipping optimal control of randomly excited nonlinear systems using semi-active ER/MR dampers", *Proceedings of SPIE, Smart Structures and Materials 2002: Smart Systems for Bridges, Structures, and Highways*, 4696, 209-218.

Zhang, J., and Roschke, P. N. (1999), "Active Control of a Tall Structure Excited by Wind", *Journal of Wind Engineering and Industrial Aerodynamics*, 83(1-3), 209-223.

2.2.3.5 Notations

Symbol	*Description*	*Unit*
$\mathbf{A}, \mathbf{B}, \mathbf{C}, \mathbf{D}, \mathbf{G}, \mathbf{H}$	matrices of SSR	-
$\mathbf{C}$	damping matrix	-
$\mathbf{I}$, $\mathbf{0}$	identity matrix, matrix of zeros	-
J	performance index / cost functional	-
$\mathbf{K}$	stiffness matrix, regulator gain matrix	-
$\mathbf{L}$	observer gain matrix	-
L	length	m
$\mathbf{M}$	mass matrix, diskrete-time observer gain matrix	-
$\mathbf{Q}$	state weight matrix	-

R	input weight factor	-
$\mathbf{V}$	intensity matrices of measurement noise	-
$\mathbf{W}$	intensity matrices of process noise	-
$\mathbf{\Phi}$	transformation matrix	-
$\mathbf{\Lambda}$	distribution vector of control forces	-
$\mathbf{\Theta}$	distribution vector of disturbance forces	-
c	viscosity	kg/s
$\mathbf{e}$	error vector	-
f	force; function	N; -
k	discrete-time variable; stiffness	-; kg/s^2
m	mass	kg
mm	number of modes	-
nn	number of nodal points	-
$\mathbf{q}$	only time-dependent vector of modes	-
r	Cartesian coordinate in the direction of the beam	m
t	time	s
u	controlled input variable of the plant	N
var	variance	-
$\mathbf{v}$	vector of measurement noise	-
$\mathbf{w}$	vector of disturbance	-
$\mathbf{x}$	vector of state variable	-
$\hat{\mathbf{x}}$	vector of estimated state variable	-
$\mathbf{y}$	vector of plant output variable	-
z	displacement	m
φ	mode shape	-
ω_0	fundamental circular frequency of undamped structure	rad/s
ζ	damping ratio	-

Superscripts	*Description*
T	transposed

Subscripts	*Description*
c	controller
dt	discrete-time

est	estimated
fe	finite element model
m	mode, modal coordinates
mea	measured
mm	number of modes
n	nodal point
nn	number of nodal points
red	reduced
sa	semi-active
u	controlled input variable of the plant

2.2.4 Other control algorithms

This chapter will give a brief introduction in fuzzy control and neural network control representing linear control approaches that are used fairly often in the field of structural control. Sometimes, they are used in combination with control approaches described in the previous chapters.

2.2.4.1 Fuzzy control

Fuzzy control represents an alternative control approach to the classical control theory which relies on the mathematical formulation of the plant (Liu et al. (2002)). The classical control strategies have been widely used for systems that may be approximated by linear, time-invariant models. However, these control strategies are rarely implemented for non-linear, time-variant, complex systems including noisy measurements. Here, fuzzy control may have its advantages.

The main idea of fuzzy control is to build a model of an expert operator who is capable of controlling the plant without thinking in mathematical terms. The person controls the plant by a set of linguistically expressed rules that result from the a priori know-how of the physics of the plant. Some characteristics of fuzzy logic may be listed here:

- Fuzzy logic is conceptually easy to understand.
- Fuzzy logic is tolerant of imprecise data.
- Fuzzy logic can model nonlinear functions of arbitrary complexity.
- Fuzzy logic is able to match any set of input-output data. This process is made particularly easy by adaptive techniques.
- Fuzzy logic can be built on top of the experience of experts.
- In direct contrast to neural networks, which take training data and generate opaque, impenetrable models, fuzzy logic relies on the experience of people who already understand the plant. When fuzzy control is called adaptive fuzzy control, then neural networks are used for the update of the implemented rules.
- Fuzzy logic can be blended with conventional control techniques and it does not necessarily replace conventional control methods. In many cases, fuzzy control systems augment them and simplify their implementation.
- Fuzzy logic is based on natural language.

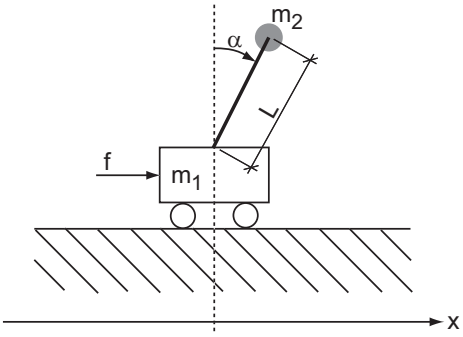

Fig. 121: Inverted pendulum on a cart.

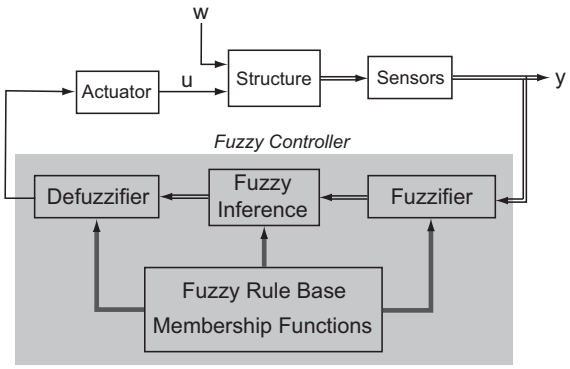

Fig. 122: Structure of a fuzzy controller.

Developing a fuzzy controller for the stabilization of the pendulum in the upper position using a motor-driven cart (Fig. 121) shall demonstrate how fuzzy control may work. The linearized equations for small angles and small angular velocities become

$$m_1 L\ddot{\alpha} = (m_1 + m_2)g\alpha - f\,, \quad m_1\ddot{x} = f - m_2 g\alpha \qquad (1), (2)$$

The fuzzy controller (Fig. 122) may be designed based on the measured angle and angular velocity

$$\mathbf{y} = [\alpha, \dot{\alpha}]^T \qquad (3)$$

Assuming a person should stabilize the inverted pendulum, the rules for pushing and pulling the cart may be similar to the fuzzy rules as following:

- If the angle is “slightly to the left” (SL) and the angular velocity is “moderate to the right”, then do not move the cart, i.e., the force shall be zero (Z).
- If the angle is “moderately to the left” (ML) and the angular velocity is “zero” (Z), then move the cart moderately to the left, i.e., the force shall accelerate the cart moderately to the left (ML).
- …

All rules for balancing the pendulum in the upper position are listed in Table 7. Each rule takes the two input variables, measured angle and measured angular velocity, and produces the output variable force, which drives the cart. The rules are IF-THEN rules, connected by logical operators such as AND, OR, and NOT. The resulting five membership functions for the example described here are: “moderately to the left“ (ML), “slightly to the left“ (SL), “zero force“ (Z), “slightly to the right“ (SR), and “moderately to the right“ (MR).

Table 7: Possible fuzzy rules for inverted pendulum.

force	$\dot{\alpha}$ =ML	$\dot{\alpha}$ =SL	$\dot{\alpha}$ =Z	$\dot{\alpha}$ =SR	$\dot{\alpha}$ =MR
α =ML	ML	ML	ML	ML	SL
α =SL	ML	ML	SL	Z	Z
α =Z	SL	SL	Z	SR	SR
α =SR	Z	Z	SR	MR	MR
α =MR	SR	MR	MR	MR	MR

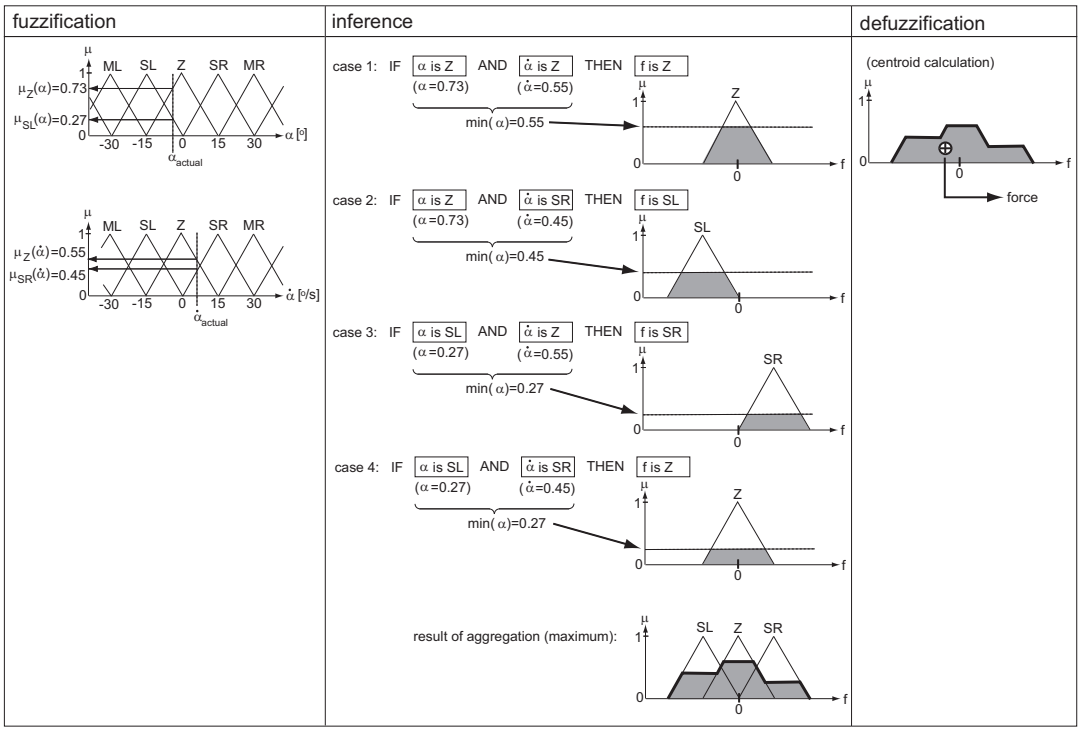

Fig. 123: The steps of fuzzification, inference, and defuzzification.

The fuzzy controller may be divided into the following three steps:

1. Fuzzification: All measured variables are transformed to the degrees of membership μ (Fig. 123 left). For this step, the range of each measured variable must be divided into sections.
2. Inference: According to the actual fuzzy variables, the corresponding rules are applied using the fuzzy operations for the logic operators, such as AND, OR, and NOT (Table 8). The implication method limits the membership function according to the degree of truth (minimum method, Fig. 123 middle). The result of the inference step is the aggregated membership function of the output variable (maximum method), in this case, the cart force.
3. Defuzzification: The most common defuzzification method is the centroid calculation, which returns the centre of area under the aggregated curve (Fig. 123 right). The position of the centre defines the value of the output variable, in this case the value of the force applied to the cart.

Table 8: Fuzzy logic operations.

AND	OR	NOT
min	max	additive complement

2.2.4.2 Neural network control

Generally, neural networks are models of static and dynamic structures that are not based on physical relations but consist on mathematical functions, whose coefficients result from “learning” or “training” using measurement data (Fig. 124). Besides the varied coefficients, also the functions itself and the structure of the neural network

may be varied. Once the structure and the functions are chosen, the neural network is trained by adjusting the coefficients using measured input data as long as the error between model output (output of the neural network) and the target data (measured plant output) is smaller than the desired error (Fig. 124).

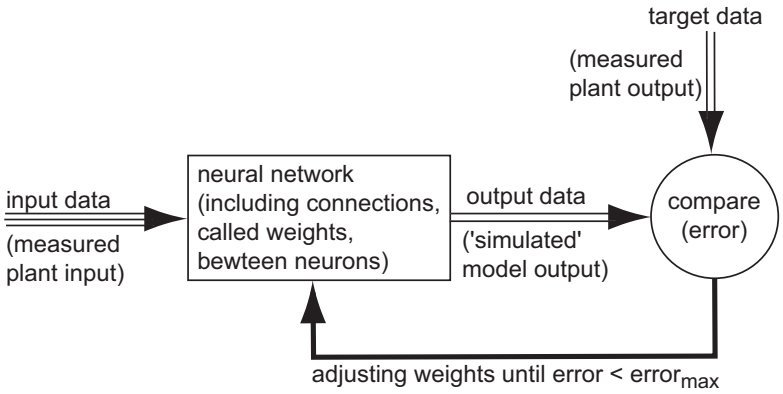

Fig. 124: Black box identification by training of neural networks.

Neural networks consist of neurons working in parallel and of several layers working in series (Fig. 125). The coefficients of the neurons are the weight factor w and the bias factor b, which scale the input i. The result n passes the transfer function f. Typical transfer functions (TF) may be:

- Hard limit TF, symmetric hard limit TF.
- Log sigmoid TF.
- Positive linear TF, linear TF.
- Saturation TF, symmetric saturation TF.
- Hyperbolic tangent sigmoid TF.
- Triangular basis TF.
- …

Several neurons together build one layer (Fig. 125). The number of neurons of each layer depends on the design of the neural network. One layer includes the same type of transfer function which must be assumed by the neural network designer. The choice of the type of transfer functions depends on the a priori know-how of the designer about the plant behaviour. Several layers together build one neural network.

Due to the black-box characteristics of neural networks, they may be the preferable modelling approach for non-linear, complex systems where physically based models lack. Within the field of structural control, neural networks are often used in order to replace a state estimator since state estimators often are based on rather simple finite element modelling approaches and therefore modelling errors may be too large (Xu et al. (2003a), Xu and Shen (2003b)). Then, using vibration measurement data of the target civil structure, a neural network may be trained in order to have a state estimator of high accuracy available for structural control.

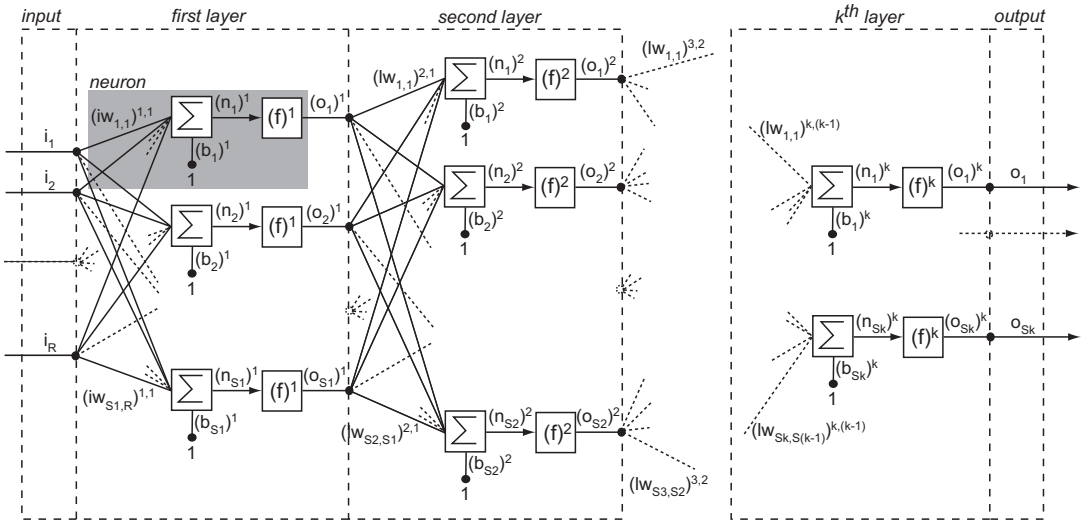

Fig. 125: Neural network consisting of neurons (weights and transfer function) and layers.

2.2.4.3 References

Liu, Y., Gordaninejad, F., Evrensel, C. A., Hitchcock, G., and Wang, X. (2002), "Variable Structure System Based Fuzzy Logic Control of Bridge Vibration Using Fail-Safe Magneto-Rheological Fluid Dampers", *Proceedings of SPIE*, S.-C. Liu and D. J. Pines (eds.), 4696, 219-227.

Xu, Z.-D., Shen, Y.-P., and Guo, Y.-Q. (2003a), "Semi-active control of structures incorporated with magnetorheological dampers using neural networks", *Journal of Smart Materials and Structures*, 12(1), 80-87.

Xu, Z.-D., and Shen, Y.-P. (2003b), "Intelligent Bi-state Control of the Structure with Magnetorheological Dampers", *Journal of Intelligent Material Systems and Structures*, 14(1), 35-42.

2.2.4.4 Notations

Symbol	*Description*	*Unit*
L	Length	m
b	bias factor	-
c	viscosity	kg/s
f	force; transfer function	N; -
g	gravitational acceleration	m/s^2
i	layer input variable, layer output variable	-
k	stiffness	kg/s^2
lw	weight factor	-
m	mass	kg
n	neuron output variable	-

o	layer output variable	-
u	controlled input variable of the plant	-
w	disturbance	N
$\mathbf{y}$	vector of plant output variables	-
x	displacement	m
α	angle	rad
μ	degree of membership	-

Superscripts	*Description*
T	transposed
k	number of layers

Subscripts	*Description*
R	number of input variables of the first layer
Sj	number of neurons of layer j

3 VIBRATION ISOLATION

The first subchapter presents passive isolators, whereas the second subchapter describes the concept of active vibration isolation.

3.1 Passive vibration isolation

3.1.1 Theoretical background

The goal of vibration isolation is to mitigate vibrations by reducing the mechanical interaction between the vibration source and the structure, equipment etc. to be protected. The general approach is to insert secondary mechanical components (anti-vibration mounts) between the vibration source and the receiver with the objective to avoid any state of significant excitation in the system. The concept of vibration isolation is illustrated in Fig. 126. A single degree of freedom system whose mass represents a structure, an equipment etc. is connected to a base support through an isolator. Generally, in vibration isolation, two cases are considered. In the first, the isolator protects the base support from the effects of dynamic force $F_S(t)$ acting directly on the supported structure. The goal of vibration isolation is to reduce the force $F_T(t)$ transmitted to the support. In the second case, the isolator protects the structure from the motion $u_S(t)$ of the base support. The goal is to reduce the absolute or relative displacement $u_T(t)$ respectively $u_T(t)-u_S(t)$ of the structure. The performance of an isolator is usually characterized by the transmissibility. It is defined by the ratio of the magnitude of the item (displacement, velocity, force etc.) transmitted by the isolator with respect to the magnitude of the exciting item.

A mechanical isolator is generally implemented as a system consisting of masses, springs and dampers. A simple model of an isolator consists of a linear spring and dashpot acting in parallel. For this isolator model, the transmissibility of the force T_F for harmonic force $F(t)$ acting on the structure is given by

$$T_F = T_u = \sqrt{\frac{1+(2\zeta s)^2}{(1-s^2)^2+(2\zeta s)^2}} \qquad (1)$$

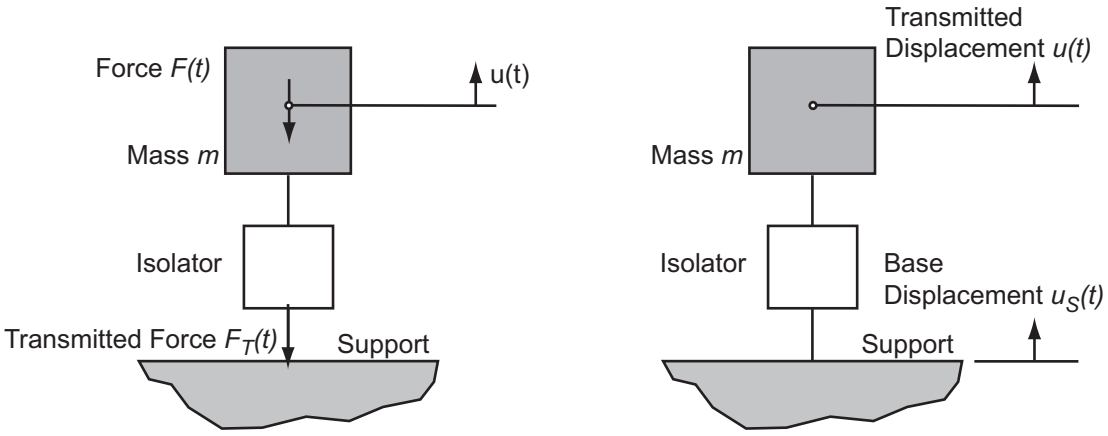

Fig. 126: Schematic representation of vibration isolation systems. Left: Isolation reducing the effects of the excitation force acting on the structure. Right: Isolation reducing the effects of a forced excitation of the support.

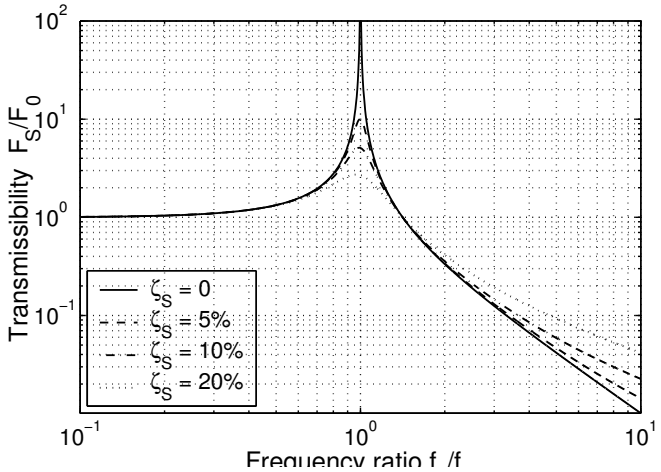

Fig. 127: Force transmissibility for an isolator consisting of a linear spring and dashpot acting in parallel for different damping ratios.

The absolute displacement transmissibility T_u for a harmonic forced displacement $u_S(t)$ at the support is described by exactly the same function as T_F. The force transmissibility T_F is illustrated in Fig. 127 for different damping ratios. This Figure shows that a significant reduction of the force as well as displacement amplitude is achieved for excitation frequencies being greater than natural frequency of the system. The application of this observation in vibration isolation is called low frequency tuning. It is characterized by selecting the natural frequency of the system to be significantly smaller than the main frequency content of the vibration source. Remarkably, in low frequency tuning, increasing the damping of the system does not improve the effectiveness of the isolation system.

An alternative vibration isolation approach consists in high tuning: The natural frequency of the system is chosen to be much greater than the main frequency content of the vibration source. In this approach, the amplitude of the transmitted force or displacement is similar to the amplitude of the excitation force or displacement. Therefore, no significant reduction can be achieved. However, high tuning reduces the risk of amplification due to resonance effects. In high tuning, the effect of damping is completely negligible. Similar transmissibility properties are obtained for non-viscous type of damping (Den Hartog (1931), Kelly (1997)).

Vibration isolation of equipment is a well established technology. Its theory and practice are covered in many books and a vast number of papers (e.g. Beranek and Vér (1992), Snowden (1979)). The first building to be isolated from ground-born vibration was situated directly above a station of the London Underground (Derham et al. (1975)). Now, the use of vibration isolation for entire building from rail traffic is becoming a common practice (Crockett (1982), Derham and Thomas (1980), Grootenhuis and Crockett (1978), Grootenhuis (1982)).

3.1.2 Design issues

3.1.2.1 Low tuning

Low tuning is the standard approach in vibration isolation because of its high effectiveness. The effectiveness increases by reducing the natural frequency of the isolated system with respect to the dominant frequency content of the excitation force. Therefore, the lowest possible frequency ratio should be addressed. However, in practice, the low tuning of natural frequency is mainly limited by displacement or velocity restrictions. In vibration isolation of manufacturing machines, production requirements usually restrict the softness of the isolation to avoid too large displacements under dead loads. The criteria provided by machine manufacturers have to be considered in the design process. The effect of all degrees of freedom (translational

and rotational as well as) has to be considered in the design in order to avoid unacceptable parasitic vibrations induced by the isolation devices.

Special attention has to be paid for start-up and shut-down of machines. During these operations, the dominant excitation force frequencies may meet for a certain time period the natural frequency of the secondary system producing significant dynamic displacements. These displacements have to be controlled either by additional vibration control devices or by a sufficiently fast start-up and shut-down operation.

3.1.2.2 High tuning

High tuning is usually applied when low tuning turns out to be impractical. High tuning is mainly applied in isolating machine vibrations when low tuning fails to meet production requirements because of a too soft secondary system. The main design issue is to provide the secondary system with a natural frequency being much larger than the highest relevant excitation force components. Detailed information about the frequency spectrum of excitation forces is mandatory for a correct tuning. If this information is partially missing, a safety factor reflecting these uncertainties may be included when specifying the natural frequency of the secondary system. Generally, in high tuning, start-up and shut-down of a machine is of little concern.

3.1.2.3 Base isolation

Base or seismic isolation of a complete structure is based on a low tuning concept (Kelly (1997)). However, because of the high energy involved during earthquake motion, several specific aspects have to be considered in the design process. The most important requirements for base isolation bearings concern the lateral flexibility and energy dissipation during earthquake loading as well as rigidity under dead loads and low level horizontal loading (e.g. wind). Shear and axial stiffness, damping properties of rubber bearing are usually provided by the manufacturer.

The period of vibration of the based isolated structure is designed to be significantly greater than the period of natural frequency of the non-isolated structure as well as the dominant period of excitation of earthquake motion. For structures with regular shape, the fundamental frequency of the isolated structure can be roughly estimated by the formula

$$f = \frac{1}{2\pi}\sqrt{\frac{m}{k}} \tag{2}$$

where m is the total mass of the building and k is the shear stiffness of the rubber bearing.

3.1.3 Testing and validation

The testing and validation of vibration isolated structures are usually done under operational conditions. In vibration isolation for machine induced vibrations, the tests are done by running the machines under the relevant operational conditions. The vibrations under start-up and shut-down procedures of the machines should also be recorded.

For base isolated structures, ambient vibration tests are the cheapest method to validate the design for low level horizontal loadings. An experimental validation of high

level loading scenarios is in most cases not feasible. A long term continuous monitoring system may be able to provide information for validation.

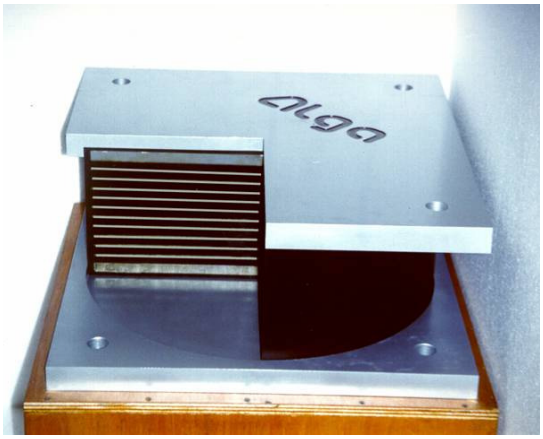

Fig. 128: Rubber bearing applied for base isolation.

Fig. 129: Shear displacement test of a rubber bearing for base isolation.

3.1.4 Implementation

The vibration isolation devices used in vibration isolation comprise steel springs, elastomeric and natural rubber pads as well as air suspension systems. These devices differ considerably with respect to size, mass, stiffness and operating frequency.

For vibration isolation of machines, the vibration isolation devices may be mounted directly under the machine. Mounting machines on a base is suitable for large dynamic forces, strongly asymmetrical machines or machines with a small mass to avoid a too soft support. The mass of the base should be very stiff and exceed significantly the mass of the machine (up to a ratio of 8:1). A large base mass reduces significantly the dynamic displacements of the secondary system. For vibration isolation in existing structures, the mass of the base may be limited by the strength of the supporting structural elements.

In base isolation of structures, natural rubber bearings are the most widely used devices. Such bearings consist of layers of rubber sheets bonded on steel plates (Fig. 128). The steel plates constrain the lateral deformation of the relative soft rubber under vertical dead loads. The vertical stiffness of rubber bearings are several order of magnitude greater than the horizontal stiffness. The lateral flexibility of bearings is tested under extreme displacements (up to 500% shear strain, Fig. 129).

3.1.5 References

Beranek, L. L., and Vér, I. L. (1992), *Noise and vibration control engineering: principles and applications*, Beranek, L. L. and Vér, I. L. (eds.), New York, J. Wiley and Sons.

Crockett, J. H. A. (1982) “Early Attempts, Research and Modern Techniques for Insulating Buildings”, *Proceedings of the International Conference on Natural Rubber for Earthquake Protection of Buildings and Vibration Isolation*, Kuala Lumpur, Malay-

sia: Rubber research Institute of Malaysia & the International Society for seismic isolation, 15-44.

Den Hartog, J. P. (1931), “Forced Vibrations with Combined Coulomb and Viscous Friction”, *Transactions of the American Society for Mechanical Engineering*, 53(9), 107-115.

Derham, C. J., and Waller, R. A. (1975), “Luxury Without Rumble”, *The Consulting Engineer*, 39(49).

Derham, C. J., and Thomas, A. G. (1980), “The Design and Use of Rubber Bearings for Vibration Isolation and Seismic Protection of Structures”, *Engineering Structures*, 2(3), 171-175.

Grootenhuis, P., and Crockett, J. H. A. (1978), “Vibration Isolation in Large Structures with Resilient Materials”, *Proceedings of the Institution of Civil Engineers Part 1-Design and Construction*, 64(MAY), 365-367.

Grootenhuis, P. (1982), “Vibration Isolation of Buildings: Some Basic Principles”, *Proceedings of the International Conference on Natural Rubber for Earthquake Protection of Buildings and Vibration Isolation*, Kuala Lumpur, Malaysia: Rubber research Institute of Malaysia & the International Society for seismic isolation. 1-14.

Kelly, J. M. (1997), *Earthquake-Resistant Design with Rubber*, Second ed. 1997, London: Springer.

Snowden, J. C. (1979), “Vibration Isolation: Use and Characterisation”, NBS Handbook, Vol. 128, U.S. National Bureau of Standards.

3.1.6 Notations

Symbol	*Description*	*Unit*
F	force	N
T	force transmissibility	N
f	frequency	Hz
u	displacement	m
ζ	damping ratio of isolated system	-

Subscripts	*Description*
S	excitation
T	transmitted
f	force
u	displacement

3.2 Active vibration isolation

3.2.1 Scope

Vibration isolation may be necessary for the following two general cases:

- Operating systems, such as engines, turbines etc., generate oscillatory forces which may excite the supporting structure (Fig. 130 i)). The target is isolating the support structure from the vibrating system in order to guarantee that, e.g., the driver in a passenger car may not be disturbed by the vibrations of the engine.
- A measurement device, such as an optical sensor, or a high precision milling machine may only work properly when it does not vibrate. Thus, vibrations of the support structure connected to these sensitive devices have to be isolated (Fig. 130 ii)).

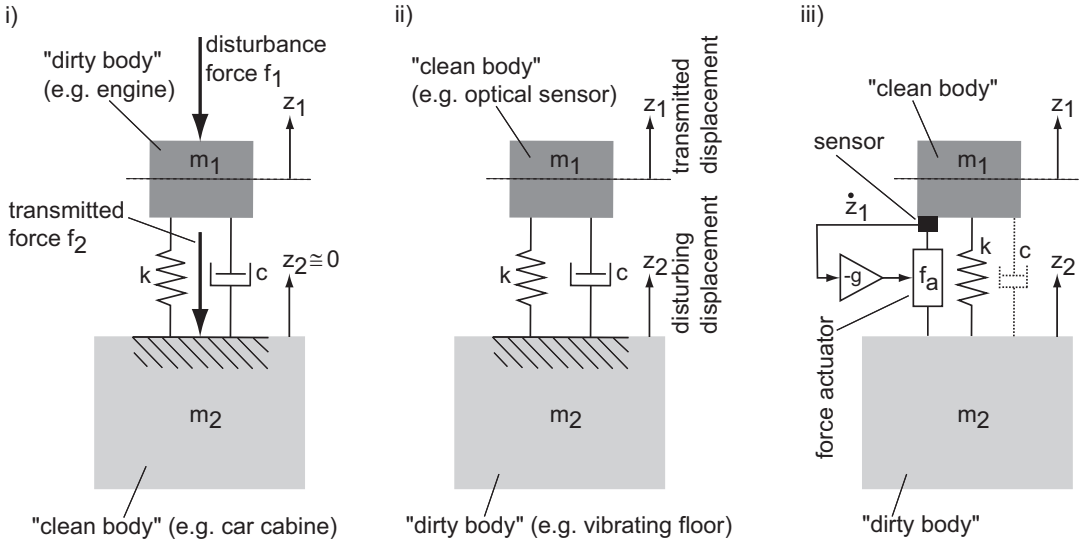

Fig. 130: i) Operating system (1) generating disturbance forces. ii) Sensitive device (1) excited by vibrating support structure (2). iii) Active vibration isolation with velocity feedback and force actuator ("skyhook damper").

For these two cases, the vibrating system is called "dirty body", the system to be isolated "clean body", and the entire system passive isolator. The disturbance or excitation force may be known (deterministic) or unknown (stochastic). Deterministic disturbances, e.g., produced by a rotating engine, may be isolated by feed forward control. Stochastic disturbances are typical for, e.g., earthquake excitations, wind loading, and any other random impact. Then, active vibration isolation requires feedback control, which will be described in the following, starting with the passive case of vibration isolation.

3.2.2 Passive isolator

In order to develop the control law for the active isolator, we start with the mathematical description of the passive isolator. The governing equations of the system i) in the time and Laplace domain become (Geering (1990))

$$m_1\ddot{z}_1 + c\dot{z}_1 + kz_1 = f_1 \quad \Leftrightarrow \quad Z_1(s)\cdot\left\{s^2\cdot m_1 + s\cdot c + k\right\} = F_1(s) \tag{1}$$

$$c\dot{z}_1 + kz_1 = f_2 \quad \Leftrightarrow \quad Z_1(s)\cdot\{s\cdot c + k\} = F_2(s) \tag{2}$$

Combining these two equations, the transmissibility from the disturbance force to the force acting on the clean body yields

$$\frac{F_2(s)}{F_1(s)} = \frac{s\cdot c + k}{s^2\cdot m_1 + s\cdot c + k} = \frac{s\cdot 2\zeta\omega_0 + \omega_0^2}{s^2 + s\cdot 2\zeta\omega_0 + \omega_0^2} \tag{3}$$

The transmissibility from the disturbing displacement to the displacement of the clean body in the time and Laplace domain becomes

$$m_1\ddot{z}_1 + c(\dot{z}_1 - \dot{z}_2) + k(z_1 - z_2) = 0 \quad \Leftrightarrow \quad Z_1(s)\cdot\{s^2\cdot m_1 + s\cdot c + k\} - Z_2(s)\cdot\{s\cdot c + k\} = 0 \tag{4}$$

$$\frac{Z_2(s)}{Z_1(s)} = \frac{s\cdot c + k}{s^2\cdot m_1 + s\cdot c + k} = \frac{s\cdot 2\zeta\omega_0 + \omega_0^2}{s^2 + s\cdot 2\zeta\omega_0 + \omega_0^2} \tag{5}$$

The identical forms of the two transmissibility equations demonstrate that the two isolation problems may be treated in the same way. The transmissibility or transfer function is analyzed in the Bode Diagram (Fig. 131). The magnitude of the transfer function is depicted for different values of the damping ratio ζ (Hamm (2002), Weber (2002)). The diagram points out:

- The region of amplification is below the critical frequency of $\sqrt{2}\omega_0$, the section above represents the region of attenuation.
- The passive isolator shows a sufficient “roll-off” behaviour of -40 dB/dec only for the undamped case, where the transmissibility is proportional to $1/s^2$ for high frequencies, but low damping results in large amplitudes around the natural frequency of the spring-mass-system.
- Increasing the damping may reduce the amplitudes around resonance frequency of the passive isolator but leads to a “roll-off” behaviour of only -20 dB/dec due to the transmissibility being proportional to $1/s$ for high frequencies. A decay rate of -20 dB/dec may not be sufficient for damping vibrations of high frequencies.

As a result, the ideal isolator should show high damping below the critical frequency for reduction of the resonance peak of the isolator and low damping above the critical frequency in order to suppress vibrations of high frequencies. Such a frequency dependent damping may only be realized by an active isolator, which consists of a feedback controlled actuator instead of the dash-pot element only (Fig. 130 iii)).

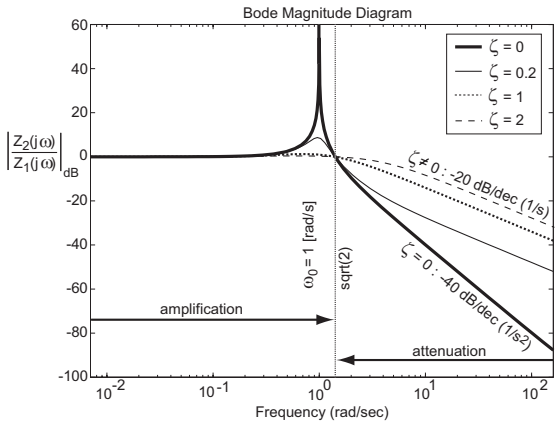

Fig. 131: Magnitude of transmissibility for different damping ratios.

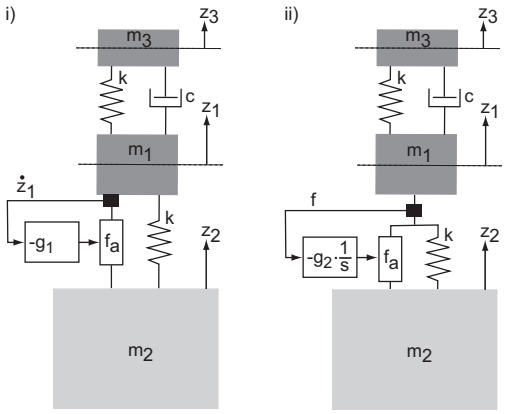

Fig. 132: i) Velocity feedback for flexible clean body. ii) Force feedback for flexible clean body.

3.2.3 Active isolator

3.2.3.1 Velocity feedback

The equation of motion of the clean body (the equation of the dirty body is not of interest) including the dash-pot for the active isolator of Fig. 130 iii) is

$$m_1\ddot{z}_1 + c\left(\dot{z}_1 - \dot{z}_2\right) + k\left(z_1 - z_2\right) = f_a \tag{6}$$

If we assume a sensor signal being proportional to the actual velocity at actuator location, this signal may be used within a negative feedback for the control of the actuator force in order to control the damping of the clean body. The equation of motion becomes

$$m_1\ddot{z}_1 + c\left(\dot{z}_1 - \dot{z}_2\right) + k\left(z_1 - z_2\right) = -g\cdot\dot{z}_1 \quad \Leftrightarrow \quad Z_1(s)\cdot\left\{s^2\cdot m_1 + s\cdot\left(c+g\right)+k\right\} = Z_2(s)\cdot\left\{s\cdot c + k\right\} \tag{7}$$

Since the control force is proportional to the absolute velocity of the clean body (Fig. 130 iii)), this control approach is also called “skyhook” damper (Lee and Jeon (2002), Preumont (2002)). Assuming the influence of the constant dash-pot on the overall damping may be negligible compared to the influence of the controlled force actuator, the transmissibility becomes

$$\frac{Z_1(s)}{Z_2(s)} = \frac{s\cdot c + k}{s^2\cdot m_1 + s\cdot\left(c+g\right)+k} \xrightarrow{c<<1} \frac{1}{\frac{m_1}{k}s^2 + s\cdot\frac{g}{k}+1} = \frac{\omega_0^2}{s^2 + s\cdot 2\zeta\omega_0 + \omega_0^2} \tag{8), (9}$$

From the equation above, the value of the feedback gain g for critical damping $\zeta = 1$ is readily visible

$$\frac{g}{k} = 2\frac{\zeta}{\omega_0} \xrightarrow{\zeta=1} g = 2k\frac{1}{\omega_0} = 2k\sqrt{\frac{m_1}{k}} = 2\sqrt{k\cdot m_1} \tag{10}$$

The resulting properties of the optimally tuned active isolator are summarized in Table 9. In order to guarantee a sufficient good "roll-off" performance of the active isolator, a constant viscous damper should be omitted if possible.

Table 9: Properties of critically damped active isolator.

Feedback gain for critical damping [-]	Corner frequency [rad/s]	Decay rate [dB/dec]
$g(\zeta = 1) = 2\sqrt{k \cdot m_1}$	$\omega_0 = \sqrt{k/m_1}$	-40

3.2.3.2 Force feedback

Velocity feedback for active isolation may be realized using an accelerometer and integrating the measurement signal. Since the acceleration of the clean body is proportional to the total force acting on the clean body

$$\ddot{z}_1 = \frac{1}{m_1} \cdot \{f_a - k(z_1 - z_2)\} \tag{11}$$

active isolation may also be realized by negative feedback of the total force (Fig. 132 ii), without flexible appendix, dash-pot omitted). The feedback gain is different compared to acceleration measurement. The transfer function of the resulting open-loop is identical to that described above. The control law for the force actuator with total force measurement and additional filter becomes

$$f_a = -\frac{g}{s} \cdot f_{mea} \cdot G_F \tag{12}$$

For clean bodies of, e.g., some tons, the main advantage of force feedback is that the values of the total force are more or less within the range of commercially available force sensors. In contrast, the values of accelerations that result from such clean bodies are very small. Accelerometers with high sensitivity for such small accelerations are hardly commercially available.

3.2.3.3 Flexible clean body

The clean body was assumed to be rigid for velocity and force feedback as well. Then, velocity and force feedback end up in the same open-loop behaviour. However, if the clean body is flexible (Fig. 132 i) and ii)), velocity and force feedback may produce different Root Loci of the open-loop depending on the mass m_3 assumed for the flexible appendix of the clean body:

- Mass m_3 small compared to m_1: The flexible appendix behaves much more rigid than the isolation system. Force and velocity feedback show a stable Root Locus for the two modes.
- Mass m_3 large compared to m_1: The Rot Locus of force feedback is still stable, whereas the Root Locus of velocity feedback shows an unstable loop for the mode of lower frequency. However, in reality, this control loop may work still stable due to the structural damping, which - neglected in the example here - moves the unstable loop into the left half plane.

3.2.4 References

Geering, H. P. (1990), *Mess- und Regelungstechnik*, 2. Auflage, Springer-Verlag Berlin Heidelberg.

Hamm, P. (2002), "Vibrations of wooden footbridges induced by pedestrians and a mechanical exciter", *Proceedings of the International Conference on Footbridge*, Paris, France, 20-22 November 2002, on CD, AFGC – OTUA (eds.).

Lee, Y., and Jeon, D. (2002), "A Study on The Vibration Attenuation of a Driver Seat Using an MR Damper", *Journal of Intelligent Material Systems and Structures*, 13(7/8), 575-579.

Preumont, A. (2002), *Vibration Control of Active Structures*, Kluwer Academic Publishers, Dordrecht.

Weber, B. (2002), "Damping of vibrating footbridges", *Proceedings of the International Conference on Footbridge*, Paris, France, 20-22 November 2002, AFGC – OTUA (eds.), on CD.

3.2.5 Notations

Symbol	*Description*	*Unit*
$F(s)$	Laplace transform of $f(t)$	-
G	transfer function	-
$Z(s)$	Laplace transform of $z(t)$	-
c	viscosity	kg/s
f	force	N
g	feedback gain	-
k	stiffness	kg/s^2
m	mass	kg
s	complex frequency variable	-
z	displacement	m
ω_0	fundamental circular frequency of the undamped structure	rad/s
ζ	damping ratio	-

Subscripts	*Description*
F	filter
a	actuator
mea	measured